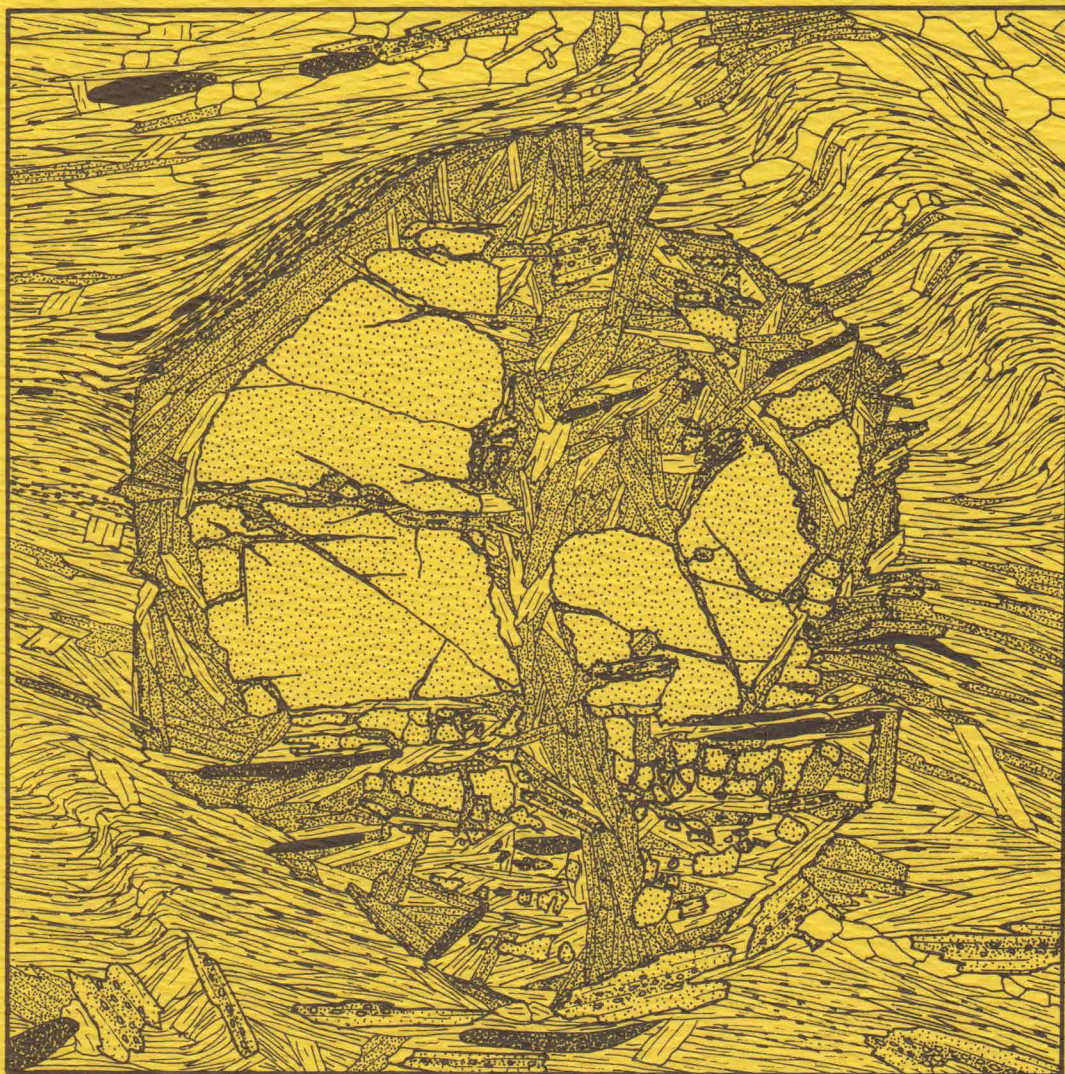


# RETROGRADE METAMORPHISM OF THE LOWER DEVONIAN LITTLETON FORMATION IN THE NEW SALEM AREA, WEST-CENTRAL MASSACHUSETTS

BY KURT T. HOLLOCHER



1 mm ———  
Sample NS 71  
Retrograded Garnet

CONTRIBUTION NO. 37  
DEPARTMENT OF GEOLOGY & GEOGRAPHY  
UNIVERSITY OF MASSACHUSETTS  
AMHERST, MASSACHUSETTS



RETROGRADE METAMORPHISM OF THE LOWER DEVONIAN  
LITTLETON FORMATION IN THE NEW SALEM AREA,  
WEST-CENTRAL MASSACHUSETTS

by

Kurt T. Hollocher

Contribution No. 37

Department of Geology and Geography

University of Massachusetts

Amherst, Massachusetts

April, 1981



## TABLE OF CONTENTS

ABSTRACT.....	1
INTRODUCTION.....	3
Location.....	3
Geography and Quaternary Cover.....	3
Regional Setting and Stratigraphy.....	5
Introduction.....	5
Stratigraphy.....	8
Deformation and metamorphism.....	10
Previous Work.....	12
Purpose of Study.....	13
Methods of Investigation.....	14
General methods.....	14
Polished thin sections.....	14
Electron microprobe analysis.....	16
Acknowledgements.....	17
DESCRIPTION OF ROCKS.....	17
Partridge Formation.....	17
Clough Quartzite.....	18
Fitch Formation.....	18
Littleton Formation.....	18
Distribution of Metamorphic Zones.....	20
Description of Analyzed Samples.....	23
U01A.....	23
NS118.....	26

NS18.....	26
NS87.....	26
NS85.....	27
NS90.....	27
NS71.....	27
MINERALOGY AND CRYSTAL CHEMISTRY.....	28
Introduction.....	28
Analyses.....	29
Sillimanite.....	30
Field occurrence.....	30
Textures in thin section.....	32
Staurolite.....	34
Field distribution and habit.....	34
Appearance in thin section.....	35
Structural formula and crystal chemistry.....	39
Structural formula recipe.....	41
Chemical analyses.....	42
Garnet.....	45
Field distribution and habit.....	45
Textures in thin section .....	46
Chemical zoning.....	48
Rim compositions.....	57
Discussion of garnet stoichiometry.....	62
Biotite.....	63
Field distribution and appearance.....	63

Appearance in thin section.....	64
Chemistry.....	66
Muscovite.....	80
Field habit.....	80
Appearance in thin section.....	80
Chemistry.....	82
Chlorite.....	100
Field appearance.....	100
Optical properties.....	101
Appearance in thin section.....	102
Chemistry.....	103
Chloritoid.....	117
Field occurrence.....	117
Appearance in thin section.....	117
Chemistry.....	119
Plagioclase.....	119
Field appearance.....	119
Appearance in thin section.....	121
Chemistry.....	122
K-feldspar.....	125
Occurrence.....	125
Chemistry.....	126
Ilmenite.....	129
Occurrence and habit.....	129
Chemistry.....	130

Anatase.....	138
Occurrence and habit.....	138
Chemistry.....	141
Stability.....	141
Sphene.....	144
Occurrence.....	144
Chemistry.....	145
Rutile.....	151
Apatite.....	152
Tourmaline.....	154
Zircon.....	155
Graphite.....	155
Allanite.....	156
Pyrite.....	157
Quartz.....	158
Weathering Products.....	158
Cathode Luminescence.....	159
PHASE RELATIONS.....	160
Introduction.....	160
Feldspars.....	160
Micas.....	162
Alkali-Alumina System.....	166
TiO <sub>2</sub> -FeO-H <sub>2</sub> O System.....	168
AKFM Tetrahedron.....	170
Muscovite Projection.....	172

RETROGRADE REACTIONS.....	174
Introduction.....	174
Sillimanite-Out Reaction.....	176
Staurolite-Out Reaction.....	180
K-feldspar-In Reaction.....	183
Garnet-Out Reactions.....	187
Introduction.....	187
Garnet rim, biotite present reaction.....	189
Garnet core, biotite present reaction.....	191
Garnet core, biotite absent reaction.....	191
Biotite-Out Reactions.....	194
Chloritoid-In Reactions.....	197
Introduction.....	197
Garnet-chlorite continuous reaction.....	198
Phengitic muscovite continuous reaction.....	200
Manganese stabilization of chloritoid.....	201
Ilmenite-Out, Anatase-In Reaction.....	205
Sulfide-Silicate Reactions.....	207
Summary of Retrograde Reactions.....	210
Mobility of Chemical Components.....	212
CONDITIONS OF METAMORPHISM.....	215
Introduction.....	215
Published Data on Univariant Reactions.....	216
Introduction.....	216
Explanation of reactions.....	217



Probable field of prograde metamorphism.....	220
Probable field of retrograde metamorphism.....	222
Coexisting Mineral P-T Estimates.....	222
Garnet-biotite thermometers.....	222
Muscovite-paragonite solvus.....	224
White mica-alkali feldspar solvi.....	226
Muscovite celadonite component.....	226
Alkali feldspar solvus.....	228
Cordierite equilibria.....	229
Garnet-plagioclase calcium partitioning.....	230
Biotite-muscovite titanium partitioning.....	231
Independent Constraints for Metamorphic Conditions.....	232
Prograde metamorphism.....	232
Retrograde metamorphism.....	233
Discussion of Prograde P and T.....	236
Discussion of Retrograde P and T.....	237
METAMORPHIC FLUID COMPOSITION.....	238
TIMING OF RETROGRADE METAMORPHISM.....	242
WATER FOR RETROGRADE HYDRATION REACTIONS.....	243
Quantity.....	243
Water Source and Consequences of Expansion.....	245
SUMMARY AND CONCLUSIONS.....	247
REFERENCES CITED.....	250

## LIST OF TABLES

1	Observed and inferred prograde assemblages.....	22
2	Observed retrograde assemblages in schists.....	23
3	Estimated modes for the analyzed samples.....	25
4	Staurolite cation site information.....	40
5	Staurolite electron microprobe analyses.....	43
6	Garnet microprobe traverse analyses.....	51
7	Garnet rim analyses.....	58
8	Biotite analyses.....	67
9	Muscovite analyses.....	83
10	Chlorite analyses.....	104
11	Chloritoid analyses.....	120
12	Plagioclase analyses.....	123
13	K-feldspar analyses.....	127
14	Ilmenite analyses.....	133
15	Average anatase analysis.....	142
16	Sphene analyses.....	146
17	Cathode luminescence of minerals.....	159
18	Ideal garnet core and rim compositions.....	189
19	Chlorite Al/Al+M <sup>+2</sup> composition versus assemblage.....	192
20	Average Fe/Fe+Mg and Fe/Fe+Mn ratios for garnet, chlorite, and chloritoid.....	204
21	Listing of the mobility of chemical components.....	214
22	Explanation for reactions in Figure 48.....	218
23	Garnet-biotite pair temperature estimates.....	224
24	White mica solvus minimum temperature estimates.....	225
25	Phengitic muscovite temperature estimates.....	227
26	Alkali feldspar geothermometer temperature estimates.....	228
27	Summary explanations for Figure 49.....	234
28	Model of retrograde metamorphic assemblages.....	244
29	Volume and water changes in retrograded zone.....	245

## LIST OF FIGURES

1	Location map of study area.....	4
2	Geologic map and stratigraphic column of central Massachusetts.....	6
3	Map of prograde and retrograde metamorphic assemblages.....	21
4	Map showing sample locations.....	24
5	Map showing prograde and retrograde sillimanite isograds.....	31
6	Sketches of fibrolite in thin section.....	33
7	Map showing the retrograde staurolite isograd.....	36
8	Sketches of staurolite and pseudomorph after staurolite, in thin section.....	37
9	Map showing chlorite rim thickness on garnets and the retrograde garnet isograd.....	47
10	Sketches of garnets in thin section.....	49
11	Plotted microprobe analyses from the garnet traverse in sample U01A.....	55
12	Sketch of biotite in an early stage of retrograde alteration, in thin section.....	66
13	Plot of all biotite analyses, K+Na versus K/K+Na.....	77
14	Plot of all biotite analyses, Al/Al+Si versus Fe/Fe+Mg.....	78
15	Plot of all muscovite analyses, K+Na versus K/K+Na.....	97
16	Plot of all muscovite analyses, Fe+Mn+Mg versus K/K+Na ratio.....	99
17	Plot of all chlorite analyses, Al/Al+Si versus Fe/Fe+Mg.....	116
18	Composite drawing of chloritoid in thin section.....	118
19	Drawings of ilmenite in thin section.....	131
20	Drawing of anatase, in reflected light.....	140
21	Composite sketch of sphene, anatase, and ilmenite in sample NS90, in thin section.....	145
22	Plots of chemical data for sphene.....	150
23	Sketch of rare rutile from sample NS101, in thin section.....	152
24	Sketches of apatite, in thin section.....	153
25	An-Ab-Or ternary feldspar plot.....	161

LIST OF FIGURES  
(Continued)

26	Plot of average mica compositions, octahedral site occupancy versus K/K+Na ratio.....	162
27	Plot of all mica analyses, $M^{+2} + Ti + (Si-3)$ versus Al+Cr, showing sample tie lines.....	164
28	Detail of tie lines in Figure 27.....	165
29	Alkali- alumina ternary system, showing feldspars and muscovite.....	167
30	TiO <sub>2</sub> -FeO-H <sub>2</sub> O ternary system, showing path of bulk composition and mineralogy.....	169
31	Schematic of the AKFM tetrahedral system.....	171
32	Muscovite projection of averaged analytical data.....	173
33	Projections showing the prograde sillimanite-in and retrograde sillimanite-out reactions.....	177
34	Schematic of the sillimanite-out reaction.....	180
35	Projections showing the prograde staurolite-in and retrograde staurolite-out reactions.....	182
36	Schematic of the staurolite-out reaction.....	184
37	Projections showing the K-feldspar-in reaction.....	186
38	Schematic showing the K-feldspar-in reaction.....	188
39	F-M edge projection showing the biotite present, garnet-out reaction.....	190
40	Expanded muscovite projection showing how assemblage effects chlorite composition.....	193
41	Schematic diagrams of the three garnet-out reactions.....	195
42	Expanded muscovite projection of a chloritoid-in mechanism.....	199
43	Expanded F-M edge projection of a chloritoid-in mechanism.....	202
44	Expanded Fe-Mn-Mg ternary system showing manganese stabilized chloritoid-in mechanism.....	203
45	Schematic of the ilmenite-out, anatase-in reaction.....	207
46	Hypothetical sulfide-silicate phase relations in the MgO-FeO-S ternary system.....	209
47	Muscovite projections summarizing retrograde phase relation changes.....	211

LIST OF FIGURES  
(Continued)

48	Mode variation ("fish") diagram summarizing assemblage changes with retrograding.....	213
49	Published reaction lines pertinent to the retrograded area.....	219
50	Summary of estimates of prograde and retrograde pressures and temperatures.....	235
51	Plot of oxygen fugacity versus temperature, showing the constrained fields of prograde and retrograde metamorphic conditions.....	239



## ABSTRACT

The retrograde zone occupies a triangular area about 4 x 13 km in the Prescott syncline, bounded by the main body of Monson Gneiss on the east and the Kempfield gneiss anticline on the west, and truncated to the south by the Middle Devonian Prescott Intrusive Complex. The most severely retrograded rocks are in the Littleton Formation, straddling the axial surface of the syncline. Acadian prograde metamorphism in schists reached staurolite or sillimanite-muscovite grade, producing the assemblage: Quartz-muscovite-biotite-garnet-staurolite-ilmenite-albite-graphite+sillimanite.

Systematic hydration of the prograde assemblage by an influx of water shifted the rocks toward limiting chlorite-K-feldspar and chlorite-chloritoid assemblages. Retrograde sillimanite, staurolite, and garnet isograds have been mapped, representing the generalized retrograde reactions: Biotite + prograde mineral  $\pm$  quartz + H<sub>2</sub>O = chlorite + muscovite  $\pm$  quartz. Biotite becomes associated with K-feldspar early in the sequence by the reaction: Biotite + muscovite + quartz + H<sub>2</sub>O = chlorite + K-feldspar. Colorless to blue zoned anatase is common as pseudomorphs after ilmenite, produced by the reaction: Ilmenite + aluminous mineral + quartz + H<sub>2</sub>O = chlorite + anatase.

The proposed retrograde hydration reactions are not the reverse of prograde dehydration reaction steps, probably due to severe disequilibrium between prograde and retrograde assemblages. Retrograde reactions cause a continuous increase in coexisting biotite and Chlorite Fe/Fe+Mg ratios; respectively from 0.52 and 0.48 in samples

containing relict staurolite, up to 0.64 and 0.62 in rocks containing muscovite-chlorite pseudomorphs after staurolite. Chlorite Fe/Fe+Mg ratios up to 0.64 are found in samples with only replacements after staurolite, garnet, and biotite, and up to 0.70 in one sample bearing chloritoid. Coexisting biotite and muscovite K/K+Na ratios range from 0.94 and 0.66 in staurolite-bearing samples to 0.996 and 0.83 in rocks with only traces of relict biotite. Muscovite also becomes increasingly phengitic with retrograding. Rational tie lines between the sheet silicates are maintained in most cases.

Estimation of conditions of metamorphism was hampered by disequilibrium between coexisting phases. Estimates for prograde metamorphism are close to 620°C and 6.0 kbar, with an  $f_{O_2}$  somewhat below the FMQ buffer curve, and an H<sub>2</sub>O-CO<sub>2</sub> dominated fluid. Estimates for retrograde conditions are poorly constrained, but are around 280°C and 3.5 kbar, with an  $f_{O_2}$  near the FMQ buffer curve, and probably with an H<sub>2</sub>O- or CH<sub>4</sub>-dominated fluid.

The retrograded area covers about 26 km<sup>2</sup>. For each kilometer in depth that the retrograded zone extends, the 26 km<sup>3</sup> of rock required an influx of about 0.26 km<sup>3</sup> of water (at STP) for the observed retrograde hydration reactions, concentrated toward the center of the area. Rock hydration resulted in a volume increase of 0.23 km<sup>3</sup> for each 26 km<sup>3</sup>, which was accommodated by local folding. The water may have been concentrated in the study area by a pressure-shadow effect around the north end of the Prescott Intrusive Complex, although the ultimate water source is not known.

Average erosion rates are estimated to have been about 8.6 cm/1000 years between the Middle Devonian Acadian orogeny and formation of the Triassic-Jurassic Connecticut Valley basin, and about 2.8 cm/1000 years since the Mesozoic. Retrograde metamorphism probably occurred between Lower Mississippian and Lower Permian, during cooling and unroofing of the Acadian orogenic terrane.

## INTRODUCTION

### Location

The New Salem retrograde zone occupies a north-south trending belt about 13 km long and up to 4 km wide, in the northwest part of central Massachusetts (Figure 1). The study area straddles the town line between Wendell and New Salem, and includes the extreme northeast corner of Shutesbury and extreme southwest corner of Orange. The area is about 5 km west of the northermost extension of the Quabbin Reservoir, 16 km east of the Connecticut River, and between Massachusetts Route 2 and U.S. Route 202. The study area lies within the Orange and Quabbin Reservoir 7.5-minute topographic quadrangles.

### Geography and Quaternary Cover

The study area is a hilly portion of the Central Massachusetts Upland (Stone, 1976). It is sparsely populated with minor logging, dairying, and horse farming as the only local industries. It lies entirely within the Quabbin Reservoir watershed, being drained by the Middle Branch and West Branch of the Swift River, and by Hop Brook.

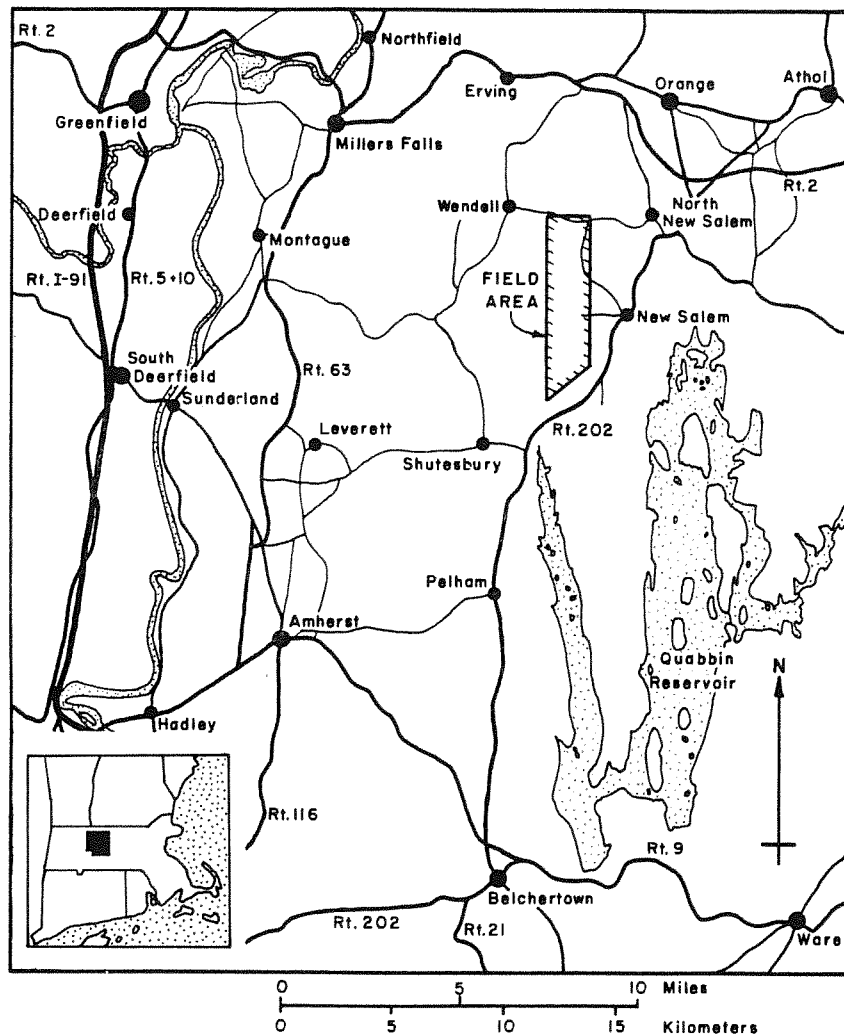


Figure 1. Location map for the area subject to this study. Minor roads and lakes not shown.

The drainage pattern is glacially disrupted with an abundance of small swamps and small, seasonal ponds. Elevations range from 398 m (1305') at the summit of Poor Farm Hill, to about 253 m (830') where the Middle Branch of the Swift River leaves the area. The vegetative cover is mainly mixed deciduous forest, postdating extensive logging operations earlier in this century. Evergreens, particularly spruce

and hemlock are locally abundant. Mountain laurel is very common in certain areas, particularly on hill slopes, and was a hindrance to field work.

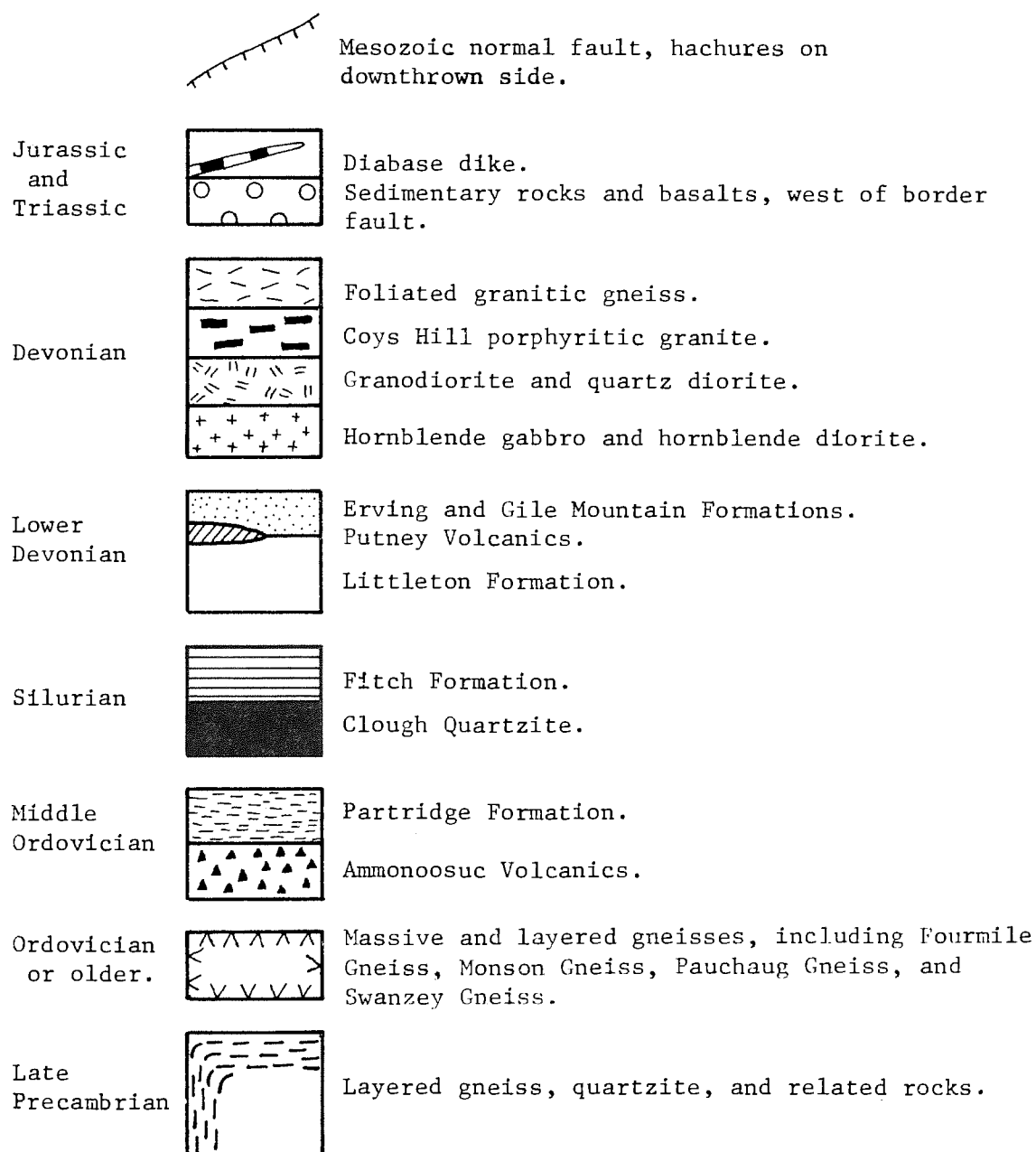
Quaternary cover consists of a thin, discontinuous layer of glacial ground moraine, probably also with fluvial valley fill deposits in low lying areas. Recent exposures on the north side of Poor Farm Hill show the till to be sandy (buff weathering) to clayey (gray weathering). Erratics are abundant, usually corresponding to local formations. Rare erratics of granitic and gneissic rocks are probably derived from exposures in the cores of gneiss domes to the north and west. A few boulders bearing red garnets and large, tabular K-feldspar phenocrysts in a quartz-feldspar-biotite groundmass are apparently of Kinsman Quartz Monzonite from the Ashuelot Pluton in New Hampshire.

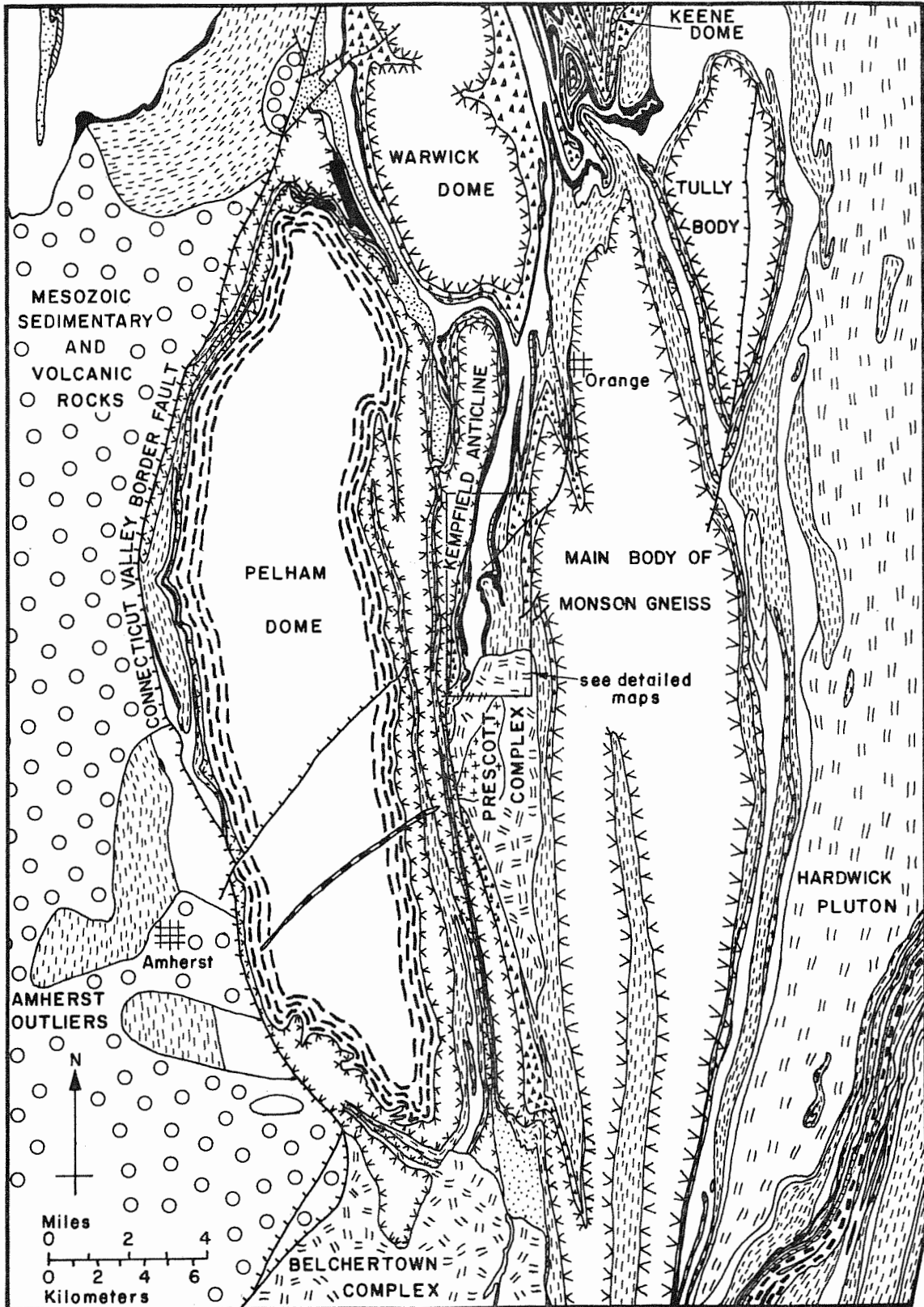
### Regional Setting and Stratigraphy

Introduction. The Bronson Hill anticlinorium is a north-northeast trending belt, extending from Long Island Sound in the south to the vicinity of the Maine-New Hampshire border (Thompson et al., 1968; King, 1969). The feature was named after Bronson Hill in Lisbon, New Hampshire, where Mr. Orrin Bronson operated a limestone quarry around the year 1850 (Hitchcock, 1877; Billings, 1937). It is bounded on the east by the Merrimack synclinorium, and on the west by the Connecticut Valley-Gaspe synclinorium. In Massachusetts (Figure 2) the west boundary is complicated by the Mesozoic Connecticut Valley Border Fault and the occurrence of Triassic-Jurassic sedimentary and



Figure 2. Geologic map and stratigraphic column of central Massachusetts, modified after Robinson (1979). The study area is located in the Littleton Formation within the small rectangle just north of the Prescott intrusive complex. Sample locations are shown in Figure 4, and detailed maps showing prograde and retrograde isograds are shown in Figures 3, 5, 7, and 9.





volcanic rocks. The Bronson Hill anticlinorium contains about twenty north-south oriented mantled gneiss domes of disputed origin (Eskola, 1948).

Stratigraphy. The geologic history of the area surrounding New Salem began in latest Precambrian or early Cambrian time with the deposition of felsic volcanics, sediments, and related rocks of the Dry Hill Gneiss and Poplar Mountain Gneiss (Robinson, 1967c and 1979; Ashenden, 1973; Naylor et al., 1973; Robinson et al., 1979). A Pb/Pb age of  $560 \pm 30$  million years has been determined on zircon from the Dry Hill Gneiss, probably a metamorphosed rhyolite, from near the town of Erving in the Pelham dome (Naylor et al., 1973; age recalculated using decay constants of Steiger and Jäger, 1977). These deposits were metamorphosed to sillimanite-orthoclase grade at some time before the Middle Ordovician (Robinson et al., 1975).

Rocks of late Precambrian to Middle Ordovician age occur overlying late Precambrian rocks in the Pelham dome, and in the cores of the Monson dome, Kempfield anticline, and other domes in the Bronson Hill anticlinorium. These are largely felsic layered and massive gneisses of probable volcanic and intrusive origin. The age and origin of these rocks has been much debated (Billings, 1937 and 1956; Chapman, 1942; Eskola, 1948; Brookins, 1965 and 1968; Page, 1968; Thompson et al., 1968; Naylor, 1971b; Robinson, 1979; Robinson et al., 1979). Pb/Pb zircon ages from the Mascoma dome in New Hampshire suggest an age of 440 to 540 million years (Naylor, 1968 and 1969). Preliminary zircon data from the Glastonbury and Monson domes also suggest ages of 440 to

450 million years (Zartman, personal communication to Robinson, 1978 and 1979, in Robinson et al., 1979).

The older rocks are unconformably overlain by the Ammonoosuc Volcanics of Middle Ordovician age. These rocks are metamorphosed mafic and felsic flows, pillow lavas, and tuffs, with minor related sedimentary deposits. The Partridge Formation overlies the Ammonoosuc, and was probably deposited as black sulfidic shales and mafic volcanics, including ultramafic rocks at some localities (Wolfe, 1978). The Partridge has been correlated with rocks along strike in western Maine that contain graptolites of Trentonian age (Harwood and Berry, 1967; correlated with late Middle Ordovician, van Eysinga, 1978).

Older rocks are overlain by the Clough Quartzite, generally a very pure, massive white quartzite or quartz pebble conglomerate. It has been dated by fossils from localities along strike in New Hampshire to be of late Llandoveryan to Wenlockian age (Boucot et al., 1958; Boucot and Thompson, 1963; Naylor and Boucot, 1965; correlated with late Lower or Middle Silurian, van Eysinga, 1978). The Clough Quartzite is overlain by calcareous rocks of the Fitch Formation. The Fitch Formation has been dated by fossils along strike in New Hampshire (Boucot and Thompson, 1963) and elsewhere in the northern Appalachians (Naylor and Boucot, 1965) to be of Ludlovian age (Upper Silurian, van Eysinga, 1978).

The youngest metamorphosed sedimentary unit in the study area is the Littleton Formation, which probably unconformably overlies older rocks (Robinson, 1963). It has been dated with fossils found in New Hampshire to be of Camden or Onondagan age (Boucot and Arndt, 1960;

correlated with late Lower Devonian, van Eysinga, 1978).

Deformation and metamorphism. During the Acadian orogeny (Middle Devonian) the region was metamorphosed and subjected to three major phases of deformation (Robinson, 1963, 1967a and b, 1979; Thompson et al., 1968; Naylor, 1971a; Tucker, 1977; Robinson et al., 1979).

These are summarised as follows:

1) East-directed nappe development, with recumbent overfolding of tens of kilometers. Four major nappes have been traced as units and named: The Cornish nappe (structurally the lowest), the Bernardston nappe, the Skitchewaug nappe, and the Fall Mountain nappe (structurally the highest). Intrusion of the Coys Hill and Hardwick plutons also occurred during or before this episode of deformation.

2) East-directed backfold stage, involving major downfolding of the Merrimack synclinorium, northward movement of the Monson gneiss body, and formation of the Prescott syncline. Maximum metamorphic grades were apparently attained during deformation phase 1 and early in phase 2. Metamorphic grade ranges from sillimanite-orthoclase-garnet-cordierite grade in the central Massachusetts metamorphic high, to chlorite grade in the Connecticut Valley-Gaspe synclinorium to the west and chlorite grade to the east of the Fitchburg Pluton.

3) Gneiss dome phase, with gravitationally induced rise of low density granitic rocks in the cores of domes and sinking of denser mantling strata. Emplacement of the Prescott and Belchertown intrusive complexes occurred early in this phase (Robinson, 1963 and 1967a; Makower, 1964; Naylor, 1971; Ashwal et al., 1979).



At least five phases of deformation post-dating gneiss dome formation have affected the New Salem area. As worked out by Robinson (1963), with modifications by D. D. Ashenden (personal communication, 1979), and the present author, these were as follows:

4) Relatively open folds trending  $N30^{\circ}E$  and plunging  $28^{\circ}$ , apparently developed contemporaneous with retrograde metamorphism. These folds have pronounced axial plane slip crenulations that apparently developed by quartz solution and local redeposition (Gray, 1979), based on textures seen in thin section. This fold set is well developed within the retrograde area but is also found locally in fresh rocks (Robinson, 1963).

5) A fold set similar to but less distinct than fold set 4, with a somewhat variable trend averaging about  $N10^{\circ}E$ . Data are not sufficient to place this fold set as being younger than set 4.

6) Poorly defined folds, trending about  $N40^{\circ}E$  with shallow plunges. These folds deform the axial surfaces of fold sets 4 and 5, above.

7) Large, open folds with nearly vertical axes that deform fold sets 4 and 5, above, but are not clearly younger than fold set 6. These folds are best exposed on the southwest-facing slopes of Poor Farm Hill, east of West Street, and are the same folds as those visible in the map pattern of Clough Quartzite in Figure 2.

8) Mesozoic faulting, related to the Connecticut Valley border fault.

Three forms of metamorphism or alteration are evident in the New Salem area that post-date the main Acadian metamorphic episode. These are summarized below, numbered in a tentative sequence after maximum

Acadian metamorphic conditions.

- 1) Acadian main phase of metamorphism.
- 2) Pervasive retrograde metamorphism in the Prescott syncline, to the north of the Prescott Intrusive Complex (this study).
- 3) Resetting of K/Ar and some Rb/Sr mineral ages to about 250 million years (Brookins, 1967; Faul et al., 1963; Zartman et al., 1970). This phenomenon is widespread in central New England, and may or may not be directly related to retrograde metamorphism in the New Salem area.
- 4) Local alteration of rocks around Mesozoic faults.

#### Previous Work

Detailed descriptions of rock types and structures in many areas of Massachusetts were presented along with singular discussions of geologic processes by Hitchcock (1841). Early mapping in southwest New Hampshire and northern Massachusetts in the Northfield and Erving areas by Hitchcock (1877) and Huntington (1877) delineated the gross distribution of rock types. The problem of gneiss dome formation was discussed by Hitchcock (1883 and 1890). It was hypothesized that they represent relict cores of an ancient volcanic island chain. Later work by Emerson (1898 and 1917) resulted in changes in formation terminology, extended reconnaissance mapping into the New Salem region, and resulted in the first geologic map of Massachusetts. Later workers, notably Billings (1937 and 1956), Hadley (1942), and Moore (1949), made a more precise classification of stratigraphy and structure along strike in western New Hampshire.

The rocks in the New Salem retrograde area were first noted by Emerson (1917, page 76). He compared the rocks along the road from Wendell to New Salem (which happens to pass over the most severely retrograded rocks) to chlorite grade phyllites in the Worcester area. A detailed study of the gneiss dome terrane in the Orange area was carried out by Robinson (1963), who also describes the retrograded area. This and subsequent studies (Robinson, 1967a, b, and c, and 1979; Thompson et al., 1968; Robinson et al., 1979) have led to a detailed understanding of regional structure, stratigraphy, and geologic History. Ashenden (1973) has studied the northern end of the Pelham dome, and the area extending southeast into the New Salem retrograde zone for the Boston Metropolitan District Commission (personal communication, 1979). Maps compiled by Robinson have been used as a base in this study.

#### Purpose of Study

The purpose of this study is to describe and interpret the changes in mineral chemistry and assemblages that occurred in the pelitic schists of the Lower Devonian Littleton Formation during a period of retrograde metamorphism in the New Salem area. Pelitic schists are among the most widespread and best known of metamorphic rock types. As such, prograde assemblages and continuous and discontinuous reactions governing the assemblages are relatively well understood. However, the widespread phenomenon of retrograde metamorphism has hardly been addressed (Abbott, 1979). In the New Salem area the Littleton and adjacent formations have been pervasively retrograded in

a systematic way from staurolite and lower sillimanite grade to chlorite-K-feldspar grade. Hence, the New Salem area presents an unusually good opportunity to study retrograde metamorphism in detail.

### Methods of Investigation

General methods. Field work was carried out during the fall of 1978, and spring and summer of 1979. Mapping of the areal distribution of retrograded rocks was done on a scale of 1:24,000 using 7.5-minute topographic quadrangle sheets. Standard brunton compass and altimeter mapping techniques were used. Mineralogy, particularly the presence or absence of staurolite, garnet, chlorite, and biotite, was judged as nearly as possible at the outcrop. The quantities of sillimanite were too small for the writer to identify in hand sample, except outcrops at station 131. Metamorphic isograds were drawn after laboratory checking of field evidence. 51 thin sections and 11 polished thin sections of representative samples from the Littleton, Fitch, and Partridge Formations were examined with petrographic transmitting and reflecting microscopes.

Polishing of chlorite-bearing thin sections. Polishing thin sections containing large amounts of chlorite, unless done carefully, results in severe plucking and erosion of chlorite and entrained minerals from the thin section surface. Because a high-grade polish is required for electron microprobe analysis, the following polishing method was devised:

- 1) Prepare the thin section using a frosted glass slide and epoxy

cement (Buehler A-B epoxy was used), and grind on a machine or glass plate to about 100  $\mu\text{m}$  rock thickness.

2) Vacuum impregnate the section using a low viscosity epoxy (Buehler C-D epoxy was used).

3) Grind thin section on a glass plate to 40  $\mu\text{m}$  thickness, using 5  $\mu\text{m}$  aluminum oxide grit for the final grinding step.

4) Using canada balsam, cement a small metal bar, or other object, onto the glass side of the thin section, to be used as a handle during polishing. The part of the handle fastened to the slide must be smaller than and centered within the area of the rock slice.

5) The polishing surfaces used were Buehler Texmet synthetic paper with an adhesive backing, and were cemented with varnish to the 8 inch aluminum or steel lap wheels. A new lap surface must be broken in by at least 30 minutes of polishing, and must not harbor contaminating coarser grit, rock particles, or hard deposits.

6) Prepare the thoroughly wetted polishing lap with about 1 cc of 0.3  $\mu\text{m}$  alpha alumina polishing grit. Add enough water to form a thin paste, and distribute it on the lap surface.

7) While operating the polishing lap at full speed (600 rpm in this case), begin polishing the thin section with sufficient water to prevent grabbing. Gentle pressure on the section should be used, not to exceed arm weight. At no time should the lap be allowed to dry out. Move the thin section slowly around the lap surface in a direction opposite lap rotation.

8) Continue step 7, above, adding water to the lap at frequent intervals and checking the polish quality occasionally. Additional



polishing grit should not be added. A high-quality polish over the entire slide takes about 90 minutes. The resulting rock thickness is about 30  $\mu\text{m}$ .

Electron microprobe analysis. Seven samples from the Littleton Formation were chosen for detailed electron microprobe chemical analysis, for precise determination of phase relations and composition trends. The instrument used was a three spectrometer, wavelength dispersive ETEC Autoprobe at the Department of Geology, University of Massachusetts, Amherst. The machine was operated by the writer between November, 1978 and August, 1980. Standard operating parameters were a beam current of 0.02  $\mu$  amperes, accelerating potential of 15,000 volts, and a chamber vacuum of about  $1 \times 10^{-5}$  torr. The electron beam diameter was about 2  $\mu\text{m}$  for oxides and garnets, and defocused to a diameter of about 20  $\mu\text{m}$  for all other minerals to inhibit volatilization of sodium, potassium, and water.

Counting time for all elements and backgrounds was 15 seconds. Background count rates were taken on both sides of the peak on the standard, and the resultant background slope extrapolated from one background measurement taken on the sample grain. Standards used were well characterized natural minerals, and a synthetic glass synthesized at high pressure. Raw count rates were first corrected for machine dead time and background count rate, then corrected for stopping power, atomic number, and specific absorption effects after the empirical alpha factor procedures of Bence and Albee (1968) and Albee and Ray (1970), through six iterations. The correction program did not

include a light element input correction, nor specific corrections for specific line or continuum secondary fluorescence, as do more modern procedures (Yakowitz et al., 1973; Springer, 1976).

### Acknowledgements

This report is submitted in partial fulfillment of the requirements for the degree of Master of Science in Geology, University of Massachusetts, Amherst. I thank Peter Peter Robinson, head of my thesis committee, for his many hours of helpful advice and discussion in the field and office, and for the use of thin sections and maps of the New Salem area. I also thank the other members of my committee, Leo Hall, Jack Cheney, and Don Wise, for their invaluable technical advice and helpful critique of this manuscript. I would also like to acknowledge the helpful advice and field information kindly given to me by David D. Ashenden, Geologist for the Metropolitan District Commission. I also thank John Schumacher for his advice on microprobe analysis interpretation. Final manuscript preparation was supported by National Science Foundation Grant EAR-7915246, to Robinson.

### DESCRIPTION OF ROCKS

#### Partridge Formation

The Partridge Formation is dominantly a rusty-weathering pyrrhotite-mica schist. It is dark brown or very dark gray on fresh surfaces, contains abundant quartz, and less commonly contains garnet. It is commonly quite weathered and consequently rather friable. In

addition to the schist, some exposures contain or are composed of amphibolite or rarely, well lineated hornblende gneiss. The Partridge Formation is highly variable in thickness in the Prescott syncline, in part due to complex folding and faulting. It is commonly 50 to 100 meters (160' to 330') thick in the western limb, and probably exceeds 500 meters (1600') on the eastern limb.

#### Clough Quartzite

The Clough Quartzite is one of the most distinctive and widespread units in the Bronson Hill anticlinorium. Within the New Salem area it is a massive white quartzite, locally with abundant "stretched" elongate quartz pebbles and rare, small, discontinuous micaceous horizons. The Clough ranges in thickness up to about 80 meters (260'), but is locally absent.

#### Fitch Formation

The Fitch Formation is poorly exposed in the New Salem area. It consists of dark, quartz-rich graphitic mica schist, calc-silicate granulite, and minor quartz marble and actinolite calc-silicate. The Fitch Formation ranges up to about 50 meters (160') in thickness in the study area, but is locally absent.

#### Littleton Formation

The Littleton Formation is relatively well exposed in the study area. To the north, where the unit is not severely retrograded, it is a quartz-rich garnet-biotite-muscovite schist with a well defined

muscovite foliation. Staurolite is common as dark brown prisms up to 2 cm long, and fibrolite may be seen in hand specimen in the extreme northeast part of the field area at outcrop 131. Typically the schist is gray-weathering and medium-gray on fresh surfaces due to ubiquitous graphite interspersed with fine grained muscovite. Some foliation surfaces exposed to weathering have a transparent rusty stain. Crenulations are very common and give rocks broken along foliation surfaces a wrinkled appearance. Schists are commonly interlayered with minor quartzite on a scale from 0.5 to 20 cm. Poorly foliated, gray-weathering quartz-mica granulite and rare calc-silicate granulite are present in some outcrops. Hornblende amphibolite beds are present at outcrop NS68, and at station NS97 there is a set of large exposures composed of quartz-tourmaline rock, bearing rare garnet. This last outcrop is very distinctly lineated and has widely spaced crenulations that were probably developed during retrograde metamorphism.

In retrograded rocks, staurolite is replaced by fine-grained pseudomorphs of muscovite and chlorite that weather out in positive relief on exposed surfaces. Chlorite is associated with garnet, and completely pseudomorphs garnet in the most severely retrograded rocks. Pyrite is rarely present in retrograded rocks, and has typically been weathered wholly or in part to hematitic material (orange-red to deep red in transmitted light).

The top of the Littleton Formation is not exposed in the New Salem area, and its thickness has been approximately doubled across the axial surface of the Prescott syncline. Therefore the minimum thickness of the Littleton Formation is approximately 300 meters (980').

### Distribution of Metamorphic Zones

Prograde metamorphism reached sillimanite-staurolite-muscovite grade in the New Salem area in metamorphic zone II of Tracy et al. (1976) and Robinson (1979), with metamorphic grade increasing toward the east-southeast. Figure 3 shows the two prograde metamorphic isograds that have been identified in the study area. The aluminosilicate polymorph isograd represents rocks which straddled the kyanite = sillimanite univariant reaction line during prograde metamorphism (Figure 49), and is extrapolated from aluminosilicate-bearing outcrops to the north and south of the map area. The occurrence of sillimanite in prograde rocks in the study area was solely dependent on bulk composition. The sillimanite-in prograde isograd represents the first occurrence of sillimanite in rock compositions present in the Littleton Formation.

The prograde assemblages observed or inferred in schists of the Littleton Formation are listed in Table 1. All prograde assemblages apparently contained quartz, biotite, muscovite, ilmenite, and graphite, with the primary difference between assemblages having been the occurrence and quantity of garnet, staurolite, sillimanite, and plagioclase. Chlorite was probably absent from the prograde assemblages (Robinson, 1963 and personal communication, 1980; Hall, 1970). Sillimanite-bearing rocks occurred only to the east of the sillimanite-in isograd. All sillimanite-bearing rocks that were observed contained staurolite and garnet, or retrograde pseudomorphs after those minerals.

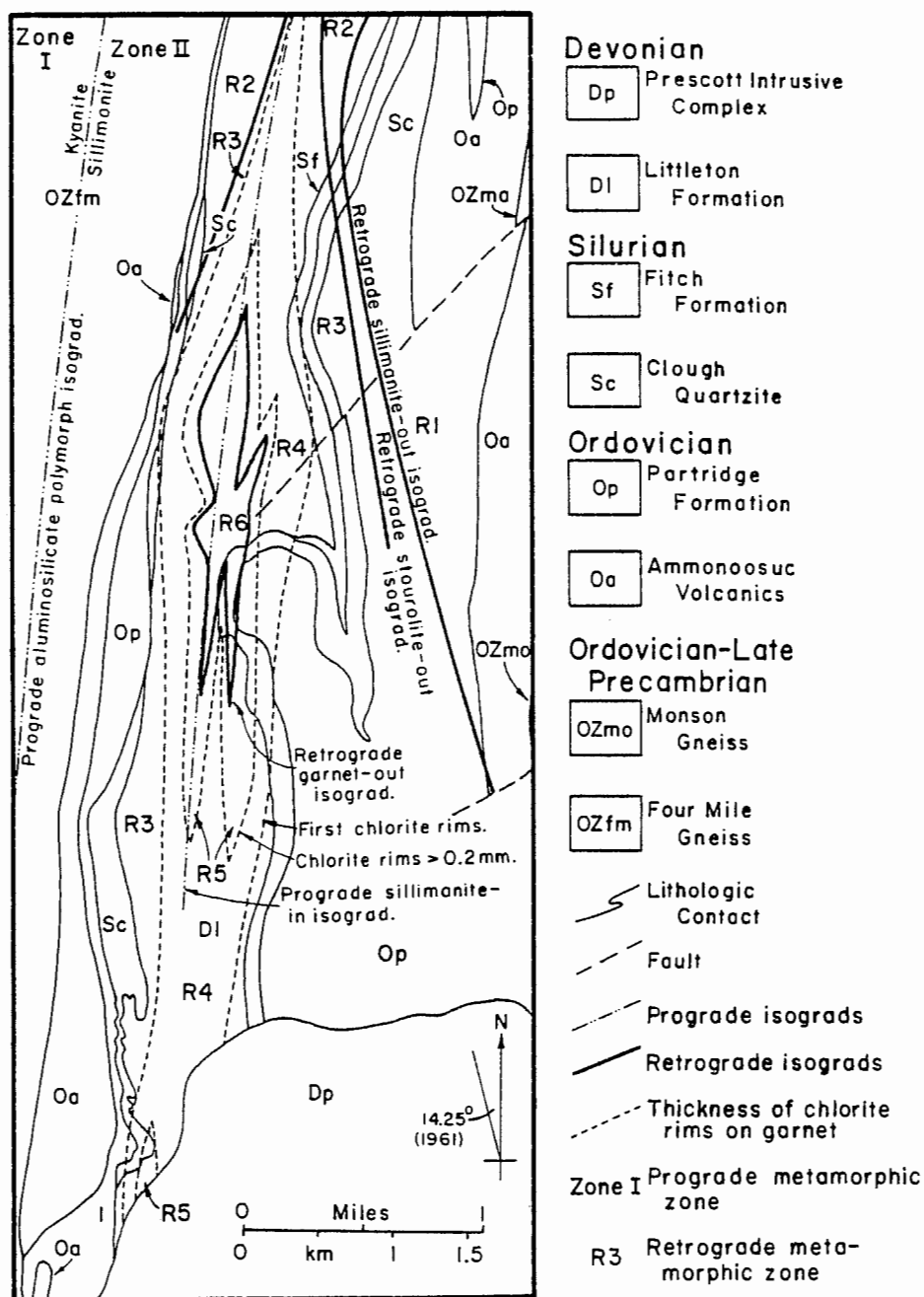


Figure 3. Map showing prograde and retrograde metamorphic isograds in the study area. Prograde metamorphic zones are labeled with roman numerals, and retrograde metamorphic zones are labeled with the prefix "R" (for retrograde).

Table 1. Prograde metamorphic assemblages observed or inferred in the Littleton Formation in the New Salem area. All assemblages are for schists and all contain quartz, muscovite, ilmenite, and graphite. Sillimanite-bearing assemblages only occurred east of the prograde sillimanite-in isograd, and plagioclase is locally present.

Garnet (rare)  
 Biotite  
 Biotite-garnet  
 Biotite-garnet-staurolite  
 Biotite-garnet-staurolite-sillimanite

Retrograde metamorphic isograds for sillimanite, staurolite, and garnet were mapped (Figure 3). Garnet was replaced systematically within the retrograded zone, allowing the mapping of one line representing the first appearance of chlorite rims on garnet, and a second line for chlorite rims equal to 0.2 mm in thickness. These five lines separate six concentric, nested retrograde metamorphic zones, labeled R1 to R6 to distinguish them from prograde metamorphic zones. The retrograde isograds separate areas of distinctly different mineral assemblages, summarized in Table 2. Note that zone R1 (sillimanite-present) is necessarily only observed to the east of the prograde sillimanite-in isograd. Zone R2 on the west could represent unretrograded rocks, however, all rocks seen in that area had at least minor quantities of chlorite.

In addition to the main changes in assemblages, retrograded rocks also contain variable quantities of anatase (after ilmenite), K-feldspar, sphene, rutile, and pyrite. Other accessories such as zircon, graphite, apatite, and tourmaline remain throughout the retrograde sequence from zones R1 to R6, although some changes in character of apatite and tourmaline do occur.

Table 2. Assemblages observed in retrograde metamorphic zones R1 to R6. Minerals that develop in retrograded rocks in variable quantity and occurrence are listed next to the main assemblages.

Retrograde Metamorphic zone	Assemblages and isograds	+ or -
R1	All prograde assemblages	Chlorite
<hr/> Sillimanite-out isograd <hr/>		
R2	Biotite-chlorite Biotite-garnet-chlorite Biotite-garnet-staurolite-chlorite	K-feldspar Anatase
<hr/> Staurolite-out isograd <hr/>		
R3 to R5	Chlorite Biotite-chlorite Biotite-garnet-chlorite Garnet-chlorite (rare) Garnet-chlorite-chloritoid (rare)	K-feldspar Anatase Rutile Sphene Pyrite
<hr/> Garnet-out isograd <hr/>		
R6	Chlorite Chlorite-biotite	K-feldspar Anatase Rutile Sphene Pyrite

#### Description of analyzed Samples

Seven samples from the Littleton Formation (Figure 4) were chosen for electron microprobe chemical analysis. Estimated modes for the seven samples are given in Table 3. Hindsight suggests that more samples with a more systematic areal distribution should have been chosen. However, the samples were chosen before the pattern of retrograde isograds was clear, and time precluded the analysis of additional samples.

U01A. Buff-weathering quartz-rich mica schist. Thin, discontinuous



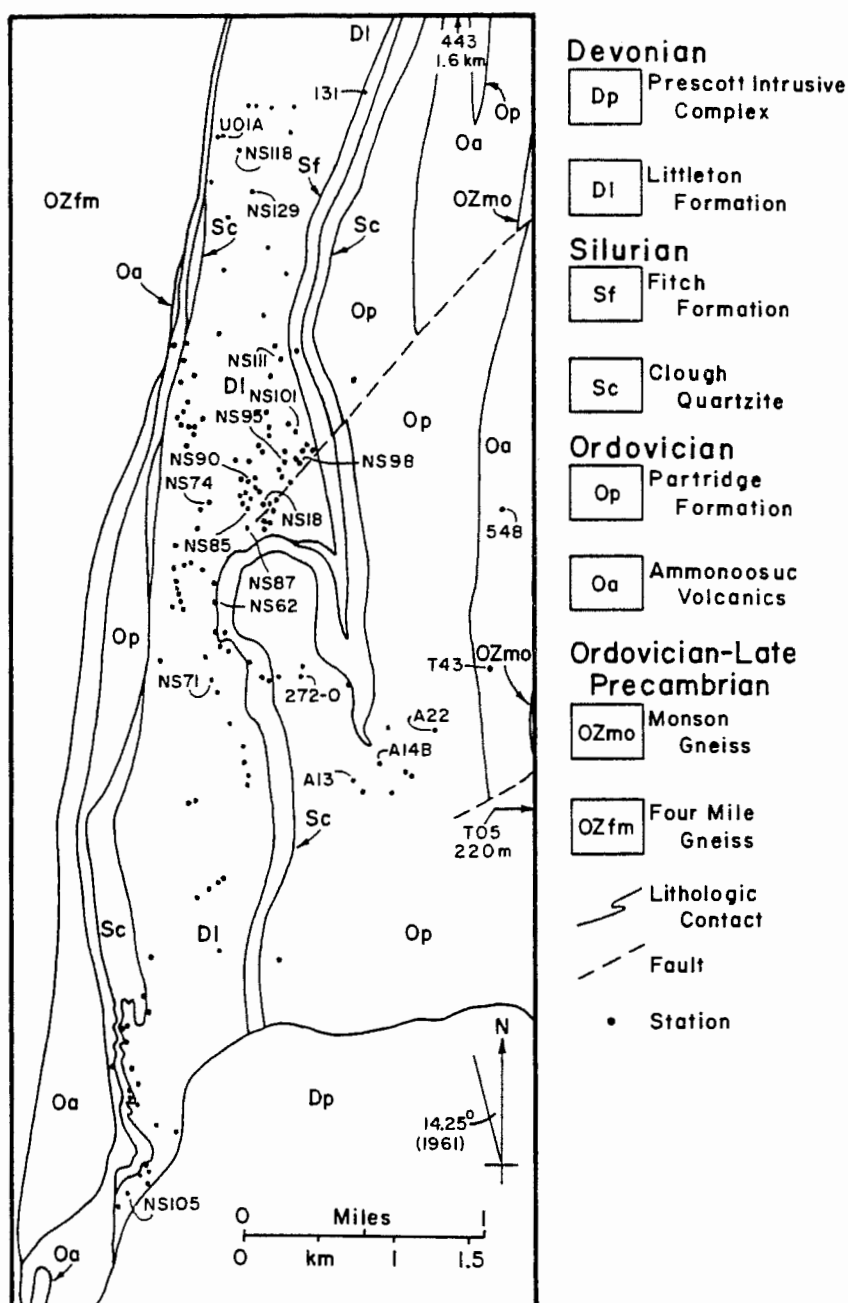


Figure 4. Map of the study area, outlined in Figure 2. All sample locations cited in the text are indicated.

Table 3. Estimated modes for the seven samples analyzed with the electron microprobe. The first six samples were all originally biotite-garnet-staurolite-muscovite schists, probably without prograde chlorite. Sample NS71 probably originated as a garnet-muscovite schist. All samples are from the Littleton Formation. Sample U01A is the least retrograded of the seven samples, and NS90 is the most retrograded. Sillimanite and rutile have been found in certain samples, but were not detected in the samples presented here.

P = Only pseudomorphs after the mineral are present.  
tr = Trace constituent, < 1%.

Zone Sample	R2 U01A	R2 NS118	R4 NS18	R5 NS87	R5 NS85	R6 NS90	R5 NS71
Quartz	55	50	45	35	50	55	30
Plagioclase	1	1	4	5	3		
K-feldspar	tr	tr		tr		2	
Staurolite	3	5	P	P	P	P	
Garnet	5	2	2	1	tr	P	1
Biotite	9	10	3	1	2	P	
Muscovite	25	30	35	45	35	32	55
Chlorite	tr	1	9	12	9	10	10
Chloritoid							4
Tourmaline	tr	tr	tr	tr	tr	tr	tr
Allanite		?	tr	tr	tr	tr	tr
Apatite	tr	tr	tr	tr	tr	tr	tr
Zircon	tr	tr	tr	tr	tr	tr	tr
Sphene			?	?	?	tr	?
Ilmenite	1	tr	1	1	1	tr	tr
Anatase	1	1	tr	tr	?	1	tr
Graphite	tr	tr	1	tr	tr	tr	tr
Pyrite	—	—	tr	—	tr	—	—
	100	100	100	100	100	100	100

quartz-rich layers alternate with mica-rich layers, with muscovite defining the foliation. A pronounced muscovite lineation is visible. Biotite books up to 1.5 mm across are abundant, lying both parallel to and at high angles to the foliation. Red garnets up to 2 mm across and dark-brown staurolite up to 1 cm long are common. Sprays of chlorite up to 5 mm across are present in parts of the outcrop. Little evidence of crenulations is seen in hand specimen or in thin section.

NS118. This sample is quite similar to sample U01A. Staurolites are larger, up to 2 cm long. Biotite oriented at angles to the muscovite foliation is rare. On a slabbed surface, chlorite as rims on staurolite may be seen, and small white plagioclase grains are visible. A few silicified fractures are visible in hand specimen, which probably developed during Mesozoic deformation.

NS18. Gray-weathering schist, with few distinct quartz-rich layers. Crenulations are abundant, and a transparent rusty staining is present on some foliation surfaces. Red garnets up to 2 mm across have thin chlorite rims, and staurolite has been entirely pseudomorphed by muscovite-chlorite intergrowths up to 3.5 cm long and 1.5 cm across. Chlorite is abundant in the matrix, and white plagioclase grains up to 2 mm across are easily distinguishable on a broken surface. Biotite books up to 1.5 mm across are difficult to distinguish on a broken surface due to poor development of the basal cleavage and dull appearance.

NS87. Gray-weathering schist, crenulations clearly evident, with few

quartz-rich layers. Garnet relicts up to 1 mm across have thick chlorite rims, and pseudomorphs after staurolite up to 2 cm long and 1 cm across are abundant. Chlorite is very abundant in the matrix. White, lens-shaped plagioclase crystals are common, and cleavage surfaces are easily distinguished. Biotite books up to 1.5 mm across are present, but they are somewhat dull in appearance due to tiny, partially detached flakes of chlorite within and around the periphery of the grains.

NS85. Gray-weathering, quartz-rich schist with well developed crenulations. Chlorite pseudomorphs after garnet are common, and minute garnet relics very rare. Muscovite-chlorite pseudomorphs after staurolite are quite large, up to 4 cm long and 1 cm across. Biotite plates up to 1.5 mm across are relatively common, but have irregular, chlorite-flecked outlines.

NS90. Buff-weathering, quartz-rich schist, with distinct crenulations. Quartz-rich and muscovite-rich layers alternate on a scale of 2 to 6 mm. Only spherical pseudomorphs after garnet were seen, weathering out as pits on exposed surfaces. Pseudomorphs after staurolite are present up to 3 cm long and 1 cm across. No biotite or primary feldspar is distinguishable. On slabbed surfaces, white lenticular to irregular bodies up to 1 mm across appear within dark chlorite masses. In thin section these are seen to be K-feldspar.

NS71. Dark-gray to somewhat rusty-weathering schist, dark-gray on freshly broken surfaces. Garnets up to 7 mm across with thick chlorite

rims are present but rare. The outcrop has well developed crenulations, and chlorite is present in the matrix. Thin, black ilmenite plates are rarely distinguishable on foliation surfaces. Chloritoid, abundant in thin section, has not been discerned in hand sample by the author. This is due to small crystal size, irregular shape, relatively poor cleavage, abundant graphite and quartz inclusions, and the dark matrix. Seven samples were taken from this bank, 3 meter long west-facing ledge. Only two samples taken from the upper, southernmost parts of the ledge were found to contain chloritoid. Minor biotite was found in the two samples taken at the lower, northern end of the outcrop. The other samples, taken at the upper north end, center, and lower south end contain chlorite with rare garnet as the only ferromagnesian silicates.

## MINERALOGY AND CRYSTAL CHEMISTRY

### Introduction

Twenty minerals of metamorphic origin have been identified in the various samples studied. In this section those minerals will be described as to their occurrence, appearance in outcrop and thin section, composition, and crystal chemistry. The results presented herein come from observations of many outcrops, hand samples, thin sections, and interpretation of electron microprobe chemical analyses. Various maps, data plots, and drawings from thin sections will be used to depict field, chemical, and textural relations between the minerals.

## Analyses

Chemical data are presented in tables, typically listing one column for each analysis or average of several analyses. Only averages are given for some minerals where composition variation in each sample was negligible or of little petrologic significance. Averages are useful for comparison purposes, and will be used in later sections for calculating reaction stoichiometries.

Each single column in the analytical tables lists oxide weight percent with all iron calculated as FeO, and cation proportions based on ideal structural formulae with ideal structural water in known hydrous minerals. A second column is used in cases where alternative methods of cation proportion calculation may apply. Recalculated cation proportions may be used to determine either structural water ( $\text{OH}^-$ ) as in sphene, or ferric iron as in ilmenite, but not both simultaneously. Calculation of ferric iron and water using electron microprobe analyses can only be done in cases where near perfect cation stoichiometry may be assumed, and cannot be used for non-stoichiometric minerals such as micas and staurolite.

All sample averages have columns of standard deviations which were calculated from the individual analyses themselves, not from theoretical counting statistics. This was done because the cumulative error from instrument stability, correction procedure, polish quality, local take-off angle, peak shift, carbon coat thickness, and counting statistics were much greater than counting statistics alone. Standard deviations are generally small for unzoned minerals such as chloritoid

and staurolite, and large for elements which are strongly zoned as in garnet and sphene.

The electron microprobe used was not set up to analyze fluorine, and all monovalent anions are taken as lattice  $\text{OH}^-$ . Weight percent water (or  $\text{H}_2\text{O} + \text{F}$ , if you will) for known hydrous minerals listed in the analytical tables is merely the difference of the oxide weight percent total from 100%.  $\text{OH}^-$  anion proportions are calculated on a basis of this  $\text{H}_2\text{O}\%$ , and an idealized cation stoichiometry. This admittedly crude estimate was not included in the analytical correction procedure, and could result in systematic errors in the corrected analysis. Errors would be manifest in slightly lower calculated percentages of the light elements, particularly sodium and magnesium, due to oxygen absorption of soft X-rays. Such errors are probably small, however, due to the relatively small amount of water present, as in staurolite, micas, and chloritoid, and to the much larger heavy element matrix effects caused by iron, especially in biotite and chlorite.

### Sillimanite

Field occurrence. The Acadian kyanite = sillimanite polymorph isograd passes approximately north-south through the Kempfield anticline, separating kyanite-staurolite grade rocks to the west from sillimanite-staurolite grade rocks to the east (Figure 5). This is the boundary between metamorphic zones I and II of Tracy et al. (1976) and Robinson (1979). A prograde sillimanite-in isograd is drawn to the east of the polymorph isograd, representing the first appearance of

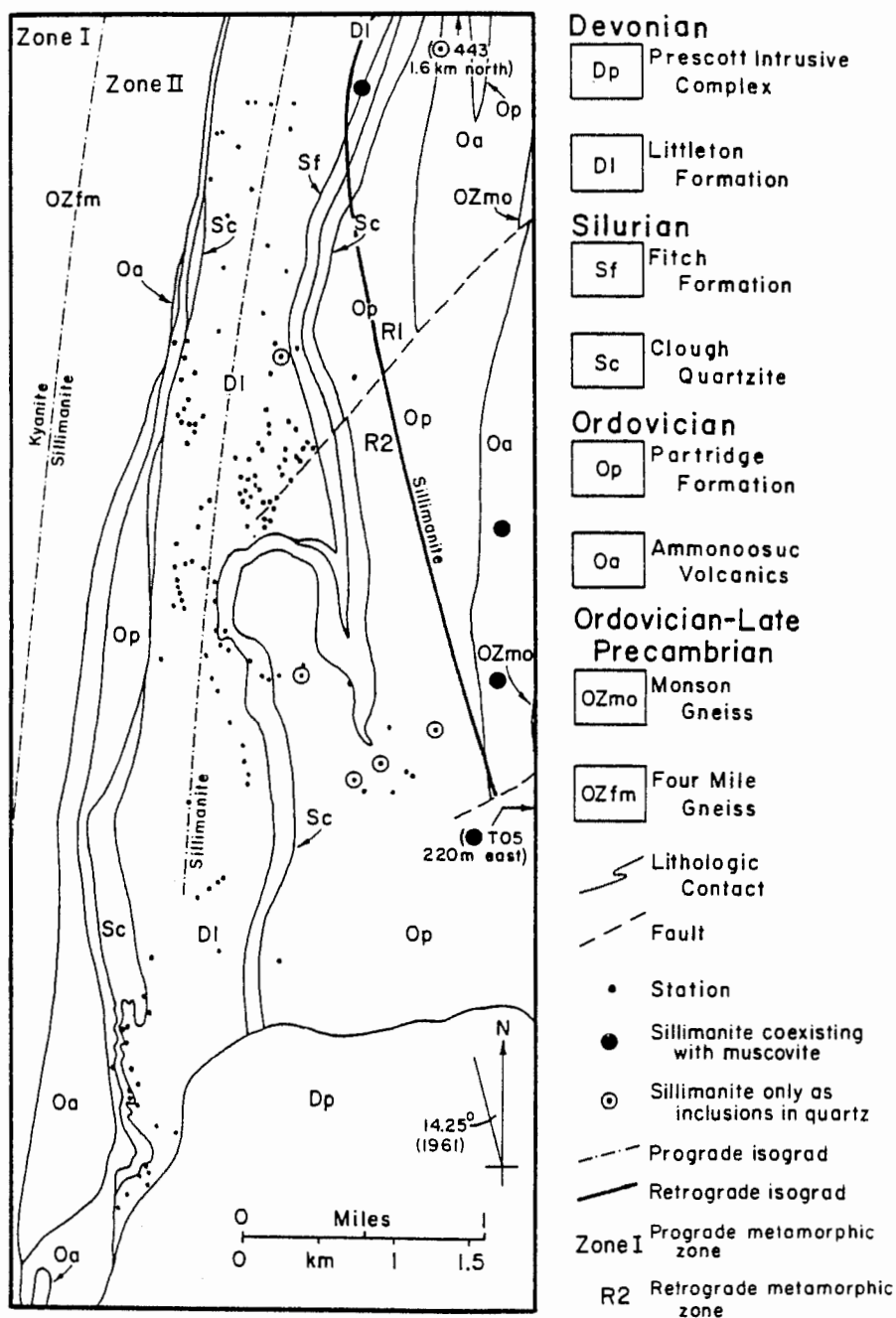


Figure 5. Map showing the three sillimanite isograds: The kyanite = sillimanite polymorph isograd, the prograde sillimanite-in isograd, and the retrograde sillimanite-out isograd. Also shown are the sillimanite-bearing outcrops, and prograde and retrograde metamorphic zones.



coexisting sillimanite and biotite with increasing metamorphic grade in rocks of the Littleton Formation (Robinson, 1963).

Control is not good for the location of the polymorph isograd due to the paucity of rocks of appropriate bulk composition. The sillimanite-in isograd for the Littleton Formation is greatly obscured by retrograde metamorphism. The Partridge Formation on the east limb of the Prescott syncline contains most of the sillimanite occurrences, due in part to the increasing metamorphic grade toward the east, and to lesser retrograde metamorphism than in the Littleton Formation. Although control is poor, a retrograde sillimanite-out isograd has been drawn as a thick solid line on the map in Figure 5. The isograd separates outcrops with coexisting sillimanite and muscovite to the east from outcrops with sillimanite existing only as inclusions within quartz to the west.

Textures in thin section. Sillimanite morphology is fibrolitic, occurring as tiny stout to acicular rods and bundles of fibers. The most fresh sillimanite in the study area occurs in the Fitch and Littleton Formations at location 131, zone R1 (Figure 6a). The sillimanite occurs as bundles of parallel to sub-parallel fibers up to 1.5 mm by 0.5 mm in size, and as individual rods up to about 700 by 50  $\mu\text{m}$  in size. The sillimanite bundles are partially altered relics embedded in knots of randomly oriented fine-grained muscovite flakes. The muscovite knots are a product of retrograde hydration reactions that consumed prograde sillimanite. Abundant rods and needles of sillimanite also occur as inclusions in quartz.

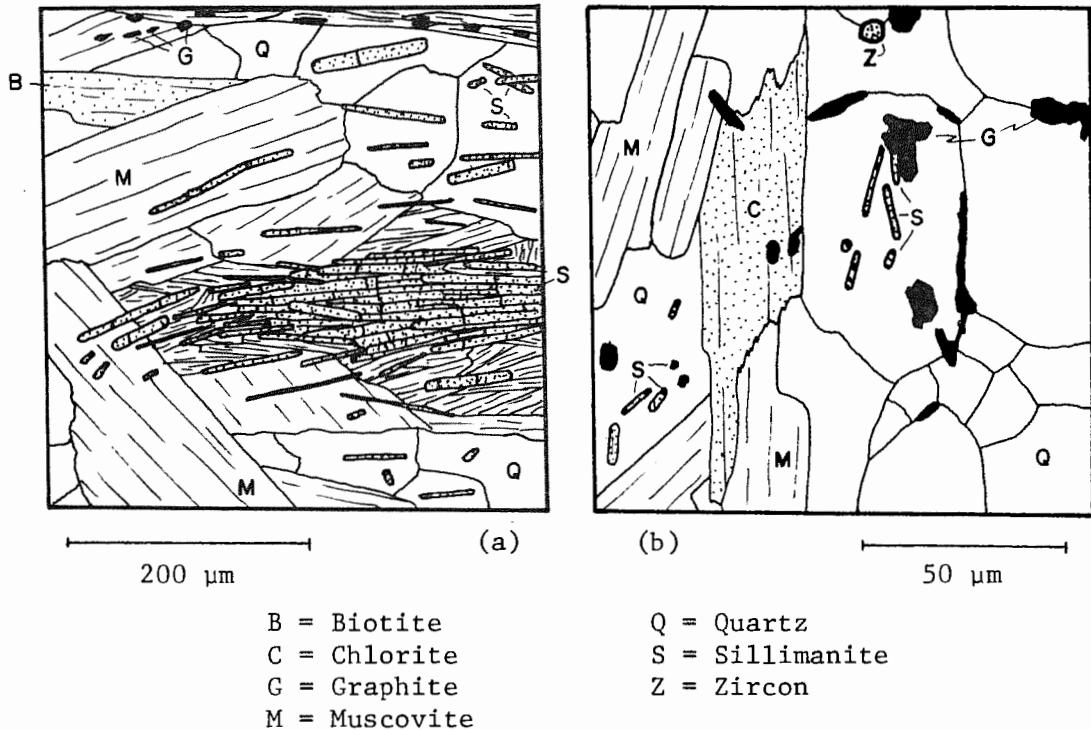


Figure 6. Fibrolite textures in thin section. a) Station 131, zone R1, Littleton Formation. A large bundle of sillimanite rods and fibers partially replaced by fine-grained muscovite, as is characteristic of sillimanite occurrences in zone R1 (Figures 3 and 5). b) Station NS111, zone R4. An example of sillimanite occurrences in zones R2 to R4, where sillimanite occurs only as tiny rods within single quartz crystals.

In more retrograded rocks (zones R2 to R6), any sillimanite in contact with muscovite or any other external grain boundary was consumed by hydration reactions. The knots of randomly oriented muscovite flakes after sillimanite are distinctive in some rocks, but recrystallization and confusion with similar muscovite knots of retrograde origin after staurolite render them useless in most cases for identifying the past presence of sillimanite.

Sillimanite as inclusions entirely within single crystals of quartz survived the effects of alteration only in cases where quartz recrystallization did not allow a grain boundary to intersect included

sillimanite. Perhaps the most remarkable occurrence is at station NS1111 (Figure 6b) in the Littleton Formation, located within 500 meters of some of the most severely retrograded rocks. Minute rods of sillimanite up to 20 by 5  $\mu\text{m}$  in size occur entirely embedded within single quartz crystals. Off the area of Figure 6b to the left is a knot of randomly oriented muscovite plates, almost certainly a replacement product of a large fibrolite mass. Sillimanite may once have been common in the eastern part of the Littleton Formation in the New Salem area, but retrograde alteration along with pervasive deformation and quartz grain recrystallization has rendered that mineral quite rare.

### Staurolite

Field distribution and habit. Staurolite is a distinctive mineral in many rocks around the northern periphery of the retrograded region in zones R1 and R2. It appears in outcrop as subhedral, dark brown, stubby to elongated, sub-parallel prisms up to 2 cm long and 0.7 cm across.

The transition in the field between rocks containing fresh staurolite and rocks containing only pseudomorphs after staurolite is easy to discern due to the large size and distinctive habit of both the crystals and pseudomorphs. Pseudomorphs are commonly large, up to 10 by 2 cm in size and are composed of a fine-grained intergrowth of muscovite and chlorite. The pseudomorphs weather out in raised relief over the exposed outcrop surfaces, and better preserved specimens faithfully represent the euhedral and even twinned

habit of the staurolite precursors. In the Partridge formation on the east limb of the Prescott syncline, pseudomorphs of coarse-grained muscovite after staurolite are apparently of prograde origin (Guidotti, 1970). These are not part of this discussion.

Outcrops containing fresh staurolite are separated from those containing only pseudomorphs by only 300 meters or so, allowing the drawing of a line separating rocks with staurolite from those with only pseudomorphs (Figure 7). This line in effect is the retrograde staurolite-out isograd, along which retrograde hydration reactions involving staurolite proceeded to completion. Staurolite persists in more severely retrograded rocks than sillimanite.

Appearance in thin section. Staurolite crystals are seen to be subhedral and poikilitic with quartz inclusions particularly toward the crystal margins. Inclusions of garnet, ilmenite, graphite, and tourmaline are also common. Staurolite is pleochroic, X = pale yellow to Z = bright yellow, biaxial positive with a  $2V$  of about  $85^\circ$ , and exhibits moderate dispersion  $r > v$ . Birefringence is in the middle first order with a retardation of about 0.014.

One of the best examples of fresh staurolite in the study area is from station U01A, zone R2 (Figure 8a). Note the large, well defined muscovite plates in the matrix and the abundant inclusions of quartz in staurolite. The first indication of incipient staurolite alteration is its association with plates or sprays of optically positive Mg-rich chlorite. In sample U01A the chlorite sprays are rare and only a few millimeters across. With increasing alteration,

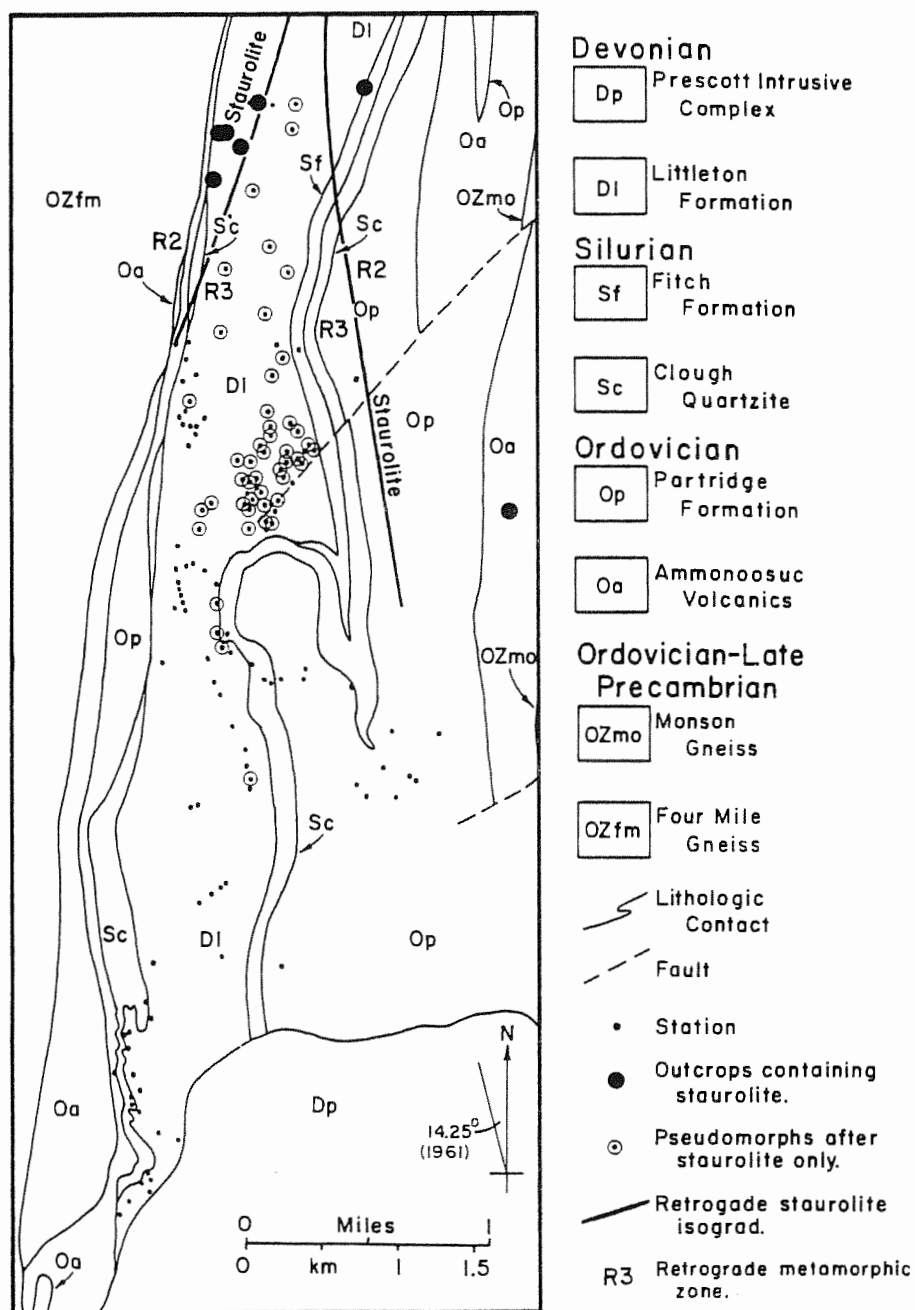
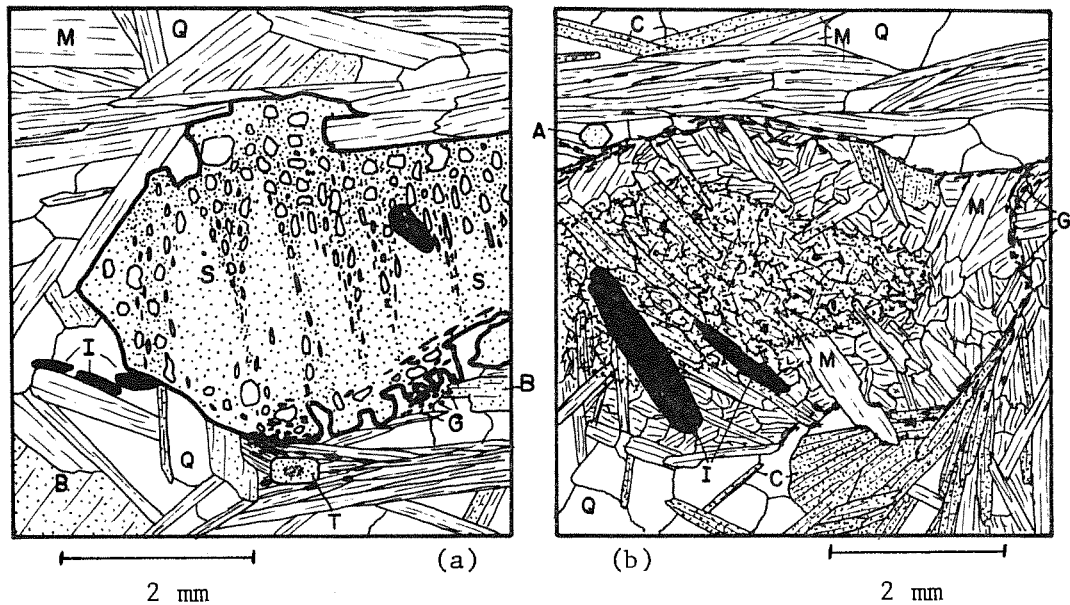


Figure 7. Map showing the retrograde staurolite isograd. Also shown are localities bearing staurolite (black dots), and localities bearing only pseudomorphs after staurolite (circled small dots). The staurolite isograd closes off the map to the north.



A = Apatite	G = Graphite	Q = Quartz
B = Biotite	I = Ilmenite	S = Staurolite
C = Chlorite	M = Muscovite	T = Tourmaline

Figure 8. Textures of staurolite in thin section. a) Station U01A, zone R2. Fresh staurolite with abundant quartz and graphite inclusions, and well formed mica plates in the matrix. b) Station NS111, zone R4. Pseudomorph after staurolite composed largely of muscovite with some chlorite. Note the outline and shading of the pseudomorph core by abundant graphite particals, and the recrystallization of some muscovite into larger, oriented plates.

as in sample NS118 (zone R2), staurolite becomes translucent around the edges with incipient development of minute sheet silicate crystals, mainly muscovite. They tiny platelets increase in size and apparently "intrude" and replace large sections of the host staurolite. Mg-chlorite is also seen to develop in patches more or less randomly dispersed throughout the thin section. The final demise of staurolite has not been observed in thin section due to a lack of outcrops for sampling, and the next view of the sequence is from about 300 meters southeast of outcrop NS118, where all staurolite has been replaced by a

mass of randomly oriented flakes of muscovite and optically negative Fe-rich chlorite.

The original extent of a staurolite crystal is commonly defined in the pseudomorph by a distinct outline of dusty graphite inclusions. Sheet silicate grains within the graphite outline are typically relatively large and better formed whereas those outside the outline tend to be smaller and more ragged, although the reverse of this pattern is seen in some specimens (Figure 8b). In Figure 8b, note the euhedral prism cross section defined by abundant graphite inclusions, and how muscovite grains in the old foliation laminae differ radically in habit from the muscovite of retrograde origin in the pseudomorph. Pseudomorphs after staurolite do not contain quartz inclusions, as doubtless did the parent staurolite, probably because staurolite breakdown took place via a quartz-consuming reaction.

Surrounding many pseudomorphs after staurolite is textural evidence (bent muscovite plates, deformed foliation) that the mass swelled as the staurolite crystal turned into an intergrowth of sheet silicates. Assuming the pseudomorph was produced only by an influx of water, alkalis, and silica after the staurolite-out reaction (reaction (4)), molar volume calculations indicate the pseudomorph volume to be 2.1 times that of the original staurolite crystal. Measurements made in thin section and on slabbed surfaces show that the pseudomorph volume is commonly between 2.0 and 2.4 times the volume of the euhedral interior, as outlined by differences in sheet silicate grain size and graphite distribution. This is consistent with the calculated volume expansion, when considering that the

pseudomorph interiors may not actually define the precise border of the parent staurolite crystal.

Structural formula and crystal chemistry. The precise structure and formula for staurolite has been a puzzle to crystallographers for many years. It has been established that most or all staurolite is monoclinic (pseudo-orthorhombic) of space group  $C2/m$ , containing two formula units per unit cell (Náray-Szabó and Sasvári, 1958).

The earliest study of staurolite crystal chemistry to use the best available analyses of very pure natural material was Juurinen (1956). He established that Ca and alkalis present in many staurolite analyses are due to impurities. He also established general composition ranges, particularly for structural water. Unfortunately Juurinen assumed a simple structural formula with full cation sites, resulting in his proposed formula  $(Fe_2Al_9Si_4O_{23}(OH)_2)$  having a unit +1 charge. Variations of Juurinen's formula have been proposed by different authors to make the charges balance. Writing the formula with only one  $OH^-$  (Náray-Szabó and Sasvári, 1958; Ganguly, 1972) balances the charge but does not agree well with most chemical data, which indicate more water. Other authors assign one  $H_2O$  per formula unit, and assume simple fractional numbers of aluminum ( $Al_{26/3}$ , Thompson, 1976) or silicon ( $Si_{15/4}$ , Richardson, 1967a; Hoschek, 1969; Hall, 1970), or complex fractional cation proportions  $((Fe_2Al_9Si_4 \times 46/47)O_{22}(OH)_2)$ , Holdaway and Lee, 1977). Such methods do in fact correspond reasonably well to some analyses. Recent detailed work indicates, however, that the formula for staurolite is even more complex.



Cation site locations and occupancies have been proposed based on single crystal X-ray diffraction and computer structural refinement methods (Smith, 1968; Griffen and Ribbe, 1973). Cation substitutions have been deduced by these authors by principal component analysis, mössbauer spectrometer information, and neutron and X-ray diffraction data. The simplified and generalized results are listed in Table 4. Both Smith (1968), and Griffen and Ribbe (1973) assume no ferric iron, based on chemical and mössbauer data, and source rock petrology, and find about one  $H_2O$  per formula unit in the samples studied.

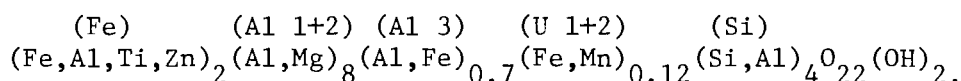
Table 4. Staurolite cation site information. Several cation sites are very similar to each other and are grouped together. Site occupancies and primary cation substitutions are after Smith (1968), and Griffen and Ribbe (1973).

Site	# of Sites	Coordination	Approximate Occupancies	Relative Size	Principal Cations
Fe	2	4	2 (full)	Large	Fe, Al, Ti, Zn
Si	4	4	4 (full)	Small	Si, Al
Al 1A	2	6	8 (full)	Medium	Al, Mg
Al 1B	2				
Al 2	4				
Al 3A	1	6	0.7 cations 1.3 vacancy	Large	Al, Fe
Al 3B	1				
U1	1	6	0.12 cations 1.88 vacancy	Very Large	Mn, Fe
U2	1				
Total	18		14.82 (+ one $H_2O$ )		
This study (23 oxygens)			14.72 (+ one $H_2O$ )		
(24 oxygens)			14.93 (+ 0.69 $H_2O$ )		

There are nine different types of cation sites, many of which are very similar in size, coordination, occupancy, and principal cations, which have been grouped together by the present writer. The

Fe, Si, Al 1, and Al 2 sites are found to be essentially full and the Al 3 and U sites to be largely vacant. The partially vacant sites and the complex and somewhat unusual cation substitutions make the precise structural formula uncertain.

On the basis of Table 4, the simplified and generalized structural formula for staurolite may be written as follows:



The main points to note in the structural formula are as follows:

- 1) The Fe, Al 1, Al 2, and Si sites are full and the Al 3 and U sites largely empty.
- 2) Mg substitutes for Al in the Al 1 and Al 2 sites, but not for iron.
- 3) About 75% of iron is in the tetrahedral Fe site, the remainder of that site being filled with Ti, Zn, and Al.
- 4) About 25% of iron is in the octahedral Al 3 and U sites.
- 5) U site occupancy is only about 1/6 that of the Al 3 site.

Structural formula recipe. As can be seen in Table 5, neither set of calculated cation proportions corresponds well to the simplified structural formulae proposed by other authors, including  $\text{Al}_{26/3}$ ,  $\text{Si}_{15/4}$ , integral  $\text{Fe}_2\text{Al}_9\text{Si}_4$ , ideal integral cation proportions multiplied times 46/47, ideal one or two  $\text{OH}^-$  per formula unit, or  $(\text{total OH}^-)-1 = 4(4-\text{Si})$ . Based on available information, particularly that summarized in Table 4, a recipe has been devised by the present writer to compute staurolite structural formulae. This is the same procedure used to calculate staurolite structural formulae in Table 5 for both sets of cation proportions. The recipe is as follows:

- 1) Calculate cation proportions to 23 oxygens, or to 24 oxygens if weight percent water can be measured.
- 2) Put all Si in the Si site, all Mn in the U site, all Mg in the Al 1, 2 site, all Cr into the Al 3 site, and all Ti and Zn into the Fe site.
- 3) Put 75% of the iron into the Fe site and 25% into the Al 3 site.
- 4) Fill the remainder of the Si site with Al.
- 5) Fill the remainder of the Fe site with Al.
- 6) Fill the remainder of the Al 1, 2 site with Al.
- 7) Put all remaining Al in the Al 3 site.
- 8) Sum the Al, Fe, Cr, and Mn present in the Al 3 and U sites.
- 9) Multiply the sum from (8) by 0.12/0.82. This product is the U site occupancy.
- 10) Add all Mn and sufficient Fe from the sum in (8) to equal the product in (9), and put into the U site.
- 11) Put all Al and Cr from (8) and remaining Fe from (10) into the Al 3 site.

Chemical analyses. Electron microprobe chemical analyses of staurolite from the Littleton Formation in the New Salem area are listed in Table 5. The individual analyses for samples U01A and NS118 were averaged because variations in staurolite composition were well within analytical uncertainty. Cation proportions for each sample average were calculated two ways. The first is on the basis of a formula unit containing 23 oxygens plus one  $\text{H}_2\text{O}$ , as was found by Juurinen (1956), Smith (1968), and Griffen and Ribbe (1973). The second method of calculation was on a basis of 24 oxygens per formula unit, with  $\text{OH}^-$  calculated from weight percent water. The average oxide weight percent total is 98.54% (1.46%  $\text{H}_2\text{O}$ ), which indicates 0.69  $\text{H}_2\text{O}$  per formula unit. The oxide

Table 5. Averaged electron microprobe analyses of staurolite. Staurolite did not appear to vary in composition in either sample within analytical uncertainty. The first column for each sample lists oxide weight percent and weight percent water by difference of oxide weight percent total from 100%. Cation proportions are calculated on a basis of 23 oxygens plus one  $H_2O$  ( $2 OH^-$ ). In parentheses is the weight percent water which would be present if the assumption of one  $H_2O$  per formula unit were correct. The second column lists cation proportions calculated on the basis of 24 oxygens, with  $H^+$  treated as another cation to give analytical  $OH^-$ . The columns on the following page list the structural formulae calculated from the cation proportions. See text.

Location	U01A			NS118		
N, Averages	15		standard deviation	19		standard deviation
$SiO_2$	27.32		0.39	27.83		0.22
$TiO_2$	0.63		0.03	0.55		0.06
$Al_2O_3$	54.06		0.59	53.70		0.27
$Cr_2O_3$	0.05		0.04	0.01		0.01
$FeO$	14.60		0.21	14.63		0.22
$MnO$	0.01		0.01	0.01		0.01
$MgO$	1.52		0.10	1.57		0.10
$ZnO$	0.29		0.18	0.31		0.05
$Na_2O$	0		-	-		-
$K_2O$	0		-	-		-
Sum	98.48		0.70	98.61		0.43
$H_2O$	1.52		0.70	1.39		0.43
	(2.16)		-	(2.14)		-
Total	100			100		

Cations / N Oxygens	23	24		23	24	
Si	3.785	3.835	0.049	3.850	3.909	0.025
Ti	0.066	0.066	0.003	0.057	0.058	0.006
Al	8.828	8.943	0.064	8.756	8.889	0.034
Cr	0.005	0.006	0.004	0.001	0.001	0.001
Fe	1.692	1.714	0.026	1.693	1.718	0.023
Mn	0.001	0.001	0.001	0.001	0.001	0.001
Mg	0.314	0.318	0.021	0.324	0.329	0.021
Zn	0.030	0.030	0.019	0.032	0.032	0.006
Total	14.721	14.913	0.022	14.714	14.937	0.020
$OH^-$	(2)	1.425	0.066	(2)	1.302	0.040
$\frac{Fe}{Fe+Mg}$	0.843	0.844	-	0.839	0.839	-

Table 5. (Staurolite analyses, continued).

Location		U01A		NS118	
N, Averages		15		19	
Cations/ N Oxygens		23	24	23	24
Fe Site	Fe	1.269	1.286	1.270	1.289
	Zn	0.030	0.030	0.032	0.032
	Ti	0.066	0.066	0.057	0.058
	Al	<u>0.635</u>	<u>0.619</u>	<u>0.641</u>	<u>0.622</u>
	Sum	<u>2.000</u>	<u>2.000</u>	<u>2.000</u>	<u>2.000</u>
Al 1, 2 Sites	Al	7.686	7.682	7.676	7.671
	Mg	<u>0.314</u>	<u>0.318</u>	<u>0.324</u>	<u>0.329</u>
		<u>8.000</u>	<u>8.000</u>	<u>8.000</u>	<u>8.000</u>
Al 3 Sites	Al	0.292	0.479	0.289	0.505
	Cr	0.005	0.005	0.001	0.001
	Fe	<u>0.317</u>	<u>0.295</u>	<u>0.320</u>	<u>0.293</u>
	Sum	<u>0.614</u>	<u>0.779</u>	<u>0.610</u>	<u>0.799</u>
U Sites	Mn	0.001	0.001	0.001	0.001
	Fe	<u>0.106</u>	<u>0.133</u>	<u>0.103</u>	<u>0.136</u>
	Sum	<u>0.107</u>	<u>0.134</u>	<u>0.104</u>	<u>0.137</u>
Si Site	Si	3.785	3.835	3.850	3.909
	Al	<u>0.215</u>	<u>0.165</u>	<u>0.150</u>	<u>0.091</u>
	Sum	<u>4.000</u>	<u>4.000</u>	<u>4.000</u>	<u>4.000</u>
Total		14.721	14.913	14.714	14.937
OH <sup>-</sup>		(2)	1.425	(2)	1.302

weight percent total is 0.69% too high to allow for one  $H_2O$  per formula unit. This amount may be too high to ascribe to systematic analytical error, and therefore the cation proportions calculated to 24 oxygens is probably the most realistic.

Because staurolite has an uncertain amount of water and is non-stoichiometric, ferric iron cannot be calculated using electron microprobe analyses. Ferric iron is probably not present in significant quantities on the basis of stoichiometric calculations done on garnet, chlorite, and ilmenite, and the presence of graphite in the same rocks as the analyzed staurolite.

### Garnet

Field distribution and habit. Garnet is one of the most widespread minerals of prograde origin in the Littleton Formation, and one of the easiest to identify in the field. In outcrop fresh garnets are pink to dark red equant crystals, most commonly two to three millimeters in diameter. Some outcrops in the southern half of the field area contain larger, red garnets up to 1 cm across.

Garnet has been affected by retrograde alteration in a region within the retrograde staurolite isograd. The first direct association of chlorite with garnet is as a thin, shiny green veneer covering part or all of the garnet on freshly exposed surfaces (zone R4). With more severe retrograding, the thin chlorite veneer thickens, finally replacing the garnet entirely (zone R6). The thickening of chlorite mantles occurs over a relatively large distance in the field. Because garnet is abundant in most outcrops, commonly has a regular size and

shape, and is typically replaced in a methodical and easily recognizable manner, concentric zones of increasing garnet replacement have been identified and mapped (Figure 9).

The outermost line in Figure 9 separates areas of outcrops with completely fresh garnets in zones R1 to R3 from garnets bearing chlorite rims in zones R4 to R6. The second line separates garnets having chlorite rims less than 0.2 mm thick in zone R4 from garnets with rims more than 0.2 mm thick in zone R5. The thickness of chlorite rims on garnets was estimated by comparison to an 0.5 mm diameter pencil lead under a 10x hand lens, and checked by measurements made in thin section. The third, innermost line on the map in effect is the retrograde garnet-out isograd, separating outcrops bearing garnet in zones R1 to R5 from those bearing only pseudomorphs after garnet in zone R6. As can be seen, the garnet-out isograd encompasses a rather small elongated area roughly in the center of the belt of Littleton Formation, approximately straddling the axial surface of the Prescott syncline.

Textures in thin section. Fresh garnets in thin section are generally subhedral, equant crystals that are isotropic and commonly faint pink. They typically contain abundant inclusions, commonly segregated into one or two concentric shells. Thin trails of minute inclusions radiating from the garnet center are also rather common. Similar inclusion trails have been identified from other metamorphic terranes as having formed at the edges of dodecahedron and trapezohedron crystal faces during garnet growth (Van der Voort, 1978). The most abundant

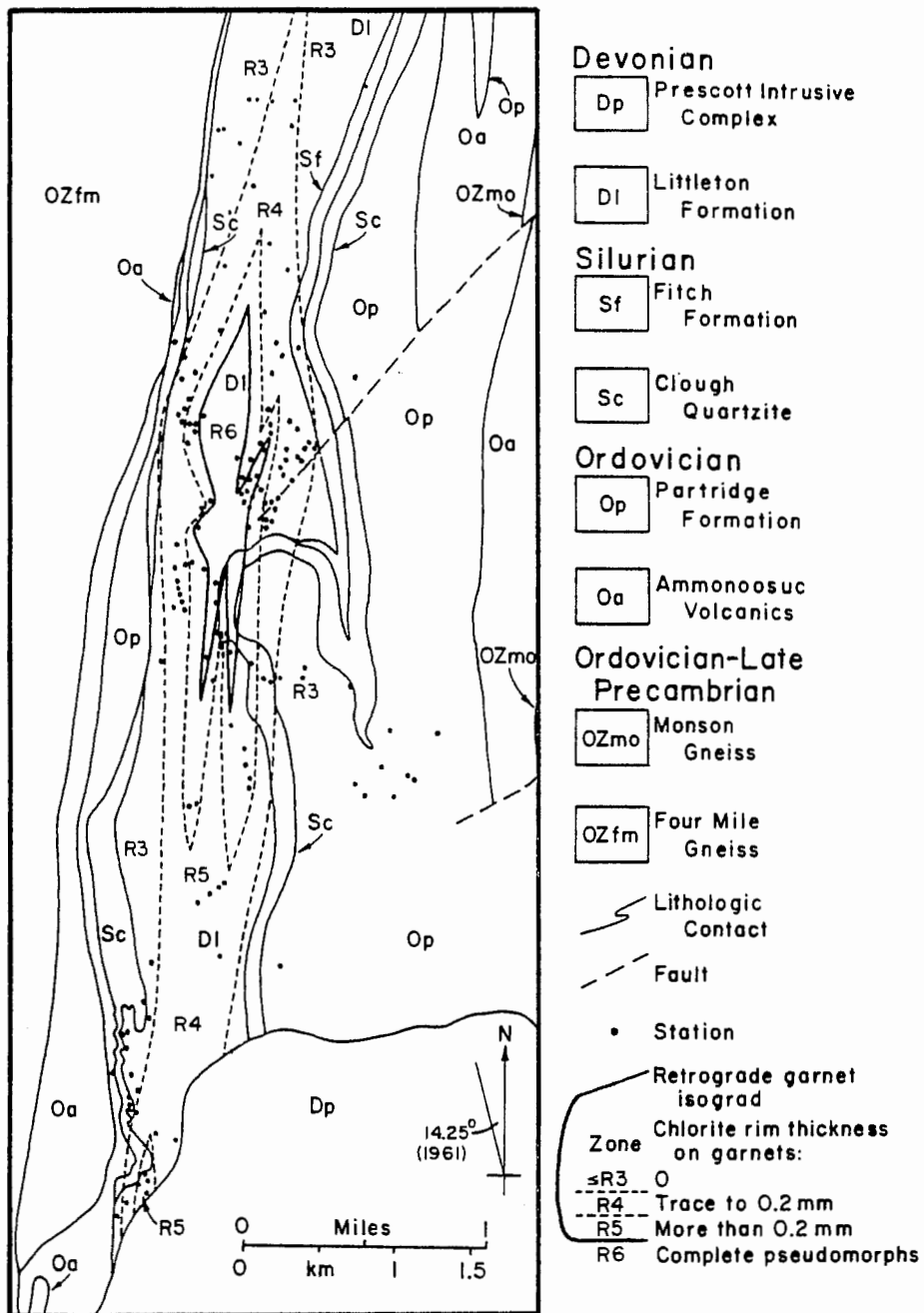


Figure 9. Map showing chlorite rim thickness on garnets, and the retrograde garnet-out isograd. The most severely retrograded rocks occur on the axial surface of the Prescott syncline in zone R6.



inclusions are of quartz and ilmenite. Inclusions of graphite, zircon, tourmaline, apatite, and muscovite, in roughly that order of abundance also occur. Sillimanite and biotite inclusions were not found.

Figure 10 is a series of four drawings of garnets in thin section showing the textural relationships during garnet breakdown. The first drawing (Figure 10a, sample U01A) is of a fresh garnet. Figure 10b (sample NS98) shows a garnet that has minor chlorite associated with its rim, belonging to zone R4 in Figure 9. Notice that in the early stages of garnet alteration, garnet is not necessarily completely enclosed by chlorite. Figures 10c and 10d (samples NS74 and NS62, respectively) depict successive stages of garnet replacement in zone R5.

In Figure 10c and 10d, fine-grained muscovite occurs intergrown with chlorite in a thin, discontinuous shell adjacent to the garnet. Muscovite in this habit is common and persists as dispersed, irregular platelets even in complete pseudomorphs after garnet. The pseudomorph in Figure 10d also contains some larger recrystallized muscovite plates of probable retrograde origin.

The regular sequence of garnet replacement shown in Figure 10 only occurs in garnets that were not fractured at the time of retrograding. Fractured garnets show the same kind of chlorite alteration along cracks as on rims, and the rims develop concentrically on each and every piece of the original crystal, allowing small pieces to vanish before large pieces. This indicates that both garnet rims and cores were in disequilibrium with the host rock during alteration.

Chemical zoning. The garnets in the study area are primarily almandine

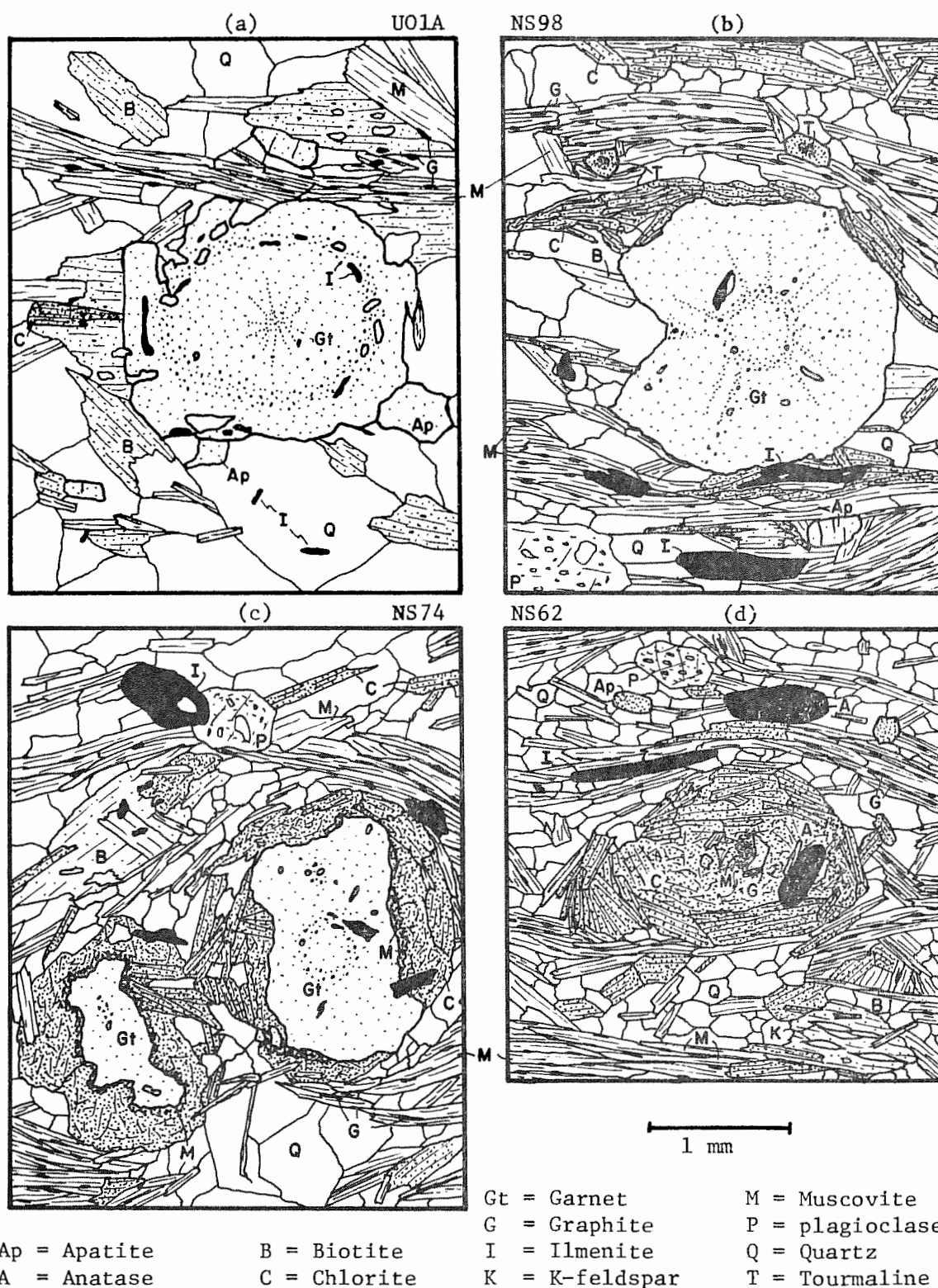


Figure 10. Drawings of garnets from various samples. The sequence from a to d shows the concentric manner of garnet alteration.

in composition, with variable quantities of pyrope, spessartine, and grossular components in solid solution. Trace quantities of andradite component may also be present. All analyzed garnets, show evidence of relict chemical zoning of the divalent cations, that apparently developed as the garnets grew during prograde metamorphism (Hollister, 1966; Anderson, 1973; Tracy et al., 1976).

The garnet from outcrop U01A (Figure 10a) was selected for a point by point microprobe traverse. The traverse was from the left edge of the garnet (as seen in the sketch), through the grain center, to the right edge of the garnet. Twenty points were analyzed at approximately 100  $\mu\text{m}$  intervals (Table 6). All inclusions were avoided by slight offsets of some analysis points. The data in Table 6 is also plotted in Figure 11 where various cations per formula unit, and Fe/Fe+Mg ratios are plotted against analysis number.

Starting at the bottom of Figure 11, the plots for Mn and Ca follow roughly bell-shaped curves with high concentrations in the core and lower concentrations in the rim. Asymmetry in the curves may be due to analytical scatter, or to the possibility that different parts of the garnet were adjacent to different minerals during growth. The change indicated by the curves is quite dramatic, 0.271 to 0.033 Mn and 0.273 to 0.069 Ca per formula unit (9.0 to 1.1% spessartine and 9.2 to 2.3% grossular components) from core to rim. This type of zoning is very common in medium-grade metamorphic rocks (Hollister, 1966; Atherton, 1968; Saxena, 1968; Hall, 1970; Thompson, 1976a), and is usually ascribed to the great affinity of garnet for the larger divalent cations. Indeed, the earliest garnet may have required Mn and/or Ca for



Table 6. (Garnet traverse, continued).

Location		U01A						
Analysis No.		47	48	49	50	51	52	53
	SiO <sub>2</sub>	37.65	37.80	36.89	37.38	37.33	36.92	37.24
	Al <sub>2</sub> O <sub>3</sub>	20.81	21.00	20.64	20.57	20.80	21.07	21.01
	FeO	33.85	33.39	32.94	33.14	33.09	34.19	35.08
	MnO	3.38	3.76	3.98	4.06	3.90	3.21	2.73
	MgO	2.10	1.95	1.94	1.98	1.76	2.04	2.23
	CaO	<u>3.01</u>	<u>3.15</u>	<u>3.21</u>	<u>3.09</u>	<u>3.27</u>	<u>2.90</u>	<u>2.21</u>
	Total	100.80	101.00	99.60	100.21	100.15	100.33	100.50
Structural Formulae								
Si Site	Si	3.019	3.023	3.000	3.018	3.015	2.981	2.999
Al Site	Al	1.968	1.976	1.979	1.960	1.981	2.007	1.995
M <sup>+2</sup> Site	Fe	2.271	2.234	2.242	2.240	2.236	2.310	2.364
	Mn	0.230	0.255	0.274	0.267	0.267	0.220	0.186
	Mg	0.252	0.233	0.235	0.239	0.213	0.246	0.268
	Ca	<u>0.259</u>	<u>0.270</u>	<u>0.279</u>	<u>0.267</u>	<u>0.283</u>	<u>0.251</u>	<u>0.191</u>
	Sum	<u>3.012</u>	<u>2.992</u>	<u>3.030</u>	<u>3.013</u>	<u>2.999</u>	<u>3.027</u>	<u>3.009</u>
	Total	7.999	7.991	8.009	7.991	7.995	8.015	8.003
Almandine	%	75.4	74.7	74.0	74.3	74.6	76.3	78.6
Spessartine	%	7.6	8.5	9.0	8.9	8.9	7.3	6.2
Pyrope	%	8.4	7.8	7.8	7.9	7.1	8.1	8.9
Grossular	%	<u>8.6</u>	<u>9.0</u>	<u>9.2</u>	<u>8.9</u>	<u>9.4</u>	<u>8.3</u>	<u>6.3</u>
Total		100%	100%	100%	100%	100%	100%	100%
	$\frac{\text{Fe}}{\text{Fe}+\text{Mg}}$	0.900	0.906	0.905	0.904	0.913	0.904	0.898

Core

Table 6. (Garnet traverse, continued).

Location		U01A					Average
Analysis No.		54	55	56	57	58	N = 20
SiO <sub>2</sub>		37.02	37.65	37.10	37.33	36.92	37.29
Al <sub>2</sub> O <sub>3</sub>		20.82	21.02	21.04	20.92	21.09	20.86
FeO		36.41	36.43	37.32	37.78	37.62	35.40
MnO		1.70	1.33	0.84	0.66	0.60	2.28
MgO		2.46	2.64	2.99	2.73	2.54	2.41
CaO		1.21	1.33	1.27	0.97	0.76	1.98
Total		99.62	100.40	100.56	100.39	99.53	100.31
Structural Formulae							
Si Site	Si	3.007	3.023	2.984	3.007	2.999	3.006
Al Site	Al	1.994	1.990	1.996	1.987	2.020	1.988
M <sup>+2</sup> Site	Fe	2.475	2.448	2.512	2.547	2.557	2.389
	Mn	0.117	0.090	0.057	0.045	0.041	0.155
	Mg	0.298	0.317	0.358	0.329	0.307	0.290
	Ca	0.105	0.114	0.109	0.084	0.076	0.175
	Sum	2.995	2.969	3.036	3.005	2.981	3.009
Total		7.996	7.982	8.016	7.999	8.000	8.003
Almandine	%	82.7	82.5	82.7	84.8	85.8	79.4
Spessartine	%	3.9	3.0	1.9	1.5	1.4	5.2
Pyrope	%	9.9	10.7	11.8	10.9	10.3	9.6
Grossular	%	3.5	3.8	3.6	2.8	2.5	5.8
Total		100%	100%	100%	100%	100%	100%
	$\frac{\text{Fe}}{\text{Fe}+\text{Mg}}$	0.893	0.885	0.875	0.886	0.893	0.892

Rim

Table 6. (Garnet traverse, continued).

N = 20                      Standard  
                                 deviation

SiO <sub>2</sub>	0.45
Al <sub>2</sub> O <sub>3</sub>	0.28
FeO	1.77
MnO	1.30
MgO	0.39
<u>CaO</u>	0.92
Total	0.69

## Structural Formulae

Si Site Si            0.015

Al Site Al            0.016

M<sup>+2</sup> Site Fe           0.130  
          Mn           0.088  
          Mg           0.048  
          Ca           0.080  
          Sum           0.028

Total                0.018

Almandine    %        4.2

Spessartine %        2.9

Pyrope        %        1.5

Grossular    %        2.7

Total                -

Fe  
Fe+Mg            0.011

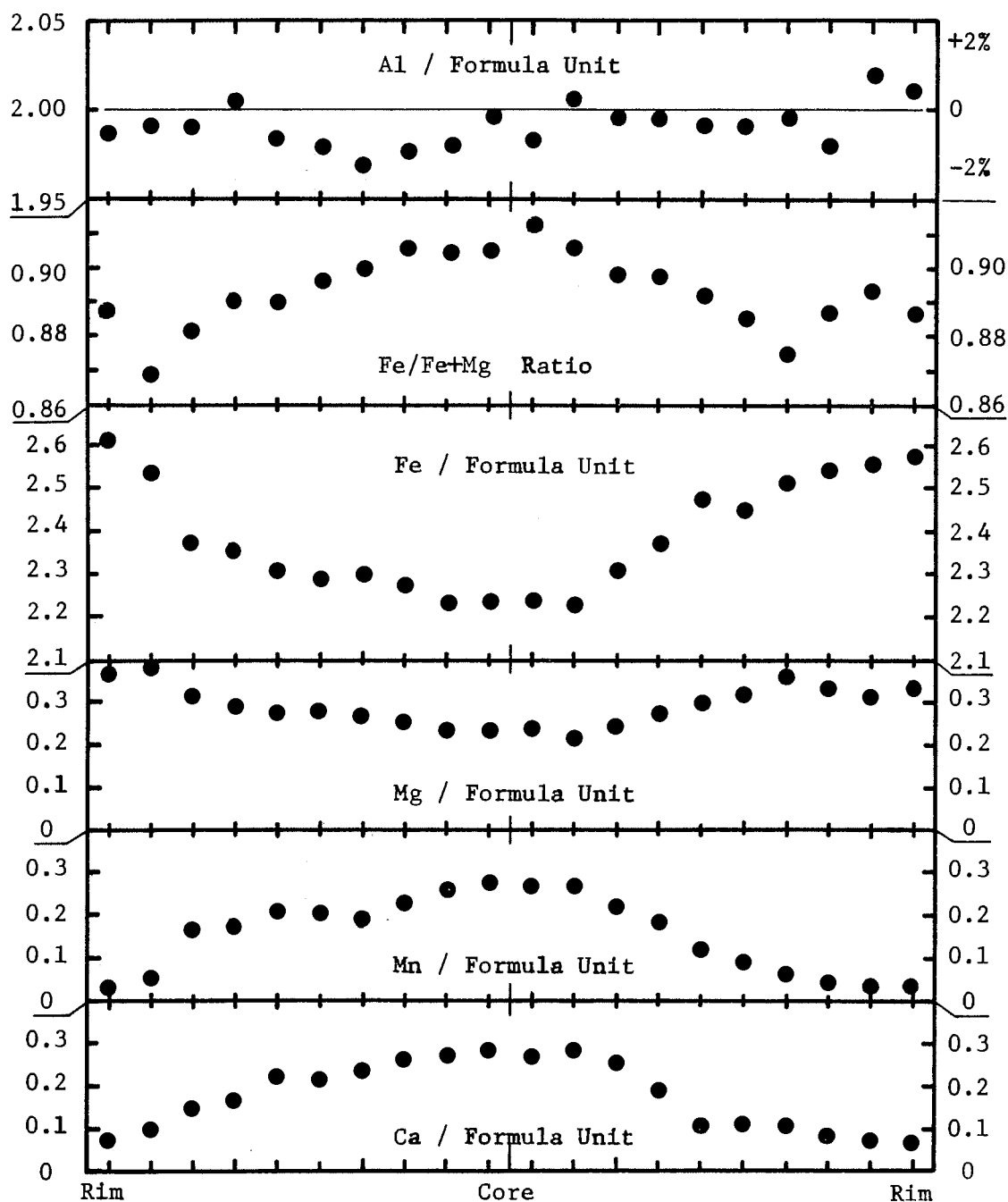


Figure 11. Plotted results from an electron microprobe traverse of a fresh garnet in sample UO1A. The 20 analysis points are spaced about 100  $\mu\text{m}$  apart in the 2 mm diameter garnet. The left rim of the garnet is adjacent to a large biotite crystal whereas the right rim is adjacent to quartz. This may in part account for the lack of symmetry in the plotted curves.



its stability (Müller and Schneider, 1971). The concentration of Ca and Mn in the garnet cores depletes the rest of the rock and later-formed garnet rims in those elements (Hollister, 1966; Saxena, 1968; Anderson and Glenn, 1973).

Mg and Fe follow trends opposite those of Mn and Ca, due at least in part to the lower affinity of garnets for the smaller cations, and to the depletion of the rock in larger divalent cations by garnet cores. Other factors may include changes in divalent cation partition coefficients with temperature (Frost, 1962; Atherton, 1968; Hietanen, 1969; Thompson, 1976c; Tracy et al., 1976; Ferry and Spear, 1977 and 1978), temperature and composition (Albee, 1965a; Saxena, 1969; Lyons and Morse, 1970; Goldman and Albee, 1977, Ghent et al., 1979), or changes in phase relations (Thompson, 1957 and 1976b). Retrograde zoning apparently does not occur in these garnets, as has been described from higher grade terranes (Evans and Guidotti, 1966; Grant and Weiblen, 1971; Tracy et al., 1976).

At the top of Figure 11 is plotted aluminum concentration per formula unit. The average is somewhat below 2 (stoichiometric) but shows no distinct core to rim trend. The irregular curve variations are due to analytical statistical scatter. One model for garnet zoning (Müller and Schneider, 1971), ascribes Mn-rich garnet cores to high rock oxidation states early in the period of garnet growth. The model fails in this case because it presumably predicts significant core andradite component as well as high core Mg and/or low core Fe/Fe+Mg ratios, neither of which is observed.

Rim compositions. Table 7 contains averaged rim compositions for the various analyzed samples. At the end of the table is the average for all 87 garnet analyses. The first column for each sample has been calculated on a basis of 12 oxygens with all Fe as FeO. The second column differs from the first in that the cation proportions were recalculated on a basis of 8 cations to obtain a hypothetical quantity of ferric iron. Oxide weight percents,  $\text{Fe}^{+2}/\text{Fe}^{+2}+\text{Mg}$  ratios, and garnet component percents were adjusted accordingly. It was also necessary to change the structural formulae somewhat to maintain rational site occupancies, although the resulting formulae are somewhat disquieting. The amount of andradite component in the analyzed garnets is at most about 0.1%, and even this amount may be the result of systematic error, as will be discussed below.

The rim compositions for samples U01A, NS118, NS18, and NS87 show a systematic decrease in Fe and Mg, and an increase in Mn and Ca with retrograding. These garnets were all originally about 2 mm in diameter and were pseudomorphed concentrically, following the trend of increasing replacement of garnet by chlorite toward the garnet isograd (Figure 9). The chemical trend is caused by exposure of successively Fe+Mg poorer and Mn+Ca richer relict garnet cores, similar to the replacement sequence depicted in Figures 10a to 10d.

Garnet in sample NS85 does not fit the chemical trend described in the preceeding paragraph, because the single garnet relict in the thin section occurred close to the original garnet rim, rather than the core. This garnet was originally about the same size and composition

Table 7. Averaged electron microprobe analyses of garnet rims from various samples. The first column for each sample contains oxide weight percent and cation proportions calculated on the basis of 12 oxygens and all ferrous iron. The second column has cation proportions and weight percents recalculated on the bases of eight cations, assuming some ferric iron. The amount of ferric iron is small and possibly subject to systematic analytical error. Fe/Fe+Mg ratios only include ferrous iron.

Location	U01A			NS118		
N, Averages	5		Standard deviation	9		Standard deviation
SiO <sub>2</sub>	36.87	36.87	0.33	36.74	36.74	0.26
Al <sub>2</sub> O <sub>3</sub>	20.86	20.86	0.40	21.12	21.12	0.42
Fe <sub>2</sub> O <sub>3</sub>	-	0.79	-	-	0.80	-
FeO	38.23	37.52	0.43	38.02	37.30	0.20
MnO	0.50	0.50	0.06	0.52	0.52	0.04
MgO	2.83	2.83	0.17	2.90	2.90	0.06
CaO	0.75	0.75	0.11	0.68	0.68	0.04
Total	100.04	100.12	0.52	99.98	100.06	0.78

#### Structural Formulae

Si Site	Si	2.986	2.982	0.023	2.977	2.972	0.015
	Al	-	0.018		-	0.028	
	Sum	2.986	3.000		2.977	3.000	
Al Site	Al	1.995	1.972	0.032	2.015	1.983	0.031
	Fe <sup>+3</sup>	-	0.048		-	0.049	
	Sum	1.995	2.020		2.015	2.032	
M <sup>+2</sup> Site	Fe <sup>+2</sup>	2.593	2.539	0.033	2.578	2.524	0.019
	Mn	0.035	0.035	0.003	0.035	0.035	0.003
	Mg	0.342	0.341	0.021	0.351	0.350	0.006
	Ca	0.065	0.065	0.010	0.059	0.059	0.004
	Sum	3.035	2.980	0.036	3.023	2.968	0.034
	Total	8.019	8.000	0.014	8.015	8.000	0.007
Almandine	%	85.4	85.2	1.0	85.2	85.0	0.5
Spessartine	%	1.2	1.2	0.1	1.2	1.2	0.1
Pyrope	%	11.3	11.4	0.7	11.6	11.8	0.2
Grossular	%	2.1	2.1	0.3	2.0	2.0	0.1
Andradite	%	-	0.1	-	-	0	-
Total		100%	100%		100%	100%	
Fe Fe+Mg		0.883	0.882	0.015	0.880	0.878	0.006

Table 7. (Garnet rims, continued).

Location	NS18		Standard deviation	NS87		Standard deviation
N, Averages	5			6		
SiO <sub>2</sub>	36.37	36.37	0.55	37.06	37.06	0.45
Al <sub>2</sub> O <sub>3</sub>	20.73	20.73	0.37	21.00	21.00	0.35
Fe <sub>2</sub> O <sub>3</sub>	–	2.03	–	–	0.78	–
FeO	36.79	34.96	0.43	34.89	34.19	0.49
MnO	2.07	2.07	0.56	3.73	3.73	0.36
MgO	2.29	2.29	0.20	1.82	1.82	0.21
CaO	1.81	1.81	0.19	2.45	2.45	0.30
Total	100.06	100.26	0.58	100.95	101.04	0.68

## Structural Formulae

Si Site	Si	2.964	2.949	0.029	2.986	2.980	0.036
	Al	-	0.051		-	0.020	
	Sum	2.964	3.000		2.986	3.000	
Al Site	Al	1.993	1.931	0.038	1.995	1.970	0.033
	Fe <sup>+3</sup>	-	0.124		-	0.047	
	Sum	1.993	2.055		1.995	2.017	
M <sup>+2</sup> Site	Fe <sup>+2</sup>	2.508	2.370	0.038	2.352	2.300	0.034
	Mn	0.143	0.142	0.024	0.255	0.254	0.025
	Mg	0.278	0.276	0.024	0.218	0.218	0.025
	Ca	0.158	0.156	0.017	0.211	0.211	0.026
	Sum	3.087	2.944	0.022	3.036	2.983	0.032
	Total	8.044	8.000	0.013	8.017	8.000	0.016
Almandine	%	81.3	80.5	1.0	77.5	77.1	1.1
Spessartine	%	4.6	4.8	1.2	8.4	8.5	0.8
Pyrope	%	9.0	9.4	0.8	7.2	7.3	0.8
Grossular	%	5.1	5.0	0.5	6.9	6.9	0.8
Andradite	%	-	0.3	-	-	0.2	-
Total		100%	100%	-	100%	100%	-
<u>Fe</u> Fe+Mg		0.900	0.896	0.018	0.915	0.913	0.21

Table 7. (Garnet rims, continued).

Location	NS85		Standard deviation	NS71		Standard deviation
N, Averages	7			14		
SiO <sub>2</sub>	37.17	37.17	0.33	36.56	36.56	0.46
Al <sub>2</sub> O <sub>3</sub>	21.21	21.21	0.39	21.14	21.14	0.44
Fe <sub>2</sub> O <sub>3</sub>	—	0.51	—	—	0.82	—
FeO	35.36	34.90	0.28	35.83	35.09	0.80
MnO	2.37	2.37	0.10	2.81	2.81	0.71
MgO	2.71	2.71	0.05	1.18	1.18	0.10
CaO	1.81	1.81	0.09	2.84	2.84	0.24
Total	100.63	100.68	0.48	100.36	100.46	0.53

## Structural Formulae

Si Site	Si	2.985	2.981	0.027	2.976	2.969	0.019
	Al	-	0.019		-	0.031	
	Sum	2.985	3.000		2.976	3.000	
Al Site	Al	2.008	1.986	0.037	2.017	1.981	0.042
	Fe <sup>+3</sup>	-	0.031		-	0.050	
	Sum	2.008	2.017		2.017	2.031	
M <sup>+2</sup> Site	Fe <sup>+2</sup>	2.375	2.340	0.019	2.436	2.380	0.053
	Mn	0.162	0.162	0.007	0.194	0.194	0.045
	Mg	0.326	0.325	0.006	0.143	0.143	0.012
	Ca	0.156	0.156	0.008	0.253	0.252	0.021
	Sum	3.019	2.983	0.020	3.026	2.969	0.027
	Total	8.012	8.000	0.007	8.019	8.000	0.012
Almandine	%	78.6	78.5	0.6	80.5	80.2	1.8
Spessartine	%	5.4	5.4	0.2	6.4	6.5	1.6
Pyrope	%	10.8	10.9	0.2	4.7	4.8	0.4
Grossular	%	5.2	5.1	0.3	8.4	8.3	0.7
Andradite	%	-	0.1	-	-	0.2	-
Total		100%	100%	-	100%	100%	-
Fe Fe+Mg		0.879	0.878	0.008	0.945	0.943	0.024

Table 7. (Garnet rims, continued).

All Garnets N = 87			Standard deviation	
SiO <sub>2</sub>	36.97	36.97	0.33	
Al <sub>2</sub> O <sub>3</sub>	21.02	21.02	0.18	
Fe <sub>2</sub> O <sub>3</sub>	-	0.72	-	
FeO	36.11	35.46	1.34	
MnO	2.19	2.19	1.18	
MgO	2.30	2.30	0.62	
CaO	1.85	1.85	0.80	
<u>Total</u>	<u>100.44</u>	<u>100.51</u>	0.35	
Structural Formulae				
Si Site	Si	2.986	2.980	0.013
	Al	-	0.020	
	Sum	2.986	3.000	
Al Site	Al	2.000	1.976	0.012
	Fe <sup>+3</sup>	-	0.044	
	Sum	2.000	2.020	
M <sup>+2</sup> Site	Fe <sup>+2</sup>	2.441	2.392	0.099
	Mn	0.152	0.152	0.081
	Mg	0.276	0.275	0.075
	Ca	0.161	0.161	0.075
	<u>Sum</u>	<u>3.030</u>	<u>2.980</u>	0.025
	Total	8.016	8.000	0.013
Almandine	%	80.6	80.3	3.1
Spessartine	%	5.0	5.1	2.6
Pyrope	%	9.1	9.2	2.5
Grossular	%	5.3	5.3	2.4
Andradite	%	-	0.1	-
Total		100%	100%	-
	<u>Fe</u>	0.898	0.897	0.024
	Fe+Mg			

as the preceeding four samples, but the local environment precluded concentric replacement. The garnet was probably fractured in some areas, allowing those parts of the crystal to alter more readily. The relict piece is also adjacent to a large quartz segregation which probably protected that side of the garnet from early destruction. A dramatic example of garnet shielded from alteration by quartz is in sample NS95 (no analyses), where one garnet in the thin section is entirely embedded in an ovoid mass of coarse-grained quartz. That garnet is absolutely fresh whereas all others in the slide are about 95% replaced by chlorite.

The garnet in sample NS71 is distinct from the other five, having been more than twice the diameter of garnets in the other five samples prior to retrograding. It is quite high in Ca, and lower in Mg than any other single garnet analysis, reflecting the Mg-poor rock composition. Sample NS71 is the only rock containing chloritoid, and also harbors the most iron-rich muscovite and chlorite of any analyzed sample.

Discussion of garnet stoichiometry. As can be seen in Table 7, neither the ferric iron corrected nor the reduced garnet stoichiometries in any single sample or the average of all 87 analyses yield satisfying numbers. The high oxide weight percent total (100.44%, or 100.51% including  $\text{Fe}_2\text{O}_3$ ) in the average of all 87 analyses indicates that some or all elements were not accurately standardized prior to analysis in a very systematic way. The structural formula indicates that the divalent cation total is quite high (3.030) and Si rather low (2.986),

indicating an excess of some divalent cation. Because of the great abundance of iron relative to the other divalent cations, it is the probable culprit.

Calculations indicate a best fit for cation proportions if average FeO weight percent were reduced to 35.71%, 0.40 weight percent lower than the actual average of 36.11% FeO. This change results in the weight percent total lowering to 100.04%, Si and Al cations increasing to 2.994 and 2.007 respectively, divalent cations decreasing to a total of 3.001, and total cations decreasing to 8.002. These are very reasonable numbers, suggesting that the assumption of excess iron is correct.

The iron standard used was P130, an almandine-spessartine garnet that supposedly contains 21.75% FeO. If the above reasoning is correct, the actual value is 21.51% FeO. The difference between the two values is actually quite small, and all silicate minerals were analyzed with P130 as the iron standard so the error is similar for all minerals. Fe/Fe+Mg ratios and partition coefficients may be inaccurate by as much as 1%, but this amount is negligible and will not be discussed further.

### Biotite

Field distribution and appearance. Biotite is very abundant in the study area, particularly in relatively unaltered rocks. In outcrop it appears as anhedral to subhedral plates or books up to about 1 or 2 mm across, shiny black on cleavage surfaces. A size range of biotite crystals is common, large crystals grading down to platelets hardly



identifiable in hand specimen. In the retrograded rocks, partially altered biotite plates tend to be rather patchy and dull in appearance with associated chlorite. In zone R6, rocks tend to be biotite-poor or biotite-absent, compared to rocks in zones R1 to R4. The trend, however, is not distinct because the point at which biotite disappears from a rock is critically dependent on bulk composition.

Appearance in thin section. Biotite is markedly pleochroic; light brownish yellow or light tan to dark orange brown or reddish brown. The absorption scheme is  $Z=Y>X$ . The crystals are apparently uniaxial negative to biaxial negative with a very small 2V. Perfect 001 cleavage is well developed. Interference colors range up to fourth order with incomplete "birds-eye maple" extinction. Inclusions of graphite, quartz, ilmenite, zircon, muscovite, feldspar, tourmaline, and apatite, roughly in order of abundance, are found. Pleochroic radiation halos in biotite are well developed adjacent to zircon and allanite, and poorly developed adjacent to apatite.

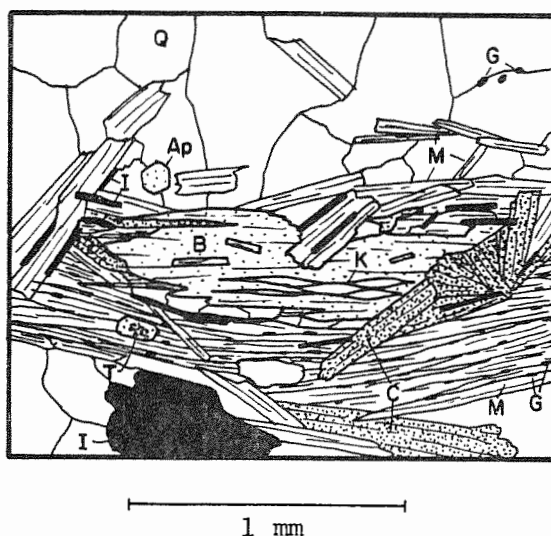
Biotite crystals range in size from about 3 mm across down to very small platelets. Of the larger crystals there are two distinct types. The first is as stout, generally elliptical grains, flattened somewhat on 001 with cores commonly choked with graphite inclusions (Figure 19a, upper right). The graphite-charged biotite interiors are quite distinctive and persist undisturbed during retrograde replacement by sheet silicates, and may be used in some cases to identify the past presence of biotite. The second habit for large biotite crystals is as clear, relatively inclusion-free, somewhat irregular plates

exhibiting a subhedral tendency on 001 (Figures 8a and 10a). Small biotite crystals exhibit morphologies similar to the large inclusion-free biotites, but are generally better developed on 001 (Figures 6a, 8a, 10a and 10b, and 19a).

It is interesting to note that biotite crystals locally have orientations at angles to the primary muscovite foliation, particularly inclusion free biotite. This suggests that the graphite-charged biotite crystals grew during development of the major muscovite foliation, whereas inclusion-deficient crystals grew largely after the main foliation developed.

With retrograde alteration, biotite becomes associated with chlorite and secondary muscovite. Biotite-muscovite and biotite-chlorite grain boundaries are typically sharp, with the secondary minerals commonly subhedral on 001. Most secondary chlorite and muscovite plates cut and "intrude" altering biotite at random angles to the biotite cleavage, with minor amounts of chlorite developed as thin lenses or layers parallel to biotite cleavages. Lenses of K-feldspar commonly develop within biotite parallel to the cleavage, occurring individually or in stacked groups. Examples of biotite associated with secondary muscovite and chlorite, both with and without lenses of K-feldspar may be seen in Figures 10c, 10d, and 12.

Although anatase is a common mineral formed during retrograde metamorphism, titanium released during biotite breakdown is apparently precipitated only as small ilmenite plates, and rarely as acicular rutile. There is no good textural evidence for the direct precipitation



A = Apatite	G = Graphite	M = Muscovite
B = Biotite	I = Ilmenite	Q = Quartz
C = Chlorite	K = K-feldspar	T = Tourmaline

Figure 12. Biotite in an early stage of being replaced by muscovite and chlorite. Station NS111. Note the ilmenite platelets, probably derived from titanium released from biotite. This example contains K-feldspar lenses within the biotite.

of anatase. Secondary ilmenite plates are flattened on 0001, and are usually inclusion free (Figure 12).

Chemistry. Biotite crystal chemistry is quite complex. In keeping with the other sheet silicate minerals described later, biotite differs in composition depending on the degree of retrograde metamorphism. Table 8 contains electron microprobe analyses and structural formulae for biotite from various samples.

In the average structural formula, the A-site occupancy is only 0.837, and the octahedral site occupancy is only 2.930 (assuming full tetrahedral sites). Calculations corrected for A-site deficiency indicate a consistent 5% solid solution toward the dioctahedral muscovite-celadonite series. Biotite compositions for any single

Table 8. Electron microprobe analyses of biotite from various samples. Structural formulae are calculated on the basis of the composition (K,Na) (Fe,Mg)<sub>3</sub>(Si<sub>3</sub>Al O<sub>10</sub>)(PH)<sub>2</sub>, containing 11 oxygens plus one water. OH<sup>-</sup> proportions calculated from H<sub>2</sub>O% on a basis of 12 oxygens.

Locality		U01A						
Analysis No.		3	4	5	11	12	13	14
SiO <sub>2</sub>		35.75	35.55	36.10	36.09	35.12	34.97	35.85
TiO <sub>2</sub>		2.06	1.98	1.90	1.69	1.59	1.54	1.54
Al <sub>2</sub> O <sub>3</sub>		19.77	19.58	19.59	20.37	20.18	19.94	20.25
Cr <sub>2</sub> O <sub>3</sub>		-	-	-	-	-	-	-
FeO		19.87	19.78	20.02	19.47	19.38	19.96	19.62
MnO		0	0.02	0.01	0.02	0	0	0.01
MgO		10.14	10.33	10.09	10.36	10.64	10.30	10.44
ZnO		-	-	-	-	-	-	-
CaO		-	-	-	-	-	-	-
Na <sub>2</sub> O		0.29	0.30	0.38	0.49	0.49	0.42	0.42
K <sub>2</sub> O		8.54	8.64	8.62	8.00	8.02	8.24	8.14
Sum		96.42	96.18	96.71	96.49	95.42	95.37	96.27
H <sub>2</sub> O		3.58	3.82	3.29	3.51	4.58	4.69	3.73
Total		100	100	100	100	100	100	100
Structural Formulae								
A Site	K	0.815	0.829	0.821	0.759	0.772	0.797	0.775
	Na	0.043	0.044	0.056	0.071	0.071	0.062	0.060
	Sum	0.858	0.873	0.877	0.830	0.843	0.859	0.835
IV Site	Si	2.675	2.670	2.695	2.681	2.646	2.648	2.675
	Al	1.325	1.330	1.305	1.319	1.354	1.352	1.325
	Sum	4.000	4.000	4.000	4.000	4.000	4.000	4.000
VI Site	Fe	1.244	1.243	1.251	1.211	1.222	1.265	1.225
	Mn	0	0.002	0.001	0.001	0	0	0.001
	Mg	1.131	1.158	1.123	1.148	1.196	1.164	1.162
	Zn	-	-	-	-	-	-	-
	Al	0.419	0.404	0.420	0.466	0.439	0.429	0.457
	Cr	-	-	-	-	-	-	-
	Ti	0.116	0.112	0.107	0.095	0.090	0.088	0.087
	Sum	2.910	2.919	2.902	2.921	2.947	2.946	2.932
Total		7.768	7.792	7.779	7.751	7.790	7.805	7.767
	OH <sup>-</sup>	1.805	1.926	1.659	1.769	2.309	2.364	1.880
	Fe/Fe+Mg	0.524	0.518	0.527	0.513	0.505	0.521	0.513
	K/K+Na	0.950	0.950	0.936	0.914	0.916	0.928	0.928
	Al/Al+Si	0.395	0.394	0.390	0.400	0.404	0.402	0.400

Table 8. (Biotite analyses, continued).

Locality		UO1A				NS118	
Analysis No.	26	27	28	29	30	40	41
SiO <sub>2</sub>	35.00	36.12	35.39	35.12	35.80	35.78	35.85
TiO <sub>2</sub>	1.91	1.59	1.61	1.67	1.50	1.39	1.32
Al <sub>2</sub> O <sub>3</sub>	19.88	20.32	19.90	20.30	20.30	19.31	19.59
Cr <sub>2</sub> O <sub>3</sub>	0.01	0	0.04	0.03	0.04	—	—
FeO	20.32	19.61	20.19	20.03	20.04	20.24	19.80
MnO	0	0	0	0	0	0	0
MgO	10.46	10.29	10.06	10.39	10.43	10.22	10.05
ZnO	0.08	0.06	0.04	0.08	0	—	—
CaO	0	0	0	0	0	0	0
Na <sub>2</sub> O	0.37	0.34	0.32	0.38	0.31	0.27	0.40
K <sub>2</sub> O	8.53	8.31	8.25	8.38	8.51	8.35	8.26
Sum	96.56	96.64	95.80	96.38	96.93	95.56	95.27
H <sub>2</sub> O	3.44	3.36	4.20	3.62	3.07	4.44	4.73
Total	100	100	100	100	100	100	100
Structural Formulae							
A Site K	0.817	0.789	0.794	0.802	0.808	0.806	0.797
Na	0.055	0.050	0.047	0.056	0.046	0.040	0.059
Sum	0.872	0.839	0.841	0.858	0.854	0.846	0.856
IV Site Si	2.628	2.685	2.667	2.633	2.663	2.704	2.709
Al	1.372	1.315	1.333	1.367	1.337	1.296	1.291
Sum	4.000	4.000	4.000	4.000	4.000	4.000	4.000
Fe	1.277	1.220	1.273	1.257	1.248	1.280	1.252
Mn	0	0	0	0	0	0	0
Mg	1.172	1.141	1.131	1.162	1.158	1.152	1.133
Zn	0.004	0.003	0.003	0.005	0	—	—
Al	0.388	0.466	0.436	0.428	0.444	0.425	0.455
Cr	0.001	0	0.002	0.002	0.003	—	—
Ti	0.108	0.089	0.092	0.094	0.084	0.079	0.076
Sum	2.950	2.919	2.937	2.948	2.937	2.936	2.916
Total	7.822	7.758	7.778	7.806	7.791	7.782	7.772
OH <sup>—</sup>	1.734	1.694	2.117	1.825	1.548	2.238	2.384
Fe/Fe+Mg	0.521	0.517	0.530	0.520	0.519	0.526	0.525
K/K+Na	0.937	0.940	0.944	0.935	0.946	0.953	0.931
Al/Al+Si	0.401	0.399	0.399	0.405	0.401	0.389	0.392

Table 8. (Biotite analyses, continued).

Locality		NS118					
Analysis No.	42	43	44	46	47	48	49
SiO <sub>2</sub>	35.53	35.50	35.60	35.49	35.58	35.73	35.34
TiO <sub>2</sub>	1.47	1.50	1.57	1.79	1.70	2.12	1.96
Al <sub>2</sub> O <sub>3</sub>	19.39	19.76	19.64	19.69	19.77	19.51	19.26
Cr <sub>2</sub> O <sub>3</sub>	-	-	-	0.01	0	0.02	0.01
FeO	20.21	20.08	20.12	19.84	19.82	20.49	20.31
MnO	0	0	0	0	0	0	0
MgO	9.95	10.11	9.65	11.13	10.91	10.40	10.29
ZnO	-	-	-	0.02	0.05	0.03	0.02
CaO	0	0	0	0	0	0	0
Na <sub>2</sub> O	0.39	0.35	0.38	0.27	0.27	0.36	0.35
K <sub>2</sub> O	8.15	8.21	8.27	8.49	8.44	8.45	8.23
Sum	95.00	95.51	95.23	96.73	96.54	97.11	95.77
H <sub>2</sub> O	5.00	4.49	4.77	3.27	3.46	2.89	4.23
Total	100	100	100	100	100	100	100
Structural Formulae							
A Site K	0.791	0.792	0.800	0.809	0.805	0.804	0.794
Na	0.058	0.051	0.056	0.040	0.040	0.052	0.052
Sum	0.849	0.843	0.856	0.849	0.845	0.856	0.846
IV Site Si	2.699	2.681	2.698	2.649	2.658	2.663	2.669
Al	1.301	1.319	1.302	1.351	1.342	1.337	1.331
Sum	4.000	4.000	4.000	4.000	4.000	4.000	4.000
VI Site Fe	1.279	1.269	1.276	1.239	1.239	1.278	1.284
Mn	0	0	0	0	0	0	0
Mg	1.128	1.139	1.091	1.238	1.216	1.156	1.160
Zn	-	-	-	0.001	0.003	0.002	0.001
Al	0.436	0.441	0.453	0.382	0.400	0.378	0.385
Cr	-	-	-	0.001	0	0.001	0.001
Ti	0.084	0.086	0.090	0.101	0.096	0.119	0.111
Sum	2.927	2.935	2.910	2.962	2.954	2.934	2.942
Total	7.776	7.778	7.766	7.811	7.799	7.790	7.788
OH <sup>-</sup>	2.521	2.263	2.405	1.648	1.744	1.457	2.132
Fe/Fe+Mg	0.531	0.527	0.539	0.500	0.505	0.525	0.525
K/K+Na	0.932	0.940	0.935	0.953	0.953	0.939	0.939
Al/Al+Si	0.392	0.396	0.394	0.395	0.396	0.392	0.391

Table 8. (Biotite analyses, continued).

Locality	NS118			NS18			
Analysis No.	50	12	13	14	19	20	26
SiO <sub>2</sub>	35.68	35.24	34.93	34.80	34.75	34.19	35.01
TiO <sub>2</sub>	1.79	1.80	2.00	2.13	2.19	2.27	1.99
Al <sub>2</sub> O <sub>3</sub>	20.25	19.84	19.40	19.21	19.05	19.21	19.36
Cr <sub>2</sub> O <sub>3</sub>	0.02	0.04	0	0.07	0.09	0.07	0.09
FeO	19.36	22.76	22.78	22.73	23.69	23.25	23.37
MnO	0	0.01	0.07	0.07	0.07	0.07	0.02
MgO	10.92	7.94	7.76	7.97	7.69	8.06	7.90
ZnO	0.02	0.08	0	0.09	0.09	0.15	0.16
CaO	0	0	0	0	0	0	0
Na <sub>2</sub> O	0.34	0.03	0.08	0.06	0.07	0.08	0.12
K <sub>2</sub> O	8.55	8.13	8.43	8.09	8.29	8.11	8.29
Sum	96.93	95.96	95.45	95.22	95.98	95.46	96.34
H <sub>2</sub> O	3.07	4.04	4.55	4.78	4.02	4.54	3.66
Total	100	100	100	100	100	100	100
Structural Formulae							
A Site K	0.811	0.790	0.826	0.794	0.812	0.798	0.807
Na	0.049	0.004	0.012	0.010	0.011	0.012	0.018
Sum	0.860	0.794	0.838	0.804	0.823	0.810	0.825
IV Site Si	2.649	2.682	2.681	2.675	2.666	2.635	2.669
Al	1.351	1.318	1.319	1.325	1.334	1.365	1.331
Sum	4.000	4.000	4.000	4.000	4.000	4.000	4.000
VI Site Fe	1.203	1.449	1.463	1.462	1.521	1.499	1.491
Mn	0	0.006	0.005	0.004	0.005	0.004	0.001
Mg	1.209	0.901	0.888	0.914	0.880	0.927	0.899
Zn	0.001	0.005	0	0.005	0.005	0.008	0.009
Al	0.422	0.463	0.437	0.416	0.390	0.381	0.412
Cr	0.001	0.003	0	0.005	0.005	0.004	0.006
Ti	0.100	0.103	0.116	0.123	0.127	0.132	0.114
Sum	2.936	2.930	2.909	2.929	2.933	2.955	2.932
Total	7.796	7.724	7.747	7.733	7.756	7.765	7.757
OH <sup>-</sup>	1.548	2.037	2.294	2.410	2.027	2.289	1.845
Fe/Fe+Mg	0.499	0.625	0.622	0.615	0.633	0.618	0.624
K/K+Na	0.943	0.995	0.986	0.988	0.987	0.985	0.978
Al/Al+Si	0.401	0.399	0.396	0.394	0.393	0.399	0.395

Table 8. (Biotite analyses, continued).

Locality		NS18					
Analysis No.	27	28	29	30	31	32	33
SiO <sub>2</sub>	34.48	34.74	34.76	34.17	34.18	35.01	34.95
TiO <sub>2</sub>	1.97	1.92	1.97	1.84	2.15	1.96	1.98
Al <sub>2</sub> O <sub>3</sub>	19.54	19.45	19.58	19.62	19.39	19.37	19.47
Cr <sub>2</sub> O <sub>3</sub>	0.05	0.10	0.06	0.07	0.09	0.10	0.09
FeO	23.42	23.37	23.44	23.10	23.15	23.05	23.49
MnO	0.08	0.02	0.04	0.05	0.05	0.05	0.07
MgO	7.99	7.99	7.84	7.93	7.73	7.73	8.00
ZnO	0	0.06	0.15	0.07	0.07	0.08	0.10
CaO	0	0	0	0	0	0	0
Na <sub>2</sub> O	0.12	0.11	0.15	0.15	0.06	0.08	0.12
K <sub>2</sub> O	8.28	8.41	8.36	8.25	8.19	8.31	8.34
Sum	95.93	96.17	96.35	95.25	95.06	95.74	96.61
H <sub>2</sub> O	4.07	3.83	3.65	4.75	4.94	4.26	3.39
Total	100	100	100	100	100	100	100
Structural Formulae							
A Site K	0.810	0.821	0.815	0.812	0.808	0.812	0.810
Na	0.018	0.017	0.023	0.022	0.009	0.013	0.018
Sum	0.828	0.838	0.838	0.834	0.817	0.825	0.828
IV Site Si	2.643	2.656	2.653	2.637	2.643	2.681	2.659
Al	1.357	1.344	1.347	1.363	1.357	1.319	1.341
Sum	4.000	4.000	4.000	4.000	4.000	4.000	4.000
VI Site Fe	1.502	1.495	1.497	1.491	1.498	1.477	1.496
Mn	0.005	0.002	0.003	0.003	0.004	0.004	0.004
Mg	0.914	0.911	0.893	0.913	0.891	0.883	0.908
Zn	0	0.003	0.008	0.004	0.004	0.005	0.005
Al	0.409	0.410	0.416	0.422	0.411	0.431	0.406
Cr	0.003	0.006	0.004	0.004	0.006	0.006	0.005
Ti	0.114	0.110	0.113	0.107	0.126	0.113	0.113
Sum	2.947	2.937	2.926	2.944	2.940	2.919	2.937
Total	7.775	7.775	7.764	7.778	7.757	7.744	7.765
OH <sup>-</sup>	2.052	1.931	1.840	2.395	2.490	2.147	1.709
Fe/Fe+Mg	0.622	0.621	0.626	0.620	0.627	0.626	0.622
K/K+Na	0.978	0.980	0.973	0.974	0.989	0.984	0.978
Al/Al+Si	0.401	0.398	0.399	0.404	0.401	0.395	0.397



Table 8. (Biotite analyses, continued).

Locality		NS87					
Analysis No.	2	4	17	19	20	21	22
SiO <sub>2</sub>	35.07	35.08	36.55	35.16	34.85	34.95	34.59
TiO <sub>2</sub>	1.76	2.06	2.13	1.88	1.92	2.09	2.06
Al <sub>2</sub> O <sub>3</sub>	19.82	18.80	18.85	19.14	18.94	18.92	19.20
Cr <sub>2</sub> O <sub>3</sub>	-	-	-	0.01	0	0.04	0.03
FeO	23.11	23.69	22.66	23.65	23.68	23.63	24.00
MnO	0.02	0.08	0.11	0.03	0.06	0.08	0.12
MgO	7.72	7.50	7.23	7.48	7.49	7.40	7.04
ZnO	-	-	-	0.10	0.11	0.10	0.13
CaO	-	-	-	0	0	0	0
Na <sub>2</sub> O	0.01	0.10	0.06	0.01	0.03	0.06	0.02
K <sub>2</sub> O	8.05	8.15	7.75	8.25	8.37	8.38	8.37
Sum	95.56	95.46	95.34	95.71	95.45	95.65	95.56
H <sub>2</sub> O	4.44	4.54	4.66	4.29	4.55	4.35	4.44
Total	100	100	100	100	100	100	100
Structural Formulae							
A Site K	0.786	0.801	0.754	0.809	0.825	0.823	0.825
Na	0.002	0.015	0.008	0.002	0.005	0.009	0.004
Sum	0.788	0.816	0.762	0.811	0.830	0.832	0.829
IV Site Si	2.681	2.701	2.782	2.698	2.689	2.690	2.672
Al	1.319	1.299	1.218	1.302	1.311	1.310	1.328
Sum	4.000	4.000	4.000	4.000	4.000	4.000	4.000
VI Site Fe	1.479	1.527	1.444	1.519	1.529	1.522	1.551
Mn	0.001	0.006	0.007	0.002	0.004	0.005	0.008
Mg	0.881	0.861	0.821	0.856	0.862	0.850	0.812
Zn	-	-	-	0.006	0.006	0.006	0.007
Al	0.469	0.408	0.475	0.431	0.412	0.407	0.421
Cr	-	-	-	0.001	0	0.003	0.002
Ti	0.102	0.120	0.112	0.109	0.112	0.121	0.120
Sum	2.932	2.922	2.859	2.924	2.925	2.914	2.921
Total	7.720	7.738	7.621	7.735	7.755	7.746	7.750
OH <sup>-</sup>	2.238	2.289	2.349	2.163	2.294	2.193	2.238
Fe/Fe+Mg	0.627	0.639	0.638	0.640	0.639	0.642	0.656
K/K+Na	0.997	0.982	0.990	0.998	0.994	0.989	0.995
Al/Al+Si	0.400	0.387	0.378	0.391	0.391	0.390	0.396

Table 8. (Biotite analyses, continued).

Locality		NS87				NS85		
Analysis No.		23	24	25	26	9	10	11
SiO <sub>2</sub>		34.37	35.61	35.19	35.36	34.84	35.02	35.04
TiO <sub>2</sub>		2.10	2.01	2.17	2.01	1.92	1.88	1.93
Al <sub>2</sub> O <sub>3</sub>		18.78	19.31	19.14	19.08	19.23	19.13	18.77
Cr <sub>2</sub> O <sub>3</sub>		0.09	0.03	0.08	0.09	0	0.03	0.09
FeO		23.86	23.31	23.33	23.31	23.21	23.55	23.24
MnO		0.06	0.05	0.07	0.04	0.13	0.11	0.08
MgO		7.43	7.37	7.40	7.56	8.37	8.07	8.03
ZnO		0.15	0.06	0.12	0.11	0.08	0.11	0.17
CaO		0	0	0	0	0	0	0
Na <sub>2</sub> O		0.05	0.04	0.09	0.05	0.14	0.14	0.19
K <sub>2</sub> O		8.33	8.18	8.09	8.15	8.56	8.46	8.48
Sum		95.23	95.97	95.68	95.76	96.39	96.41	95.89
H <sub>2</sub> O		4.77	4.03	4.32	4.24	3.61	3.59	4.11
Total		100	100	100	100	100	100	100
Structural Formulae								
A Site	K	0.824	0.796	0.791	0.796	0.834	0.825	0.831
	Na	0.008	0.006	0.013	0.007	0.007	0.007	0.009
	Sum	0.832	0.802	0.804	0.803	0.841	0.832	0.840
IV Site	Si	2.666	2.715	2.697	2.706	2.658	2.673	2.689
	Al	1.334	1.285	1.303	1.294	1.342	1.327	1.311
	Sum	4.000	4.000	4.000	4.000	4.000	4.000	4.000
VI Site	Fe	1.549	1.486	1.496	1.493	1.482	1.504	1.492
	Mn	0.004	0.003	0.005	0.003	0.008	0.007	0.005
	Mg	0.860	0.838	0.846	0.863	0.953	0.918	0.919
	Zn	0.008	0.003	0.007	0.007	0.005	0.007	0.009
	Al	0.385	0.452	0.426	0.428	0.388	0.395	0.387
	Cr	0.005	0.002	0.005	0.006	0	0.002	0.005
	Ti	0.123	0.115	0.125	0.116	0.111	0.108	0.112
	Sum	2.934	2.899	2.910	2.916	2.947	2.941	2.929
Total		7.766	7.701	7.714	7.719	7.788	7.773	7.769
	OH <sup>-</sup>	2.405	2.032	2.178	2.137	1.820	1.810	2.072
	Fe/Fe+Mg	0.643	0.639	0.639	0.634	0.609	0.621	0.619
	K/K+Na	0.990	0.993	0.984	0.991	0.992	0.992	0.989
	Al/Al+Si	0.392	0.390	0.391	0.389	0.394	0.392	0.387

Table 8. (Biotite analyses, continued).

Locality		NS85					
Analysis No.	12	13	14	15	16	17	18
SiO <sub>2</sub>	35.13	35.34	35.08	35.12	35.81	34.19	35.19
TiO <sub>2</sub>	1.67	1.76	1.70	1.66	1.55	1.65	1.65
Al <sub>2</sub> O <sub>3</sub>	18.45	19.39	18.74	19.02	18.33	18.84	19.03
Cr <sub>2</sub> O <sub>3</sub>	0.06	0.06	0.04	0.10	0.02	0.02	0.04
FeO	23.33	23.29	22.99	23.40	22.70	23.54	23.26
MnO	0.10	0.09	0.10	0.11	0.05	0.11	0.12
MgO	8.05	8.06	7.86	8.11	8.35	8.23	8.22
ZnO	0.07	0.17	0.14	0.15	0.10	0.12	0.11
CaO	0	0	0	0	0	0	0
Na <sub>2</sub> O	0.02	0.04	0	0	0	0	0
K <sub>2</sub> O	8.25	8.67	8.60	8.71	8.42	8.25	8.52
Sum	<u>95.30</u>	<u>96.87</u>	<u>95.25</u>	<u>96.38</u>	<u>95.33</u>	<u>94.95</u>	<u>96.14</u>
H <sub>2</sub> O	4.70	3.13	4.75	3.62	4.67	5.05	3.86
Total	<u>100</u>	<u>100</u>	<u>100</u>	<u>100</u>	<u>100</u>	<u>100</u>	<u>100</u>
Structural Formulae							
A Site K	0.812	0.840	0.848	0.850	0.852	0.818	0.832
Na	0.003	0.005	0	0	0	0	0
Sum	<u>0.815</u>	<u>0.845</u>	<u>0.848</u>	<u>0.850</u>	<u>0.852</u>	<u>0.818</u>	<u>0.832</u>
IV Site Si	2.720	2.682	2.707	2.684	2.749	2.656	2.690
Al	<u>1.280</u>	<u>1.318</u>	<u>1.293</u>	<u>1.316</u>	<u>1.251</u>	<u>1.344</u>	<u>1.310</u>
Sum	<u>4.000</u>	<u>4.000</u>	<u>4.000</u>	<u>4.000</u>	<u>4.000</u>	<u>4.000</u>	<u>4.000</u>
VI Site Fe	1.505	1.479	1.485	1.497	1.458	1.530	1.488
Mn	0.007	0.006	0.007	0.007	0.004	0.007	0.008
Mg	0.926	0.912	0.904	0.925	0.956	0.954	0.938
Zn	0.004	0.009	0.008	0.009	0.006	0.007	0.006
Al	0.396	0.417	0.413	0.398	0.408	0.381	0.405
Cr	0.004	0.003	0.002	0.006	0.001	0.002	0.003
Ti	<u>0.097</u>	<u>0.101</u>	<u>0.099</u>	<u>0.095</u>	<u>0.089</u>	<u>0.097</u>	<u>0.095</u>
Sum	<u>2.939</u>	<u>2.927</u>	<u>2.918</u>	<u>2.937</u>	<u>2.922</u>	<u>2.978</u>	<u>2.943</u>
Total	7.754	7.772	7.766	7.787	7.774	7.796	7.775
OH <sup>-</sup>	2.369	1.578	2.395	1.825	2.354	2.546	1.946
Fe/Fe+Mg	0.619	0.619	0.622	0.618	0.604	0.616	0.613
K/K+Na	0.996	0.994	1.000	1.000	1.000	1.000	1.000
Al/Al+Si	0.381	0.393	0.387	0.390	0.376	0.394	0.389

Table 8. (Biotite analyses, continued).

Locality	U01A	Standard	NS118	Standard	NS18	Standard
N, Averages	12	deviation	10	deviation	13	deviation
SiO <sub>2</sub>	35.57	0.44	35.61	0.15	34.71	0.35
TiO <sub>2</sub>	1.72	0.19	1.66	0.26	2.01	0.14
Al <sub>2</sub> O <sub>3</sub>	20.03	0.29	19.62	0.29	19.42	0.20
Cr <sub>2</sub> O <sub>3</sub>	0.02	0.02	0.01	0.01	0.07	0.03
FeO	19.86	0.29	20.02	0.33	23.20	0.30
MnO	0.01	0.01	0	-	0.05	0.02
MgO	10.33	0.17	10.36	0.48	7.89	0.12
ZnO	0.05	0.03	0.03	0.01	0.08	0.05
CaO	0	-	0	-	0	-
Na <sub>2</sub> O	0.38	0.07	0.34	0.05	0.09	0.04
K <sub>2</sub> O	8.35	0.22	8.34	0.14	8.27	0.11
Sum	96.32	0.49	95.99	0.78	95.79	0.49
H <sub>2</sub> O	3.68	0.49	4.01	0.78	4.21	0.49
Total	100	-	100	-	100	-
Structural Formulae						
A Site K	0.798	0.021	0.801	0.007	0.809	0.010
Na	0.055	0.010	0.049	0.007	0.014	0.005
Sum	0.853	0.016	0.850	0.006	0.838	0.014
IV Site Si	2.663	0.021	2.677	0.023	2.660	0.017
Al	1.337	0.023*	1.323	0.019*	1.340	0.017*
Sum	4.000	-	4.000	-	4.000	-
VI Site Fe	1.244	0.022	1.260	0.026	1.488	0.020
Mn	0	-	0	-	0.004	0.001
Mg	1.154	0.020	1.162	0.045	0.901	0.014
Zn	0.003	0.002	0.003	0.001	0.005	0.003
Al	0.432	-	0.417	-	0.415	-
Cr	0.002	0.001	0.001	0.001	0.004	0.002
Ti	0.097	0.011	0.094	0.014	0.116	0.008
Sum	2.932	0.016	2.937	0.016	2.933	0.012
Total	7.785	0.021	7.787	0.014	7.771	0.016
OH <sup>-</sup>	1.855	0.296	2.021	0.393	2.122	0.247
Fe/Fe+Mg	0.519	0.007	0.520	0.014	0.623	0.005
K/K+Na	0.936	0.012	0.942	0.009	0.965	0.006
Al/Al+Si	0.399	0.004	0.394	0.003	0.398	0.003

\* Total aluminum.

Table 8. (Biotite analyses, continued).

Locality	NS87	Standard	NS85	Standard	All		Standard
N, Averages	11	deviation	10	deviation	Biotite		deviation
					56		
SiO <sub>2</sub>	35.16	0.57	35.09	0.40	35.21		0.37
TiO <sub>2</sub>	2.02	0.12	1.74	0.13	1.84		0.17
Al <sub>2</sub> O <sub>3</sub>	19.09	0.29	18.89	0.33	19.43		0.45
Cr <sub>2</sub> O <sub>3</sub>	0.05	0.04	0.05	0.03	0.04		0.02
FeO	23.48	0.38	23.25	0.25	21.98		1.85
MnO	0.07	0.03	0.10	0.02	0.05		0.04
MgO	7.42	0.18	8.14	0.16	8.81		1.41
ZnO	0.11	0.02	0.12	0.03	0.08		0.04
CaO	0	-	0	-	0		-
Na <sub>2</sub> O	0.05	0.03	0.02	0.07	0.18		0.17
K <sub>2</sub> O	8.19	0.19	8.49	0.16	8.32	Ideal	0.11
Sum	95.64	0.21	95.89	0.64	95.94	96.03	0.26
H <sub>2</sub> O	4.36	0.21	4.11	0.64	4.06	3.97	0.26
Total	100	-	100	-	100		-
Structural Formulae							
A Site K	0.802	0.022	0.831	0.014	0.808		0.013
Na	0.007	0.004	0.003	0.004	0.029		0.025
Sum	0.806	0.022	0.834	0.013	0.837		0.019
IV Site Si	2.700	0.031	2.686	0.028	2.676		0.017
Al	1.300	0.025*	1.314	0.024*	1.324		0.024*
Sum	4.000	-	4.000	-	4.000		-
VI Site Fe	1.508	0.032	1.492	0.019	1.400		0.134
Mn	0.004	0.002	0.007	0.001	0.005		0.003
Mg	0.850	0.020	0.930	0.019	0.997		0.148
Zn	0.006	0.001	0.007	0.002	0.005		0.002
Al	0.429	-	0.394	-	0.418		-
Cr	0.002	0.002	0.003	0.002	0.002		0.001
Ti	0.116	0.007	0.100	0.008	0.105		0.011
Sum	2.915	0.021	2.933	0.017	2.930		0.009
Total	7.724	0.039	7.767	0.012	7.767		0.025
OH <sup>-</sup>	2.198	0.106	2.072	0.323	2.047	2.000	0.131
Fe/Fe+Mg	0.640	0.007	0.616	0.006	0.584		0.059
K/K+Na	0.995	0.005	0.996	0.004	0.965		0.028
Al/Al+Si	0.390	0.005	0.389	0.006	0.394		0.005

\* Total aluminum.

sample do not vary within analytical uncertainty. There is no evidence that even large crystals are significantly zoned.

The biotite analyses indicate a distinct trend in the alkali cations. K/K+Na ratios vary systematically from about 0.936 in sample U01A (R2) to about 0.996 in sample NS85 (R5), one of the most severely retrograded rocks still containing biotite. This trend may be seen in Figure 13 where K+Na is plotted versus K/K+Na ratios for all biotite analyses. The trend is from lower K/K+Na ratios in staurolite-bearing samples, toward higher K/K+Na ratios in the more severely retrograded

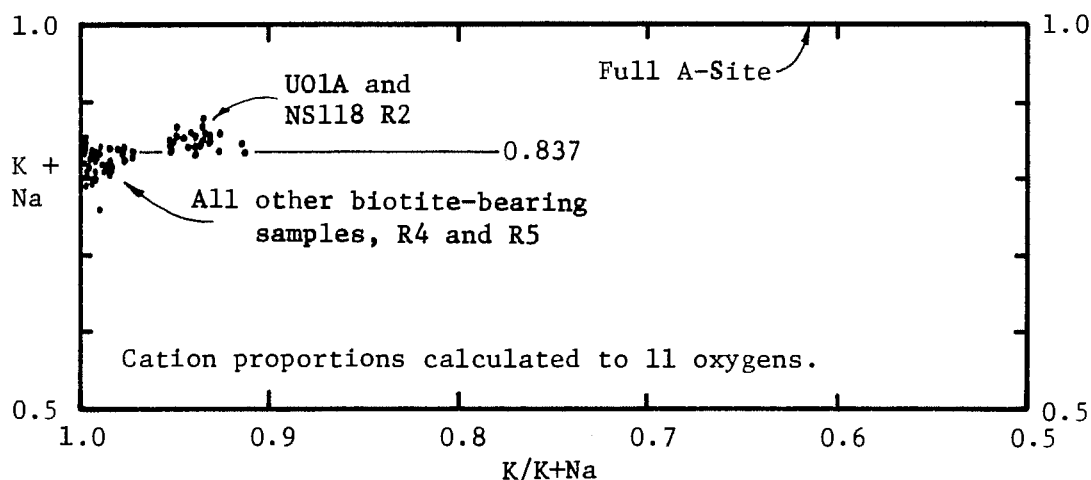


Figure 13. Individual biotite analyses, with A-site occupancy plotted versus K/K+Na ratios. The right hand cluster is data from rocks containing staurolite and the left hand cluster for rocks containing only pseudomorphs after staurolite. The trend is toward higher K and possibly lower A-site filling with retrograding.

rocks bearing only pseudomorphs after staurolite. The gap between the two clusters probably represents biotite compositions for intermediate stages of staurolite breakdown that were not sampled in this study.

The data plot also indicates a slight decrease in A-site occupancy from

about 0.852 to about 0.826 with increasing K/K+Na ratios. It is not clear if this small difference is significant.

A marked trend in Fe/Fe+Mg ratios for biotite is also indicated by the analyses. In Figure 14, Al/Al+Si ratios are plotted versus Fe/Fe+Mg ratios for all biotite analyses. The data again fall into clusters, the more Mg-rich group composed of data from zone R2, and the Fe-rich group composed of data from zones R4 and R5. The two main groups are separated by a gap that is probably due to intermediate stages of staurolite breakdown that were not sampled. In the iron-rich data cluster, a small group of points from sample NS87 (R5) contains the most iron-rich biotite analyzed and the least amount of relict biotite.

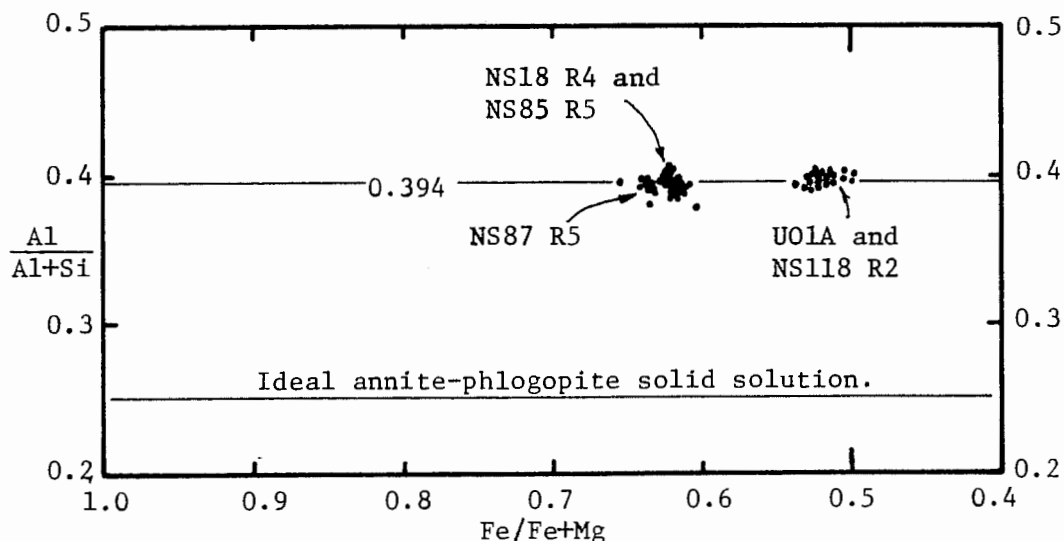


Figure 14. Al/Al+Si ratios plotted versus Fe/Fe+Mg ratios for all biotite analyses. The cluster of points on the right is for samples containing staurolite, and the left cluster for samples containing only pseudomorphs after staurolite. The trend is toward iron enrichment with retrograding, paralleling the K enrichment trend.

Biotite was clearly originally present in sample NS90 (Zone R6), based on relict textures. The last traces of biotite in that sample were probably virtually K-end member, with Fe/Fe+Mg ratios somewhat higher than 0.640, the ratio in sample NS87.

Zinc, manganese, and chromium apparently increase by factors of two or more with retrograding, although concentrations of these elements are close to instrumental detection limits. ZnO probably increases in concentration due to zinc released during staurolite breakdown, because virtually no zinc is taken up by chlorite and very little by muscovite. MnO increases in concentration from nearly zero in samples U01A and NS118 (Zone R2), to 0.10% in sample NS85 (Zone R5) due to manganese released during garnet breakdown. The reason for the chromium trend is uncertain.

Octahedral and tetrahedral aluminum both show a slight decreasing trend with degree of alteration from about 1.767 per formula unit for samples containing staurolite to about 1.714 for rocks bearing only pseudomorphs. This trend has been described from prograde terranes (Wenk, 1970) and reflects some re-equilibration of biotite toward lower metamorphic temperatures. The trend will be discussed in a later section and will be related to a similar change in muscovite chemistry.

TiO<sub>2</sub> appears to exhibit a slight trend toward higher concentrations with retrograding. The change, however, is small and is opposite to what one would expect with decreasing metamorphic grade (Kwak, 1968; Guidotti et al., 1974 and 1977). Because there is no large variation in titanium, the mode of its substitution into the biotite structure



could not be determined. The most likely substitution is:  $M^{+2} + 2Si = Ti + 2^{IV}Al$  (Guidotti et al., 1977; Tracy, 1978), although more complicated substitutions have been proposed (Holdaway, 1980).

### Muscovite

Field habit. Muscovite is ubiquitous in the schists of the New Salem area and is one of the most abundant minerals of prograde origin. Large crystals are rarely seen in outcrop, but schistose rocks broken parallel to the foliation yield shiny, relatively smooth surfaces due to sheets of sub-parallel muscovite plates. The fresh surface is from white to dark gray, depending on graphite content. Muscovite is also present as scattered plates and small books that assume random orientations, and as fine-grained intergrowths with chlorite and other minerals as replacement products of sillimanite, staurolite, garnet, and biotite.

Appearance in thin section. Muscovite is biaxial negative with a 2V of about 30°, and distant dispersion  $r > v$ . Inclusions are less abundant than in biotite, but graphite is quite common in foliation-defining plates and muscovite that has grown to replace graphite-bearing parent minerals, such as biotite or staurolite. Inclusions of ilmenite, zircon, quartz, sillimanite, and tourmaline are rare. Muscovite is colorless, exhibits well developed 001 cleavage, is commonly subhedral on 001, has parallel extinction, and in less altered rocks may be intergrown parallel to 001 with biotite.

Muscovite occurs in several distinct habits, the most common of which defines the main foliation. The plates are commonly about 20 to 30  $\mu\text{m}$  thick and 200 to 500  $\mu\text{m}$  in width, flattened on 001. The plates usually occur in muscovite-rich layers alternating with quartz-rich layers on a scale from 0.1 to several millimeters. Muscovite-rich layers are typically associated with graphite, which is concentrated along grain boundaries. The foliation commonly bends around large crystals or pseudomorphs of garnet and staurolite, and in many rocks has been severely deformed by crenulations produced during retrograde metamorphism. Examples of foliation-type muscovite are in Figures 6a (top), 8a and 8b, 10a to 10d, 12, 18, 19, and 21.

The second type of muscovite habit are crystals of prograde origin that are more equant than the foliation muscovite. These occur up to 2 mm across as isolated crystals or in poorly defined groups, are randomly oriented, are most abundant in the quartz-rich layers, and are commonly subhedral on 001. Inclusions are rare. This type of muscovite probably grew after the foliation developed while temperatures were still high. They are quite common in undisturbed rocks, having been extensively recrystallized during deformation that occurred during retrograde metamorphism. Examples are present in Figures 6a, 8a, 10a, and 12.

Fine-grained muscovite occurring as intergrowths with chlorite, replacing sillimanite, staurolite, and garnet, is the most common habit for muscovite of retrograde origin. Crystals tend to be small, ragged, and irregular in shape and random in orientation. Replacements after

sillimanite tend to be almost entirely muscovite (Figure 6a), and pseudomorphs after staurolite usually have muscovite intergrown with minor chlorite, commonly exhibiting a bimodal grain size distribution (Figure 8b). Muscovite is exceedingly fine-grained in pseudomorphs after garnet, and is quite subordinate in abundance to chlorite (Figures 10c and 10d). Inclusions are rare, except where the muscovite replaced a graphite-bearing parent mineral.

Well formed muscovite of retrograde origin developed locally, particularly where associated with biotite (Figure 12), and in pseudomorphs after other minerals possibly from recrystallization of fine-grained muscovite (Figures 8b, 10a to 10d, and 12). Inclusions are rare, except where the crystals replaced a graphite-charged parent mineral such as staurolite (Figure 8b) or biotite.

Chemistry. Muscovite chemistry is quite complex, especially when considering that many muscovite crystals are chemically zoned. Table 9 is a listing of individual chemical analyses of muscovite from all seven analyzed samples, and sample averages.

The A-site has an average occupancy of 0.972, larger than the occupancy of 0.837 for coexisting biotite.  $K/(K+Na)$  ratios in muscovite follow a K-enrichment trend similar to that of biotite. The range of alkali ratios is much greater than in biotite, extending from 0.653 to 0.905 (Figure 15). A-site occupancy shows no distinct trend with retrograding.  $K/(K+Na)$  ratios are less clumped than biotite because the dearth of analyses between the two main clumps due to

Table 9. Electron microprobe analyses of muscovite from various samples. Structural formulae were calculated on the basis of the composition  $(K,Na)Al_2(Si_3AlO_{10})(OH)_2$ , containing 11 oxygens plus one  $H_2O$ .  $OH^-$  anion proportions were calculated from  $H_2O\%$  on a basis of 12 oxygens.

Locality		U01A						
Analysis No.		6	7	20	21	32	33	34
SiO <sub>2</sub>		46.21	46.17	46.43	46.21	45.86	46.10	45.95
TiO <sub>2</sub>		0.43	0.38	0.40	0.37	0.41	0.40	0.45
Al <sub>2</sub> O <sub>3</sub>		37.90	38.81	38.41	37.92	36.75	36.25	36.78
Cr <sub>2</sub> O <sub>3</sub>		-	-	-	-	0.01	0.04	0.03
FeO		0.80	0.76	0.92	0.82	0.95	0.79	0.86
MnO		0	0	0	0	0	0	0
MgO		0.40	0.34	0.38	0.40	0.41	0.43	0.47
ZnO		-	-	-	-	0	0	0
CaO		-	-	-	-	0	0	0
Na <sub>2</sub> O		2.49	2.42	2.41	2.46	2.70	2.43	2.46
K <sub>2</sub> O		7.67	7.59	7.49	7.32	7.75	7.63	7.59
Sum		95.90	96.47	96.44	95.50	94.84	94.07	94.59
H <sub>2</sub> O		4.10	3.53	3.56	4.50	5.16	5.93	5.41
Total		100	100	100	100	100	100	100
Structural Formulae								
A Site	K	0.639	0.628	0.619	0.610	0.654	0.647	0.641
	Na	0.315	0.304	0.303	0.312	0.347	0.314	0.316
	Sum	0.954	0.932	0.922	0.922	1.001	0.961	0.957
IV Site	Si	3.014	2.989	3.007	3.019	3.033	3.063	3.039
	Al	0.986	1.011	0.993	0.981	0.967	0.937	0.961
	Sum	4.000	4.000	4.000	4.000	4.000	4.000	4.000
VI Site	Fe	0.044	0.042	0.050	0.045	0.053	0.044	0.048
	Mn	0	0	0	0	0	0	0
	Mg	0.039	0.033	0.037	0.039	0.040	0.042	0.047
	Zn	-	-	-	-	0	0	0
	Al	1.929	1.952	1.941	1.940	1.899	1.905	1.908
	Cr	-	-	-	-	0.001	0.002	0.002
	Ti	0.021	0.019	0.020	0.019	0.021	0.020	0.023
	Sum	2.033	2.046	2.048	2.043	2.014	2.013	2.028
Total		6.987	6.978	6.970	6.965	7.015	6.974	6.985
	OH <sup>-</sup>	1.775	1.529	1.542	1.949	2.234	2.568	2.343
	Fe/Fe+Mg	0.530	0.560	0.575	0.536	0.570	0.512	0.505
	K/K+Na	0.670	0.674	0.671	0.662	0.653	0.673	0.670
	Fe+Mn+Mg	0.083	0.075	0.087	0.084	0.093	0.086	0.095

Table 9. (Muscovite analyses, continued).

Locality	U01A		NS118				
Analysis No.	35	36	30	31	32	33	34
SiO <sub>2</sub>	46.10	46.41	45.49	45.83	46.30	46.48	46.60
TiO <sub>2</sub>	0.39	0.37	0.32	0.37	0.37	0.39	0.48
Al <sub>2</sub> O <sub>3</sub>	36.77	37.42	36.71	36.56	36.96	37.31	37.22
Cr <sub>2</sub> O <sub>3</sub>	0.03	0	—	—	—	—	—
FeO	0.88	0.67	0.92	1.20	0.97	0.94	0.97
MnO	0	0	0.03	0	0	0	0
MgO	0.39	0.42	0.25	0.37	0.25	0.23	0.20
ZnO	0	0	—	—	—	—	—
CaO	0	0	0	0	0	0	0
Na <sub>2</sub> O	2.73	2.43	2.27	2.09	2.76	2.60	2.65
K <sub>2</sub> O	7.48	7.81	8.37	8.26	7.32	7.44	7.26
Sum	94.77	95.73	94.36	94.68	94.93	95.39	95.38
H <sub>2</sub> O	5.33	4.27	5.64	5.32	5.07	4.61	4.62
Total	100	100	100	100	100	100	100
Structural Formulae							
A Site K	0.631	0.651	0.712	0.700	0.615	0.622	0.606
Na	0.350	0.308	0.294	0.269	0.353	0.331	0.337
Sum	0.981	0.959	1.006	0.969	0.968	0.953	0.943
IV Site Si	3.043	3.031	3.031	3.042	3.049	3.045	3.050
Al	0.957	0.969	0.969	0.958	0.951	0.955	0.950
Sum	4.000	4.000	4.000	4.000	4.000	4.000	4.000
VI Site Fe	0.049	0.037	0.052	0.067	0.053	0.052	0.053
Mn	0	0	0.002	0	0	0	0
Mg	0.039	0.041	0.025	0.037	0.025	0.022	0.039
Zn	0	0	—	—	—	—	—
Al	1.906	1.929	1.915	1.903	1.919	1.927	1.923
Cr	0.002	0	—	—	—	—	—
Ti	0.019	0.018	0.016	0.018	0.018	0.019	0.024
Sum	2.015	2.025	2.010	2.025	2.015	2.020	2.039
Total	6.996	6.984	7.016	6.994	6.983	6.973	6.982
OH <sup>-</sup>	2.308	1.849	2.442	2.304	2.195	1.996	2.001
Fe/Fe+Mg	0.557	0.474	0.675	0.644	0.679	0.703	0.576
K/K+Na	0.643	0.679	0.708	0.722	0.635	0.653	0.643
Fe+Mn+Mg	0.088	0.078	0.079	0.104	0.078	0.074	0.092

Table 9. (Muscovite analyses, continued).

Locality		NS118						
Analysis No.	36	37	38	39	51	52	53	
SiO <sub>2</sub>	45.65	45.28	45.58	46.07	46.31	46.49	46.30	
TiO <sub>2</sub>	0.38	0.35	0.44	0.46	0.41	0.48	0.34	
Al <sub>2</sub> O <sub>3</sub>	37.71	36.70	36.55	36.97	36.47	36.49	36.54	
Cr <sub>2</sub> O <sub>3</sub>	—	—	—	—	—	—	—	
FeO	0.85	1.00	1.01	0.93	0.83	0.89	0.79	
MnO	0	0	0.02	0.03	0.02	0	0.01	
MgO	0.24	0.26	0.31	0.28	0.30	0.28	0.28	
ZnO	—	—	—	—	—	—	—	
CaO	0	0	0	0	0	0	0	
Na <sub>2</sub> O	2.83	2.75	2.65	2.59	2.64	2.38	2.66	
K <sub>2</sub> O	7.37	7.33	7.42	7.28	7.36	7.53	7.45	
Sum	95.03	93.67	93.98	94.61	94.34	94.51	94.37	
H <sub>2</sub> O	4.97	6.33	6.02	5.39	5.66	5.49	5.63	
Total	100	100	100	100	100	100	100	
Structural Formulae								
A Site K	0.620	0.625	0.631	0.614	0.622	0.636	0.630	
Na	0.362	0.356	0.343	0.332	0.339	0.305	0.342	
Sum	0.982	0.981	0.974	0.946	0.961	0.941	0.972	
IV Site Si	3.005	3.027	3.037	3.042	3.066	3.070	3.065	
Al	0.995	0.973	0.963	0.958	0.934	0.930	0.935	
Sum	4.000	4.000	4.000	4.000	4.000	4.000	4.000	
VI Site Fe	0.047	0.056	0.067	0.052	0.046	0.049	0.044	
Mn	0	0	0.001	0.002	0.001	0	0.001	
Mg	0.024	0.026	0.031	0.028	0.030	0.028	0.028	
Zn	—	—	—	—	—	—	—	
Al	1.933	1.920	1.909	1.921	1.913	1.914	1.918	
Cr	—	—	—	—	—	—	—	
Ti	0.019	0.018	0.022	0.023	0.021	0.024	0.017	
Sum	2.023	2.020	2.030	2.026	2.011	2.015	2.008	
Total	7.005	7.001	7.004	6.972	6.972	6.956	6.980	
OH <sup>-</sup>	2.152	2.741	2.607	2.334	2.451	2.377	2.438	
Fe/Fe+Mg	0.662	0.683	0.684	0.650	0.605	0.636	0.611	
K/K+Na	0.631	0.637	0.648	0.649	0.647	0.676	0.648	
Fe+Mn+Mg	0.071	0.082	0.099	0.082	0.077	0.077	0.073	

Table 9. (Muscovite analyses, continued).

Locality		NS118					NS18	
Analysis No.	54	55	56	57	58	15	16	
SiO <sub>2</sub>	46.40	45.50	45.92	46.24	45.88	46.83	46.31	
TiO <sub>2</sub>	0.38	0.39	0.37	0.38	0.35	0.23	0.25	
Al <sub>2</sub> O <sub>3</sub>	37.66	36.87	37.24	36.73	36.44	37.14	36.18	
Cr <sub>2</sub> O <sub>3</sub>	0	0.03	0.03	0.04	0.01	0	0	
FeO	0.92	0.84	0.79	0.87	0.96	1.49	1.27	
MnO	0	0	0	0	0	0	0	
MgO	0.44	0.42	0.31	0.38	0.42	0.59	0.53	
ZnO	0	0	0	0	0	0	0.02	
CaO	0	0	0	0	0	0	0	
Na <sub>2</sub> O	2.31	2.59	2.45	2.42	2.53	0.95	1.61	
K <sub>2</sub> O	7.82	7.73	7.66	7.64	7.47	9.50	8.93	
Sum	95.93	94.37	94.77	94.70	94.06	96.28	95.73	
H <sub>2</sub> O	4.07	5.63	5.23	5.30	5.94	3.72	4.27	
Total	100	100	100	100	100	100	100	
Structural Formulae								
A Site K	0.652	0.656	0.645	0.644	0.634	0.795	0.750	
Na	0.292	0.334	0.314	0.314	0.326	0.121	0.206	
Sum	0.944	0.990	0.959	0.958	0.960	0.916	0.956	
IV Site Si	3.026	3.022	3.030	3.053	3.051	3.039	3.046	
Al	0.974	0.978	0.970	0.947	0.949	0.961	0.954	
Sum	4.000	4.000	4.000	4.000	4.000	4.000	4.000	
VI Site Fe	0.050	0.047	0.044	0.049	0.054	0.082	0.070	
Mn	0	0	0	0	0	0	0	
Mg	0.043	0.042	0.031	0.038	0.042	0.053	0.038	
Zn	0	0	0	0	0	0	0.001	
Al	1.924	1.910	1.929	1.914	1.908	1.909	1.902	
Cr	0	0.002	0.001	0.002	0.001	0	0	
Ti	0.019	0.019	0.019	0.019	0.018	0.011	0.013	
Sum	2.036	2.020	2.024	2.022	2.023	2.055	2.024	
Total	6.980	7.010	6.983	6.980	6.983	6.971	6.980	
OH <sup>-</sup>	1.762	2.438	2.265	2.295	2.572	1.611	1.849	
Fe/Fe+Mg	0.538	0.528	0.587	0.563	0.563	0.607	0.648	
K/K+Na	0.691	0.663	0.673	0.672	0.660	0.868	0.785	
Fe+Mn+Mg	0.093	0.089	0.075	0.087	0.096	0.135	0.108	

Table 9. (Muscovite analyses, continued).

Locality		NS18					
Analysis No.	18	34	35	36	37	38	39
			Rim ...	Core ...	Rim		
SiO <sub>2</sub>	46.70	46.73	46.59	45.45	45.54	45.74	45.35
TiO <sub>2</sub>	0.53	0.27	0.28	0.34	0.36	0.51	0.52
Al <sub>2</sub> O <sub>3</sub>	37.46	37.33	37.15	35.83	35.04	36.06	36.17
Cr <sub>2</sub> O <sub>3</sub>	0	0	0	0.05	0.06	0.03	0.07
FeO	0.86	1.00	1.31	0.93	1.42	0.94	1.17
MnO	0	0	0	0	0	0	0
MgO	0.39	0.46	0.53	0.38	0.70	0.40	0.43
ZnO	0.07	0	0.02	0.15	0.12	0.12	0
CaO	0	0	0	0	0	0	0
Na <sub>2</sub> O	1.91	1.40	1.39	2.14	0.79	2.08	2.07
K <sub>2</sub> O	8.42	9.01	9.11	8.79	10.48	8.71	8.56
Sum	96.34	96.20	96.38	94.06	94.51	94.59	94.34
H <sub>2</sub> O	3.66	3.80	3.62	5.94	5.49	5.41	5.66
Total	100	100	100	100	100	100	100
Structural Formulae							
A Site K	0.700	0.751	0.760	0.753	0.901	0.741	0.730
Na	0.242	0.177	0.177	0.278	0.103	0.269	0.268
Sum	0.942	0.928	0.937	1.031	1.004	1.010	0.998
IV Site Si	3.039	3.050	3.044	3.049	3.065	3.047	3.030
Al	0.961	0.950	0.956	0.951	0.935	0.953	0.970
Sum	4.000	4.000	4.000	4.000	4.000	4.000	4.000
VI Site Fe	0.047	0.055	0.072	0.052	0.080	0.053	0.066
Mn	0	0	0	0	0	0	0
Mg	0.038	0.045	0.052	0.039	0.070	0.040	0.043
Zn	0.004	0	0.001	0.007	0.006	0.006	0
Al	1.914	1.924	1.906	1.884	1.846	1.881	1.880
Cr	0	0	0	0.003	0.003	0.002	0.003
Ti	0.026	0.013	0.014	0.018	0.018	0.026	0.026
Sum	2.029	2.037	2.045	2.003	2.023	2.008	2.018
Total	6.971	6.965	6.982	7.034	7.027	7.018	7.016
OH <sup>-</sup>	1.585	1.645	1.568	2.572	2.377	2.343	2.451
Fe/Fe+Mg	0.553	0.550	0.581	0.571	0.533	0.570	0.606
K/K+Na	0.743	0.809	0.811	0.730	0.897	0.734	0.731
Fe+Mn+Mg	0.085	0.100	0.124	0.091	0.150	0.093	0.109



Table 9. (Muscovite analyses, continued).

Locality		NS18				NS87		
Analysis No.		40	41	27	28	29	30	31
				Core ... Rim				
SiO <sub>2</sub>		45.68	45.52	45.78	46.53	44.39	45.57	44.55
TiO <sub>2</sub>		0.28	0.27	0.41	0.42	0.44	0.53	0.56
Al <sub>2</sub> O <sub>3</sub>		35.80	35.72	35.98	34.84	36.29	35.68	36.22
Cr <sub>2</sub> O <sub>3</sub>		0.07	0.05	0.03	0.01	0.06	0	0.07
FeO		1.35	1.06	0.88	1.10	1.26	0.91	1.01
MnO		0	0	0	0	0.01	0	0
MgO		0.54	0.53	0.35	0.68	0.34	0.36	0.41
ZnO		0.01	0.05	0.04	0.04	0.04	0	0.04
CaO		0	0	0	0	0	0	0
Na <sub>2</sub> O		1.63	1.60	1.81	1.11	1.90	1.69	1.65
K <sub>2</sub> O		8.99	8.95	9.21	10.01	9.12	8.89	9.19
Sum		94.35	93.75	94.49	94.74	93.85	93.63	93.70
H <sub>2</sub> O,F		5.65	6.25	5.51	5.26	6.15	6.37	6.30
Total		100	100	100	100	100	100	100
Structural Formulae								
A Site	K	0.767	0.768	0.785	0.853	0.786	0.763	0.791
	Na	0.212	0.209	0.235	0.145	0.249	0.220	0.216
	Sum	0.979	0.977	1.010	0.998	1.035	0.983	1.007
IV Site	Si	3.056	3.059	3.056	3.106	2.996	3.063	3.006
	Al	0.944	0.941	0.944	0.894	1.004	0.937	0.994
		4.000	4.000	4.000	4.000	4.000	4.000	4.000
VI Site	Fe	0.076	0.060	0.050	0.061	0.072	0.052	0.057
	Mn	0	0	0	0	0.001	0	0
	Mg	0.054	0.053	0.035	0.068	0.034	0.036	0.042
	Zn	0.001	0.003	0.002	0.002	0.002	0	0.002
	Al	1.880	1.891	1.889	1.850	1.885	1.891	1.888
	Cr	0.003	0.003	0.002	0.001	0.003	0	0.004
	Ti	0.015	0.014	0.021	0.021	0.022	0.027	0.029
	Sum	2.029	2.024	1.999	2.003	2.019	2.006	2.022
Total		7.008	7.001	7.009	7.001	7.054	6.989	7.029
	OH <sup>-</sup>	2.447	2.709	2.386	2.278	2.663	2.758	2.728
	Fe/Fe+Mg	0.585	0.531	0.588	0.473	0.679	0.591	0.576
	K/K+Na	0.783	0.786	0.777	0.855	0.759	0.776	0.786
	Fe+Mn+Mg	0.130	0.113	0.085	0.129	0.107	0.088	0.096

Table 9. (Muscovite analysis, continued).

Locality		NS87					
Analysis No.	32	33	34	35	36	29	30
							Rim..
SiO <sub>2</sub>	45.50	45.44	45.83	45.67	45.76	45.40	44.96
TiO <sub>2</sub>	0.30	0.28	0.29	0.36	0.34	0.53	0.33
Al <sub>2</sub> O <sub>3</sub>	36.17	35.86	35.66	35.31	35.41	36.22	35.74
Cr <sub>2</sub> O <sub>3</sub>	0.02	0.04	0.06	0.05	0.02	0.06	0.05
FeO	1.16	1.13	1.00	1.48	1.22	1.00	1.08
MnO	0.01	0	0.03	0.05	0.02	0.01	0.02
MgO	0.51	0.49	0.50	0.66	0.53	0.43	0.46
ZnO	0.03	0.07	0.10	0.04	0.02	0	0.02
CaO	0	0	0	0	0	0	0
Na <sub>2</sub> O	1.29	1.54	1.45	1.29	1.49	1.83	0.74
K <sub>2</sub> O	9.76	9.09	9.59	9.36	9.30	8.79	10.23
Sum	94.75	93.94	94.51	94.27	94.03	94.27	93.63
H <sub>2</sub> O,F	5.25	6.06	5.49	5.73	5.97	5.73	6.37
Total	100	100	100	100	100	100	100
Structural Formulae							
A Site	K	0.832	0.779	0.819	0.802	0.797	0.884
	Na	0.168	0.201	0.189	0.168	0.183	0.098
	Sum	1.000	0.980	1.008	0.970	0.980	0.982
IV Site	Si	3.039	3.052	3.065	3.065	3.073	3.042
	Al	0.961	0.948	0.935	0.935	0.927	0.958
		4.000	4.000	4.000	4.000	4.000	4.000
VI Site	Fe	0.065	0.064	0.056	0.083	0.069	0.062
	Mn	0.001	0	0.002	0.003	0.001	0.001
	Mg	0.051	0.050	0.050	0.067	0.053	0.046
	Zn	0.002	0.003	0.005	0.002	0.001	0.001
	Al	1.888	1.892	1.878	1.859	1.877	1.894
	Cr	0.002	0.002	0.003	0.002	0.001	0.003
	Ti	0.015	0.014	0.015	0.018	0.018	0.017
	Sum	2.024	2.025	2.009	2.034	2.020	2.024
	Total	7.024	7.005	7.017	7.004	7.000	7.006
	OH <sup>-</sup>	2.273	2.624	2.377	2.481	2.585	2.758
	Fe/Fe+Mg	0.560	0.561	0.528	0.553	0.566	0.574
	K/K+Na	0.832	0.795	0.813	0.827	0.813	0.900
	Fe+Mn+Mg	0.117	0.114	0.108	0.153	0.123	0.109

Table 9. (Muscovite analyses, contined).

## Locality

Analysis No.	31	32	33	34	35	36	37
	..... Core .....			..... Rim .....			
SiO <sub>2</sub>	44.97	45.41	45.29	45.63	45.28	45.66	45.38
TiO <sub>2</sub>	0.36	0.30	0.41	0.31	0.36	0.46	0.30
Al <sub>2</sub> O <sub>3</sub>	36.11	36.12	36.10	36.48	35.70	35.68	36.20
Cr <sub>2</sub> O <sub>3</sub>	0.04	0.02	0.02	0	0.02	0.11	0.04
FeO	1.06	0.94	1.00	1.10	1.91	1.50	1.25
MnO	0	0.04	0.02	0	0.03	0	0.04
MgO	0.35	0.48	0.41	0.34	0.63	0.53	0.51
ZnO	0.01	0.09	0	0	0.02	0	0.08
CaO	0	0	0	0	0	0	0
Na <sub>2</sub> O	1.28	1.27	1.47	1.44	0.71	0.88	1.63
K <sub>2</sub> O	9.30	9.75	9.23	8.94	10.39	10.20	9.27
Sum	93.48	94.42	94.07	94.24	95.05	95.02	94.70
H <sub>2</sub> O,F	6.52	5.58	5.93	5.76	4.95	4.98	5.30
Total	100	100	100	100	100	100	100

## Structural Formulae

A Site	K	0.801	0.833	0.790	0.762	0.889	0.870	0.791
	Na	0.168	0.166	0.192	0.187	0.093	0.114	0.211
	Sum	0.969	0.999	0.982	0.949	0.982	0.984	1.002
IV Site	Si	3.035	3.041	3.037	3.046	3.034	3.050	3.031
	Al	0.965	0.959	0.963	0.954	0.966	0.950	0.969
	Sum	4.000	4.000	4.000	4.000	4.000	4.000	4.000
VI Site	Fe	0.060	0.053	0.056	0.062	0.107	0.084	0.070
	Mn	0	0.002	0.001	0	0.002	0	0.002
	Mg	0.035	0.048	0.042	0.034	0.063	0.053	0.051
	Zn	0.001	0.004	0	0	0.001	0	0.004
	Al	1.909	1.894	1.892	1.918	1.855	1.861	1.883
	Cr	0.002	0.001	0.001	0	0.002	0.006	0.002
	Ti	0.019	0.015	0.042	0.016	0.019	0.024	0.015
	Sum	2.026	2.017	2.034	2.030	2.049	2.028	2.032
Total		6.995	7.016	7.016	6.979	7.013	7.012	7.034
OH <sup>-</sup>		2.823	2.416	2.568	2.494	2.143	2.156	2.295
Fe/Fe+Mg		0.632	0.525	0.571	0.646	0.629	0.613	0.579
K/K+Na		0.827	0.884	0.804	0.803	0.905	0.884	0.789
Fe+Mn+Mg		0.095	0.101	0.099	0.096	0.172	0.137	0.123

Table 9. (Muscovite analyses, continued).

Locality	NS85			NS90			
Analysis No.	38	8	9	10	11	12	13
SiO <sub>2</sub>	45.82	46.14	46.35	45.81	44.31	46.38	46.12
TiO <sub>2</sub>	0.29	0.51	0.44	0.47	0.47	0.46	0.46
Al <sub>2</sub> O <sub>3</sub>	35.95	36.66	36.78	37.05	36.72	37.19	37.08
Cr <sub>2</sub> O <sub>3</sub>	0.10	0.04	0.10	0.09	0.04	0.08	0.02
FeO	1.12	1.14	1.03	0.98	0.96	0.98	0.82
MnO	0	0	0.02	0	0	0	0
MgO	0.58	0.44	0.45	0.38	0.38	0.35	0.34
ZnO	0.02	0.08	0.05	0.04	0.05	0.01	0.06
CaO	0	0	0	0	0	0	0
Na <sub>2</sub> O	1.36	1.26	1.38	1.76	1.87	1.64	1.77
K <sub>2</sub> O	9.47	9.74	9.16	8.97	8.76	9.21	8.99
Sum	94.71	96.01	95.76	95.55	93.56	96.30	95.66
H <sub>2</sub> O	5.29	3.99	4.24	4.45	6.44	3.70	4.34
Total	100	100	100	100	100	100	100
Structural Formulae							
A Site	K	0.806	0.819	0.769	0.755	0.754	0.769
	Na	0.176	0.161	0.177	0.225	0.245	0.208
	Sum	0.982	0.980	0.946	0.980	0.999	0.977
IV Site	Si	3.056	3.038	3.048	3.021	2.988	3.034
	Al	0.944	0.962	0.952	0.979	1.012	0.966
	Sum	4.000	4.000	4.000	4.000	4.000	4.000
VI Site	Fe	0.063	0.063	0.057	0.054	0.054	0.054
	Mn	0	0	0.001	0	0	0
	Mg	0.058	0.043	0.044	0.037	0.038	0.035
	Zn	0.001	0.004	0.003	0.002	0.003	0.001
	Al	1.883	1.886	1.900	1.903	1.908	1.903
	Cr	0.005	0.003	0.005	0.004	0.002	0.005
	Ti	0.015	0.025	0.022	0.024	0.024	0.023
	Sum	2.025	2.024	2.032	2.024	2.029	2.021
	Total	7.007	7.004	6.978	7.004	7.028	6.998
	OH <sup>-</sup>	2.291	1.728	1.836	1.927	2.789	1.602
	Fe/Fe+Mg	0.521	0.594	0.564	0.593	0.587	0.607
	K/K+Na	0.821	0.836	0.813	0.770	0.755	0.787
	Fe+Mn+Mg	0.121	0.106	0.102	0.091	0.092	0.078

Table 9. (Muscovite analyses, continued).

Locality		NS90						NS71
Analysis No.		14	15	16	17	18	19	1
SiO <sub>2</sub>		46.10	46.57	46.52	46.28	46.56	44.89	44.18
TiO <sub>2</sub>		0.33	0.24	0.51	0.49	0.51	0.46	0.15
Al <sub>2</sub> O <sub>3</sub>		35.49	36.77	37.40	37.42	37.24	37.93	37.57
Cr <sub>2</sub> O <sub>3</sub>		0.03	0	0.05	0.06	0.12	0.02	-
FeO		1.47	1.40	1.13	1.01	0.78	0.87	1.17
MnO		0	0	0	0	0	0	0.01
MgO		0.57	0.57	0.39	0.34	0.38	0.87	0.14
ZnO		0.06	0.10	0	0.07	0.11	0.14	-
CaO		0	0	0	0	0	0	0
Na <sub>2</sub> O		0.87	0.61	1.35	1.73	1.66	1.52	1.85
K <sub>2</sub> O		10.05	10.76	9.64	8.90	8.86	8.86	8.82
Sum		94.97	97.02	96.99	96.30	96.22	95.12	93.89
H <sub>2</sub> O		5.03	2.98	3.01	3.70	3.78	4.88	6.11
Total		100	100	100	100	100	100	100
Structural Formulae								
A Site	K	0.856	0.899	0.801	0.743	0.739	0.749	0.756
	Na	0.113	0.078	0.171	0.220	0.210	0.195	0.241
	Sum	0.969	0.977	0.972	0.963	0.949	0.944	0.997
IV Site	Si	3.075	3.048	3.028	3.025	3.040	2.971	2.970
	Al	0.925	0.952	0.972	0.975	0.960	1.029	1.030
	Sum	4.000	4.000	4.000	4.000	4.000	4.000	4.000
VI Site	Fe	0.082	0.077	0.064	0.055	0.043	0.049	0.066
	Mn	0	0	0	0	0	0	0.001
	Mg	0.057	0.056	0.038	0.034	0.037	0.043	0.014
	Zn	0.003	0.004	0	0.004	0.005	0.007	-
	Al	1.867	1.886	1.899	1.909	1.908	1.932	1.948
	Cr	0.002	0	0.003	0.003	0.006	0.001	-
	Ti	0.017	0.012	0.025	0.025	0.025	0.023	0.008
	Sum	2.028	2.035	2.029	2.030	2.024	2.055	2.037
	Total	6.997	7.012	7.001	6.993	6.973	6.999	7.034
	OH <sup>-</sup>	2.178	1.290	1.303	1.602	1.637	2.113	2.646
	Fe/Fe+Mg	0.590	0.579	0.627	0.618	0.538	0.533	0.825
	K/K+Na	0.883	0.920	0.824	0.772	0.779	0.793	0.758
	Fe+Mn+Mg	0.139	0.133	0.102	0.089	0.080	0.092	0.081

Table 9. (Muscovite analyses, continued).

Locality		NS71					
Analysis No.	2	3	4	5	6	7	8
SiO <sub>2</sub>	45.56	45.09	45.60	44.45	45.63	44.74	45.56
TiO <sub>2</sub>	0.22	0.21	0.24	0.23	0.20	0.21	0.23
Al <sub>2</sub> O <sub>3</sub>	36.96	36.51	36.63	37.00	36.92	37.00	36.85
Cr <sub>2</sub> O <sub>3</sub>	0.01	0.04	0.06	0.04	0.01	0	0
FeO	1.16	1.26	1.50	1.33	1.29	1.50	1.22
MnO	0	0	0	0	0	0.01	0
MgO	0.41	0.38	0.41	0.37	0.35	0.41	0.38
ZnO	0.07	0	0	0	0.02	0	0
CaO	0	0	0	0	0	0	0
Na <sub>2</sub> O	1.61	1.73	1.74	1.72	1.67	1.59	1.52
K <sub>2</sub> O	9.12	9.02	8.91	8.78	9.08	8.89	9.07
Sum	95.12	94.24	95.09	93.92	95.17	94.35	94.83
H <sub>2</sub> O	4.88	5.76	4.91	6.08	4.83	5.65	5.17
Total	100	100	100	100	100	100	100
Structural Formulae							
A Site	K	0.772	0.772	0.755	0.753	0.768	0.770
	Na	0.207	0.225	0.224	0.225	0.215	0.197
	Sum	0.979	0.997	0.979	0.978	0.983	0.967
IV Site	Si	3.022	3.021	3.028	2.987	3.026	3.028
	Al	0.978	0.979	0.972	1.013	0.974	0.972
	Sum	4.000	4.000	4.000	4.000	4.000	4.000
VI Site	Fe	0.065	0.071	0.084	0.075	0.072	0.068
	Mn	0	0	0	0	0	0
	Mg	0.041	0.039	0.040	0.037	0.034	0.038
	Zn	0.004	0	0	0	0.001	0
	Al	1.913	1.906	1.896	1.920	1.913	1.917
	Cr	0.001	0.002	0.003	0.002	0.001	0
	Ti	0.011	0.011	0.012	0.012	0.010	0.012
	Sum	2.035	2.029	2.035	2.046	2.031	2.035
	Total	7.014	7.026	7.014	7.024	7.014	7.002
	OH <sup>-</sup>	2.113	2.494	2.126	2.633	2.091	2.239
Fe/Fe+Mg		0.613	0.645	0.677	0.670	0.679	0.642
K/K+Na		0.789	0.774	0.771	0.770	0.781	0.796
Fe+Mn+Mg		0.106	0.110	0.124	0.112	0.106	0.106

Table 9. (Muscovite analyses, continued).

Location	U01A	NS118		NS18		
N, Averages	9	Standard deviation	17	Standard deviation	11	Standard deviation
SiO <sub>2</sub>	46.16	0.19	46.02	0.41	46.00	0.59
TiO <sub>2</sub>	0.40	0.03	0.39	0.05	0.35	0.12
Al <sub>2</sub> O <sub>3</sub>	37.45	0.87	36.89	0.41	36.41	0.79
Cr <sub>2</sub> O <sub>3</sub>	0.02	0.02	0.02	0.02	0.03	0.03
FeO	0.83	0.09	0.92	0.10	1.16	0.22
MnO	0	–	0.01	–	0	–
MgO	0.40	0.04	0.31	0.07	0.50	0.10
ZnO	0	–	0	–	0.05	0.06
CaO	0	–	0	–	0	–
Na <sub>2</sub> O	2.50	0.12	2.54	0.20	1.60	0.61
K <sub>2</sub> O	7.59	0.15	7.57	0.32	9.04	0.59
Sum	95.35	0.85	94.67	0.56	95.14	1.04
H <sub>2</sub> O	4.65	0.85	5.33	0.56	4.86	1.04
Total	100	–	100	–	100	–

## Structural Formulae

A Site	K	0.635	0.015	0.639	0.029	0.765	0.051
	Na	0.318	0.017	0.326	0.025	0.205	0.058
	Sum	0.953	0.026	0.965	0.018	0.970	0.038
IV Site	Si	3.026	0.022	3.042	0.017	3.047	0.010
	Al	0.974	-	0.958	-	0.953	-
	Sum	4.000	-	4.000	-	4.000	-
VI Site	Fe	0.046	0.005	0.052	0.007	0.064	0.012
	Mn	0	-	0	-	0	-
	Mg	0.040	0.004	0.030	0.007	0.049	0.010
	Zn	0	-	0	-	0.002	0.003
	Al	1.923	0.040*	1.918	0.022*	1.891	0.028*
	Cr	0.002	0.001	0.002	0.001	0.002	0.002
	Ti	0.020	0.002	0.019	0.002	0.017	0.006
	Sum	2.031	0.014	2.021	0.008	2.025	0.015
	Total	6.984	0.015	6.986	0.016	6.995	0.025
	OH <sup>-</sup>	2.014	0.391	2.308	0.242	2.040	0.437
	Fe/Fe+Mg	0.535	0.039	0.634	0.056	0.566	0.035
	K/K+Na	0.666	0.011	0.662	0.026	0.789	0.056
	Fe+Mn+Mg	0.086	0.006	0.082	0.010	0.113	0.022

\* Total aluminum.

Table 9. (Muscovite analyses, continued).

Location	NS87	Standard deviation	NS85	Standard deviation	NS90	Standard deviation
N, Averages	10		10		12	
SiO <sub>2</sub>	45.50	0.62	45.38	0.28	46.00	0.70
TiO <sub>2</sub>	0.39	0.10	0.37	0.08	0.45	0.08
Al <sub>2</sub> O <sub>3</sub>	35.74	0.46	36.03	0.26	36.98	0.59
Cr <sub>2</sub> O <sub>3</sub>	0.04	0.02	0.05	0.04	0.05	0.04
FeO	1.12	0.18	1.20	0.30	1.05	0.21
MnO	0.01	0.02	0.02	0.02	0	-
MgO	0.48	0.12	0.47	0.09	0.42	0.15
ZnO	0.04	0.03	0.02	0.03	0.06	0.04
CaO	0	-	0	-	0	-
Na <sub>2</sub> O	1.51	0.25	1.26	0.33	1.45	0.39
K <sub>2</sub> O	9.35	0.34	9.56	0.69	9.33	0.61
Sum	94.18	0.42	94.36	0.53	95.79	1.19
H <sub>2</sub> O	5.82	0.42	5.64	0.53	4.21	1.19
Total	100	-	100	-	100	-
Structural Formulae						
A Site K	0.801	0.027	0.817	0.046	0.784	0.050
Na	0.197	0.033	0.164	0.048	0.186	0.049
Sum	0.998	0.019	0.981	0.015	0.970	0.017
IV Site Si	3.052	0.028	3.040	0.008	3.029	0.027
Al	0.948	-	0.960	-	0.971	-
Sum	4.000	-	4.000	-	4.000	-
VI Site Fe	0.063	0.010	0.067	0.016	0.058	0.012
Mn	0.001	0.001	0.001	0.001	0	-
Mg	0.048	0.012	0.047	0.009	0.041	0.009
Zn	0.002	0.001	0.001	0.002	0.003	0.002
Al	1.880	0.042*	1.887	0.021*	1.901	0.042*
Cr	0.002	0.001	0.002	0.002	0.003	0.002
Ti	0.020	0.005	0.019	0.008	0.022	0.004
Sum	2.016	0.011	2.024	0.009	2.028	0.010
Total	7.014	0.019	7.005	0.014	6.998	0.014
OH <sup>-</sup>	2.520	0.182	2.442	0.229	1.823	0.515
Fe/Fe+Mg	0.568	0.052	0.588	0.044	0.586	0.029
K/K+Na	0.803	0.030	0.833	0.052	0.808	0.050
Al/Al+Si	0.112	0.020	0.115	0.024	0.099	0.019

\* Total aluminum.



Table 9. (Muscovite analyses, continued).

	NS71 8	Standard deviation	Grand Average N=69**		Standard deviation
SiO <sub>2</sub>	45.10	0.58	45.86		0.32
TiO <sub>2</sub>	0.21	0.03	0.39		0.03
Al <sub>2</sub> O <sub>3</sub>	36.93	0.31	36.61		0.64
Cr <sub>2</sub> O <sub>3</sub>	0.02	0.02	0.03		0.01
FeO	1.30	0.13	1.04		0.14
MnO	0	-	0.01		0.01
MgO	0.36	0.09	0.42		0.07
ZnO	0.01	0.03	0.03		0.03
CaO	0	-	0		-
Na <sub>2</sub> O	1.68	0.10	1.86		0.56
K <sub>2</sub> O	8.96	0.13	8.66	Ideal	0.91
Sum	94.57	0.54	94.91	95.38	0.61
H <sub>2</sub> O	5.43	0.54	5.09	4.62	0.61
Total	100	-	100		-
Structural Formula					
A Site K	0.765	0.008	0.733		0.075
Na	0.217	0.014	0.239		0.071
Sum	0.982	0.011	0.972		0.015
IV Site Si	3.009	0.022	3.040		0.010
Al	0.991	-	0.960		-
Sum	4.000	-	4.000		-
VI Site Fe	0.073	0.007	0.058		0.008
Mn	0	-	0		-
Mg	0.035	0.009	0.041		0.007
Zn	0.001	0.001	0.001		0.001
Al	1.915	0.036*	1.902		0.025*
Cr	0.001	0.001	0.002		0.001
Ti	0.011	0.001	0.019		0.002
Sum	2.036	0.008	2.023		0.005
Total	7.016	0.010	6.995		0.011
OH <sup>-</sup>	2.351	0.237	2.204	2.000	0.264
Fe/Fe+Mg	0.676	0.064	0.586		0.032
K/K+Na	0.779	0.012	0.754		0.070
Fe+Mn+Mg	0.108	0.014	0.099		0.014

\*\* Average excludes sample NS71, which is anomalously poor in Ti and Si. This average is used for stoichiometric calculations.

\* Total aluminum

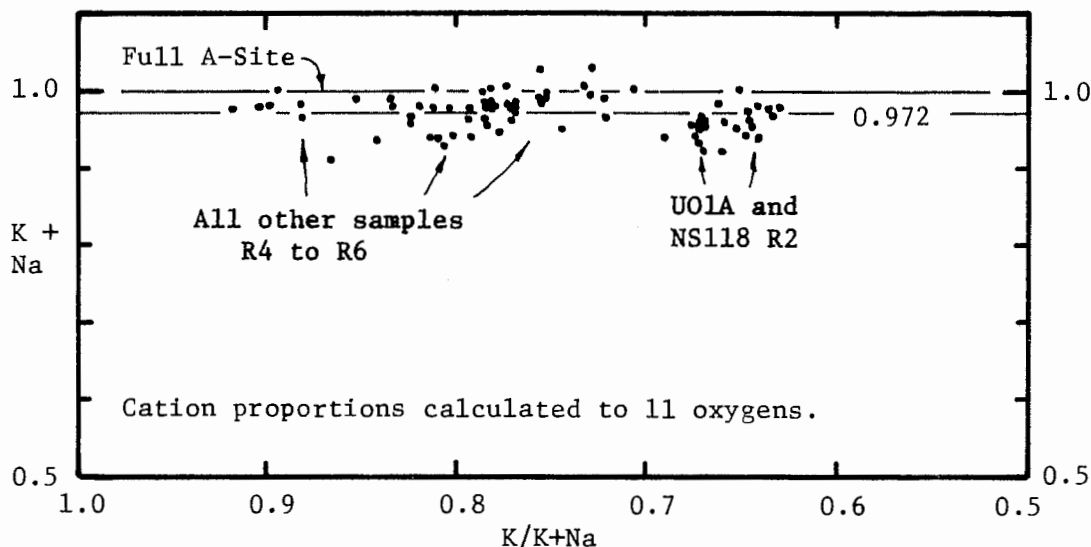


Figure 15. Individual muscovite analyses with A-site occupancy plotted versus K/K+Na ratio. The right hand cluster is composed of staurolite-bearing rocks, and the rest of the data for all other samples. Note that the gap between the two groups of data is not as distinct as that for biotite, Figure 12, due to muscovite zoning.

staurolite breakdown is filled in to some degree by data from muscovite crystals that are zoned with respect to K/K+Na ratios. Muscovite in samples NS18, NS87, NS85, and NS90 (zones R4 to R5) tend to have low K/K+Na ratios in cores and high ratios in rims.

The documenting of zoned muscovite was difficult, due to the use of a defocused electron beam, instrument instability, operator inexperience, and to the fact that muscovite cores tended to be flatter and more highly polished than the rims. The latter reason resulted in most analyses being taken from muscovite cores before the zoning was discovered, and only three good examples of zoned muscovite were secured. Analyzed zoned muscovite is identified in Table 9 (samples NS18, NS87, and NS85) and the extent of zoning

depicted in Figure 16.

Zoning is especially prevalent in muscovite that developed prior to retrograde metamorphism. Muscovite in samples U01A and NS118 (zone R2) are not significantly zoned because the amount of biotite breakdown was minimal. Sample NS71 does not show significant variation in muscovite alkali ratios because muscovite was always the only alkali-bearing phase in that rock.

Divalent cations are present in muscovite in various quantities, representing solid solutions between muscovite and other mica end member components. Calculations (see Figures 26 and 27) indicate a consistent 3.4% solid solution toward the biotite-eastonite trioctahedral mica series by the substitution:  $3(\text{Fe}, \text{Mg}) = 2^{\text{VI}}\text{Al} + \text{vacancy}$  (Tracy et al., 1976; Guidotti, 1978). In addition to this slight deviation from dioctahedral stoichiometry there is a rather wide range of solid solution between muscovite and celadonite by the tschermaks substitution:  $\text{M}^{+2}\text{Si} = \text{IVAl}^{\text{VI}}\text{Al}$ , ranging from 1.2 to 15.0% for individual analyses. Celadonite will be taken as the general mica end member:  $\text{KAlM}^{+2}\text{Si}_4\text{O}_{10}(\text{OH})_2$  (after Guidotti and Sassi, 1976). Phengitic muscovite will refer to muscovite trending toward compositions intermediate between muscovite and celadonite.

Figure 16 is a plot of total Fe+Mn+Mg cations per formula unit versus K/(K+Na) ratios. Dashed arrows show the apparent composition trend for muscovite cores during staurolite and partial garnet breakdown. Solid arrows show actual zoning trends measured by electron microprobe (see Table 9). The trend from low K and  $\text{M}^{+2}$  to

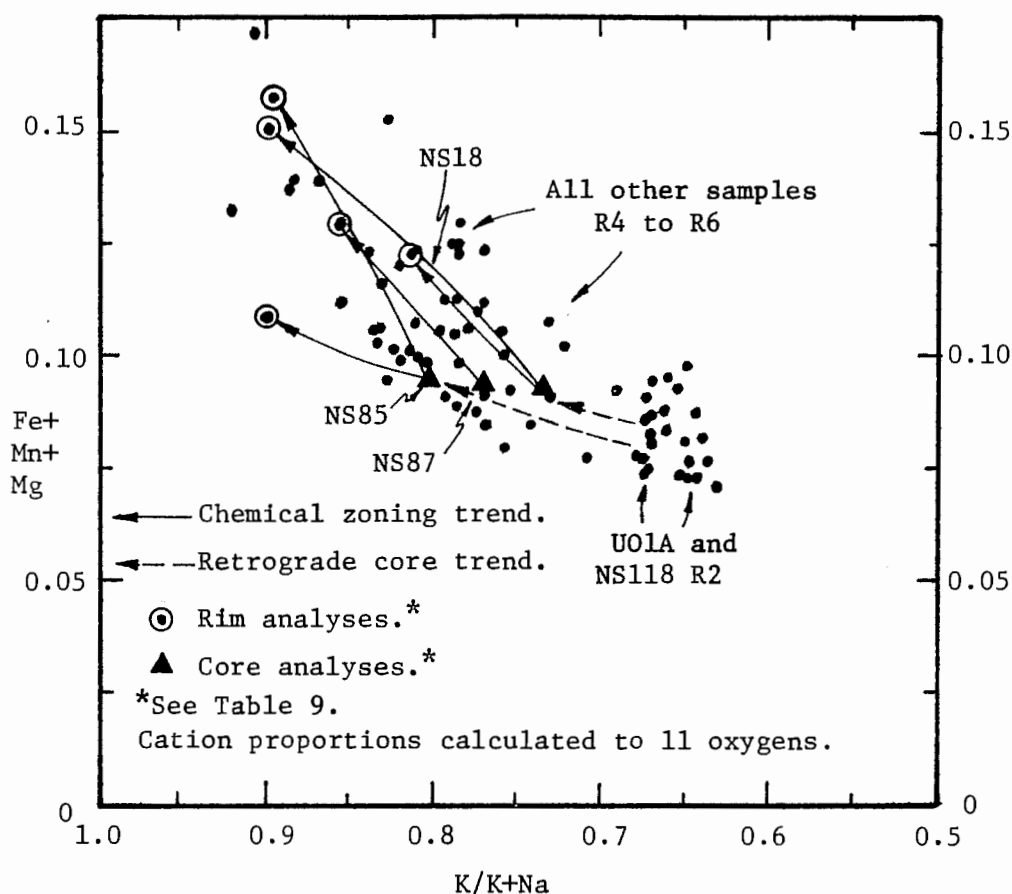


Figure 16. Total Fe+Mn+Mg in muscovite plotted against K/(K+Na) ratios. The cluster of points in the lower right is for samples containing staurolite, and the rest for more severely retrograded rocks. The trend toward higher celadonite component and higher potassium with retrograding is quite well developed.

high K and  $M^{+2}$  is distinct. There is no recognizable trend in Fe/Fe+Mg ratios for muscovite, except for sample NS71 which is distinctly more iron-rich than the other samples. This is because these muscovites coexist with iron-rich chloritoid and the most pyrope-poor garnet of any analyzed in this study.

Muscovite aluminum concentration decreases with retrograding, particularly for  $^{VI}Al$ , due to increasing amounts of tschermaks type substitution in the more retrograded (more potassic) micas, as

described above.

ZnO increases from zero to about 0.04 weight percent with the destruction of staurolite. The values are small but consistent in many analyses and therefore probably real. It is interesting to note that Zn/Fe ratios for muscovite are much higher than for coexisting biotite, as found in prograde rocks by Albee (1972).  $\text{Cr}_2\text{O}_3$  and  $\text{TiO}_2$  do not vary at all within analytical uncertainty. Because of the lack of variation in  $\text{TiO}_2$  concentration in analyzed muscovite, the mechanism of substitution of Ti into the structure could not be deduced. However, the most probable type of substitution is the ilmenite type:  $\text{Fe}+\text{Ti} = 2^{\text{VI}}\text{Al}$ , which maintains muscovite dioctahedral stoichiometry (Guidotti, 1973 and 1978; Tracy, 1978).

### Chlorite

Field Appearance. Chlorite is the most widespread and easily recognizable mineral of retrograde origin. It is visible in hand specimen in zones R1 and R2, even where sillimanite and apparently fresh staurolite is present. The chlorite occurs as small isolated plates and sprays up to 1 cm across, at random angles to the foliation. Chlorite is very common in zones R3 to R6, occurring throughout the matrix, associated with biotite, and in pseudomorphs after staurolite and garnet. Chlorite in pseudomorphs after staurolite is intergrown with secondary muscovite and is commonly varied in abundance, distribution, and crystal size, and in some

cases forms a thin rind. Garnet is rimmed by chlorite within the retrograde staurolite-out isograd (zone R4) and is replaced in a regular manner until only spherical pseudomorphs remain (zone R6). In many of the most severely retrograded rocks, chlorite is the only ferromagnesian mineral remaining, excepting tourmaline.

Optical properties. Chlorite is pleochroic pale yellow to medium- or light-green with absorption  $X=Y>Z$  or  $X<Y=Z$  for optically positive and negative varieties, respectively. Optically positive chlorite has negative elongation (parallel to cleavage) with anomalous brown to greenish-brown interference colors and a retardation probably not exceeding 0.004. Optically negative chlorite has positive elongation with anomalous blue to blue-gray interference colors, and a retardation also probably not exceeding 0.004. Dispersion is strong,  $r<v$ .

The transition between positive and negative chlorite occurs in most rocks at an intermediate stage of staurolite breakdown, outside of the retrograde staurolite isograd. Samples U01A and NS118 contain optically positive chlorite with Fe/Fe+Mg ratios up to 0.488, whereas all other analyzed samples contain optically negative chlorite with ratios as low as 0.570. Therefore, the transition between optically positive and negative varieties, when anomalous interference colors are purplish, is interpolated to occur at about Fe/Fe+Mg = 0.52. Above and below the optic transition composition, the 2V is variable in any one sample from about 10° to 40°, and is not correlated with composition.

Appearance in thin section. Chlorite occurs as plates, sprays, aggregates of plates, and intergrowths with muscovite and other minerals. Chlorite sprays occur in the matrix or associated with retrograded biotite, staurolite, and garnet, and their pseudomorphs (Figures 8b, 10c and 10d, and 12). Chlorite plates of various sizes are found in the matrix alone, in groups, or in intergrowths with muscovite and quartz (various figures). Individual chlorite plates are commonly subhedral on 001, about 2 to 5 times as wide as they are thick, and rarely exceed 2 mm in width.

Well formed plates also occur around pseudomorphs after garnet and staurolite (Figures 8b, 10c and 10d), adjacent to and growing into biotite (Figures 10a, 10c, and 10d, and 12) and chloritoid (Figure 18), and in parallel stacks and layers (Figure 10b). Chlorite in pseudomorphs after staurolite tends to be poorly formed, random in orientation, and varied in distribution. Chlorite in the cores of pseudomorphs after garnet tends to be very small and ragged in form (Figure 10c and 10d), although larger recrystallized plates occur.

Inclusions are not common except zircon and graphite, which occurs abundantly where chlorite has replaced graphite-bearing parts of parent minerals such as biotite or staurolite. Inclusions of ilmenite, muscovite, quartz, rutile, and garnet are also found. Pleochroic radiation halos are well developed around zircon and allanite, and weakly developed around apatite in some cases. Halos surrounding small zircon inclusions may have two to four concentric

shells of different pleochroic intensities.

Chemistry. Chemically all chlorite in the study area is ripidolite, as defined by Hey (1954), occurring within the limits of 2.5 and 2.8 Si per formula unit and Fe/Fe+Mg between 0.2 and 0.8. Chlorite is chemically more simple than the micas because it is not zoned and has no alkali cation site (Table 10).

Aluminum is found to be partitioned about equally between the tetrahedral and octahedral sites (assuming full tetrahedral sites). Ca, K, and Na are present in some analyses. These three elements were analyzed to detect submicroscopic intergrowths with micas or chlorite-mica or chlorite-clay mixed layer phases (Boles and Coombs, 1977), neither of which were found. The Ca and alkalis listed in the analyses may be explained by several factors, but are in such small quantity that they may be considered negligible.

The major variation in chemistry is in the Fe/Fe+Mg ratio the total range of which is 0.481 to 0.717, greater than for biotite. Chlorite in only two samples occur at iron compositions higher than biotite: NS90 (zone R6) in which all staurolite, biotite, and garnet and nearly all ilmenite has been destroyed, and NS71 which contains chloritoid, very iron-rich muscovite, and Mg-poor garnet. A plot of Al/(Al+Si) ratios versus Fe/Fe+Mg ratios (Figure 17) has several clusters of data. The most Mg-rich chlorite (samples U01A and NS118, zone R2) contain staurolite, and the large central group contains only pseudomorphs after staurolite (samples NS18, NS87, NS85, and NS90, zones R4 to R6). Biotite-bearing samples cluster about the



Table 10. Electron microprobe analyses of chlorite from various samples. Structural formula was calculated on a basis of the composition  $(\text{Fe,Mg,Al})_6(\text{Si,Al})_4\text{O}_{10}(\text{OH})_8$ , containing 14 oxygens and four  $\text{H}_2\text{O}$ .  $\text{OH}^-$  anion proportions were calculated on a basis of 18 oxygens, with  $\text{H}_2\text{O}$  weight percent.

Location		U01A						
Analysis No.		15	16	17	18	19	37	38
$\text{SiO}_2$		24.92	24.66	24.38	24.53	24.76	24.21	24.73
$\text{TiO}_2$		0.11	0.11	0.10	0.07	0.12	0.12	0.06
$\text{Al}_2\text{O}_3$		24.24	24.53	24.16	24.44	23.90	24.12	23.63
$\text{Cr}_2\text{O}_3$		-	-	-	-	-	0	0.03
$\text{FeO}$		25.35	25.29	25.67	25.23	25.42	26.11	24.44
$\text{MnO}$		0	0	0	0	0	0.01	0.01
$\text{MgO}$		15.37	15.24	15.19	15.22	15.32	15.34	16.07
$\text{ZnO}$		-	-	-	-	-	0	0
$\text{CaO}$		-	-	-	-	-	0	0
$\text{Na}_2\text{O}$		0	0.02	0	0.01	0.04	0.03	0
$\text{K}_2\text{O}$		0	0	0	0	0	0	0
Sum		89.99	89.85	89.50	89.50	89.56	89.94	88.97
$\text{H}_2\text{O}$		10.01	10.15	10.50	10.50	10.44	10.06	11.03
Total		100	100	100	100	100	100	100
Structural Formulae								
IV Site	Si	2.546	2.523	2.513	2.521	2.546	2.492	2.549
	Al	1.454	1.477	1.487	1.479	1.454	1.508	1.451
	Sum	4.000	4.000	4.000	4.000	4.000	4.000	4.000
VI Sites	Fe	2.168	2.166	2.215	2.170	2.187	2.248	2.108
	Mn	0	0	0	0	0	0.001	0.001
	Mg	2.342	2.326	2.336	2.333	2.349	2.355	2.471
	Zn	-	-	-	-	-	0	0
	Al	1.467	1.484	1.451	1.483	1.445	1.419	1.422
	Cr	-	-	-	-	-	0	0.002
	Ti	0.009	0.009	0.007	0.006	0.009	0.009	0.005
	Sum	5.986	5.985	6.009	5.992	5.990	6.032	6.009
	Total	9.986	9.985	10.009	9.992	9.990	10.032	10.009
Alkali	Ca	-	-	-	-	-	0	0
Cations	Na	0	0.004	0	0.002	0.009	0.005	0
	K	0	0	0	0	0	0	0
	Sum	0	0.004	0	0.002	0.009	0.005	0
	Total	9.986	9.989	10.009	9.994	9.999	10.037	10.009
	$\text{OH}^-$	7.194	7.295	7.546	7.546	7.503	7.230	7.927
	Fe/Fe+Mg	0.481	0.482	0.487	0.482	0.482	0.488	0.460
	Al/Al+Si	0.534	0.540	0.539	0.540	0.532	0.540	0.530

Table 10. (Chlorite analyses, continued).

Location		U01A		NS118			NS18	
Analysis No.		39	23	24	25	26	1	2
SiO <sub>2</sub>		24.48	24.70	24.40	24.36	24.09	22.93	22.70
TiO <sub>2</sub>		0.12	0.16	0.07	0.14	0.10	0.06	0.08
Al <sub>2</sub> O <sub>3</sub>		23.77	23.40	23.74	23.87	23.69	24.71	24.76
Cr <sub>2</sub> O <sub>3</sub>		0.01	-	-	-	-	-	-
FeO		26.00	25.43	25.23	25.00	25.00	31.22	31.43
MnO		0.01	0	0.01	0.02	0.01	0.04	0.13
MgO		15.45	15.03	14.84	15.06	15.01	10.82	10.81
ZnO		0	-	-	-	-	-	-
CaO		0	-	-	-	-	0	0
Na <sub>2</sub> O		0.03	-	-	-	-	0	0
K <sub>2</sub> O		0	-	-	-	-	0	0
Sum		<u>89.83</u>	<u>88.72</u>	<u>88.29</u>	<u>88.45</u>	<u>87.90</u>	<u>89.78</u>	<u>89.91</u>
H <sub>2</sub> O,F		10.13	11.27	11.71	11.55	12.10	10.22	10.09
Total		<u>100</u>	<u>100</u>	<u>100</u>	<u>100</u>	<u>100</u>	<u>100</u>	<u>100</u>
Structural Formulae								
IV Site	Si	2.520	2.566	2.546	2.534	2.525	2.432	2.410
	Al	<u>1.480</u>	<u>1.434</u>	<u>1.454</u>	<u>1.466</u>	<u>1.475</u>	<u>1.568</u>	<u>1.590</u>
	Sum	4.000	4.000	4.000	4.000	4.000	4.000	4.000
VI Sites	Fe	2.239	2.211	2.203	2.176	2.193	2.771	2.793
	Mn	0.001	0	0.001	0.002	0.001	0.003	0.012
	Mg	2.371	2.330	2.310	2.337	2.346	1.713	1.712
	Zn	0	-	-	-	-	-	-
	Al	1.405	1.433	1.467	1.463	1.454	1.524	1.511
	Cr	0.001	-	-	-	-	-	-
	Ti	<u>0.009</u>	<u>0.012</u>	<u>0.006</u>	<u>0.011</u>	<u>0.008</u>	<u>0.005</u>	<u>0.006</u>
	Sum	<u>6.026</u>	<u>5.986</u>	<u>5.987</u>	<u>5.989</u>	<u>6.002</u>	<u>6.016</u>	<u>6.034</u>
	Total	10.026	9.986	9.987	9.989	10.002	10.016	10.034
Alkali	Ca	0	-	-	-	-	0	0
	Na	0.006	-	-	-	-	0	0
	K	0	-	-	-	-	0	0
	Sum	<u>0.006</u>	<u>0</u>	<u>0</u>	<u>0</u>	<u>0</u>	<u>0</u>	<u>0</u>
	Total	10.032	9.986	9.987	9.989	10.002	10.016	10.034
OH <sup>-</sup>		7.280	8.099	8.416	8.301	8.696	7.345	7.251
Fe/Fe+Mg		0.486	0.487	0.488	0.482	0.483	0.618	0.620
Al/Al+Si		0.534	0.528	0.534	0.536	0.537	0.560	0.563

Table 10. (Chlorite analyses, continued).

Location		NS18						
Analysis No.		3	4	5	6	7	8	9
SiO <sub>2</sub>		24.85	23.99	24.70	24.23	24.90	25.36	23.99
TiO <sub>2</sub>		0.11	0.09	0.19	0.11	0.13	0.08	0.10
Al <sub>2</sub> O <sub>3</sub>		23.43	23.40	22.58	23.09	22.47	22.96	23.19
Cr <sub>2</sub> O <sub>3</sub>		-	-	-	-	-	-	0.03
FeO		30.63	31.69	31.06	31.45	32.24	30.95	30.47
MnO		0.04	0.06	0.15	0.19	0.15	0.09	0.19
MgO		10.28	10.11	9.38	9.83	10.09	10.54	11.18
ZnO		-	-	-	-	-	-	0.02
CaO		0	0	0	0	0	0	0
Na <sub>2</sub> O		0.02	0.01	0	0	0	0	0
K <sub>2</sub> O		0	0	0.03	0	0	0	0
Sum		89.36	89.35	88.09	88.90	89.98	89.98	89.17
H <sub>2</sub> O		10.64	10.65	11.91	11.10	10.01	10.01	10.83
Total		100	100	100	100	100	100	100
Structural Formulae								
IV Site	Si	2.629	2.561	2.665	2.598	2.643	2.666	2.553
	Al	<u>1.371</u>	<u>1.439</u>	<u>1.335</u>	<u>1.402</u>	<u>1.357</u>	<u>1.334</u>	<u>1.447</u>
	Sum	4.000	4.000	4.000	4.000	4.000	4.000	4.000
VI Sites	Fe	2.712	2.831	2.804	2.821	2.863	2.723	2.714
	Mn	0.004	0.005	0.014	0.018	0.013	0.008	0.017
	Mg	1.622	1.609	1.509	1.571	1.597	1.653	1.774
	Zn	-	-	-	-	-	-	0.002
	Al	1.553	1.507	1.539	1.516	1.456	1.513	1.464
	Cr	-	-	-	-	-	-	0.003
	Ti	<u>0.008</u>	<u>0.007</u>	<u>0.015</u>	<u>0.009</u>	<u>0.011</u>	<u>0.006</u>	<u>0.008</u>
	Sum	<u>5.899</u>	<u>5.959</u>	<u>5.881</u>	<u>5.935</u>	<u>5.940</u>	<u>5.903</u>	<u>5.982</u>
Total		9.899	9.959	9.881	9.935	9.940	9.903	9.982
<hr/>								
Alkali Cations	Ca	0	0	0	0	0	0	0
	Na	0.004	0.001	0	0	0	0	0
	K	<u>0</u>	<u>0</u>	<u>0.006</u>	<u>0</u>	<u>0</u>	<u>0</u>	<u>0</u>
	Sum	<u>0.004</u>	<u>0.001</u>	<u>0.006</u>	<u>0</u>	<u>0</u>	<u>0</u>	<u>0</u>
Total		9.903	9.960	9.887	9.953	9.940	9.903	9.982
OH <sup>-</sup>		7.647	7.654	8.559	7.977	7.194	7.194	7.783
Fe/Fe+Mg		0.626	0.638	0.650	0.642	0.642	0.622	0.605
Al/Al+Si		0.527	0.535	0.519	0.529	0.516	0.516	0.533

Table 10. (Chlorite analyses, continued).

Location		NS18				NS87		
Analysis	No.	10	11	11	12	14	15	16
	SiO <sub>2</sub>	24.23	23.99	24.52	25.02	25.37	25.10	25.33
	TiO <sub>2</sub>	0.09	0.08	0.07	0.10	0.07	0.06	0.07
	Al <sub>2</sub> O <sub>3</sub>	23.62	23.55	23.34	23.28	22.33	23.07	23.53
	Cr <sub>2</sub> O <sub>3</sub>	0.05	0.07	—	—	—	—	—
	FeO	30.55	30.28	29.42	29.82	29.44	29.58	29.66
	MnO	0.17	0.17	0.12	0.21	0.23	0.18	0.17
	MgO	11.41	11.27	9.85	10.27	9.94	10.39	10.03
	ZnO	0	0	—	—	—	—	—
	CaO	0	0.01	—	—	—	—	—
	Na <sub>2</sub> O	0	0	0.01	0	0.02	0	0
	K <sub>2</sub> O	0	0	0	0	0	0	0
	Sum	90.12	89.42	87.33	88.70	87.40	88.38	88.79
	H <sub>2</sub> O	9.88	10.58	12.67	11.30	12.60	11.62	11.21
	Total	100	100	100	100	100	100	100
Structural Formulae								
IV Site	Si	2.547	2.541	2.643	2.657	2.732	2.672	2.680
	Al	1.453	1.459	1.357	1.343	1.268	1.328	1.320
	Sum	4.000	4.000	4.000	4.000	4.000	4.000	4.000
VI Sites	Fe	2.688	2.685	2.654	2.650	2.653	2.635	2.626
	Mn	0.015	0.015	0.011	0.018	0.022	0.016	0.015
	Mg	1.789	1.781	1.585	1.627	1.596	1.650	1.583
	Zn	0	0	—	—	—	—	—
	Al	1.476	1.484	1.610	1.573	1.568	1.569	1.617
	Cr	0.004	0.006	—	—	—	—	—
	Ti	0.007	0.006	0.006	0.008	0.006	0.004	0.005
	Sum	5.979	5.977	5.866	5.876	5.845	5.874	5.846
	Total	9.979	9.977	9.866	9.976	9.845	9.874	9.846
Alkali	Ca	0	0.001	—	—	—	—	—
Cations	Na	0	0	0.003	0	0.004	0	0
	K	0	0	0	0	0	0	0
	Sum	0	0.001	0.003	0	0.004	0	0
	Total	9.979	9.978	9.868	9.876	9.849	9.874	9.846
	OH <sup>—</sup>	7.100	7.604	9.106	8.121	9.055	8.351	8.056
	Fe/Fe+Mg	0.600	0.601	0.626	0.620	0.624	0.615	0.624
	Al/Al+Si	0.535	0.537	0.529	0.523	0.509	0.520	0.523

Table 10. (Chlorite analyses, continued).

Location		NS87						NS85
Analysis No.		50	51	52	53	54	55	39
	SiO <sub>2</sub>	23.42	23.58	24.29	23.71	22.21	22.26	24.16
	TiO <sub>2</sub>	0.10	0.08	0.06	0.07	0.13	0.09	0.12
	Al <sub>2</sub> O <sub>3</sub>	23.10	22.85	22.25	22.60	22.70	22.83	22.96
	Cr <sub>2</sub> O <sub>3</sub>	0.03	0.07	0.02	0.01	0.10	0.07	0.04
	FeO	31.16	31.57	31.91	32.00	31.30	31.29	29.71
	MnO	0.19	0.23	0.24	0.24	0.27	0.30	0.18
	MgO	11.38	11.38	10.81	10.60	10.71	10.87	12.56
	ZnO	0.01	0.09	0	0.05	0.03	0	0
	CaO	0	0	0.06	0	0	0	0
	Na <sub>2</sub> O	0	0	0	0	0	0	0
	K <sub>2</sub> O	0	0	0.09	0	0	0	0
	Sum	89.39	89.13	89.78	89.28	87.45	87.71	89.73
	H <sub>2</sub> O	10.61	10.87	10.22	10.72	12.55	12.29	10.27
	Total	100	100	100	100	100	100	100
Structural Formulae								
IV Site	Si	2.501	2.532	2.590	2.547	2.442	2.439	2.545
	Al	1.499	1.468	1.410	1.453	1.558	1.561	1.455
	Sum	4.000	4.000	4.000	4.000	4.000	4.000	4.000
VI Sites	Fe	2.785	2.838	2.848	2.876	2.880	2.869	2.619
	Mn	0.018	0.021	0.022	0.022	0.025	0.028	0.016
	Mg	1.813	1.708	1.719	1.698	1.757	1.776	1.973
	Zn	0.001	0.007	0	0.004	0.003	0	0
	Al	1.409	1.426	1.389	1.410	1.436	1.389	1.397
	Cr	0.002	0.006	0.002	0.001	0.009	0.006	0.003
	Ti	0.008	0.006	0.007	0.005	0.011	0.007	0.010
	Sum	6.036	6.012	5.987	6.016	6.121	6.075	6.018
	Total	10.036	10.012	9.987	10.016	10.121	10.075	10.018
Alkali	Ca	0	0	0.007	0	0	0	0
Cations	Na	0	0	0	0	0	0	0
	K	0	0	0.012	0	0	0	0
	Sum	0	0	0.019	0	0	0	0
	Total	10.036	10.012	10.006	10.016	10.121	10.075	10.018
	OH <sup>-</sup>	7.625	7.812	7.345	7.704	9.019	8.832	7.381
	Fe/Fe+Mg	0.606	0.624	0.624	0.629	0.621	0.618	0.570
	Al/Al+Si	0.538	0.533	0.519	0.529	0.551	0.547	0.528

Table 10. (Chlorite analyses, continued).

Location		NS85						
Analysis	No.	40	41	42	43	44	45	46
	SiO <sub>2</sub>	24.10	23.54	24.21	23.85	23.81	23.50	23.95
	TiO <sub>2</sub>	0.11	0.11	0.13	0.10	0.08	0.11	0.10
	Al <sub>2</sub> O <sub>3</sub>	23.14	23.02	22.78	23.17	23.40	22.76	22.31
	Cr <sub>2</sub> O <sub>3</sub>	0.13	0.12	0.04	0.06	0.02	0.04	0.02
	FeO	30.26	30.11	30.14	30.43	29.43	29.71	30.96
	MnO	0.18	0.16	0.17	0.18	0.15	0.22	0.11
	MgO	12.08	11.85	12.01	11.34	11.82	11.52	11.92
	ZnO	0	0	0	0	0	0	0
	CaO	0	0.02	0.01	0.02	0.03	0.04	0.01
	Na <sub>2</sub> O	0	0	0	0.04	0.01	0.02	0
	K <sub>2</sub> O	0	0	0	0	0	0	0
	Sum	90.00	88.93	89.49	89.19	88.75	87.92	89.38
	H <sub>2</sub> O	10.00	11.07	10.51	10.81	11.25	12.08	10.62
	Total	100	100	100	100	100	100	100
Structural Formulae								
IV Site	Si	2.538	2.513	2.563	2.539	2.533	2.535	2.554
	Al	1.462	1.487	1.437	1.461	1.467	1.465	1.446
	Sum	4.000	4.000	4.000	4.000	4.000	4.000	4.000
VI Sites	Fe	2.667	2.690	2.670	2.711	2.620	2.682	2.762
	Mn	0.016	0.015	0.015	0.016	0.013	0.021	0.010
	Mg	1.897	1.887	1.896	1.800	1.875	1.853	1.895
	Zn	0	0	0	0	0	0	0
	Al	1.411	1.411	1.407	1.449	1.469	1.431	1.358
	Cr	0.011	0.010	0.004	0.005	0.002	0.004	0.001
	Ti	0.009	0.009	0.011	0.008	0.007	0.009	0.008
	Sum	6.011	6.022	6.006	5.989	5.986	6.000	6.034
	Total	10.011	10.022	10.006	9.989	9.986	10.000	10.034
Alkali	Ca	0	0.002	0.001	0.002	0.003	0.004	0.001
	Na	0	0	0	0.009	0.001	0.005	0
	K	0	0	0	0	0	0	0
	Sum	0	0.002	0.001	0.011	0.004	0.009	0.001
	Total	10.011	10.024	10.007	10.000	9.990	10.009	10.035
	OH <sup>-</sup>	7.187	7.956	7.553	7.769	8.085	8.682	7.632
	Fe/Fe+Mg	0.584	0.588	0.585	0.601	0.583	0.591	0.593
	Al/Al+Si	0.531	0.536	0.526	0.534	0.537	0.333	0.523

Table 10. (Chlorite analyses, continued).

Location		NS85				NS90		
Analysis No.		47	48	49	50	20	21	22
	SiO <sub>2</sub>	23.20	23.87	23.81	24.17	24.95	25.53	25.00
	TiO <sub>2</sub>	0.13	0.11	0.10	0.08	0.09	0.07	0.10
	Al <sub>2</sub> O <sub>3</sub>	23.32	22.91	22.54	22.91	22.73	21.71	21.94
	Cr <sub>2</sub> O <sub>3</sub>	0.08	0.06	0.02	0	—	—	—
	FeO	30.00	29.86	31.68	31.79	31.76	31.89	31.93
	MnO	0.17	0.19	0.24	0.29	0.15	0.21	0.16
	MgO	12.27	11.75	10.60	10.75	10.05	9.82	9.90
	ZnO	0.01	0	—	—	—	—	—
	CaO	0	0.01	0	0	0	0.01	0.01
	Na <sub>2</sub> O	0	0	—	—	0	0.06	0.03
	K <sub>2</sub> O	0	0	—	—	0	0	0
	Sum	89.18	88.76	88.99	89.99	89.73	89.30	89.07
	H <sub>2</sub> O	10.82	11.24	11.01	10.01	10.27	10.70	10.93
	Total	100	100	100	100	100	100	100
Strucutural Formulae								
IV Site	Si	2.470	2.548	2.561	2.566	2.647	2.725	2.680
	Al	1.530	1.452	1.439	1.434	1.353	1.275	1.320
	Sum	4.000	4.000	4.000	4.000	4.000	4.000	4.000
VI Sites	Fe	2.673	2.667	2.851	2.823	2.820	2.849	2.864
	Mn	0.016	0.017	0.022	0.026	0.014	0.019	0.015
	Mg	1.948	1.870	1.701	1.702	1.591	1.564	1.583
	Zn	0.001	0	—	—	—	—	—
	Al	1.398	1.431	1.419	1.435	1.491	1.458	1.453
	Cr	0.007	0.005	0.001	0	—	—	—
	Ti	0.010	0.009	0.008	0.007	0.007	0.005	0.008
	Sum	6.053	5.999	6.002	5.993	5.923	5.895	5.923
	Total	10.053	9.999	10.002	9.993	9.923	9.895	9.923
Alkali Cations	Ca	0	0.001	0	0	0	0.001	0.001
	Na	0	0	—	—	0	0.013	0.006
	K	0	0	—	—	0	0	0
	Sum	0	0.001	0	0	0	0.014	0.007
	Total	10.053	10.000	10.002	9.993	9.923	9.909	9.930
	OH <sup>—</sup>	7.776	8.078	7.913	7.194	7.381	7.690	7.855
	Fe/Fe+Mg	0.578	0.588	0.626	0.624	0.639	0.646	0.644
	Al/Al+Si	0.542	0.531	0.527	0.528	0.518	0.501	0.509

Table 10. (Chlorite analyses, continued).

Location		NS90					NS71	
Analysis No.		23	24	25	26	27	9	10
SiO <sub>2</sub>		24.97	24.79	24.63	24.91	24.90	22.58	22.79
TiO <sub>2</sub>		0.08	0.06	0.09	0.10	0.07	0.01	0.07
Al <sub>2</sub> O <sub>3</sub>		22.37	22.18	22.73	21.72	22.61	23.33	23.42
Cr <sub>2</sub> O <sub>3</sub>		-	-	-	-	-	-	-
FeO		31.36	32.03	30.82	31.34	30.93	32.90	33.70
MnO		0.17	0.23	0.27	0.12	0.15	0.10	0.06
MgO		9.64	9.55	10.16	10.23	10.53	8.22	7.95
ZnO		-	-	-	-	-	-	-
CaO		0	0	0.02	0	0.02	-	-
Na <sub>2</sub> O		0.02	0.05	0.05	0.06	0.08	-	-
K <sub>2</sub> O		0	0	0	0	0	-	-
Sum		88.61	88.89	88.77	88.48	89.29	87.14	87.99
H <sub>2</sub> O		11.39	11.11	11.23	11.52	10.71	12.86	12.01
Total		100	100	100	100	100	100	100
Structural Formulae								
IV Site	Si	2.680	2.665	2.635	2.682	2.646	2.503	2.508
	Al	1.320	1.335	1.365	1.318	1.354	1.497	1.492
	Sum	4.000	4.000	4.000	4.000	4.000	4.000	4.000
VI Sites	Fe	2.817	2.882	2.760	2.823	2.751	3.050	3.103
	Mn	0.016	0.021	0.025	0.011	0.013	0.009	0.006
	Mg	1.543	1.532	1.622	1.642	1.670	1.359	1.304
	Zn	-	-	-	-	-	-	-
	Al	1.512	1.478	1.503	1.439	1.481	1.552	1.547
	Cr	-	-	-	-	-	-	-
	Ti	0.007	0.005	0.007	0.008	0.006	0.001	0.006
	Sum	5.895	5.918	5.917	5.923	5.921	5.971	5.966
Total		9.895	9.918	9.917	9.923	9.921	9.971	9.966
Alkali Cations	Ca	0	0	0.002	0	0.002	-	-
	Na	0.007	0.011	0.010	0.013	0.017	-	-
	K	0	0	0	0	0	-	-
	Sum	0.007	0.011	0.012	0.013	0.019	-	-
Total		9.902	9.929	9.929	9.936	9.940	9.971	9.966
OH <sup>-</sup>		8.185	7.984	8.071	8.279	7.697	9.264	8.631
Fe/Fe+Mg		0.646	0.653	0.630	0.632	0.622	0.692	0.704
Al/Al+Si		0.514	0.514	0.521	0.507	0.517	0.549	0.548



Table 10. (Chlorite analyses, continued).

Location		NS71						
Analysis No.		11	12	13	14	15	16	17
	SiO <sub>2</sub>	22.62	22.48	21.74	21.94	21.91	22.10	22.80
	TiO <sub>2</sub>	0.06	0.07	0.10	0.04	0.02	0.12	0.09
	Al <sub>2</sub> O <sub>3</sub>	24.06	24.02	23.62	23.63	23.29	23.17	23.91
	Cr <sub>2</sub> O <sub>3</sub>	—	—	—	0.03	0	0.03	0.03
	FeO	33.88	33.56	34.01	33.69	33.40	33.86	33.12
	MnO	0.09	0.05	0.08	0.14	0.13	0.10	0.07
	MgO	7.50	7.78	7.82	8.08	8.23	8.31	8.34
	ZnO	—	—	—	0.08	0.08	0.09	0.08
	CaO	—	—	—	0	0	0	0
	Na <sub>2</sub> O	—	—	—	0.04	0.04	0.01	0.04
	K <sub>2</sub> O	—	—	—	0	0	0	0
	Sum	88.21	87.96	87.37	87.67	87.10	87.79	88.52
	H <sub>2</sub> O	11.79	12.04	12.63	12.33	12.90	12.21	11.48
	Total	100	100	100	100	100	100	100
Structural Formulae								
IV Site	Si	2.483	2.472	2.423	2.436	2.446	2.452	2.489
	Al	1.517	1.528	1.577	1.564	1.554	1.548	1.511
	Sum	4.000	4.000	4.000	4.000	4.000	4.000	4.000
VI Sites	Fe	3.113	3.088	3.172	3.130	3.121	3.144	3.020
	Mn	0.008	0.005	0.007	0.013	0.012	0.009	0.007
	Mg	1.227	1.276	1.300	1.337	1.370	1.375	1.355
	Zn	—	—	—	0.007	0.006	0.007	0.007
	Al	1.599	1.588	1.528	1.530	1.513	1.484	1.562
	Cr	—	—	—	0.003	0	0.003	0.003
	Ti	0.005	0.006	0.008	0.004	0.002	0.010	0.008
	Sum	5.952	5.963	6.015	6.024	6.024	6.032	5.962
	Total	9.952	9.963	10.015	10.024	10.024	10.032	9.962
Alkali	Ca	—	—	—	0	0	0	0
Cations	Na	—	—	—	0.008	0.008	0.001	0.008
	K	—	—	—	0	0	0	0
	Sum	—	—	—	0.008	0.008	0.001	0.008
	Total	9.952	9.963	10.015	10.032	10.032	10.033	9.970
	OH <sup>-</sup>	8.473	8.653	9.077	8.861	9.271	8.775	8.250
	Fe/Fe+Mg	0.717	0.708	0.709	0.701	0.695	0.696	0.690
	Al/Al+Si	0.557	0.558	0.562	0.559	0.556	0.553	0.552

Table 10. (Chlorite analyses, continued).

Location	U01A	Standard	NS118	Standard	NS18	Standard	
N, Averages	8	deviation	4	deviation	11	deviation	
SiO <sub>2</sub>	24.58	0.23	24.39	0.25	24.17	0.81	
TiO <sub>2</sub>	0.10	0.02	0.12	0.04	0.10	0.03	
Al <sub>2</sub> O <sub>3</sub>	24.10	0.31	23.68	0.18	23.43	0.74	
Cr <sub>2</sub> O <sub>3</sub>	0.01	0.02	—	—	0.05	0.02	
FeO	25.44	0.52	25.17	0.21	31.09	0.59	
MnO	0	—	0.01	0.01	0.13	0.06	
MgO	15.40	0.28	14.99	0.10	10.52	0.64	
ZnO	0	—	—	—	0.01	—	
CaO	0	—	—	—	0	—	
Na <sub>2</sub> O	0.02	0.02	—	—	0	—	
K <sub>2</sub> O	0	—	—	—	0	—	
Sum	89.65	0.34	88.36	0.34	89.50	0.60	
H <sub>2</sub> O	10.35	0.34	11.64	0.34	10.50	0.60	
<u>Total</u>	<u>100</u>	—	<u>100</u>	—	<u>100</u>	—	
Structural Formulae							
IV Site	Si	2.526	0.020	2.543	0.018	2.568	0.095
	Al	1.474	0.033*	1.457	0.030*	1.432	0.089*
	Sum	4.000	—	4.000	—	4.000	—
VI Sites	Fe	2.188	0.046	2.196	0.015	2.764	0.062
	Mn	0	—	0.001	0.001	0.011	0.005
	Mg	2.360	0.047	2.331	0.015	1.666	0.094
	Zn	0	—	—	—	0.001	—
	Al	1.447	—	1.455	—	1.504	—
	Cr	0.001	0.001	—	—	0.004	0.002
	Ti	0.008	0.002	0.009	0.003	0.008	0.003
	Sum	6.004	0.018	5.992	0.007	5.958	0.049
	<u>Total</u>	<u>10.004</u>	<u>0.018</u>	<u>9.992</u>	<u>0.007</u>	<u>9.958</u>	<u>0.049</u>
<hr/>							
Alkali	Ca	0	—	—	—	0	—
Cations	Na	0.003	0.003	—	—	0.001	—
	K	0	—	—	—	0	0.001
	Sum	0.003	0.003	—	—	0.001	0.002
	<u>Total</u>	<u>10.007</u>	<u>0.019</u>	<u>9.992</u>	<u>0.007</u>	<u>9.958</u>	<u>0.047</u>
	OH <sup>—</sup>	7.438	0.244	8.365	0.244	7.546	0.431
	Fe/Fe+Mg	0.481	0.009	0.485	0.002	0.624	0.017
	Al/Al+Si	0.536	0.004	0.534	0.004	0.533	0.015

\* Total aluminum.

Table 10. (Chlorite analyses, continued).

Location		NS87	Standard	NS85	Standard	NS90	Standard
N, Averages		11	deviation	12	deviation	8	deviation
SiO <sub>2</sub>		24.07	1.14	23.85	0.30	24.96	0.26
TiO <sub>2</sub>		0.08	0.02	0.11	0.02	0.08	0.01
Al <sub>2</sub> O <sub>3</sub>		22.90	0.41	22.94	0.31	22.25	0.43
Cr <sub>2</sub> O <sub>3</sub>		0.05	0.04	0.05	0.04	—	—
FeO		30.65	1.06	30.34	0.76	31.51	0.47
MnO		0.22	0.05	0.19	0.05	0.19	0.05
MgO		10.57	0.53	11.71	0.58	9.99	0.32
ZnO		0.03	0.04	0	—	—	—
CaO		0.01	0.02	0.01	0.01	0.01	0.01
Na <sub>2</sub> O		0	—	0.01	0.02	0.04	0.03
K <sub>2</sub> O		0.01	0.03	0	—	0	—
Sum		88.59	0.89	89.21	0.59	89.02	0.41
H <sub>2</sub> O		11.41	0.89	10.79	0.59	10.98	0.41
Total		100	—	100	—	100	—
Structural Formulae							
IV Site	Si	2.585	0.099	2.539	0.026	2.670	0.029
	Al	1.415	0.057*	1.461	0.037*	1.330	0.048*
	Sum	4.000	—	4.000	—	4.000	—
VI Sites	Fe	2.756	0.111	2.703	0.073	2.821	0.046
	Mn	0.020	0.005	0.017	0.004	0.017	0.005
	Mg	1.683	0.080	1.858	0.084	1.593	0.048
	Zn	0.003	0.003	0	—	—	—
	Al	1.491	—	1.418	—	1.477	—
	Cr	0.004	0.003	0.004	0.004	—	—
	Ti	0.007	0.002	0.009	0.001	0.007	0.001
	Sum	5.964	0.100	6.009	0.020	5.915	0.012
	Total	9.964	0.100	10.009	0.020	9.915	0.012
Alkali	Ca	0.001	0.002	0.001	0.001	0.001	0.001
Cations	Na	0.001	—	0.001	0.003	0.010	0.005
	K	0.001	0.003	0	—	0	—
	Sum	0.003	0.006	0.002	0.004	0.011	0.006
	Total	9.967	0.103	10.011	0.018	9.926	0.013
	OH <sup>-</sup>	8.200	0.640	7.754	0.423	7.891	0.295
	Fe/Fe+Mg	0.621	0.006	0.593	0.017	0.639	0.010
	Al/Al+Si	0.529	0.012	0.531	0.005	0.513	0.007

\* Total aluminum.

Table 10. (Chlorite analyses, continued).

	NS71 9	Standard deviation	Grand Average,	N=46**	Standard deviation
SiO <sub>2</sub>	22.33	0.41	24.15		0.28
TiO <sub>2</sub>	0.06	0.04	0.10		0.01
Al <sub>2</sub> O <sub>3</sub>	23.61	0.33	23.31		0.51
Cr <sub>2</sub> O <sub>3</sub>	0.02	0.02	0.03		0.02
FeO	33.57	0.37	29.29		2.96
MnO	0.09	0.03	0.13		0.10
MgO	8.03	0.28	12.08		2.39
ZnO	0.08	0.01	0.01		0.01
CaO	0	-	0.01		0.01
Na <sub>2</sub> O	0.03	0.02	0.01		0.01
K <sub>2</sub> O	0	-	0	Ideal	-
Sum	87.92	0.48	89.14	88.87	0.56
H <sub>2</sub> O	12.18	0.48	10.86	11.13	0.56
Total	100	-	100		-
Structural Formulae					
IV Site	Si	2.468	0.030	2.555	0.023
	Al	<u>1.532</u>	0.033*	<u>1.445</u>	0.021*
	Sum	4.000	-	4.000	-
VI Sites	Fe	3.105	0.047	2.597	0.302
	Mn	0.008	0.003	0.012	0.009
	Mg	1.323	0.050	1.899	0.343
	Zn	0.007	0.001	0.001	0.001
	Al	1.545	-	1.464	-
	Cr	0.002	0.002	0.003	0.002
	Ti	<u>0.006</u>	0.003	<u>0.008</u>	0.001
	Sum	<u>5.996</u>	0.033	<u>5.984</u>	0.023
	Total	9.996	0.033	9.984	0.023
Alkali	Ca	0	-	0.001	0.001
Cations	Na	0.006	0.004	0.001	0.001
	K	<u>0</u>	-	<u>0</u>	-
	Sum	<u>0.006</u>	0.004	<u>0.002</u>	0.001
	Total	10.002	0.034	9.986	0.024
	OH <sup>-</sup>	8.753	0.345	7.805	8.000
	Fe/Fe+Mg	0.701	0.009	0.578	0.072
	Al/Al+Si	0.555	0.005	0.532	0.003

\*\* Excludes samples NS90 and NS71, which have anomalous Al/Al+Si ratios.

\* Total aluminum.

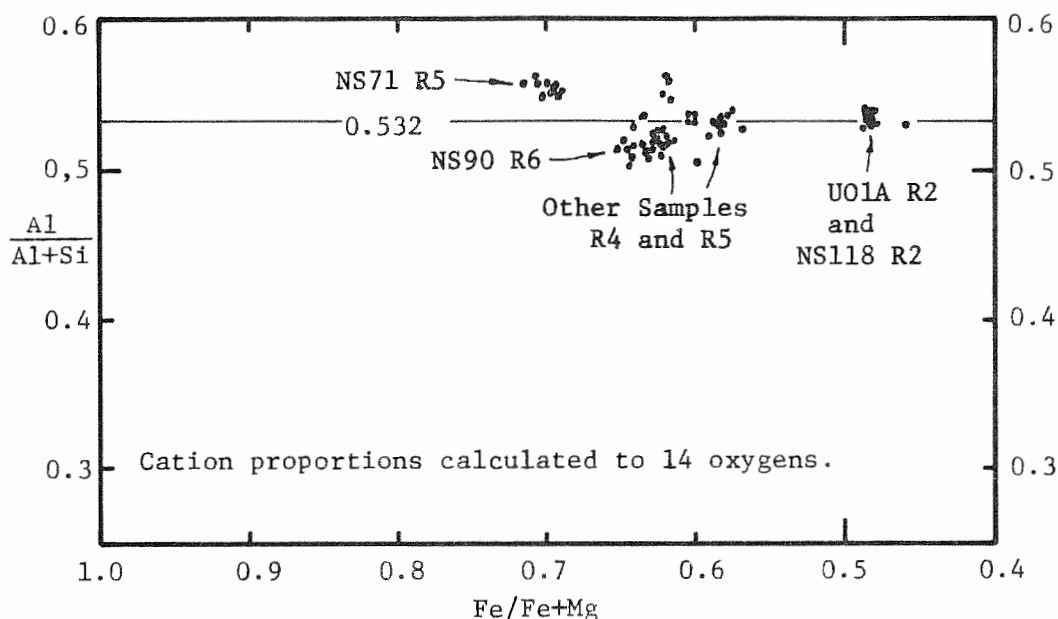


Figure 17. All chlorite data with Al/Al+Si ratios plotted versus Fe/Fe+Mg ratios. The trend toward higher iron compositions with retrograding is well developed.

line at  $Al/Al+Si = 0.532$ , constrained by muscovite-garnet-biotite-chlorite four phase volumes in AKFM space. Data from sample NS90 are at lower aluminum compositions because of chlorite-muscovite-K-feldspar tie plane constraints. Sample NS71 is constrained to higher aluminum and iron compositions than other samples by chloritoid and very pyrope-poor garnet.

Titanium and zinc display no trend with retrograding; zinc in part due to very low quantities detected and in part due to lack of data. The low values do support the trend for Zn/Fe ratios: chlorite < biotite < muscovite, as has been found in prograde rocks (Albee, 1972). Manganese shows a relatively strong trend from zero in sample UO1A to about 0.2% in the most severely retrograded rocks,

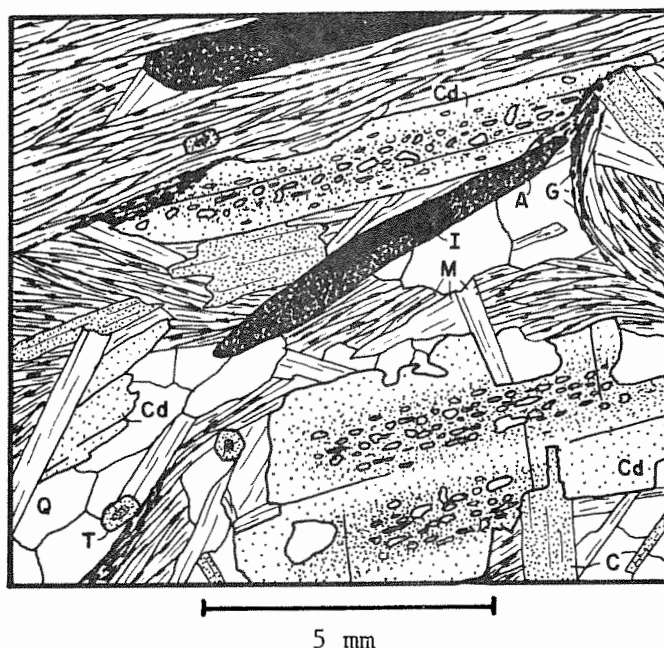
well above the detection limits of the electron microprobe. The trend parallels the biotite Mn enrichment trend caused by manganese released during garnet breakdown. Mn abundance also supports the finding of Thompson (1976b) that Mn/Mn+Fe+Mg ratios in chlorite are greater than in coexisting biotite, although this is puzzling in that Fe/Fe+Mg ratios show the opposite trend.

### Chloritoid

Field occurrence. Chloritoid is very rare in the study area, only occurring in certain parts of outcrop NS71 in zone R5. Chloritoid is almost certainly of retrograde origin with an obscure paragenesis, as will be discussed below. Although chloritoid itself has not been identified in hand specimen, the rock it resides in is dark gray due to graphite, and has a pronounced muscovite foliation. The rock has been severely deformed by crenulations of probable retrograde origin. Biotite is present only in certain parts of the outcrop, separate from those parts containing chloritoid. No feldspar was seen either in thin section or at the outcrop. Garnets are rare with thick chlorite rims (zone R5).

Appearance in thin section. The chloritoid is biaxial positive with a 2V of about 50°, and strong  $r > v$  dispersion. It is pleochroic with the absorption scheme: X = pale green, Y = pale blue, Z = pale yellow. It is not clear if the chloritoid in this sample is monoclinic or triclinic (Halferdahl, 1961)

Chloritoid forms flat plates, subhedral on 001, and rarely exceeds 1.5 mm in width and 0.2 mm in thickness. The plates have tapered or beveled edges as seen perpendicular to the C-axis. Looking perpendicular to 001, the plates are irregular in outline with some tendency towards crystal faces on 110 (Figure 18).



A = Anatase	G = Graphite	Q = Quartz
C = Chlorite	I = Ilmenite	T = Tourmaline
Cd = Chloritoid	M = Muscovite	

Figure 18. Composite drawing showing habit of chloritoid in sample NS71. As is shown, chloritoid may occur in various orientations with respect to the main foliation, and is rife with quartz inclusions. Cleavage cracks on 001 and 110 are commonly displayed. Note that chlorite and muscovite are common, but biotite and feldspar do not occur with chloritoid. Ilmenite is partially altered to anatase.

Lamellar twinning on 001 is very common. 001 cleavage is fairly well developed and 110 cleavage is also present (after Heinrich, 1969).

Chloritoid plates are found in all orientations but are most commonly sub-parallel to the foliation. The plates may have been rotated into alignment with the foliation by deformation during retrograde metamorphism. Inclusions of quartz and graphite are extremely common. Quartz is typically concentrated in the crystal cores, whereas graphite commonly follows the pattern set in the surrounding matrix.

Chemistry. Chloritoid was found not to be zoned, so only a sample average is given (Table 11). The structural formula (after Brindley and Harrison, 1952; Harrison and Brindley, 1957; Deer et al., 1976; Ribbe, 1980a) was calculated on a basis of 12 oxygens and two  $H_2O$ . Because there is no zoning or other chloritoid localities in the study area, little can be said about substitutions or chemical trends. Chloritoid is one of the most iron-rich silicates in the New Salem area, second only to garnet in the same sample. It has several times more zinc than coexisting muscovite, the only other zinc-bearing mineral. Chloritoid contains much more manganese than chlorite, and much less than coexisting ilmenite or garnet. The amounts of titanium and chromium are vanishingly small, and calcium and the alkalis were not detected in any analysis.

#### Plagioclase

Field appearance. Sodic feldspar is a relatively common mineral in the Littleton Formation in the New Salem area. It is a mineral of prograde origin that apparently was unaffected by retrograde



Table 11. Average probe analysis of chloritoid. Core and rim analyses were used for the average, and chloritoid was not found to be chemically zoned. Cation proportions were calculated on a basis of the formula;  $(\text{Fe,Mg})_2\text{Al}_3\text{Al}(\text{Si}_4\text{O}_{10})(\text{OH})_4$ , containing 12 oxygens plus two  $\text{H}_2\text{O}$ .  $\text{OH}^-$  proportions were calculated from  $\text{H}_2\text{O}\%$  on a basis of 14 oxygens.

		Average N=10	Standard deviation	
	$\text{SiO}_2$	24.05	0.35	
	$\text{TiO}_2$	0.03	0.03	
	$\text{Al}_2\text{O}_3$	41.29	0.22	
	$\text{Cr}_2\text{O}_3$	0.02	0.02	
	$\text{FeO}$	25.52	0.23	
	$\text{MnO}$	0.41	0.07	
	$\text{MgO}$	1.65	0.07	
	$\text{ZnO}$	0.09	0.05	
	$\text{CaO}$	0	-	
	$\text{Na}_2\text{O}$	0	-	
	$\text{K}_2\text{O}$	0	Ideal	-
	Sum	93.06	92.82	0.48
	$\text{H}_2\text{O}$	6.94	7.18	0.48
	Total	100		
Structural Formula				
Si IV Site	Si	1.985	0.022	
	Al	0.015	-	
	Sum	2.000	-	
Small Al VI Site	Al	3.000	0.025 (total Al)	
Large Al VI Site	Al	0.999	-	
	Cr	0.001	0.001	
	Sum	1.000	-	
Large M <sup>+2</sup> VI Site	Fe	1.763	0.016	
	Mn	0.029	0.005	
	Mg	0.203	0.008	
	Zn	0.005	0.003	
	Al	0.006	-	
	Ti	0.002	0.002	
	Sum	2.008	0.018	
	Total	8.008	0.013	
	$\text{OH}^-$	3.917	4.000	0.270
	$\frac{\text{Fe}}{\text{Fe+Mg}}$	0.897	0.004	

metamorphism. Plagioclase grains in some hand specimens are white, anhedral, equant to elongate, and up to 3 mm long and 1.5 mm thick. The white, cloudy to opaque appearance is due to abundant quartz inclusions and distinguishes the feldspar from the darker-appearing transparent matrix quartz. Some specimens, however, contain small ( $\approx 1$  mm) plagioclase crystals deficient in inclusions, and are not distinguishable in hand specimen from quartz.

Appearance in thin section. The sodic feldspar is all optically biaxial positive with very large  $2V$ 's. Indices of refraction are almost always less than quartz. The crystals have two cleavage sets, and birefringence is up to first order white. Twinning is rare.

The largest plagioclase grains are the white crystals identifiable in hand specimen, which range up to about 3 mm in length, are anhedral to subhedral, and are commonly somewhat elongated (Figures 10b to 10d; found in the analyzed samples NS118, NS18, and NS87). Plagioclase grains occur singly or in aggregates of two or three crystals that are filled with quartz inclusions, which gives them a characteristic white appearance in hand specimen. Inclusions of graphite are common, and inclusions of muscovite, ilmenite, and zircon are also found. Optically distinguishable chemical zoning is common, typically from calcic cores to slightly more sodic rims.

The second plagioclase habit is as small, irregular, nearly inclusion-free and virtually unzoned grains, rarely up to 1 mm in length. This type of plagioclase is present in the analyzed samples U01A and NS85, but cannot be identified in hand specimen. In thin

section it must be identified by more subtle properties than gross habit, such as cleavage, low relief relative to quartz, and crystal outline. No plagioclase intergrowths with sheet silicates or distinct rims were seen, as could develop if plagioclase were produced in retrograde metamorphic reactions.

Chemistry. All plagioclase in the analyzed samples is chemically simple. Table 12 contains analytical data for the sodic feldspars in the analyzed samples. For each sample is listed the range of An, Ab, and Or compositions observed. In every case the more sodic end of the range is the rim composition, and the more calcic end is the core composition. The sodic feldspars contain no barium, and only very small quantities of potassium that does not vary within analytical uncertainty. The very small amount of solid solution toward K-feldspar in plagioclase coexisting with muscovite is common in medium grade metamorphic rocks (Evans and Guidotti, 1966; Thompson, et al., 1977; Tracy, 1978; Cheney and Guidotti, 1979; Labotka, 1980). The range in anorthite content is from 0.8 to 13.0%, all analyses inclusive. Zoning from calcic cores to sodic rims over a range of 5 or 6 An% is found only in the cloudy plagioclase in samples NS118, NS18, and NS87. The clear, inclusion-deficient feldspars in samples U01A and NS85 are virtually unzoned within analytical uncertainty.

The presence of zoned or unzoned plagioclase is without apparent regard to degree of retrograding. This is evidence supporting optical evidence that plagioclase is only a product of prograde

Table 12. Averaged electron microprobe analyses of sodic feldspars from various samples. The feldspars are commonly zoned with sodic rims and more calcic cores and are probably best represented in the ranges of albite-anorthite compositions listed below each sample average. The variation in potassium content is not significant.

Location		U01A	Standard	NS118	Standard	NS18	Standard
N, Averages		5	deviation	5	deviation	5	deviation
Feldspar type		clear		white		white	
	SiO <sub>2</sub>	67.24	0.78	67.43	0.62	66.31	0.52
	Al <sub>2</sub> O <sub>3</sub>	21.17	0.25	20.69	0.48	20.75	0.43
	CaO	1.87	0.07	0.71	0.36	1.73	0.49
	BaO	0	-	0	-	0	-
	Na <sub>2</sub> O	10.87	0.23	11.30	0.32	10.82	0.21
	K <sub>2</sub> O	0.07	0.01	0.03	0.01	0.07	0.01
	<u>Total</u>	<u>101.22</u>	<u>0.54</u>	<u>100.15</u>	<u>0.20</u>	<u>99.68</u>	<u>0.48</u>
Structural Formulae							
IV Site	Si	2.915	0.016	2.944	0.021	2.919	0.022
	Al	<u>1.082</u>	0.016	<u>1.065</u>	0.023	<u>1.077</u>	0.021
	Sum	3.997	0.004	4.009	0.005	3.996	0.002
A Site	Ca	0.087	0.003	0.033	0.017	0.082	0.023
	Ba	0	-	0	-	0	-
	Na	0.914	0.024	0.958	0.029	0.924	0.020
	K	<u>0.004</u>	0.001	<u>0.002</u>	0.001	<u>0.004</u>	0.001
	Sum	<u>1.005</u>	0.022	<u>0.993</u>	0.021	<u>1.010</u>	0.008
	<u>Total</u>	<u>5.002</u>	<u>0.020</u>	<u>5.002</u>	<u>0.017</u>	<u>5.006</u>	<u>0.007</u>
Albite %		90.9%	2.4	96.5%	2.9	91.5%	2.0
Range		90.5-91.5		94.0-99.1		88.0-94.4	
Anorthite %		8.7%	0.3	3.3%	1.7	8.1%	2.3
Range		8.2-9.1		0.8-5.7		5.3-11.5	
K-feldspar %		0.4%	0.1	0.2%	0.1	0.4%	0.1
Range		<u>0.3-0.4</u>		<u>0.1-0.3</u>		<u>0.3-0.5</u>	
Total		100%	-	100%	-	100%	-

Table 12. (Continued).

Location		NS87		NS85		All Plagioclase	
N, Averages		5	Standard deviation	5	Standard deviation	25	Standard deviation
Feldspar type		white		clear			
	SiO <sub>2</sub>	66.50	0.77	64.16	0.34	66.33	1.30
	Al <sub>2</sub> O <sub>3</sub>	20.80	0.66	22.21	0.31	21.12	0.64
	CaO	0.96	0.49	2.68	0.04	1.59	0.52
	BaO	0	-	0	-	0	-
	Na <sub>2</sub> O	10.90	0.49	10.03	0.24	10.78	0.46
	K <sub>2</sub> O	0.06	0.01	0.08	0.01	0.06	0.02
	<u>Total</u>	<u>99.22</u>	1.16	<u>99.16</u>	0.62	<u>99.88</u>	0.85
Structural Formulae							
IV Site	Si	2.932	0.034	2.847	0.012	2.911	0.038
	Al	<u>1.082</u>	0.038	<u>1.162</u>	0.012	<u>1.094</u>	0.039
	Sum	4.014	0.009	4.009	0.003	4.005	0.008
A Site	Ca	0.045	0.023	0.127	0.002	0.075	0.037
	Ba	0	-	0	-	0	-
	Na	0.933	0.042	0.864	0.019	0.919	0.035
	K	<u>0.003</u>	-	<u>0.004</u>	0.001	<u>0.003</u>	0.001
	Sum	<u>0.981</u>	0.030	<u>0.995</u>	0.018	<u>0.997</u>	0.011
	<u>Total</u>	<u>4.995</u>	0.020	<u>5.004</u>	0.016	<u>5.002</u>	0.004
Albite %		95.1%	4.3	86.8%	1.9	92.2%	2.8
Range		91.9-97.6		86.5-87.5		86.5-99.1	
Anorthite %		4.6%	2.4	12.8%	0.2	7.5%	1.1
Range		2.1-7.7		12.1-13.0		0.8-13.0	
K-feldspar %		0.3%	-	0.4%	0.1	0.3%	-
Range		<u>0.3-0.4</u>		<u>0.4-0.5</u>		<u>0.1-0.5</u>	
Total		100%	-	100%	-	100%	-

metamorphism and was not produced during retrograde metamorphism.

It is interesting to note that although many analyses fall into the range of peristerite unmixing (Smith, 1975), no evidence of exsolution textures was seen.

### K-feldspar

Occurrence. Potassium feldspar is a relatively common product of retrograde metamorphism in the New Salem area. It has not been identified in the field because of the extremely small crystal size. It can be seen on slabbed surfaces of sample NS90, occurring as tiny white lenses and irregular patches within chlorite.

K-feldspar commonly appears in thin section as small, thin, lens-shaped grains up to about 100  $\mu\text{m}$  wide and 20  $\mu\text{m}$  thick, within and parallel to the cleavage of large biotite crystals. K-feldspar grains, when small, are typically isolated from all other minerals except biotite and its inclusions. Examples of this most common habit may be seen in Figures 10d and 12. In some rocks, particularly in zones R5 and R6 with little remaining biotite, K-feldspar touches other minerals outside of the host biotite, including quartz, muscovite, chlorite, and albite. With the trend of decreasing quantities of biotite and increasing modal K-feldspar, the lenses increase in size and abundance, and in many cases have coalesced into polycrystalline masses of K-feldspar up to 1 mm across occur, still retaining textural evidence of having developed as lenses within biotite crystals.

The optical properties of K-feldspar were very difficult to determine, in part because of the small size of the crystals, and because of the very peculiar mottled appearance of the grains under crossed nicols. Each lens of K-feldspar is commonly divided into several domains with indistinct boundaries and slightly differing birefringence. This indicates that each lens is in fact made up of several tiny crystals. No cleavages are visible in any K-feldspar grain. The optical evidence, while poor, indicates that K-feldspar is optically negative with a 2V variable from zero to about 30 or 40°. The mineral is therefore probably sanidine.

The presence of coexisting K-feldspar-chlorite+~~muscovite~~+~~albite~~+~~biotite~~+zeolite in zeolite and lower greenschist facies metamorphic rocks and hydrothermally altered rocks is rather common (Coombs, 1954; Chayes, 1955; Zen, 1960; Fawcett, 1963; Harrison and Campbell, 1963; Velde, 1965; McNamara, 1966; Albee, 1968; Coombs et al., 1970; Mather, 1970; Boles and Coombs, 1977; Ferry, 1978). The significance of coexisting K-feldspar and chlorite in the New Salem area is that it is the best evidence for low temperatures during retrograde metamorphism. This is in contrast to less severely retrograded terranes not containing K-feldspar-chlorite assemblages that could have developed at temperatures not far below prograde temperatures (Billings, 1937; Thompson et al., 1977).

Chemistry. Table 13 is a listing of analyses of K-feldspar from three of the samples containing that mineral. A fourth sample, NS87, was found to contain K-feldspar by its habit and characteristic pale blue-

Table 13. Averaged electron microprobe analyses of K-feldspar from various samples. Cation proportions were calculated on a basis of the formula  $KAlSi_3O_8$ , containing 8 oxygens. Sample NS87 also contains K-feldspar, but the grains were too small to analyze. Variations in composition between single analyses and whole samples were not significant.

Location	U01A	NS118		NS90		
N, Averages	5	Standard deviation	5	Standard deviation	5	Standard deviation
SiO <sub>2</sub>	64.55	0.20	63.84	0.45	64.70	0.47
Al <sub>2</sub> O <sub>3</sub>	18.59	0.15	18.38	0.22	18.26	0.09
CaO	0	-	0	-	0	-
BaO	0.02	0.02	0.15	0.07	0.26	0.06
Na <sub>2</sub> O	0.07	0.02	0.04	0.02	0.07	0.02
K <sub>2</sub> O	16.43	0.29	16.59	0.13	16.32	0.22
<u>Total</u>	<u>99.66</u>	0.43	<u>99.00</u>	0.63	<u>99.61</u>	0.68
Structural Formulae						
IV Site Si	2.992	0.006	2.989	0.012	3.004	0.003
Al	<u>1.016</u>	0.006	<u>1.015</u>	0.012	<u>1.000</u>	0.004
Sum	4.008	0.004	4.004	0.006	4.004	0.002
A Site Ca	0	-	0	-	0	-
Ba	0	-	0.003	0.001	0.005	0.001
Na	0.006	0.002	0.004	0.002	0.006	0.002
K	<u>0.977</u>	0.016	<u>0.992</u>	0.020	<u>0.971</u>	0.009
Sum	<u>0.983</u>	0.016	<u>0.999</u>	0.020	<u>0.982</u>	0.007
<u>Total</u>	<u>4.991</u>	0.012	<u>5.003</u>	0.016	<u>4.986</u>	0.005
Albite %	0.6%	0.2	0.4%	0.1	0.6%	0.1
Celsian %	0	-	0.3%	0.2	0.5%	0.2
K-feldspar %	<u>99.4%</u>	1.6	<u>99.3%</u>	2.0	<u>93.9%</u>	0.9
Total	<u>100%</u>	-	<u>100%</u>	-	<u>100%</u>	-



Table 13. (K-feldspar analyses, continued).

All K-feldspar		
N, Averages	15	Standard deviation
SiO <sub>2</sub>	64.36	0.45
Al <sub>2</sub> O <sub>3</sub>	18.41	0.17
CaO	0	-
BaO	0.14	0.12
Na <sub>2</sub> O	0.06	0.02
K <sub>2</sub> O	16.45	0.14
<u>Total</u>	<u>99.42</u>	0.37
Structural Formulae		
IV Site Si	2.995	0.008
Al	<u>1.010</u>	0.009
Sum	4.005	0.002
A Site Ca	0	-
Ba	0.004	0.003
Na	0.005	0.001
K	<u>0.980</u>	0.011
<u>Sum</u>	<u>0.989</u>	0.010
Total	4.993	0.009
Albite %	0.5%	0.1
Celsian %	0.4%	0.3
K-feldspar %	<u>99.1%</u>	0.3
	100%	-

green fluorescence under electron beam excitation. The exposed feldspar surface is too small to analyze in this case. As can be seen in Table 13, K-feldspar chemistry is very simple. Only trace quantities of albite and celsian components are in solid solution with sanidine, and variations in composition are within analytical uncertainty. No calcium was detected. The small amount of solid solution toward albite in plagioclase-bearing rocks could indicate very low temperatures at the time of retrograde metamorphism, or disequilibrium with respect to plagioclase.

### Ilmenite

Occurrence and habit. Ilmenite is the only oxide mineral of prograde origin in the study area. Ilmenite is rarely visible in hand samples of fine-grained rocks as thin, black plates up to 2 mm across. Ilmenite occurs in various habits and is found to be both prograde and retrograde in origin.

In reflected light, all ilmenite is bireflectant pale tan to pale pinkish tan in air, and tan to light pinkish brown under oil. No difference in color or reflectivity can be seen between parts of single grains, grains of different origin, or grains from different samples.

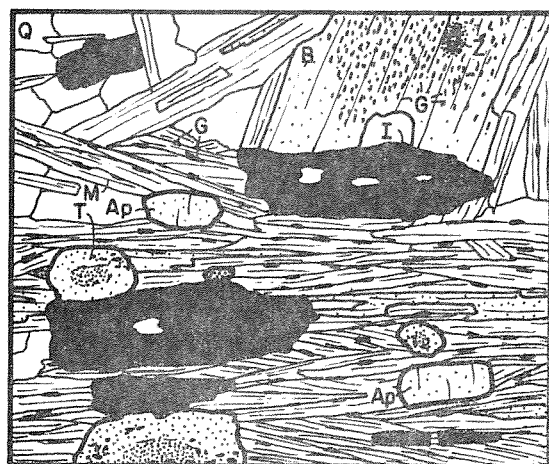
The most common habit of ilmenite of prograde origin is as plates, two to five times as wide as they are thick, oriented parallel to the foliation, and ranging up to about 2 mm in width. The grains are flattened on 0001 with blunt, somewhat irregular edges

and poorly developed prism faces. Spherical to sub-rounded inclusions of quartz are common, and inclusions of muscovite are rare. Ilmenite is included in a variety of minerals, particularly staurolite and garnet. Examples of large, platy prograde ilmenite can be seen in Figures 8a and 8b, 10a to 10d, 18, and 19a and 19d. Note the presence of quartz inclusions that penetrate the entire oxide grain thickness in thin section. Figure 19b is a drawing of an ilmenite crystal seen in reflected light. Note the abundance of rounded quartz inclusions and the lack of alteration to anatase. Many drawings of minerals in this section show some ilmenite partly altered to anatase, as will be discussed in the next section.

In the southern part of the field area ilmenite plates tend to be thinner and more tapered at the edges (Figure 19c). In rocks strongly deformed during the retrograde episode, ilmenite plates of the thin type were more susceptible to bending and breaking than the more stubby plates, as shown in Figure 19c.

Ilmenite was also produced during retrograde metamorphism from titanium released by altering biotite (Figure 19d, same as Figure 12). In contrast to the large quartz-bearing plates of prograde origin, retrograde ilmenite contains no quartz inclusions, rarely exceeds 0.2 mm in maximum dimension, and is interstitial to the sheet silicates. It appears that ilmenite (rarely rutile) is the mineral sink for titanium released from altering biotite, rather than anatase.

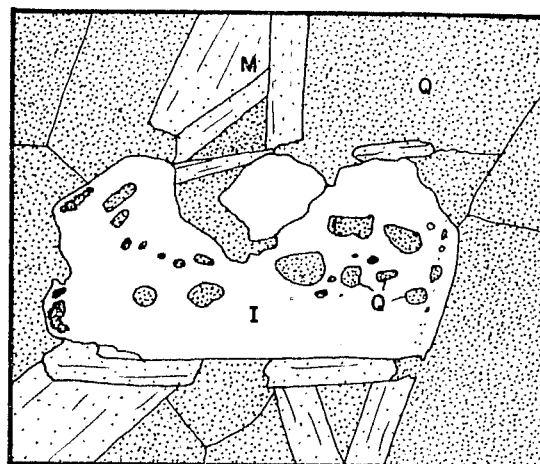
Chemistry. Ilmenite is surprisingly varied in composition between samples, but homogenous in any one sample. For each average probe



UO1A

0.2 mm

(a)



(b)

0.2 mm

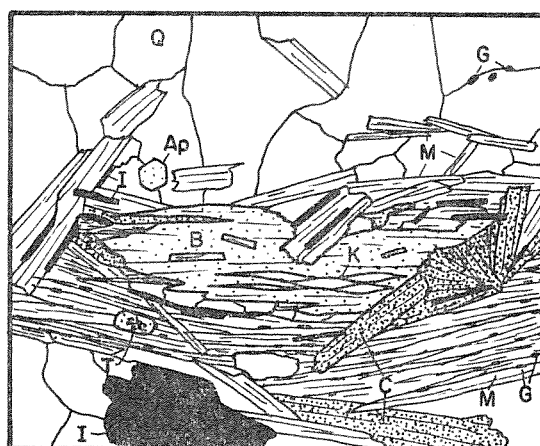
NS74



NS105

0.2 mm

(c)



(d)

1 mm

NS111

A = Anatase  
Ap = Apatite  
B = Biotite  
C = Chlorite

G = Graphite  
I = Ilmenite  
K = K-feldspar  
M = Muscovite

Q = Quartz  
T = Tourmaline  
Z = Zircon

Figure 19. Drawings of ilmenite in thin section. a) Large, thick ilmenite plates of prograde origin, parallel to the foliation. Note quartz inclusions. b) Drawing of ilmenite in reflected light, showing the abundant rounded quartz inclusions. c) Large, thin, tapered ilmenite plates of prograde origin. Ilmenite is partially altered to anatase, and is severely deformed in crenulation folds. d) Small ilmenite plates of retrograde origin, precipitated from titanium released from altering biotite. Also present is a large grain of prograde origin.

analysis (Table 14) there are two columns. The first column was calculated in the normal manner, with all Fe as FeO. The second column was recalculated to gain insight into possible hematite solid solution.

The major variation in composition is in the pyrophanite component; from 0.3 to 0.8% in samples containing garnet, staurolite, and biotite, to about 3 or 4% in samples containing partially altered biotite and garnet, and about 8% in sample NS90 which contains only replacements after staurolite, biotite, garnet, and all but traces of ilmenite. This general trend in ilmenite manganese content is caused primarily by Mn released during garnet breakdown, manganese being strongly partitioned into ilmenite over the sheet silicates. In sample NS90, more than 95% of the ilmenite has been replaced by anatase, and the single analyzed grain (Figure 20) comprises about half of all ilmenite remaining in the thin section. That ilmenite grain is remarkable, containing about 20 times the concentration of MnO as coexisting chlorite. Concentrations of Cr, Mg, and Zn are at or below instrumental detection limits, and are of trivial importance.

Hematite component, calculated on a basis of cation stoichiometry, is in excellent agreement with respect to balanced site occupancies and oxide weight percent totals. Hematite is therefore apparently in solid solution with ilmenite to the extent of about 2% (except for 0.7% in sample NS71). This is much too low for ilmenite to coexist with magnetite in medium-grade schists

Table 14. Averages of electron microprobe analyses of ilmenite from various samples. For each sample there are two columns. The first column contains the oxide weight percent and structural formulae based on the formula unit  $(\text{Fe,Mn})\text{TiO}_3$  containing three oxygens, with all iron as  $\text{Fe}^{+2}$ . The second column contains oxide weight percent and structural formulae recalculated on a basis of two cations to include  $\text{Fe}^{+3}$ . The consistently high cation totals in all 80 analyses indicate that  $\text{Fe}^{+3}$  is present in small quantities and that the second column in each case is more representative of actual mineral compositions and structural formulae.

Locality	U01A		Standard		NS118		Standard	
N, Averages	10		deviation		10		deviation	
$\text{TiO}_2$	51.49	51.49	0.19		51.56	51.56	0.23	
$\text{Al}_2\text{O}_3$	0	0	-		0	0	-	
$\text{Cr}_2\text{O}_3$	0.01	0.01	0.01		0	0	-	
$\text{Fe}_2\text{O}_3$	-	2.21	-		0	2.53	-	
$\text{FeO}$	47.91	45.92	0.25		48.38	46.10	0.30	
$\text{MnO}$	0.35	0.35	0.09		0.14	0.14	0.04	
$\text{MgO}$	0	0	-		0.06	0.06	0.05	
$\text{ZnO}$	0	0	-		0	0	-	
Total	99.76	99.98	0.29		100.14	100.39	0.51	
Structural Formulae								
Ti Site	Ti	0.986	0.979	0.003	0.984	0.976	0.002	
	$\text{Fe}^{+3}$	-	0.021	-	-	0.024	-	
	Cr	0	0	-	0	0	-	
	Sum	0.986	1.000	0.003	0.984	1.000	0.002	
Fe Site	$\text{Fe}^{+3}$	-	0.021	-	-	0.024	-	
	$\text{Fe}^{+2}$	1.020	0.971	0.005	1.027	0.971	0.003	
	Mn	0.008	0.008	0.002	0.003	0.003	0.001	
	Mg	0	0	-	0.002	0.002	0.002	
	Zn	0	0	-	0	0	-	
	Sum	1.028	1.000	0.006	1.032	1.000	0.003	
Total		2.015	2.000	0.005	2.016	2.000	0.002	
Hematite %	-	2.1	-		-	2.4	-	
Ilmenite %	99.2	97.1	0.5		99.5	97.1	0.3	
Pyrophanite %	0.8	0.8	0.2		0.3	0.3	0.1	
Other	0	0	-		0.2	0.2	0.2	
Total	100%	100%	-		100%	100%	-	

Table 14. (Ilmenite analyses, continued).

Locality	NS18		Standard deviation		NS87		Standard deviation	
N, Averages	10		10		10		10	
TiO <sub>2</sub>	51.83	51.83	0.17		51.76	51.76	0.27	
Al <sub>2</sub> O <sub>3</sub>	0	0	-		0	0	-	
Cr <sub>2</sub> O <sub>3</sub>	0.01	0.01	0.02		0	0	-	
Fe <sub>2</sub> O <sub>3</sub>	-	1.69	-		-	1.90	-	
FeO	46.74	45.22	0.75		46.28	44.57	0.35	
MnO	1.34	1.34	0.04		1.96	1.96	0.09	
MgO	0	0	-		0.02	0.02	0.02	
ZnO	0.02	0.02	0.01		0.04	0.04	0.04	
Total	99.94	100.11	0.87		100.06	100.25	0.38	
Structural Formulae								
Ti Site Ti	0.989	0.984	0.004		0.987	0.981	0.003	
Fe <sup>+3</sup>	-	0.016	-		-	0.019	-	
Cr	0	0	-		0	0	-	
Sum	0.989	1.000	0.004		0.987	1.000	0.003	
Fe Site Fe <sup>+3</sup>	-	0.016	-		-	0.017	-	
Fe <sup>+2</sup>	0.992	0.955	0.008		0.982	0.939	0.005	
Mn	0.029	0.029	0.001		0.042	0.042	0.002	
Mg	0	0	-		0.001	0.001	0.001	
Zn	0	0	-		0.001	0.001	0.001	
Sum	1.021	1.000	0.010		1.026	1.000	0.005	
Total	2.010	2.000	0.005		2.013	2.000	0.003	
Hematite %	-	1.6	-		-	1.7	-	
Ilmenite %	97.1	95.5	0.8		95.6	93.9	0.5	
Pyrophanite %	2.9	2.9	0.1		4.2	4.2	0.2	
Other %	0	0	-		0.2	0.2	0.2	
Total	100%	100%			100%	100%		

Table 14. (Ilmenite analyses, continued).

Locality		NS85		Standard deviation	NS90		Standard deviation
N, Averages		7			10		
TiO <sub>2</sub>		51.12	51.12	0.18	51.58	51.58	0.28
Al <sub>2</sub> O <sub>3</sub>		0	0	-	0	0	-
Cr <sub>2</sub> O <sub>3</sub>		0.02	0.02	0.02	0.04	0.04	0.02
Fe <sub>2</sub> O <sub>3</sub>		-	2.94	-	-	2.33	-
FeO		47.30	44.65	0.21	44.85	42.75	0.53
MnO		1.32	1.32	0.05	3.76	3.76	0.23
MgO		0.02	0.02	0.02	0.01	0.01	0.01
ZnO		0.06	0.06	0.06	0.04	0.04	0.04
<u>Total</u>		<u>99.84</u>	<u>100.13</u>	<u>0.34</u>	<u>100.28</u>	<u>100.51</u>	<u>0.48</u>
Structural Formulae							
Ti Site	Ti	0.980	0.971	0.001	0.985	0.978	0.003
	Fe	-	0.029	-	-	0.022	-
	Cr	0	0	-	0	0	-
	Sum	<u>0.980</u>	<u>1.000</u>	0.001	<u>0.985</u>	<u>1.000</u>	0.003
Fe Site	Fe <sup>+3</sup>	-	0.027	-	-	0.022	-
	Fe <sup>+2</sup>	1.009	0.943	0.002	0.947	0.896	0.010
	Mn	0.028	0.028	0.001	0.081	0.081	0.005
	Mg	0.001	0.001	0.001	0	0	-
	Zn	0.001	0.001	0.001	0.001	0.001	0.001
	Sum	<u>1.039</u>	<u>1.000</u>	0.002	<u>1.029</u>	<u>1.000</u>	0.006
	Total	<u>2.019</u>	<u>2.000</u>	0.001	<u>2.014</u>	<u>2.000</u>	0.003
Hematitie %		-	2.8	-	-	2.2	-
Ilmenite %		97.0	94.3	0.2	91.9	89.6	1.0
Pyrophanite %		2.8	2.8	0.1	8.0	8.1	0.5
Other %		0.2	0.2	0.2	0.1	0.1	0.1
Total		<u>100%</u>	<u>100%</u>	-	<u>100%</u>	<u>100%</u>	-



Table 14. (Ilmenite analyses, continued).

Locality	NS71		Standard deviation	7 Samples		Standard deviation	
N, Averages	10			67			
TiO <sub>2</sub>	52.05	52.05	0.78	51.65	51.65	0.29	
Al <sub>2</sub> O <sub>3</sub>	0	0	—	0	0	—	
Cr <sub>2</sub> O <sub>3</sub>	0.02	0.02	0.01	0.01	0.01	0.01	
Fe <sub>2</sub> O <sub>3</sub>	—	0.73	—	—	2.00	—	
FeO	46.35	45.69	0.45	46.81	45.01	1.17	
MnO	1.05	1.05	0.38	1.42	1.42	1.02	
MgO	0.01	0.01	0.01	0.02	0.02	0.02	
ZnO	0	0	—	0.02	0.02	0.02	
<u>Total</u>	<u>99.46</u>	<u>99.53</u>	1.04	<u>99.93</u>	<u>100.13</u>	0.27	
Structural Formulae							
Ti Site	Ti	0.995	0.993	0.015	0.987	0.981	0.004
	Fe <sup>+3</sup>	—	0.007	—	—	0.019	—
	Cr	0	0	—	0	0	—
	<u>Sum</u>	<u>0.995</u>	<u>1.000</u>	0.015	<u>0.987</u>	<u>1.000</u>	0.004
Fe Site	Fe <sup>+3</sup>	—	0.007	—	—	0.019	—
	Fe <sup>+2</sup>	0.986	0.970	0.015	0.994	0.949	0.026
	Mn	0.023	0.023	0.008	0.031	0.031	0.025
	Mg	0	0	—	0.001	0.001	0.001
	Zn	0	0	—	0	0	—
	<u>Sum</u>	<u>1.009</u>	<u>1.000</u>	0.008	<u>1.026</u>	<u>1.000</u>	0.009
<u>Total</u>		<u>2.004</u>	<u>2.000</u>	0.004	<u>2.013</u>	<u>2.000</u>	0.005
Hematite %							—
	—	0.7	—	—	1.9	—	—
Ilmenite %	97.7	97.0	1.5	96.8	94.9	2.6	—
Pyrophanite %	2.3	2.3	0.8	3.1	3.1	2.5	—
Other %	0	0	—	0.1	0.1	0.1	—
<u>Total</u>	<u>100%</u>	<u>100%</u>	—	<u>100%</u>	<u>100%</u>	—	—

Table 14. (Ilmenite analyses, continued).

Locality	8 Samples*		Standard
N, Averages	80		deviation
TiO <sub>2</sub>	51.57	51.57	0.32
Al <sub>2</sub> O <sub>3</sub>	0	0	-
Cr <sub>2</sub> O <sub>3</sub>	0.01	0.01	0.01
Fe <sub>2</sub> O <sub>3</sub>	-	2.11	-
FeO	46.91	45.01	1.11
MnO	1.32	1.32	1.15
MgO	0.02	0.02	0.02
ZnO	0.02	0.02	0.02
<u>Total</u>	<u>99.85</u>	<u>100.06</u>	0.33

## Structural Formulae

Ti Site	Ti	0.986	0.980	0.004
	Fe <sup>+3</sup>	-	0.020	-
	Cr	0	0	-
	<u>Sum</u>	<u>0.986</u>	<u>1.000</u>	0.004
Fe Site	Fe <sup>+3</sup>	-	0.020	-
	Fe <sup>+2</sup>	0.997	0.950	0.028
	Mn	0.029	0.029	0.025
	Mg	0.001	0.001	0.001
	Zn	0	0	-
	<u>Sum</u>	<u>1.027</u>	<u>1.000</u>	0.009
<u>Total</u>		<u>2.013</u>	<u>2.000</u>	0.005
Hematite %	-	2.0	-	
Ilmenite %	97.0	95.0	2.8	
Pyrophanite %	2.9	2.9	2.5	
Other %	0.1	0.1	0.1	
<u>Total</u>	<u>100%</u>	<u>100%</u>	-	

\* Average including 13 analyses from sample NS74.

(Rumble, 1976). Presumably the low oxidation state of the rocks in the study area is due to graphite limiting of  $f_{O_2}$ .

### Anatase

Occurrence and habit. Anatase is a common mineral of retrograde origin in the study area. It has not been identified in hand specimen because of the small grain size. In thin section, anatase is seen to be entirely pseudomorphic after ilmenite. Anatase is typically colorless, rarely medium-blue in irregular patches or chevron zones. Blue areas are pleochroic colorless to medium or light blue with absorption  $\alpha > \epsilon$ . Repetitive zoning of blue and colorless zones occurs on a scale of 1 to 10  $\mu\text{m}$ . Anatase is seen to be uniaxial negative with extreme birefringence and higher relief than sphene. Because of the very high refractive indices and the total internal reflections at anatase-quartz interfaces, anatase is very hard to see through without using the sub-stage condensing lens.

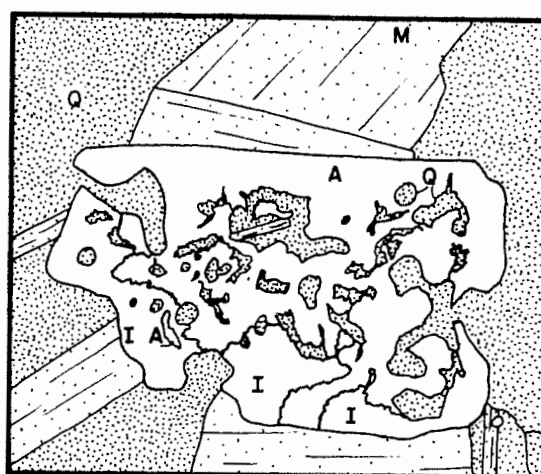
The replacement of ilmenite by anatase is apparently not dependent on parent grain size or shape. Nucleation of anatase occurred at one or more points on the surface of the ilmenite crystal, and growth proceeded along highly irregular but very sharp surfaces that were not controlled by crystallographic orientation of either mineral. The resulting pseudomorph after ilmenite may be made up of one or more single anatase crystals, depending on the number of original nucleation sites. Anatase

optic orientations apparently bear no relation to the host ilmenite. Relict ilmenite may reside either as "islands" entirely within anatase or along the rim of the composite grain.

The amount of ilmenite replacement in any one sample is highly variable. Some unaltered grains are randomly distributed among partially and completely pseudomorphed grains in the same thin section. The extent of ilmenite replacement is highly variable in field distribution and follows no clear areal pattern. In no rock was all ilmenite completely replaced by anatase, although in some samples modal anatase exceeds modal ilmenite by more than 20:1.

Examples of partial or complete pseudomorphs of anatase after ilmenite are illustrated in Figures 10d, 18, 19c, 20, and 21. Figure 20 is a drawing of a partial pseudomorph after ilmenite as seen in reflected light. Note the serrate, irregular boundary between anatase and relict ilmenite. Two types of quartz inclusions are evident in Figure 20: Rounded inclusions that are probably relict from the original ilmenite host (Figure 19), and irregular quartz inclusions with cusped or serrate outlines of presumed retrograde origin.

Assuming constant  $\text{TiO}_2$ , anatase cannot replace ilmenite on a 1:1 volume ratio because the molar volume of ilmenite ( $\text{FeTiO}_3$ ) is about  $31.69 \text{ cm}^3$ , whereas the molar volume of anatase ( $\text{TiO}_2$ ) is only about  $20.52 \text{ cm}^3$  (Cromer and Herrington, 1955; Weast, 1976; Robie et al., 1978). The direct replacement of ilmenite by anatase results in a 35% volume reduction. In thin section, however, the volume



0.1 mm

A = Anatase  
I = Ilmenite

M = Muscovite  
Q = Quartz

Figure 20. Drawing of a nearly complete pseudomorph of anatase after ilmenite in sample NS118, as seen in reflected light. The boundary between anatase and ilmenite is very irregular. Quartz inclusions are present in both morphologies: Rounded grains relict from the original ilmenite, and irregular grains presumably of retrograde origin.

reduction is rarely observed. A 35% decrease of volume results in only a 19% reduction in pseudomorph area (that seen in thin section), and a 13% reduction in any linear dimension. In most instances this small change may be difficult to notice. Rounded quartz inclusions that abound in parent ilmenite persist in pseudomorphous anatase, thus effectively reducing the volume change of a composite grain. Secondary, ragged and cusped-shaped quartz inclusions that apparently grew along the advancing anatase-ilmenite boundary effectively increase the volume of the pseudomorphed grain. The effect of dimension laws, inert quartz filling, and secondary quartz inclusions all reduce the noticeable change in pseudomorph size with respect to

the host ilmenite.

Chemistry. Table 15 is an average of all anatase chemical analyses, showing oxide weight percents, cation proportions, and composition ranges. All  $\text{TiO}_2$  weight percents are low. The titanium standard is an ilmenite, and unfortunately the electron microprobe computer was not programmed to adequately correct for Ti  $K_\alpha$  fluorescence caused by Fe  $K_\alpha$  X-ray excitation, resulting in low apparent titanium concentrations.

In the analyses, silica is present in significant quantities, probably as minute quartz inclusions that happened to overlap the analyzed volume. Calcium, with silica, may be present as minute inclusions of sphene. Aluminum, iron, and zinc occur in significant quantities, but cannot be ascribed to any included phases and probably occupy lattice sites. MnO and MgO are not present in significant quantities. No difference in composition was detected between colorless and blue anatase.

Stability. Anatase is found in low-grade metamorphic rocks (McNamara, 1965; Mielde and Schreyer, 1972; Rumble, 1976), and commonly replaces titanium-rich minerals such as ilmenite or sphene (Mitchel, 1964; Deer et al., 1976; Itaya and Banno, 1980; this work). However, it has not been clear in the past if anatase has a true stability field despite its widespread occurrence. Hydrothermal experiments have shown that anatase can form from altering titanium minerals (Lindh, 1972). It has also been demonstrated that reaction

Table 15. Average of all electron microprobe analyses of anatase. The low totals are due to inadequate correction factors (see text). Analyses are from all samples except NS18 and NS85.

Various samples		N=10	Range
SiO <sub>2</sub>	0.15		0-0.52
TiO <sub>2</sub>	91.02		88.01-94.56
Al <sub>2</sub> O <sub>3</sub>	0.04		0-0.27
FeO	0.16		0.04-0.49
MnO	0		0-0.01
MgO	0		0-0.03
ZnO	0.05		0-0.10
CaO	0.16		0.03-0.25
Total	91.58		88.72-95.08

#### Structural Formulae

Ti Site	Si	0.002	0-0.007
	Ti	0.995	0.989-0.998
	Al	0.001	0-0.005
	Fe	0.002	0.001-0.006
	Mn	0	0
	Mg	0	0-0.001
	Zn	0.001	0-0.001
	Ca	0.002	0.001-0.003
Total		1.003	1.000-1.005

boundaries may be drawn in P-T space separating fields of anatase, rutile, and other  $\text{TiO}_2$  polymorphs (Osborn, 1953; Dachille et al., 1968). Such reaction boundaries cannot be construed as phase stability field boundaries because they are defined only by the forward reaction, anatase = rutile (Dachille, 1969; Jamieson and Olinger, 1969). The reverse reaction has never been demonstrated, except at geologically unreasonable conditions of around  $1700^\circ\text{C}$  at one atmosphere pressure where reversal experiments indicate a true field boundary (Beard and Foster, 1967).

Hydrothermal and theoretical studies of anatase = rutile reaction kinetics have shown that the reaction obeys first order rate laws (McNamara, 1965). In simple  $\text{TiO}_2\text{-H}_2\text{O}$  systems, the time for reaction becomes too long to measure (at moderate pressures) at about  $610^\circ\text{C}$  (Rao, 1961; Lindh, 1972), although in one experiment using hydrothermal solutions of alkali-berillium-fluoride flux, anatase transformed into rutile at temperatures as low as  $250^\circ\text{C}$  (Osborn, 1953).

Thermodynamic calculations indicate that anatase has no stability field with respect to rutile, at geologically reasonable conditions (Rao, 1961; Schuling and Vink, 1967; Jamieson and Olinger, 1969; Rumble, 1976). Anatase is found in nature for the following reasons: 1)  $\Delta G^\circ$  of the reaction anatase = rutile is small, making both polymorphs nearly as likely to form in any reaction ( $\Delta G^\circ = -50$  to  $-150$  cal/mole, Rao, 1961;  $-20$  to  $-250$  cal/mole, Schuling and Vink, 1967;  $-600$  cal/mole, Robie et al., 1978).



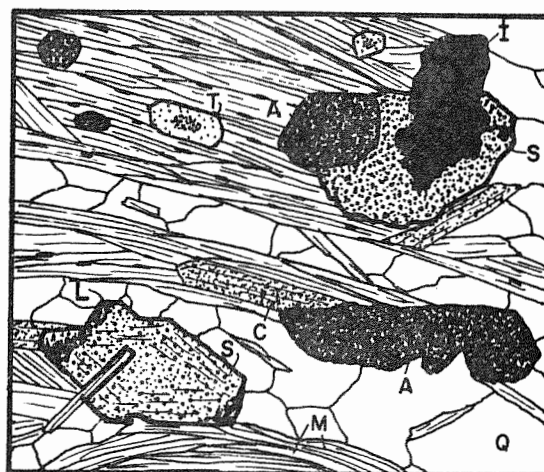
2) The activation energy of transition from anatase to rutile is large, about 80 kcal/mole (Rao, 1961), making the reaction very sluggish at low temperatures. In effect, at low temperatures and pressures, both rutile and anatase are nearly as easily produced and the transition between the two very difficult.

Under proper conditions, anatase is apparently more easily nucleated than rutile during the breakdown of a titanium-rich mineral such as ilmenite, in spite of the fact that anatase is unstable with respect to rutile. This may be because the open spacing of  $(\text{TiO}_6)$  octahedra in the parent mineral is more similar to the open framework of anatase relative to the more closely packed structure in rutile.

### Sphene

Occurrence. Sphene has been positively identified only in sample NS90, and it is almost certainly of retrograde origin. Sphene is probably the primary sink for calcium released from the gossular component of retrograding garnets, as has been found by Itaya and Banno (1980). Sphene occurs as single and twinned crystals, euhedral to subhedral in form, up to 200  $\mu\text{m}$  long. Sphene may also occur in other samples as trace inclusions in anatase (see previous section on anatase). Sphene grains are found both independent of the other oxides, or growing in contact with anatase and/or ilmenite (Figure 21).

Sphene is colorless, or pleochroic colorless to faint brown.



A = Anatase	I = Ilmenite	Q = Quartz
C = Chlorite	L = Leucoxene	S = Sphene
G = Graphite	M = Muscovite	T = Tourmaline

Figure 21. Composite drawing showing textural relationships between sphene, the oxides, and silicates (sample NS90). Note the euhedral outline and hint of concentric zoning on the sphene grain to the lower left. Parts of that grain are altered to leucoxene, doubtless a weathering product.

It is biaxial positive with a  $2V$  of about  $25^\circ$ , and has extreme birefringence (high order whites) and dispersion ( $r > v$ ). Sphene has a relief lower than anatase, but higher than apatite or the sheet silicates. Sphene is concentrically zoned in the larger crystals with respect to refractive index, and pleochroic radiation halos are not present in adjacent chlorite.

Chemistry. Chemically, sphene is more complex than the coexisting Fe-Ti oxides. Table 16 lists seven analyses of sphene from sample NS90. There are two major types of substitution in the analyzed

Table 16. Electron microprobe analyses of sphene from sample NS90A. For each analysis there are two columns. The first lists oxide weight percent, total H<sub>2</sub>O % (difference of oxide total from 100 %), cation ratios (based on the formula CaTiSiO<sub>5</sub>, containing 5 oxygens), and OH<sup>-</sup> proportion (calculated from H<sub>2</sub>O weight % above). The second column contains H<sub>2</sub>O weight % (recalculated from corrected stoichiometry mole % water), cation ratios recalculated on a basis of 3 cations, and OH<sup>-</sup> proportions based on cation charge and 5 anions.

Analysis No.	1		2		3	
SiO <sub>2</sub>	29.90		30.16		29.89	
TiO <sub>2</sub>	36.49		38.58		35.82	
Al <sub>2</sub> O <sub>3</sub>	3.19		1.85		3.62	
Cr <sub>2</sub> O <sub>3</sub>	0.06		0.02		0.04	
FeO	0.02		0.09		0.19	
MnO	0		0		0	
MgO	0.06		0.02		0.10	
ZnO	0.08		0.04		0.10	
CaO	29.70		29.76		27.51	
Na <sub>2</sub> O	0.03		0.06		0.03	
Sum	99.53	99.53	100.58	100.58	97.30	97.30
H <sub>2</sub> O	0.47	0.89	-0.58	0.64	2.70	0.54
Total	100.00	100.42	100.00	101.22	100.00	97.84

## Structural Formulae

Si Site	Si	0.983	0.963	0.981	0.967	0.996	0.985
	Al	0.017	0.037	0.019	0.033	0.004	0.015
	Sum	1.000	1.000	1.000	1.000	1.000	1.000
Ti Site	Ti	0.900	0.882	0.944	0.931	0.898	0.888
	Al	0.106	0.084	0.052	0.037	0.138	0.125
	Cr	0.002	0.002	0	0	0.001	0.001
	Mg	0.003	0.003	0.001	0.001	0.005	0.005
	Fe	0	0	0.002	0.002	0.005	0.005
	Zn	0.002	0.002	0.001	0.001	0.002	0.002
	Sum	1.013	0.973	1.000	0.972	1.049	1.026
Ca Site	Ca	1.045	1.024	1.038	1.024	0.983	0.972
	Na	0.003	0.003	0.004	0.004	0.002	0.002
	Sum	1.048	1.027	1.042	1.028	0.985	0.974
	Total	3.061	3.000	3.042	3.000	3.034	3.000
	OH <sup>-</sup>	0.100	0.190	-0.125	0.138	0.575	0.115

Table 16. (Sphene analyses, continued).

Analysis No.	4		5		6	
SiO <sub>2</sub>	30.36		28.87		29.72	
TiO <sub>2</sub>	35.32		41.15		36.79	
Al <sub>2</sub> O <sub>3</sub>	3.91		1.86		3.67	
Cr <sub>2</sub> O <sub>3</sub>	0.10		0.06		0.09	
FeO	0.13		0.29		0.08	
MnO	0		0		0	
MgO	0.08		0.08		0.01	
ZnO	0.05		0.09		0.18	
CaO	28.26		28.34		27.83	
Na <sub>2</sub> O	0		0.03		0.06	
Sum	98.21	98.21	100.77	100.77	98.43	98.43
H <sub>2</sub> O	1.79	0.67	-0.77	0.33	1.57	0.56
Total	100.00	98.87	100.00	101.10	100.00	98.99

## Structural Formulae

Si Site	Si	1.002	0.988	0.938	0.931	0.980	0.968
	Al	0	0.012	0.062	0.069	0.020	0.032
	Sum	1.002	1.000	1.000	1.000	1.000	1.000
Ti Site	Ti	0.877	0.864	1.006	0.999	0.913	0.902
	Al	0.152	0.138	0.009	0.001	0.123	0.109
	Cr	0.004	0.004	0.002	0.002	0.003	0.003
	Mg	0.004	0.004	0.004	0.004	0.005	0.005
	Fe	0.004	0.004	0.008	0.008	0.002	0.002
	Zn	0.001	0.001	0.002	0.002	0.004	0.004
	Sum	1.042	1.015	1.031	1.016	1.050	1.025
Ca Site	Ca	1.000	0.985	0.988	0.981	0.984	0.971
	Na	0	0	0.003	0.003	0.004	0.004
	Sum	1.000	0.985	0.991	0.984	0.988	0.975
	Total	3.044	3.000	3.022	3.000	3.038	3.000
	OH <sup>-</sup>	0.379	0.142	-0.166	0.071	0.336	0.120

Table 16. (Sphene analyses, continued).

Analysis No.	7	Average,		N=7	Standard deviation (uncorrected)	
SiO <sub>2</sub>	29.95		29.84		0.47	
TiO <sub>2</sub>	35.46		37.09		2.10	
Al <sub>2</sub> O <sub>3</sub>	4.56		3.24		1.03	
Cr <sub>2</sub> O <sub>3</sub>	0.07		0.06		0.03	
FeO	0.13		0.13		0.09	
MnO	0		0		-	
MgO	0.09		0.06		0.03	
ZnO	0.03		0.08		0.05	
CaO	27.74		28.45		0.85	
Na <sub>2</sub> O	0		0.03		0.02	
Sum	98.03	98.03	98.98	98.98	1.33	
H <sub>2</sub> O	1.97	0.62	1.02	0.62	1.33	
Total	100.00	98.65	100.00	99.60	-	
Structural Formulae						
Si Site	Si	0.989	0.976	0.981	0.968	0.021
	Al	0.011	0.024	0.019	0.032	-
	Sum	1.000	1.000	1.000	1.000	-
Ti Site	Ti	0.881	0.869	0.917	0.905	0.045
	Al	0.167	0.152	0.107	0.092	0.041 (total Al)
	Cr	0.002	0.002	0.002	0.002	0.001
	Mg	0.005	0.005	0.004	0.004	0.001
	Fe	0.003	0.003	0.003	0.003	0.003
	Zn	0.001	0.001	0.002	0.002	0.001
	Sum	1.059	1.032	1.035	1.008	-
Ca Site	Ca	0.982	0.968	1.003	0.990	0.027
	Na	0	0	0.002	0.002	0.002
	Sum	0.982	0.968	1.005	0.992	0.028
	Total	3.041	3.000	3.040	3.000	0.012
	OH <sup>-</sup>	0.419	0.132	0.217	0.132	0.285

sphene. The first is a relatively constant substitution of about 2 or 3% of Al for Si in the tetrahedral site, possibly compensated by hydroxyl in place of oxygen. The second substitution, Al for Ti, is much more variable and follows distinct trends. Figure 22 shows data plots which indicate that the refractive index zoning in sphene is due to the substitution  $(\text{TiO})^{+2} = (\text{AlOH})^{+2}$  (also may be written  $\text{Ti}^{+4} = \text{Al}^{+3} + \text{H}^{+}$ , or  $2\text{TiO}_2 = \text{Al}_2\text{O}_3 \cdot \text{H}_2\text{O}$ ), as has been found in other low-grade metamorphic sphene (Coombs et al., 1976; Boles and Coombs, 1977; Ribbe, 1980).

In Figure 22a,  $\text{Al}_2\text{O}_3$  is shown to increase with decreasing total weight percent, because of increasing structural  $\text{OH}^-$  with aluminum. Figure 22b is similar to 21a, but Al is represented as cations per formula unit. In both Figures 22a and 22b, the aluminum remaining at the 100% "Y" intercept crudely represents the relatively constant amount of aluminum in the  $^{\text{IV}}\text{Si}$  site. In Figure 22c weight %  $\text{TiO}_2$  is plotted against total weight percent. The best fit line through the data has a slope opposite that of graphs 21a and 21b, because total weight percent increases as titanium displaces water from the structure. Figure 21d shows Ti cations per formula unit plotted against Al cations per formula unit. The best fit lines display a superb Ti to Al inverse correlation, with line slopes very close to -1. This supports the ideal  $(\text{TiO})^{+2} = (\text{AlOH})^{+2}$  substitution mechanism given above. Again, the gap between zero Al and the  $\text{Ti} = 1$  "X" intercept of the best fit lines (Figures 22c and 22d) roughly represents the small amount of aluminum substituting for silicon.

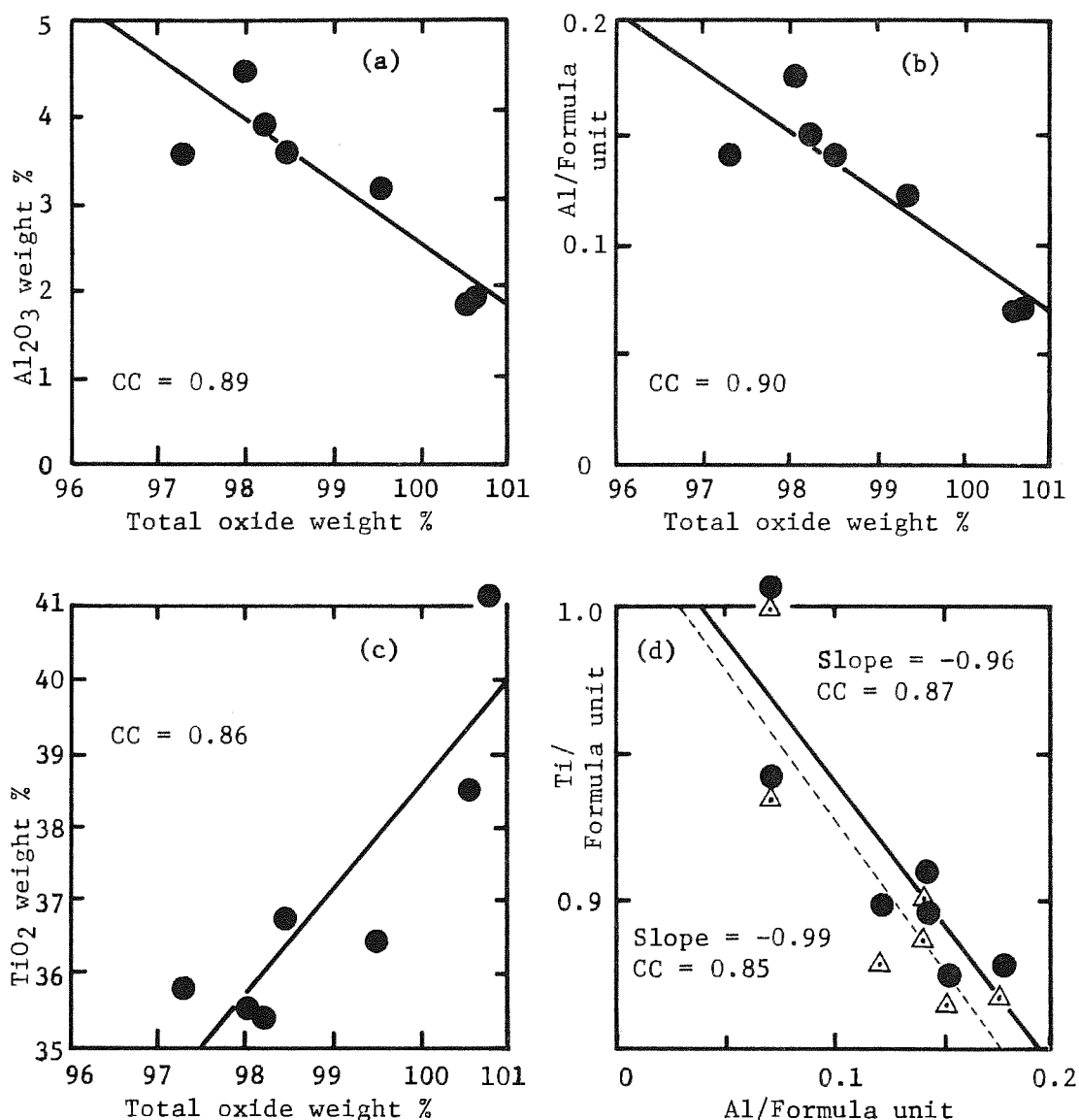


Figure 22. Analytical data from sphene in sample NS90, plotted in various ways to demonstrate the probable substitution mechanism:  $\text{TiO}^{+2} = \text{AlOH}^{+2}$ . Black dots are for weight percents and cation proportions uncorrected for stoichiometry. Open triangles are for cation proportions recalculated to 3 cations. Lines are linear regression best fits through the data. "CC" is the correlation coefficient for each regression line, all of which are good enough to indicate real trends. The anomalous intercepts in plots a, b, and d, that indicate the presence of aluminum even at full Ti site occupancy and 100% weight totals (indicating no structural  $\text{OH}^-$ ), corresponds to some Al for Si substitution in the Si site.

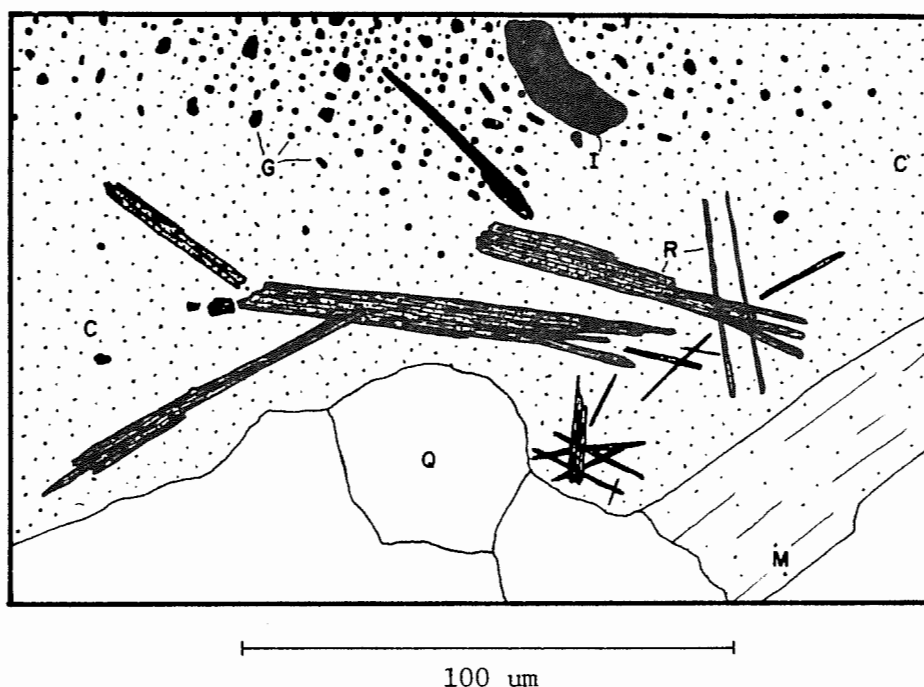
Cr, Fe, Mg, Zn, and Na are present in sphene in trace amounts and show no trends. Silica, tetrahedral aluminum, and calcium also show no trends when plotted against each other, or against other chemical constituents.

### Rutile

Rutile occurs as splintered rods and thin needles up to 150  $\mu$ m long. It is relatively abundant in sample NS101 and is rare in samples NS89 and NS61. Anatase is not present in these samples. The needles are light yellow-brown and slightly pleochroic,  $e > o$ . The needles have high birefringence, very high relief relative to chlorite, parallel cleavage, and positive elongation. They occur along with retrograde ilmenite that has formed from titanium and iron released during biotite breakdown. Rutile occurs only entirely within chlorite and relict biotite, whereas retrograde ilmenite plates more commonly reside in muscovite and chlorite external to biotite.

Figure 23 is a drawing of several rutile crystals from sample NS101. The crystals are embedded in chlorite and are close to but not touching quartz and muscovite. At the top of Figure 23 is an ilmenite grain that may be of retrograde origin, and also a profusion of graphite grains in concentrations relict from the parent biotite. The habit of rutile indicates that it nucleated and grew apart from ilmenite, rather than by pseudomorphic replacement of ilmenite as was anatase.





C = Chlorite  
G = Graphite

I = Ilmenite  
M = Muscovite

Q = Quartz  
R = Rutile

Figure 23. Rutile needles within chlorite, surrounding altering biotite, in sample NS101. Biotite is present off the top of the drawing, and graphite concentrations in chlorite are relict from parent biotite. The ilmenite shown may be of retrograde origin.

### Apatite

Apatite is ubiquitous in the study area, occurring as short, stout prisms with blunt terminations and somewhat more irregular or elongate shapes up to 400  $\mu\text{m}$  long. Prism faces are fairly common and many crystals have a distinct basal parting. Apatite is uniformly uniaxial negative, has very low birefringence, high relief relative to quartz and the sheet silicates, low relief relative to garnet, and negative elongation. Many apatite crystals

are surrounded by weak radiation haloes in adjacent biotite and chlorite. Inclusions of graphite are common. A drawing of fresh apatite (zone R2) may be seen in Figure 24a, and in less detailed drawings throughout this section.

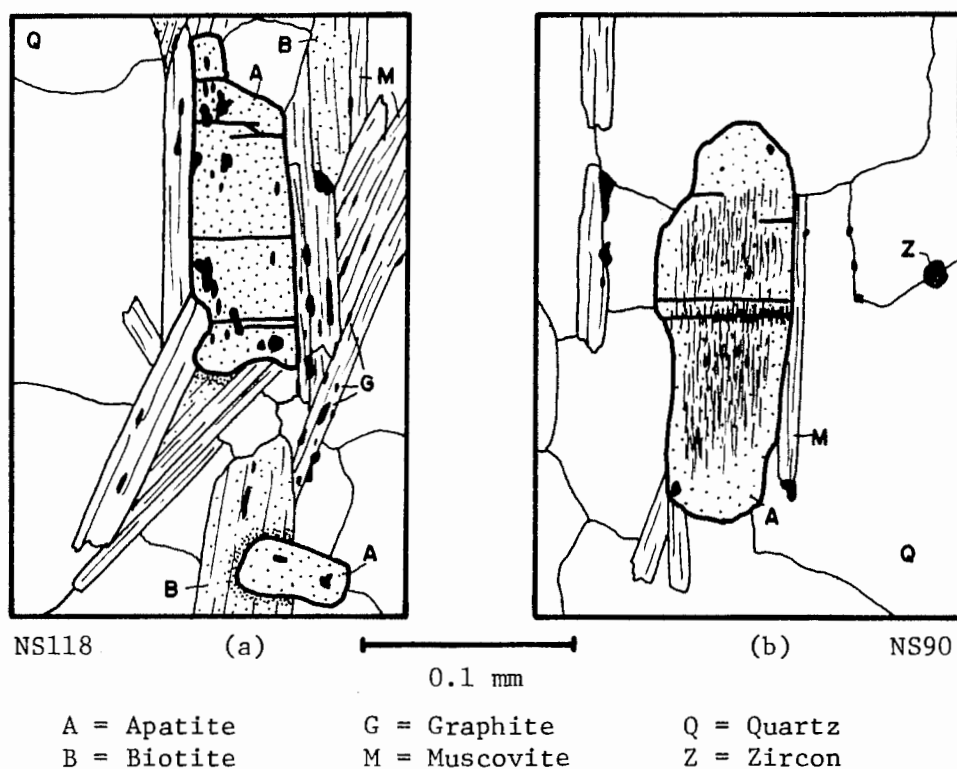


Figure 24. Apatite crystals. a) Fresh apatite showing subhedral prismatic habit and radiation halos where adjacent to biotite. Inclusions are probably graphite. b) Apatite from the severely retrograded sample NS90. Note the tiny needle-shaped bodies oriented parallel with the C-axis. Small ovoid inclusions are probably quartz.

Apatite appears to have changed little in shape with retrograding, crystals remaining prismatic with hexagonal end sections, but the internal appearance did change. Figure 24b is a sketch of

an apatite crystal from sample NS90 (zone R6). Within the apatite grain are abundant needle-shaped bodies oriented parallel to the c-crystallographic axis. The apatite grains also contain many tiny colorless ovoid inclusions.

The needle-shaped bodies are non-pleochroic and appear dark, probably due to their small size, and in fact are probably colorless. Neither the needles nor the tiny ovoid inclusions have any noticeable birefringence. The needle shaped bodies are suspected by the writer to be leached voids in the apatite crystal, perhaps due to a core composition somewhat different than the needle-free rims. The small ovoid inclusions are probably quartz.

### Tourmaline

Tourmaline is a very common accessory mineral in the study area. Blunt pseudo-hexagonal prisms up to 1 mm long are abundant in most rock samples; outcrop NS97 being remarkable in that it contains roughly 25% tourmaline. Tourmaline crystals are typically color zoned, and presumably also zoned in composition. Colors are varied, but commonly are darker green in cores with olive green rims. Olive cores and darker green rims are also rather common. Tourmaline with medium blue cores and olive green rims, and entirely blue or olive green crystals also occur in some samples.

All tourmaline is strongly pleochroic with absorption  $\alpha > \beta > \gamma$ . Tourmaline has negative elongation and is uniaxial negative, with maximum interference colors in middle second order. Inclusions of

graphite are quite common and inclusions of quartz and zircon less common. Drawings of tourmaline may be found in several figures throughout this section.

### Zircon

Zircon has been identified in virtually every thin section from the study area. The grains are colorless, equant to somewhat elongate, and angular to subrounded. No distinct crystal faces were seen. The grains are most commonly about 5 to 10  $\mu\text{m}$  in their longest dimension, and rarely exceed 50  $\mu\text{m}$ . The various shapes and sizes of zircon grains indicate that they did not crystallize in situ, which probably would have resulted in distinguishable crystal outlines. The zircons may have retained their detrital shapes since deposition in the Devonian. Most zircons are radioactive and are surrounded by pleochroic haloes in adjacent biotite and chlorite. The halos vary in size but rarely exceed 30  $\mu\text{m}$  in thickness. Some radiation haloes in chlorite are composed of two to four concentric shells of varied pleochroic intensity, and are particularly common in samples NS17 and NS95.

### Graphite

Abundant fine-grained opaque material exists in virtually every sample, and is the cause of the dark gray shading in many rocks in the Littleton Formation. In thin section the dusty opaque material is irregular to platy or rarely hexagonal, and rarely exceeds 10  $\mu\text{m}$

in width. It is assumed that the fine-grained, dusty material is not ilmenite because of its distinctive but rare hexagonal shape, finer grain size than most identifiable ilmenite, and its stubborn refusal to take a high polish compared to ilmenite platelets. Therefore, the fine-grained opaque material is probably graphite. Crystalline graphite has been identified optically and by X-ray diffraction in the Littleton Formation about 13 km north-northeast of the study area (Huntington, 1975), and by X-ray diffraction in ultramafic rocks of the Partridge Formation about 11 km north-northeast (Wolfe, 1978).

Graphite is included within virtually every mineral except the oxides and sphene. Rare opaque inclusions in large zircon grains may be graphite. In the matrix graphite is concentrated at grain boundaries, particularly those of old foliation muscovite plates. Concentrations of fine-grained graphite are common within large biotite and staurolite crystals, and sheet silicate replacements after those minerals (Figures 18a and 22). Graphite may be seen in virtually every drawing in this section, displaying hexagonal outlines in some of the more detailed sketches. The presence of abundant graphite limited the rock to low oxygen fugacities during metamorphism, explaining the lack of more than trace amounts of ferric iron in garnet (Table 5) and ilmenite (Table 12).

#### Allanite

Allanite is present as an accessory mineral in thin sections from several samples. It occurs as small grains, rarely as large

as 50  $\mu\text{m}$  in width and up to 200  $\mu\text{m}$  in length, commonly with euhedral outlines. Colors range from greenish-brown to orange-red. All are metamict or nearly so, and are surrounded by thick pleochroic halos where adjacent to biotite or chlorite.

### Pyrite

Pyrite has been identified as relics in two samples, using a reflected light microscope. It occurs as small discrete cubes and small isolated clumps of cubes and irregular forms up to 1 mm long. There are only one or two occurrences per slide, and in most cases they have been completely pseudomorphed by weathering products, deep-red to orange-brown in color.

The presence of pyrite instead of pyrrhotite is something of a puzzle, as pyrrhotite is the most abundant sulfide in high-grade rocks with pyrite only occurring with very Mg-rich silicates (Thompson, 1972; Robinson, 1977; Hutcheon, 1979). Pyrite is quite common, however, in very low-grade metamorphic rocks, particularly those bearing chlorite (McNamara, 1965; Condie, 1967; Ramsay, 1973; Coombs et al., 1976; this work). The occurrence of pyrite in the study area indicates mixed volatile retrograde hydration reactions involving water, graphite, sulfides, and silicates, that favored chlorite-muscovite-pyrite assemblages over biotite-pyrrhotite assemblages.

### Quartz

Quartz is the most abundant mineral in the study area. In outcrop it occurs in discrete quartzite layers up to about 0.3 meters thick, and also in abundance in the schistose layers. Single grains may be seen in outcrop up to about 5 mm across in rare instances. Inclusions of graphite and the sheet silicates are abundant, and zircon, ilmenite, sillimanite, apatite, and tourmaline have been seen. Quartz is found as inclusions in staurolite, garnet, the sheet silicates, tourmaline, apatite, ilmenite, anatase, chloritoid, and albite.

In most rocks, even those having undergone severe retrograde and earlier deformation, quartz is equant and annealed, without strain shadows and commonly having  $120^\circ$  grain boundary intersections against adjacent quartz grains. In a few rocks, however, strain shadows and fine-scale strain lamellae may be seen. In one sample (A04), fibrous quartz was seen to have grown in one axial plane slip zone. The fibers are oriented at a small acute angle to the slip plane, and probably grew during deformation after the phase of pervasive retrograde metamorphism and quartz annealing discussed here.

### Weathering Products

The most common weathering products are limonite and/or goethite, which occur as thin films along cracks in garnet, along grain boundaries, and as a thin, transparent stain on outcrop

surfaces and foliation planes. The stain is orange to orange-brown or orange-red on outcrop surfaces, and generally orange or orange-red, orange-brown, red-brown, or deep red in transmitted light. The deep red replacement after pyrite may be hematite that formed preferentially to hydrated iron oxides in the locally acidic and somewhat reducing environment of the pyrite pseudomorph. Minor quantities of leucoxene may be seen around some sphene crystals in sample NS90 (Figure 20).

#### Cathode Luminescence

Many minerals fluoresce at visible wavelengths when excited by energetic photons or particles. Table 17 is a list of the eight minerals in the study area that were seen by the author to fluoresce under electron beam excitation in the electron microprobe. The minerals are listed in alphabetical order along with relative

Table 17. Relative brightness and apparent color of minerals fluorescing under electron beam excitation. Listing is in alphabetical order.

<u>Mineral</u>	<u>Brightness</u>	<u>Color</u>
Anatase	Bright	Yellow-Green
Apatite	Faint	Blue-White
K-feldspar	Faint	Greenish Blue-White
Muscovite	Very Faint	White ?
Plagioclase	Faint	Blue-White
Quartz	Very Bright	Yellow-Orange
Sphene	Moderate	Light Green
Zircon	Moderate	Light Blue

brightness and color of the fluorescing spot. The properties were noted using minimum beam diameter (about 2  $\mu\text{m}$ ), and a standard beam



potential of 15,000 volts and current of 0.02  $\mu$  amperes. The brightest fluorescence was observed in quartz, where the glowing spot could be observed even when viewed with reflected light illumination. The most dim fluorescing mineral was muscovite, on which the glowing spot could barely be seen with no illumination. Fluorescence color is, of course, subjective.

## PHASE RELATIONS

### Introduction

The preceeding section was a discussion of the mineralogy and crystal chemistry of minerals identified in the Littleton Formation in this study. Each mineral was described separately, many with plots showing individual analytical data points. The following will be a discussion of rock mineralogy and chemistry as assemblages, largely by using averaged mineral analyses to construct phase diagrams. This section may be considered as a prelude to the next section where specific mineral reactions controlling phase relations will be discussed.

### Feldspars

Plagioclase apparently did not change in composition during retrograding. The presence of plagioclase and its composition is due to rock bulk composition and prograde metamorphic history. K-feldspar is of retrograde origin, and does not vary in composition from nearly end-member sanidine. In most rocks K-feldspar occurs

only within biotite, so any discussion of two coexisting feldspars is dubious. However, in some rocks K-feldspar may be seen to extend beyond biotite boundaries, and indeed even to touch plagioclase. This being the case, Figure 25 has been drawn to show K-feldspar - plagioclase tie lines in the feldspar ternary system.

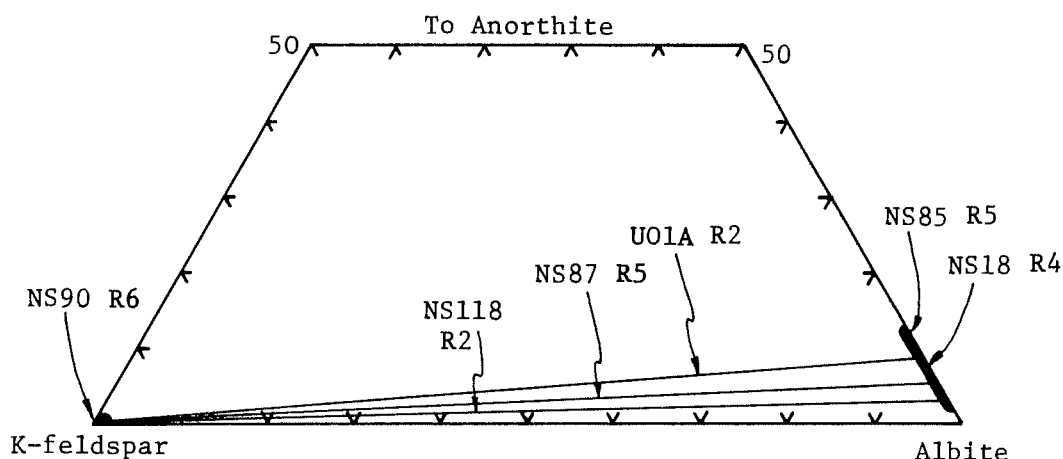


Figure 25. Plot of averaged feldspar analyses from various samples, excluding specimen NS71, which contains no feldspar. The plagioclase composition field extends to include all 25 analyses. The extent of solid solution between the two feldspars is exaggerated. Note that the An content of the plagioclase is not related to degree of retrograding.

As can be seen in Figure 25, there is no pattern in plagioclase composition, or in the presence or absence of either feldspar with degree of retrograding. In retrograded rocks, sphene is the only identified calcium sink for the grossular component released from garnet, although it is possible that minor quantities of retrograde plagioclase were missed. K-feldspar is present in both the least and most retrograded rocks, with and without plagioclase of various

An contents. The extremely limited amount of solid solution between the two feldspars indicates either very low temperatures at the time of K-feldspar growth (Stormer, 1975; Whitney and Stormer, 1977; Ferry, 1978 and 1980), disequilibrium, or both.

### Micas

K/K+Na ratios of coexisting biotite and muscovite changed more or less continuously during retrograde metamorphism. In sample U01A (the freshest analyzed sample), biotite and muscovite have K/K+Na ratios of 0.936 and 0.666, respectively, with sodium strongly partitioned into paragonitic muscovite. With retrograding (Figure 26) the potassium end member component of biotite had greater stability than the sodium component. In every reaction that consumed

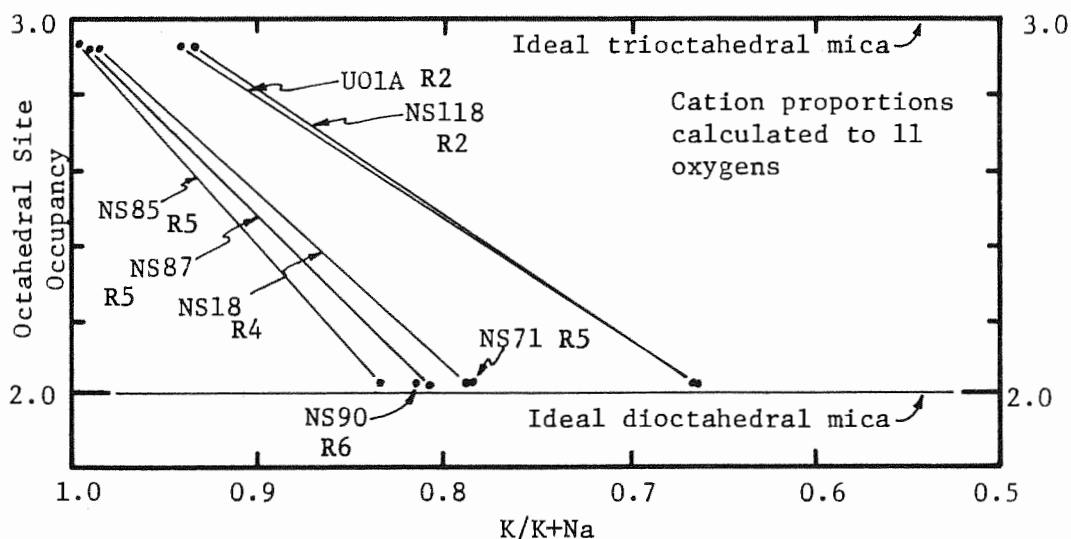


Figure 26. Averaged chemical analyses of micas from various samples, plotted with octahedral site occupancy versus K/K+Na ratios. Micas in sample U01A are closest to prograde compositions

biotite, the sodium component was released somewhat preferentially, increasing the K/K+Na ratio in both muscovite and biotite while increasing the quantity of muscovite and decreasing the quantity of biotite. This process continued in the more severely retrograded rocks until the last trace of potassium end member biotite vanished, thereby fixing the K/K+Na ratio of muscovite to the original average mica ratio (corrected for K-feldspar).

In rocks with higher K/K+Na ratios, and/or lower aluminum than the ideal case presented in the preceding paragraph, K-feldspar may abbreviate the trend of potassium enrichment of muscovite, as in sample NS90. In that rock, K-feldspar consumed substantial quantities of potassium so the average muscovite composition is somewhat more sodic than that in sample NS85, which has no K-feldspar. In sample NS71 there is no evidence that biotite or feldspar ever existed, so muscovite K/K+Na ratios in that sample remained constant during retrograde metamorphism.

Figure 27 is a plot of all mica analyses, with total  $M^{+2}+Ti+(Si-3)$  versus total  $M^{+3}$ , after Tracy (1978). The area between the dioctahedral mica (muscovite-celadonite) series and the trioctahedral (biotite-eastonite) series represents the composition field of most micas. The two thick diagonal lines represent the tschermaks type  $M^{+2}Si = \text{}^{\text{IV}}\text{Al} \text{}^{\text{VI}}\text{Al}$  substitution which maintains mica octahedral site stoichiometry. The range of muscovite compositions from nearly pure muscovite toward celadonite is clearly developed, as described previously. Biotite also exhibits a somewhat smaller range of

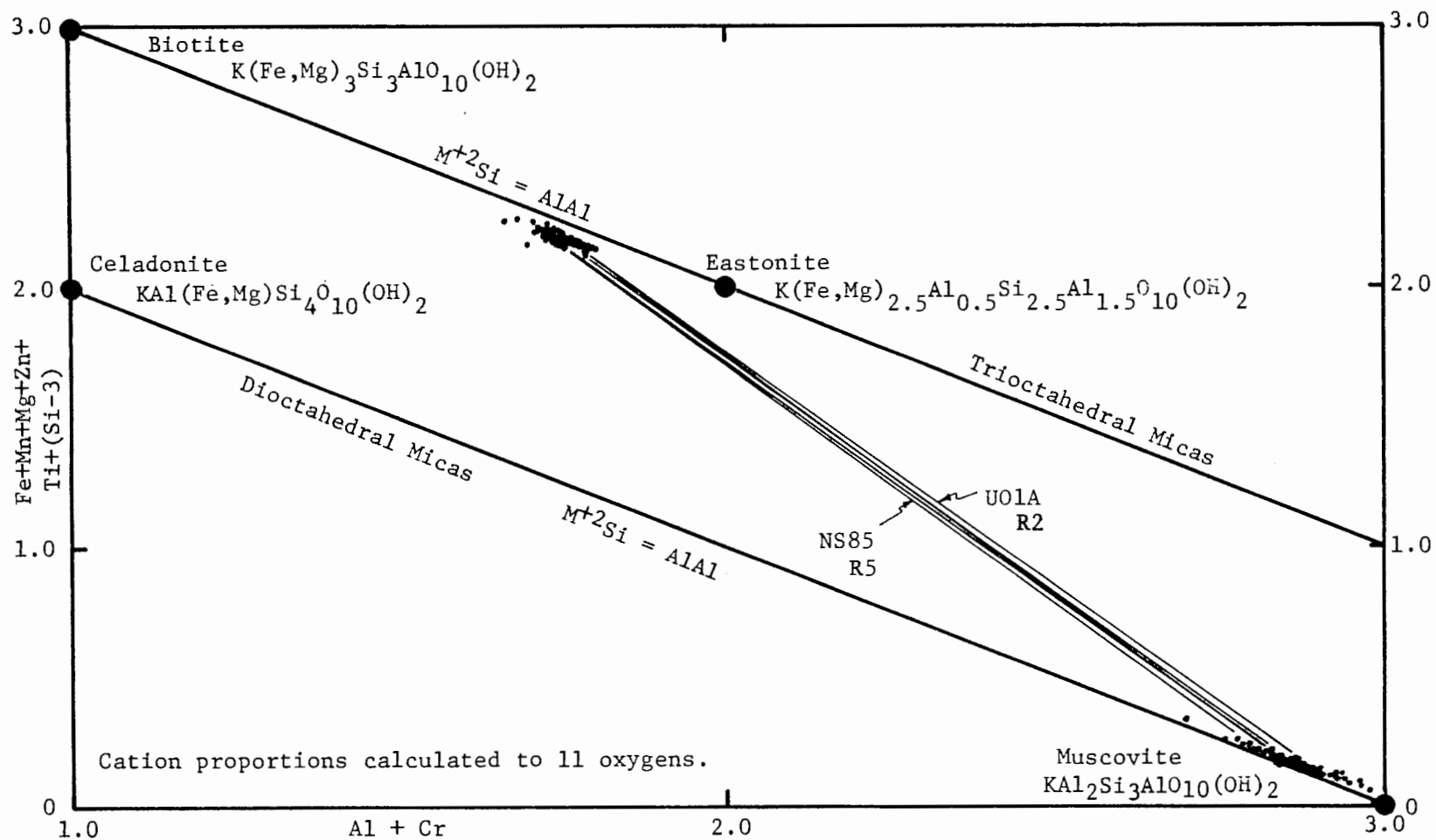


Figure 27. Mica pair plot, after Tracy (1978). The trend with retrograding toward celadonite is well developed in muscovite. The trend toward less aluminous biotite is evident, but less well developed. Note the small displacement of data points toward the center of the plot. See Figure 28 for detail of tie lines.

compositions in this plot, paralleling the muscovite trend toward lower aluminum compositions.

Most data points for both micas are slightly displaced toward the center of the mica field by the substitution of  $3M^{+2}$  for  $2^{VI}Al$  + vacancy in muscovite, and the reverse for biotite. This type of substitution does not maintain constant octahedral site occupancy, and is largely responsible for the slight octahedral site deficiency in biotite and excess in muscovite (Figure 26 and 27).

Tie lines connecting average mica compositions in Figure 27 do not cross, with the exception of the mica pairs in sample NS18 (see Figure 28 for tie line detail). The trend toward higher  $M^{+2}$  and lower

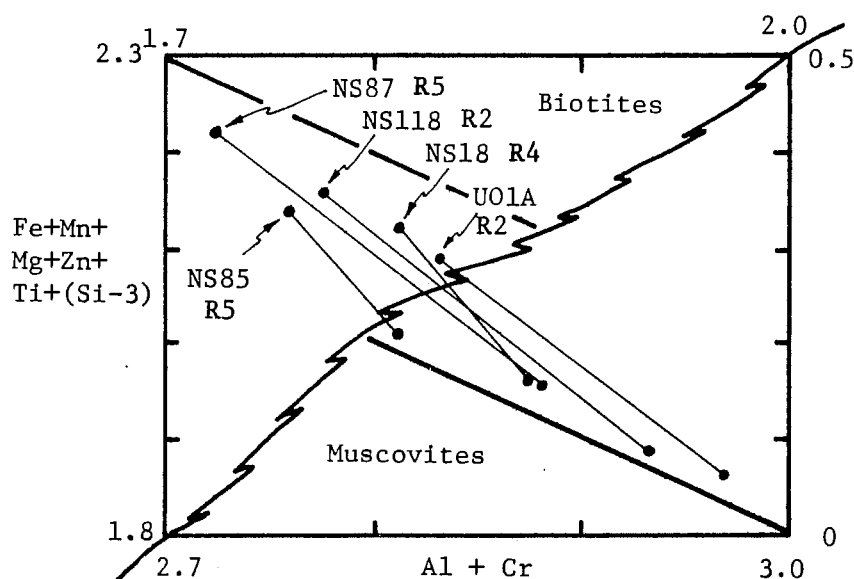


Figure 28. Detail of tie lines in Figure 27. Relative positions of data points for each mica type are identical to Figure 27, but with expanded scales.

aluminum with retrograding in both micas parallels the  $K/K+Na$  ratio trend (Figure 26) remarkably closely, considering that the mica

composition variations evident in Figure 27 are of much smaller magnitude, and therefore more susceptible to analytical and sampling errors.

#### Alkali-Alumina System

Now that K-Na mineral trends have been described, a synopsis of K-feldspar-plagioclase-muscovite phase relations is in order. Figure 29 is a projection showing the feldspars and averaged muscovite chemical analyses of all seven analyzed samples. Note that samples UO1A, NS118, and NS87 contain two feldspars plus muscovite, samples NS18 and NS85 contain no K-feldspar, NS90 contains no plagioclase, and NS71 contains neither feldspar. Feldspar compositions do not vary at all in this projection within analytical uncertainty. The slight decrease in alumina in the more retrograded micas is evident, as is the high alumina muscovite in sample NS71.

Sample NS71 clearly contains no feldspar because the high aluminum muscovite is embedded within the muscovite composition field, and is thus not exposed to fields of feldspar stability. All other severely retrograded rocks contain feldspars, so coexisting muscovite is constrained to somewhat lower aluminum compositions (Guidotti, 1973). It is not clear why the more retrograded samples do not define a more distinct set of two and three phase fields, but it is probably because the feldspars did not equilibrate with the micas.

The very high sodium content of muscovite in all samples is contrary to compositions predicted by white mica solvus curve

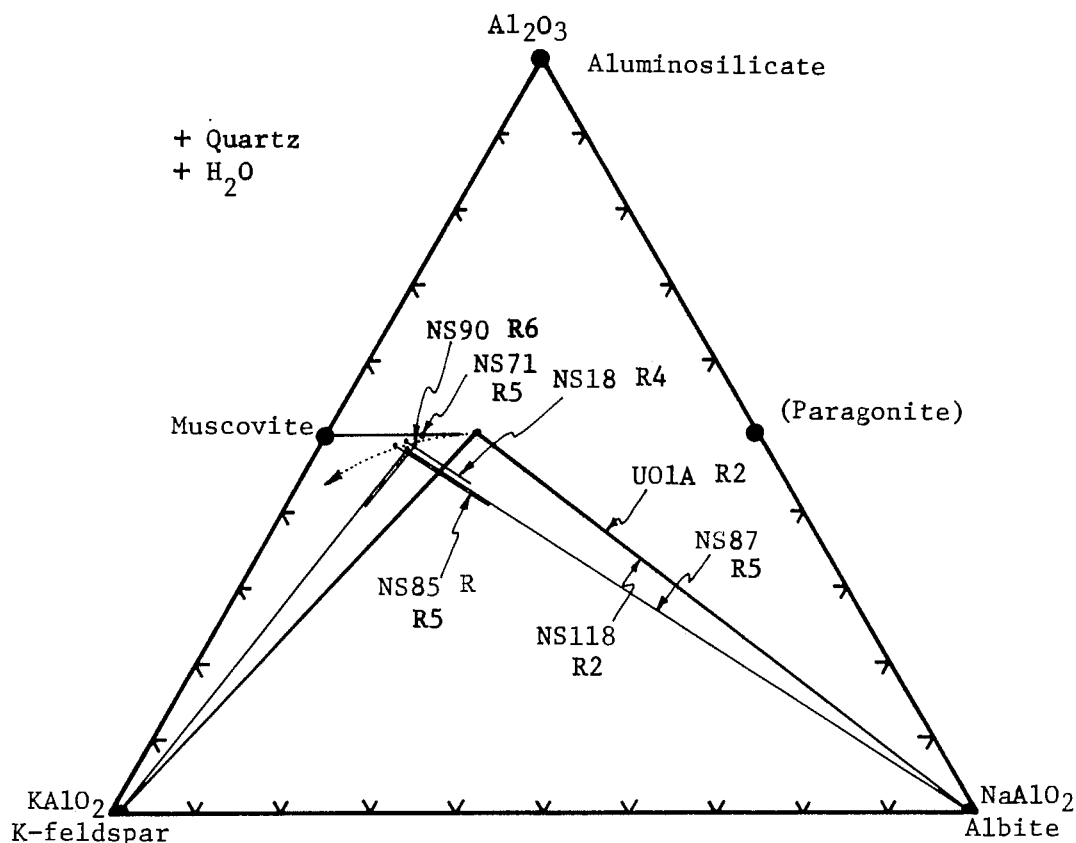


Figure 29. Alkali-alumina ternary system showing feldspar and muscovite compositions for the various samples. Samples U01A, NS118, and NS87 have two feldspars, samples NS18 and NS85 have only plagioclase, sample NS90 has only sanidine, and sample NS71 has neither feldspar. The dotted arrow is a possible retrograde trend of muscovite toward more phengitic compositions.

determinations (Eugster et al., 1972; Thompson, 1974). Reactions involving paragonite, plagioclase, muscovite, and aluminosilicate should limit paragonite content of muscovite to a maximum of about 19% at 2 kbar (Thompson, 1974), and about 20% at 6 kbar (Thompson, 1974; Chatterjee and Froese, 1975; corrected for raising of the solvus and paragonite-out reaction curves at elevated pressures, after Eugster et al., 1972).



Although theoretical and analytical evidence is good for a maximum of about 20 to 25% paragonite component in muscovite in medium- and high-grade metamorphic rocks (Albee, 1965c; Albee and Chodos, 1965; Eugster et al., 1972; Thompson, 1974; Guidotti, 1970 and 1978; Tracy, 1978; Cheney and Guidotti, 1979), there is abundant evidence for greater amounts of solid solution under apparently different conditions (Rosenfeld, 1956; Rosenfeld et al., 1958; Zen and Albee, 1964; McNamara, 1965; Hall, 1970; Thompson et al., 1977; Rumble, 1978; Abbott, 1979; Labotka, 1980; this work).

The least retrograded samples from the study area have muscovite with paragonite contents up to 33.4%, and even the most retrograded muscovites have average paragonite contents of 16.7%, although some rims are as low as paragonite 9.5% (sample NS85). Robinson, Hall, and Ahmad (unpublished X-ray diffraction data, 1970) have determined that muscovite in schists with up to 31% paragonite component (sample 836, Ca-free muscovite) exists in the Orange area, Massachusetts, without paragonite, exolved white mica, or mixed layer phases. It is not yet clear why there is such a discrepancy between theoretical, laboratory and various field observations of muscovite Na content.

#### TiO<sub>2</sub>-(Fe,Mn)O-H<sub>2</sub>O System

Figure 30 is the ternary system: TiO<sub>2</sub>-(Fe,Mn)O-H<sub>2</sub>O, which represents the major oxides (anatase and ilmenite) and three of the most important silicates in the study area (staurolite, biotite, and chlorite). The system is projected from quartz, muscovite, graphite,

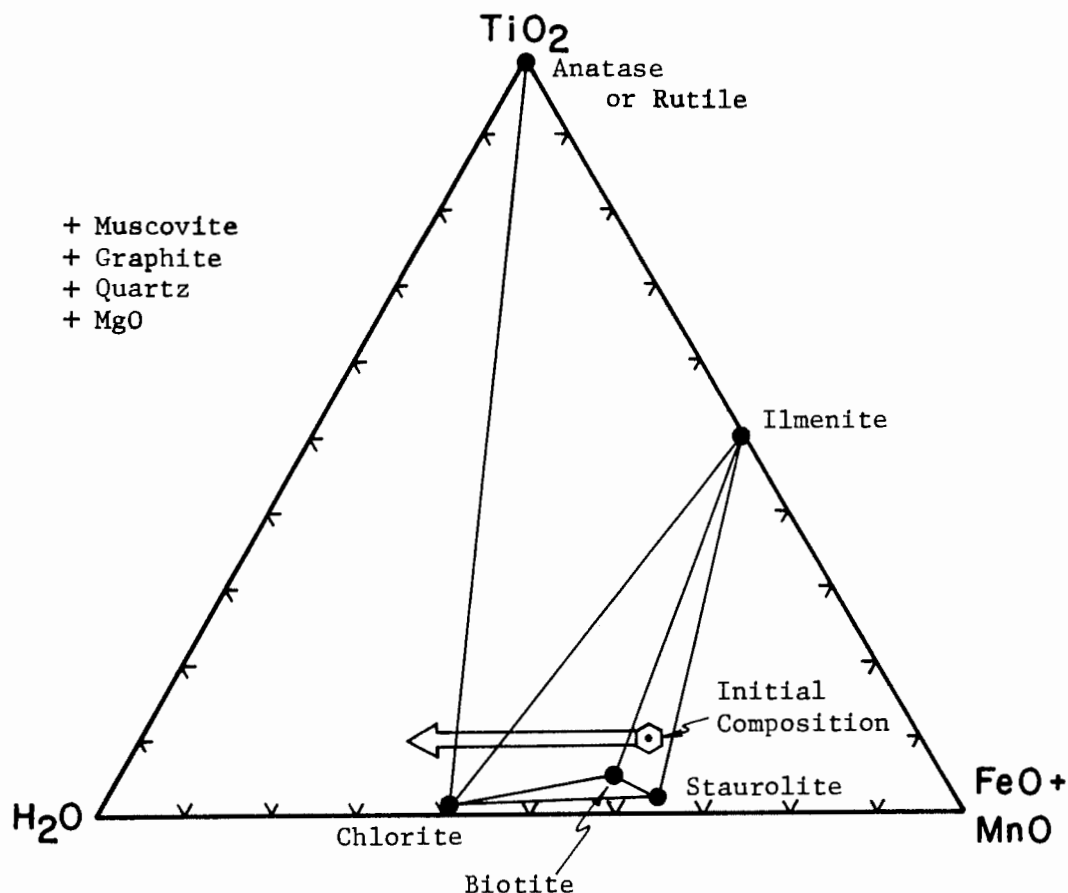


Figure 30.  $\text{TiO}_2$ -(Fe,Mn)O- $\text{H}_2\text{O}$  chemical system relating the major silicate assemblages to oxides. The initial prograde bulk composition is relatively anhydrous, and retrograde hydration caused the bulk composition to move into fields of more hydrous assemblages, the most hydrous being anatase-chlorite.

and MgO. Garnet contains substantial quantities of calcium and lies outside the system. This system is extremely simplified and in some ways misleading, but nevertheless relates changes in oxide and silicate assemblages with the degree of retrograde hydration of the relatively anhydrous prograde assemblages.

Prograde assemblages occurred in the relatively anhydrous three phase field: ilmenite-biotite-staurolite. Addition of water to the

rock resulted in staurolite breakdown, moving the bulk composition into the more hydrous ilmenite-biotite-chlorite three phase field. Although anatase does occur in some rocks with staurolite and biotite, anatase is much more common in biotite-staurolite-free rocks. Further addition of water moved the rock composition into the three phase field, anatase-chlorite-ilmenite, a very common assemblage in the most severely retrograded rocks within the retrograde garnet isograd. Further rock hydration would produce anatase and chlorite at the expense of ilmenite, although in no rock was ilmenite completely destroyed.

#### AKFM Tetrahedron

Much of the discussion in the following pages will concern projections out of the AKFM four component system, shown in Figure 31. A brief comment on this very important system is in order. First and most important, the K-apex includes sodium, and is located at  $(K,Na)AlO_2$  rather than extending to  $(K,Na)_2O$ , to eliminate much mineralogically useless volume. MnO has also been added to the F-apex. Note the wide composition fields of biotite and muscovite. Chlorite and garnet Fe/Fe+Mg ratios vary, resulting in composition fields paralleling the F-M edge. Both garnet and chlorite fields vary somewhat in width due to variable  $Ca/Ca+M^{+2}+Al$  in garnet, and  $Al/M^{+2}+Al$  in chlorite. Staurolite and chloritoid composition fields are exaggerated in size. The composition ranges of these two minerals is very restricted in the study area, although pure iron end members

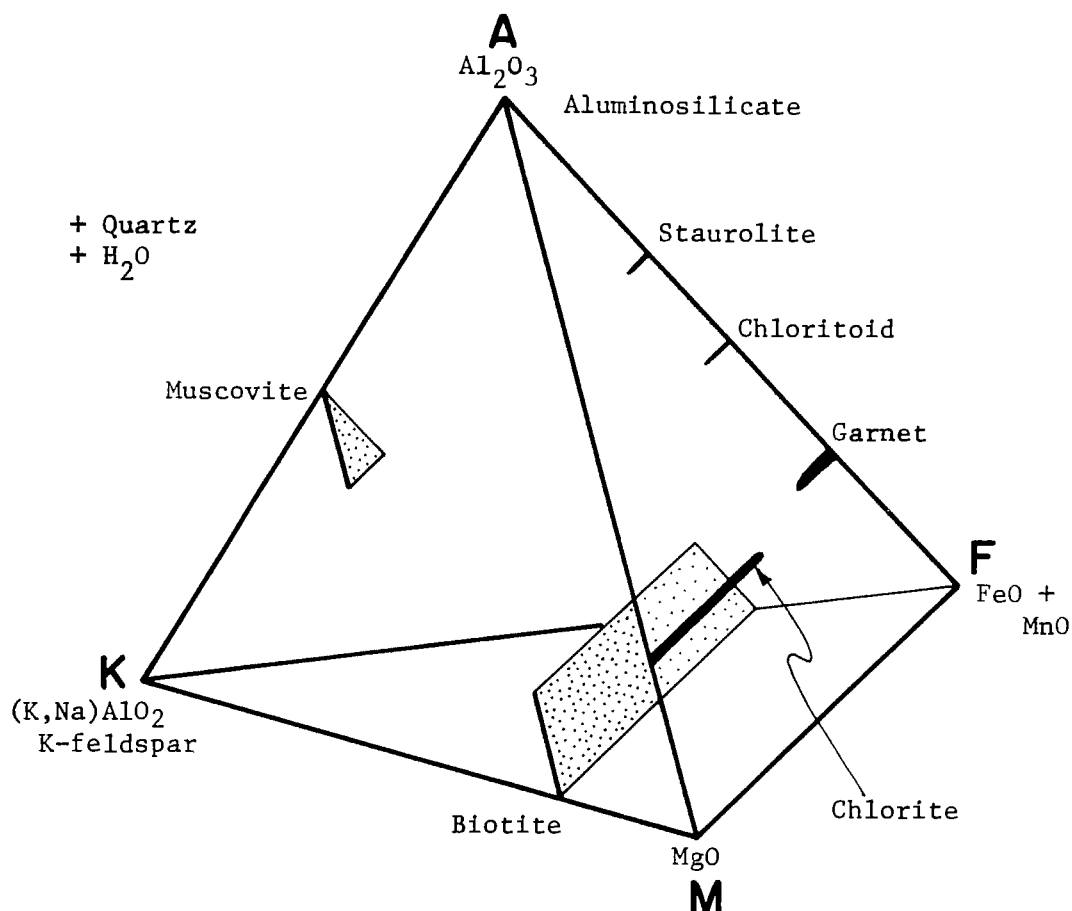


Figure 31. AKFM tetrahedron, showing the most important silicates present in the study area. At the K-apex alkalis are present as  $(K,Na)AlO_2$ , with the aluminum subtracted from the A-apex. Sodium pertains only to that in muscovite, biotite, and K-feldspar solid solutions.  $MnO$  is added to the F-apex. Projections out of the AKFM volume will be used profusely in later parts of this work.

have been produced in the laboratory (Richardson, 1967a, 1967b, 1968; Ganguly, 1972).

Two projections out of the AKFM volume are utilized in this study. The first is the projection of all phases from muscovite onto the AFM face, after Thompson (1957). This widely utilized graphic method leaves all alkali-deficient minerals on the AFM face,

projects biotite compositions to below the F-M edge and projects K-feldspar beyond the F-M edge through infinity to the A-apex.

The second projection to be used is made by projecting the AKFM tetrahedron parallel to the F-M edge onto a plane perpendicular to the F-M edge. This allows continuous and discontinuous reactions involving muscovite to be presented, and will be used later in this work. It is important to note that the F-M edge projection is only used to project thin slices out of the AKFM tetrahedron which contain four phase limiting volumes, to avoid crossing tie lines.

#### Muscovite Projection

Figure 32 is a muscovite projection out of the modified AKFM tetrahedron, on which are plotted average mineral compositions from all seven analyzed samples. Presumably, prior to retrograding sample UO1A was composed of the assemblage: Staurolite-garnet-biotite. The composition of garnet in contact with biotite and staurolite in sample UO1A is the most Mg-rich of the garnet field shown. The first chlorite appeared, as shown, at  $\text{Fe}+\text{Mn}/\text{Fe}+\text{Mn}+\text{Mg}$  ratios of about 0.481, 0.038 lower than 0.519 for coexisting biotite. Sample NS118 is similar to UO1A but slightly more retrograded. The interval between data from samples NS118 and the more retrograded sample NS85 represents the completion of staurolite breakdown, which released large amounts of iron to the sheet silicates.

Biotite is finally lost from the assemblage, as in sample NS90, probably by limiting alkali reactions involving muscovite and

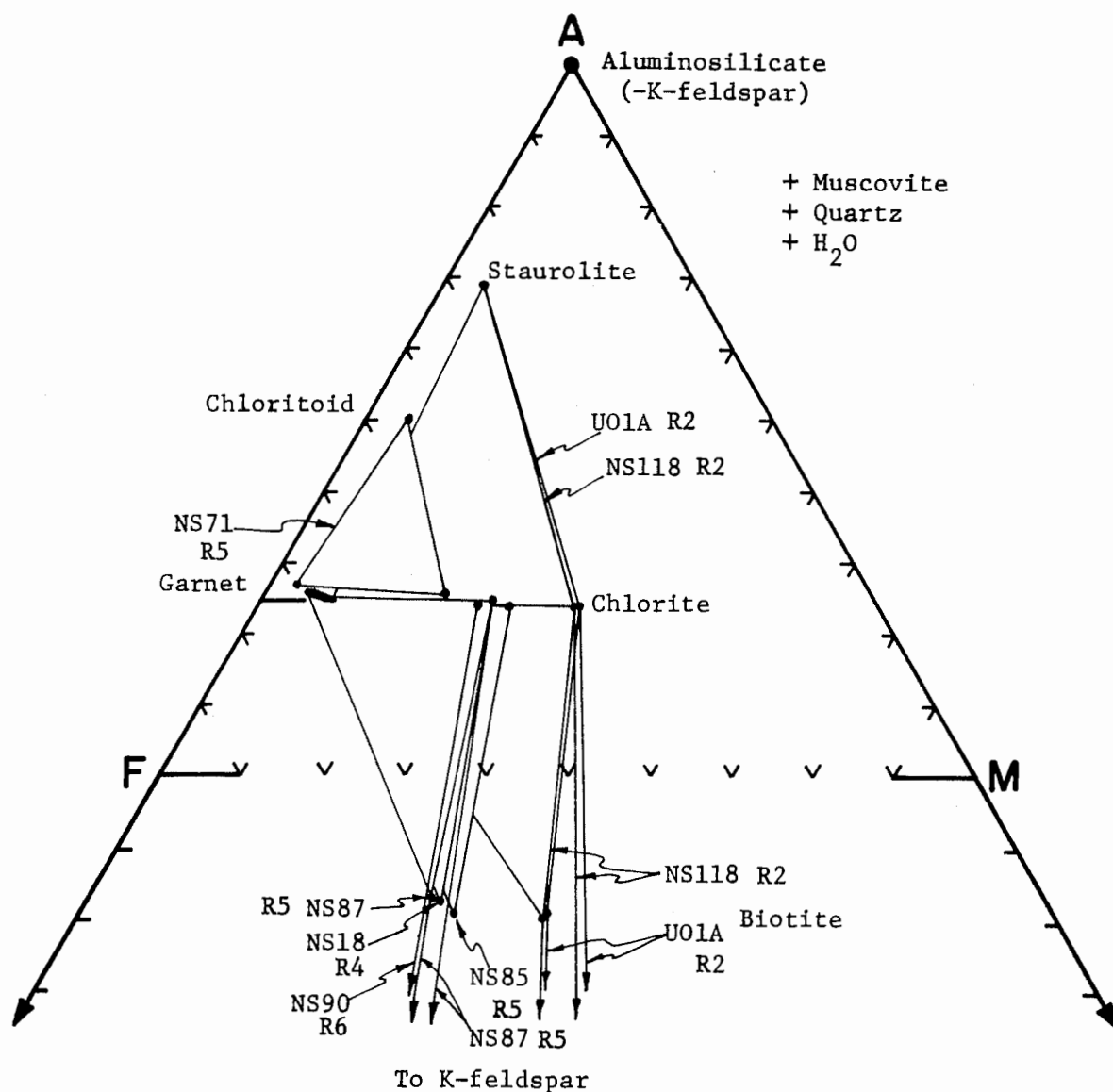


Figure 32. Muscovite projection showing averages of electron microprobe mineral analyses for all seven samples, and tie lines connecting coexisting phases. Note the progression of biotite and chlorite toward higher iron compositions with retrograding. The garnet field is rather wide due to variable grossular component, which is not in this projection. Tie lines to K-feldspar are radial to the A-apex.

K-feldspar, discussed below. Because garnet did not reequilibrate with the rest of the rock, the last garnet to vanish was not

constrained to any particular composition. The garnets in sample NS87 were fortuitously unfractured and therefore altered concentrically, resulting in exposure of garnet cores in the extreme Fe-rich end of the garnet composition field shown in Figure 32. Chlorite in sample NS90 is lower in aluminum than chlorite in biotite-bearing samples (Figures 17 and 32) because of constraints imposed by chlorite-muscovite-K-feldspar tie planes rather than biotite-chlorite-muscovite-garnet limiting volumes (Figure 40).

Overall, biotite  $\text{Fe}+\text{Mn}/\text{Fe}+\text{Mn}+\text{Mg}$  ratios vary from 0.519 in sample U01A to 0.640 in sample NS87. Chlorite ratios vary from 0.481 to 0.625 for samples containing biotite, and 0.640 for sample NS90 which no longer contains biotite.

Sample NS71 is unique in containing chloritoid. Chloritoid and grossular-rich garnet, with celadonite-poor, iron-rich muscovite constrain chlorite to high aluminum compositions, with a very high  $\text{Fe}+\text{Mn}/\text{Fe}+\text{Mn}+\text{Mg}$  ratio of 0.701. Little else can be said about this assemblage at this point because of its scarcity.

## RETROGRADE REACTIONS

### Introduction

In this chapter the chemical reactions that probably occurred during retrograde metamorphism will be examined. The reactions have been revealed by careful consideration of rock petrology and texture, as seen in the field and thin section and by the use of electron microprobe mineral analyses. The stoichiometry of chemical reactions

is critically dependent on mineral composition. This study supports the use of realistic mineral compositions, and the compositions proposed for sheet silicates by Holdaway (1980).

The petrologic literature was of limited value in deciphering the chemical reactions that occurred during the retrograde episode. The sequence of retrograde assemblages appears to be superficially very similar to published sequences of prograde-type assemblages (Thompson, 1957; Zen, 1960; Albee, 1965b and 1968; Evans and Guidotti, 1966; Turner, 1968; Seifert, 1970; Thompson, 1976b; Thompson et al., 1977). Many published prograde reactions appear to be superficially similar to the retrograde reactions, but in fact most are not supported by the evidence in the New Salem area (Turnock, 1960; Fawcett, 1963; Fawcett and Yoder, 1963; Velde, 1965; Richardson, 1967b and 1968; Hoschek, 1968; Hsu, 1968; Ganguly, 1969a and 1972; Kramm, 1973; Ramsay, 1973; Thompson, 1976a; Ferry, 1979; Labotka, 1980). In some cases, reactions have been published that do appear to be similar to certain retrograde reactions in the study area (Hoschek, 1967 and 1969; Hsu, 1968), or at least such reactions have been implied or hinted at in the discussion (Chayes, 1955; Ernst, 1963; McNamara, 1966; Mather, 1970; Kramm, 1973; Itaya and Banno, 1980).

The retrograde metamorphic reactions are of three types: 1) Reactions that consume minerals of prograde origin, for example sillimanite, staurolite, biotite, ilmenite, and garnet, and create new minerals, such as chlorite, chloritoid, and anatase. 2)



Continuous solid solution composition changes of the sheet silicates of both prograde and retrograde origin. 3) Combinations of the above reactions occurring simultaneously.

A number of minerals will not be discussed in this section. The accessory minerals zircon, apatite, rutile, allanite, and tourmaline will be ignored due to their minor abundance, apparent ambivalence to the retrograde process, or lack of data. Quartz is an excess inert component that will be shown in appropriate reactions but not discussed. Plagioclase is relatively common but apparently does not take part in any retrograde reactions.

#### Sillimanite-Out Reaction

Sillimanite was the first mineral of the prograde assemblage to disappear in the retrograded rocks. Sillimanite is commonly replaced by intergrowths of randomly oriented secondary muscovite in rocks not associated with any specific retrograded zone, so the following discussion may be applicable to many rocks outside of the New Salem area.

To put the retrograde reaction into proper perspective, Figure 33a to 33b shows the change in phase relations in muscovite projection during the reaction which first allowed sillimanite to coexist with biotite, with increasing metamorphic grade (reaction (1)). Muscovite-staurolite-chlorite tie planes in the AKFM volume are broken in favor of muscovite-sillimanite-biotite tie planes, by the reaction:

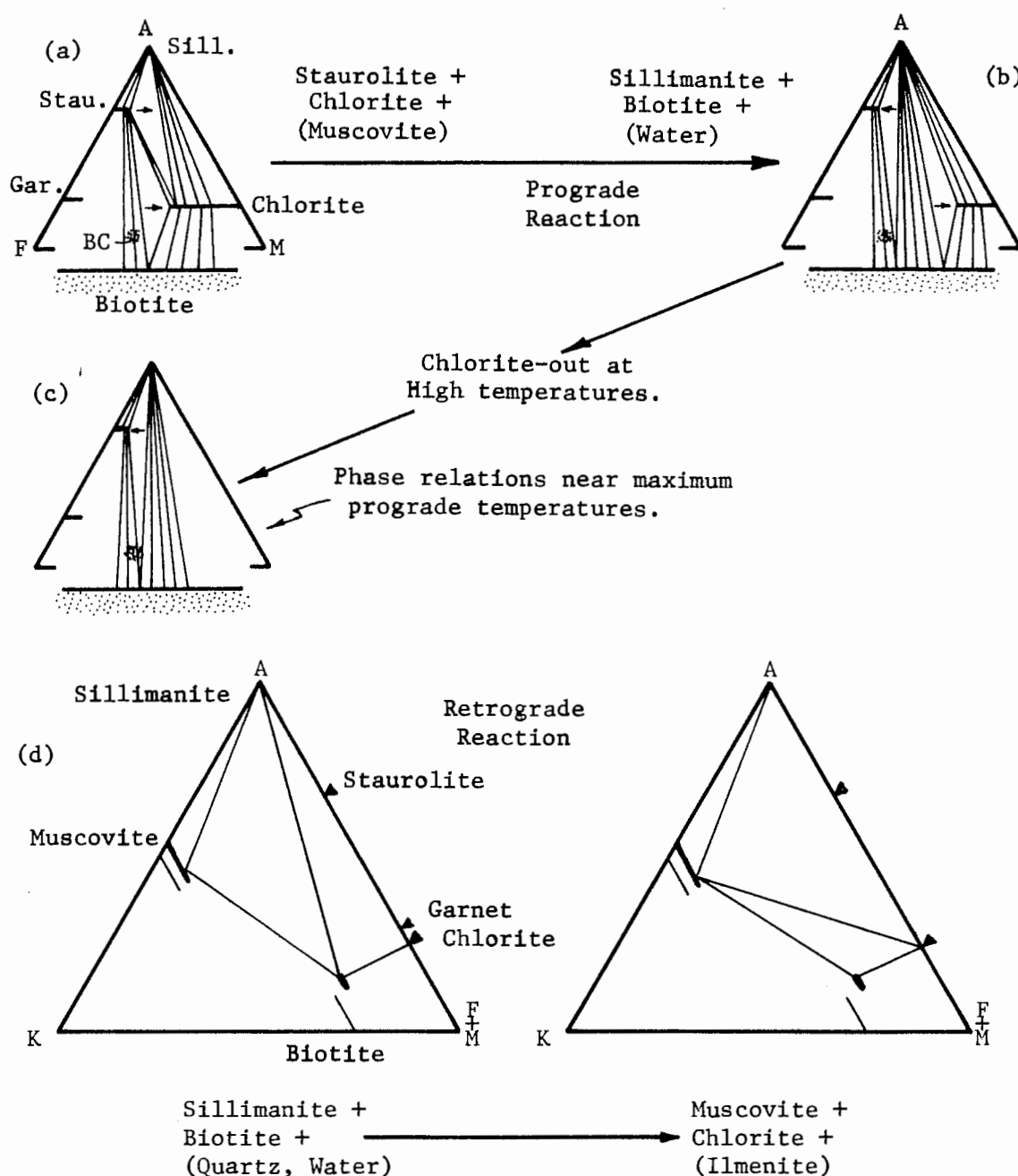
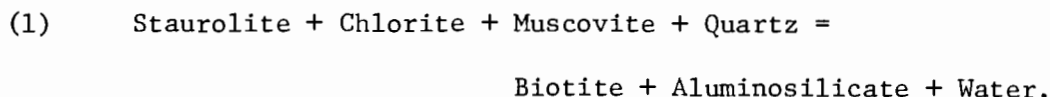


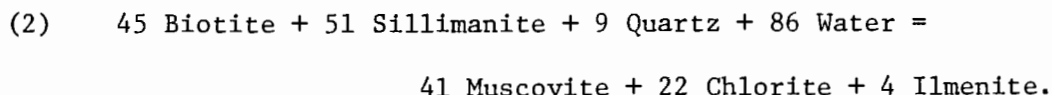
Figure 33. Reactions involving sillimanite. a) Muscovite projection showing the change in phase relations resulting from the prograde dehydration reaction:  $\text{Staurolite} + \text{chlorite} + \text{muscovite} = \text{sillimanite} + \text{biotite} + \text{water}$ . Chlorite probably does not persist to high temperatures (b to c). d) F-M edge projection showing the retrograde change of phase relations within the AKFM volume. Note that no staurolite is produced in the retrograde reaction, as would be required by the reverse of the prograde reaction.



This reaction apparently occurs in the kyanite zone in central Massachusetts, well to the west of the study area (Robinson, 1963; Hall, 1970; Tracy et al., 1976).

The first appearance of sillimanite in rocks of the Littleton Formation (Figure 5, prograde sillimanite-in isograd) probably occurred by pivoting of the sillimanite-staurolite-biotite three phase field toward higher iron compositions, to allow the rock composition to become embedded in the field of sillimanite stability (Figure 33b to 33c). Alternatively, prograde production of ilmenite and/or Fe-rich garnet could have driven the effective bulk composition in the muscovite projection toward higher Mg compositions for the same result.

Note in Figure 33a and in the sillimanite-in reaction (1) that the reverse of the prograde reaction clearly requires the production of staurolite at the expense of biotite and sillimanite. This does not take place during retrograde metamorphism, as there is no petrologic evidence for the retrograde production of staurolite in those rocks having contained sillimanite. Figure 33d shows the compatibility changes in F-M edge projection that occur in the probable retrograde reaction. The balanced equation for the reaction using electron microprobe analyses is as follows:



The reaction is in fact more complex than it appears. It decreases the modal proportion of biotite, increases modal muscovite, and marks the first appearance of chlorite. The muscovite component released during biotite breakdown is enriched in Na relative to remaining biotite, and enriched in potassium relative to prograde muscovite. This requires that the compositions of the biotite and muscovite reservoirs change with respect to K and Na. Similarly the chlorite component released during biotite breakdown is enriched in Mg relative to remaining biotite, requiring a redistribution of Mg and Fe between the two minerals. Also, initiation of the sillimanite-out reaction probably marks the beginning of muscovite composition change toward celadonite.

The constraints of rational tie lines, changing mineral compositions, and homogeneous biotite and chlorite require simple charge coupled cation exchange reactions to occur continuously during sillimanite breakdown. The cation exchanges are  $\text{Na} = \text{K}$  for biotite-muscovite pairs (Figure 26) and  $\text{Fe} = \text{Mg}$  for biotite-chlorite pairs (Figure 32). Substitution of divalent cations into muscovite occurs primarily by the tschermaks substitution,  ${}^{\text{IV}}\text{Al} {}^{\text{VI}}\text{Al} = \text{SiM}^{+2}$ .

Figure 34 schematically shows the retrograde sillimanite-out reaction, coupled with re-equilibration reactions of the sheet silicates. The sheet silicate reservoirs, shown in boxes, represent the modal proportions of those minerals that take part in the reactions and change composition with retrograde metamorphism. Thick arrows represent the main pathways of reaction components,

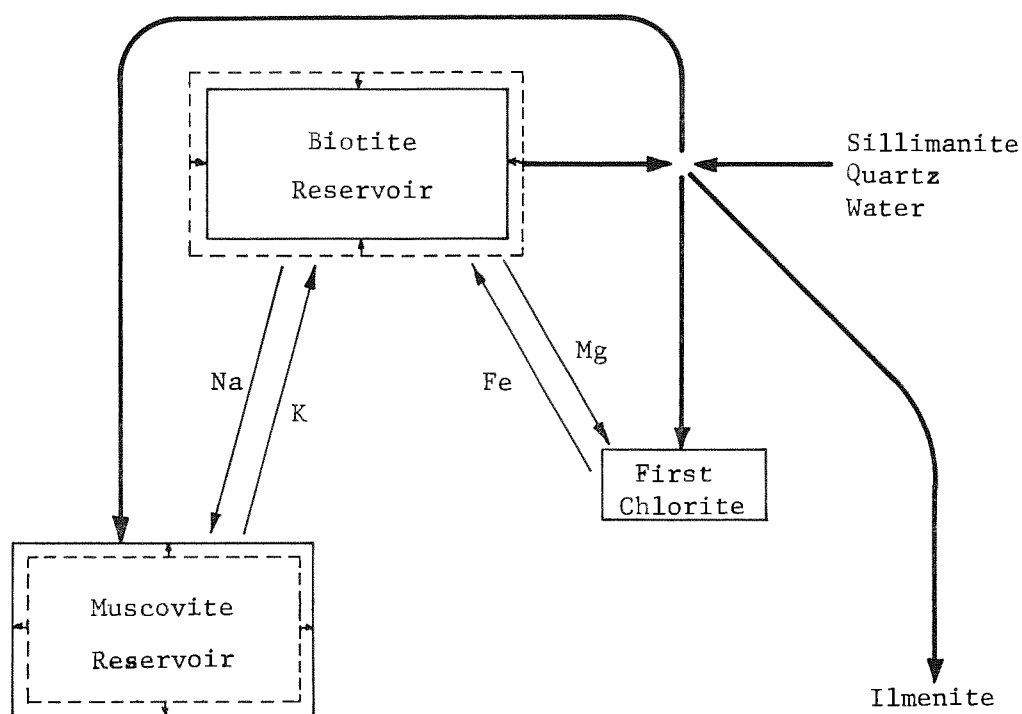


Figure 34. Schematic of the retrograde sillimanite-out reaction: (2) Biotite + sillimanite + quartz + water = muscovite + chlorite + ilmenite. Biotite preferentially releases its muscovite component enriched in Na, and its chlorite component enriched in Mg. This requires continuous cation exchanges between these minerals to maintain equilibrium, as shown. Titanium released from biotite becomes ilmenite.

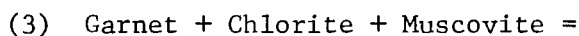
and thin, labeled arrows represent charge coupled cation exchanges that serve to maintain rational tie lines between the sheet silicates.

#### Staurolite-Out Reaction

Staurolite was much more abundant in the prograde rocks than was sillimanite in the study area. Staurolite was consumed by retrograde hydration reactions within the retrograde sillimanite-out isograd (zones R3 to R6). As with the sillimanite-out reaction,

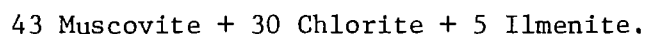
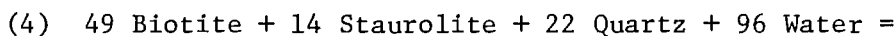
the staurolite-out reaction will be compared to the prograde first appearance reaction.

Figure 35a shows in muscovite projection the phase relation change which first allowed staurolite to coexist with biotite in pelitic schists. The prograde reaction may be written as follows:



This reaction may be viewed as the breaking of garnet-chlorite-muscovite tie planes in favor of staurolite-biotite-muscovite tie planes within the AKFM tetrahedron. While it has been demonstrated that this reaction can occur in schists during prograde metamorphism, the reverse did not take place during retrograde metamorphism. There is no petrographic evidence for the retrograde production of garnet, and garnet generally appears to be unaffected by the retrograde process until staurolite has vanished.

Figure 35b shows the change in phase relations in F-M edge projection as it appears in retrograded rocks. Note that garnet is not involved in the reaction. Using analyzed compositions of coexisting phases, the balanced retrograde reaction that consumed staurolite is as follows:



Ilmenite (rarely rutile) is apparently the sink for titanium released during biotite breakdown, as described previously.

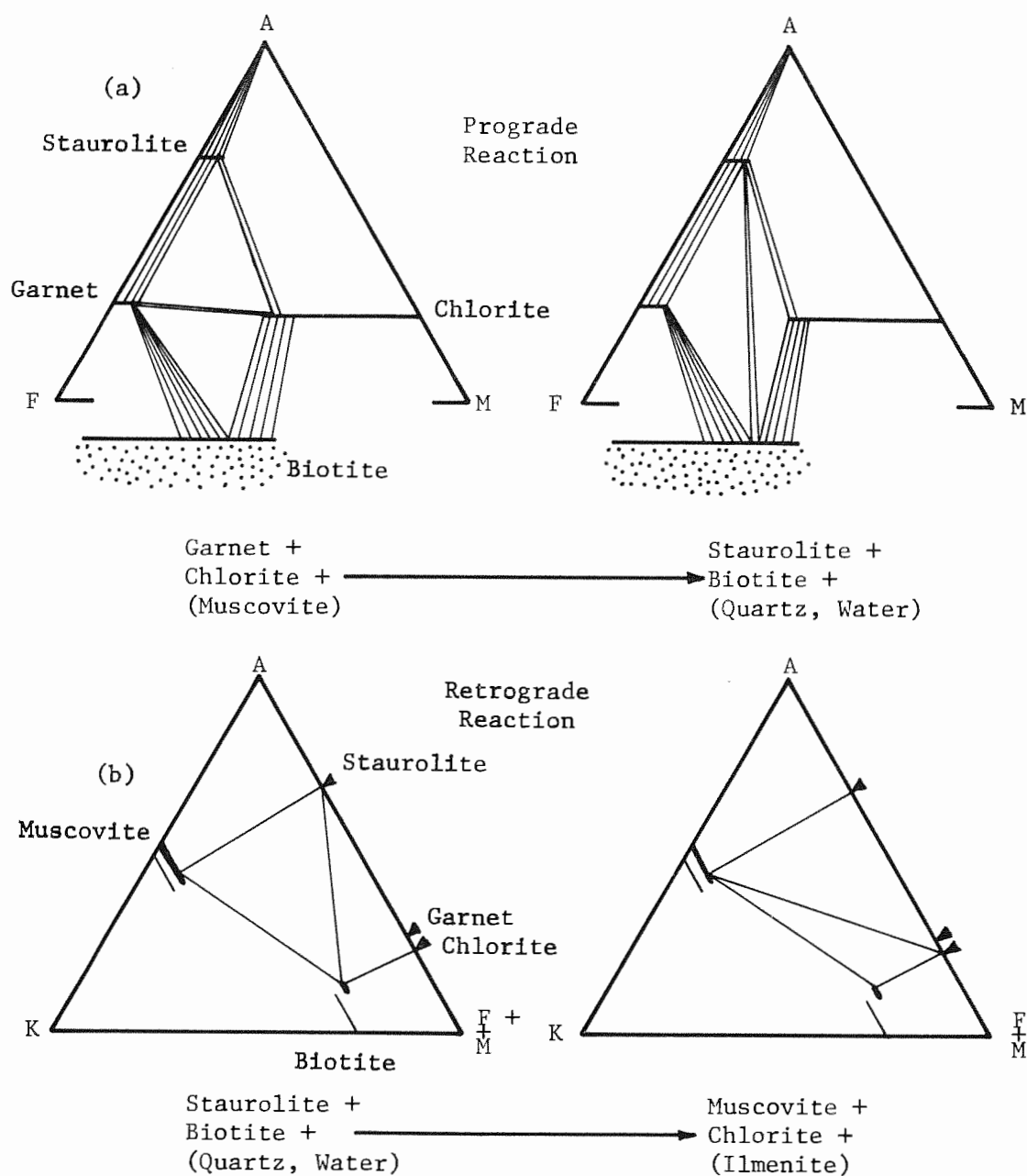


Figure 35. Reactions involving staurolite. a) Muscovite projection showing the change in phase relations by the prograde dehydration reaction: (3)  $\text{Garnet} + \text{chlorite} + \text{muscovite} = \text{staurolite} + \text{biotite} + \text{water}$ . The retrograde reaction shows similar changes, but does not involve garnet. b) F-M edge projection showing the change of phase relations within the AKFM tetrahedron that take place via the retrograde hydration reaction: (4)  $\text{Staurolite} + \text{biotite} + \text{quartz} + \text{water} = \text{muscovite} + \text{chlorite} + \text{ilmenite}$ . It can be seen that the retrograde staurolite-out reaction does not involve garnet.

Because staurolite has a high Fe/Fe+Mg ratio, its destruction may result in a dramatic change in the Fe/Fe+Mg ratios of the relict sheet silicates. Both biotite and chlorite in rocks with only pseudomorphs after staurolite are significantly more iron-rich than in rocks containing abundant staurolite. The reaction also consumes large amounts of biotite, allowing changes in K/K+Na ratios of coexisting biotite-muscovite pairs. Muscovite becomes substantially more phengitic with the disappearance of staurolite (Figure 16). Rational tie lines are maintained between coexisting biotite-muscovite and biotite-chlorite pairs.

Charge-coupled cation exchanges allow re-equilibration between the sheet silicates, as described above. Figure 36 shows the staurolite-out reaction drawn schematically. The sheet silicates are depicted as variably sized boxes to indicate that they represent relatively homogeneous chemical reservoirs that change in abundance and composition as the reaction proceeds. The pathways of major reaction components are shown as thick arrows and cation exchanges that occur between the sheet silicates are shown as thin, labeled arrows. Staurolite does not change composition during alteration, within analytical uncertainty.

#### K-feldspar-In Reaction

The coexisting pair chlorite-K-feldspar, is one of the best indications of low temperatures during retrograde metamorphism. Knowledge of the reactions producing chlorite-K-feldspar assemblages



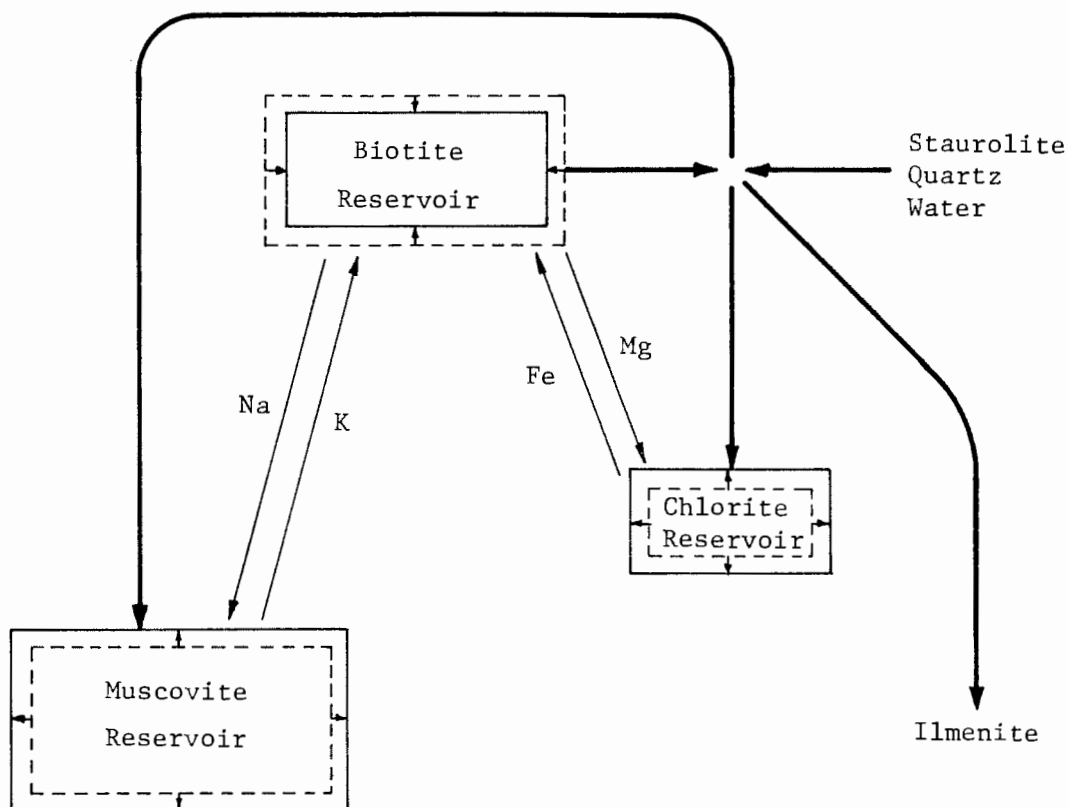


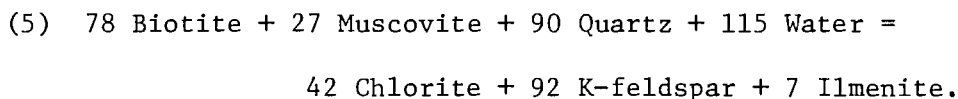
Figure 36. Schematic diagram of the staurolite-out reaction: (4)  $\text{Staurolite} + \text{biotite} + \text{quartz} + \text{water} = \text{muscovite} + \text{chlorite} + \text{ilmenite}$ . Included are the continuous coupled cation exchange reactions that produce continuous composition changes in the sheet silicates while maintaining rational tie lines.

in the New Salem area may have important implications for the understanding of low-grade metamorphic rocks generally.

K-feldspar forms very early in the retrograde sequence, occurring in samples containing relict staurolite. Although chlorite-K-feldspar tie lines are probably stable in the retrograde limiting assemblage (quartz-muscovite-chlorite-K-feldspar-sphene-anatase-graphite $\pm$ plagioclase), it should be stressed that K-feldspar (sanidine) entirely enclosed within biotite is not stable with

respect to microcline, nor probably with the rest of the rock.

The first coexisting chlorite-K-feldspar pair probably initiated at very high Mg compositions (Figure 37a). As biotite broke down, the K-feldspar-chlorite-biotite three phase field swept continuously toward higher Fe compositions. This mechanism is probably analogous to prograde relations (Mather, 1970). Chemical data indicate that the three phase chlorite-biotite-K-feldspar field is only a few mole percent wide with respect to Fe and Mg (Figure 32). Using electron microprobe analyses, the reaction can be written as follows:



As in reactions (2) and (4), it was assumed that ilmenite was the sink for titanium released from biotite.

The phase relation changes produced by this reaction can best be seen in F-M edge projection (Figure 37b). There it is clear how biotite-muscovite tie lines are broken in favor of K-feldspar-chlorite tie lines. Because K-feldspar is nearly pure end member composition, the mica components used in the above reaction must necessarily also have been nearly pure end member, tending to enrich the remaining micas in Na. Na enrichment is not evident in most rocks because other reactions occurring contemporaneously were probably forcing mica compositions toward lower sodium, and because of the small quantities of K-feldspar produced. An exception is sample NS90, which contains roughly two modal percent K-feldspar, no

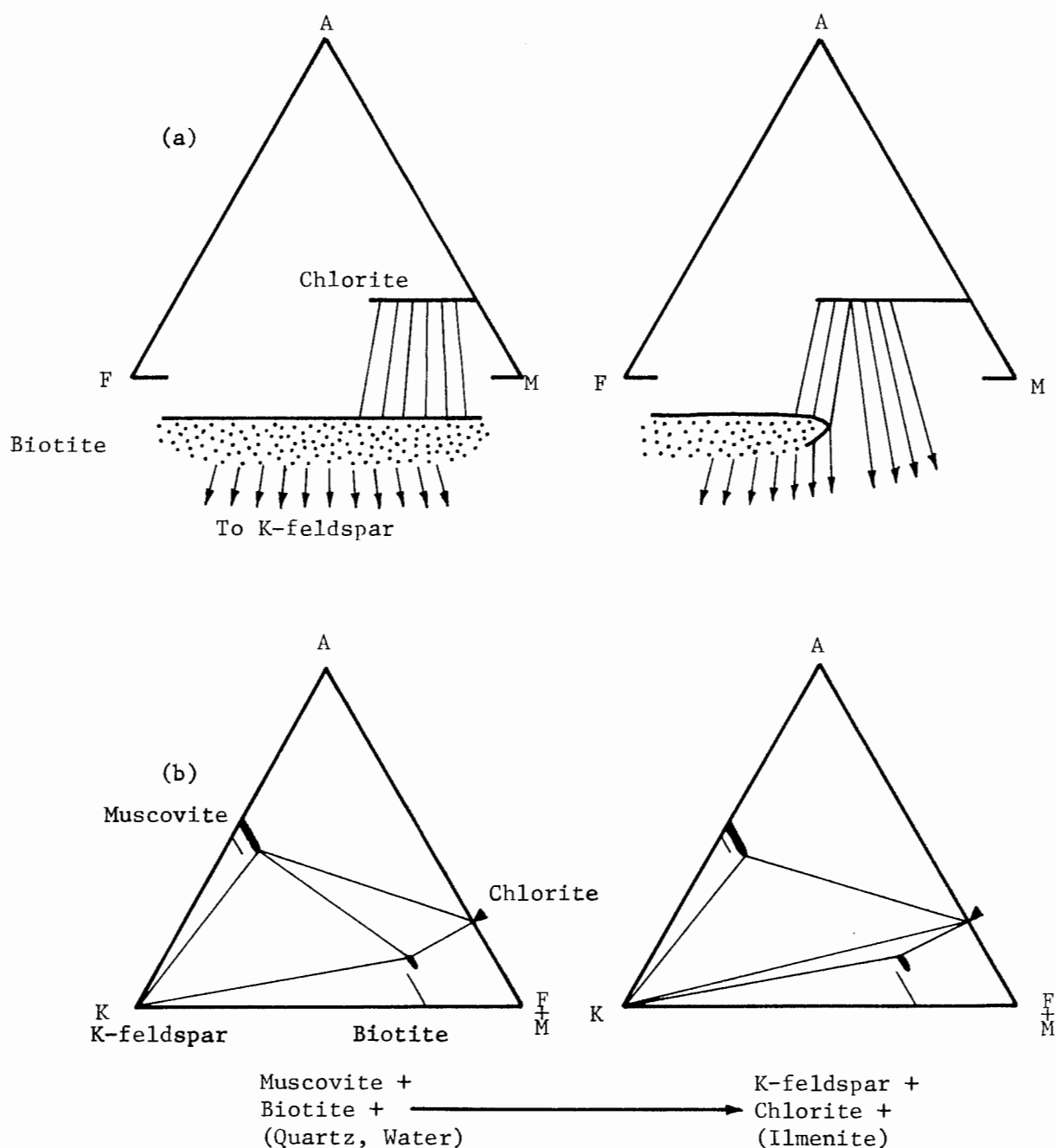


Figure 37. The K-feldspar-producing reaction (5), two views. a) The three phase stability field of chlorite-biotite-K-feldspar probably initiated at the Mg side of the diagram, and proceeded toward iron-bearing compositions by the reaction: Biotite + muscovite + quartz + water = chlorite + K-feldspar + ilmenite. b) This reaction is shown in F-M edge projection as the breaking of muscovite-biotite tie lines in favor of chlorite-K-feldspar tie lines.

relict biotite, and more sodic muscovite than other less retrograded samples.

As with the previous sillimanite- and staurolite-out reactions (2 and 4), K-feldspar production also results in substantial changes in sheet silicate compositions. A schematic of the K-feldspar producing reaction is shown in Figure 38, where the pathways of major reaction components are shown as thick arrows and coupled cation exchanges between sheet silicates in thin, labeled arrows. Note that muscovite is consumed in the reaction but is still the major sink for sodium, allowing nearly pure end member K-feldspar to be produced.

#### Garnet-Out Reactions

Introduction. In the Littleton Formation there is scarcely an outcrop that is not abounding with almandine-rich garnets or their pseudomorphs. The garnets were replaced by chlorite and chlorite-muscovite intergrowths in a regular manner (Figures 9 and 10), as described above. Notwithstanding the regular progression of replacement, the reactions by which garnet disappeared were apparently quite complex.

In the previous three sections there was only one reasonable reaction each, governing the replacement of sillimanite and of staurolite, and the formation of K-feldspar. Garnet-out reactions are more complex than sillimanite, staurolite, and K-feldspar reactions for three reasons: 1) The garnet contains calcium.

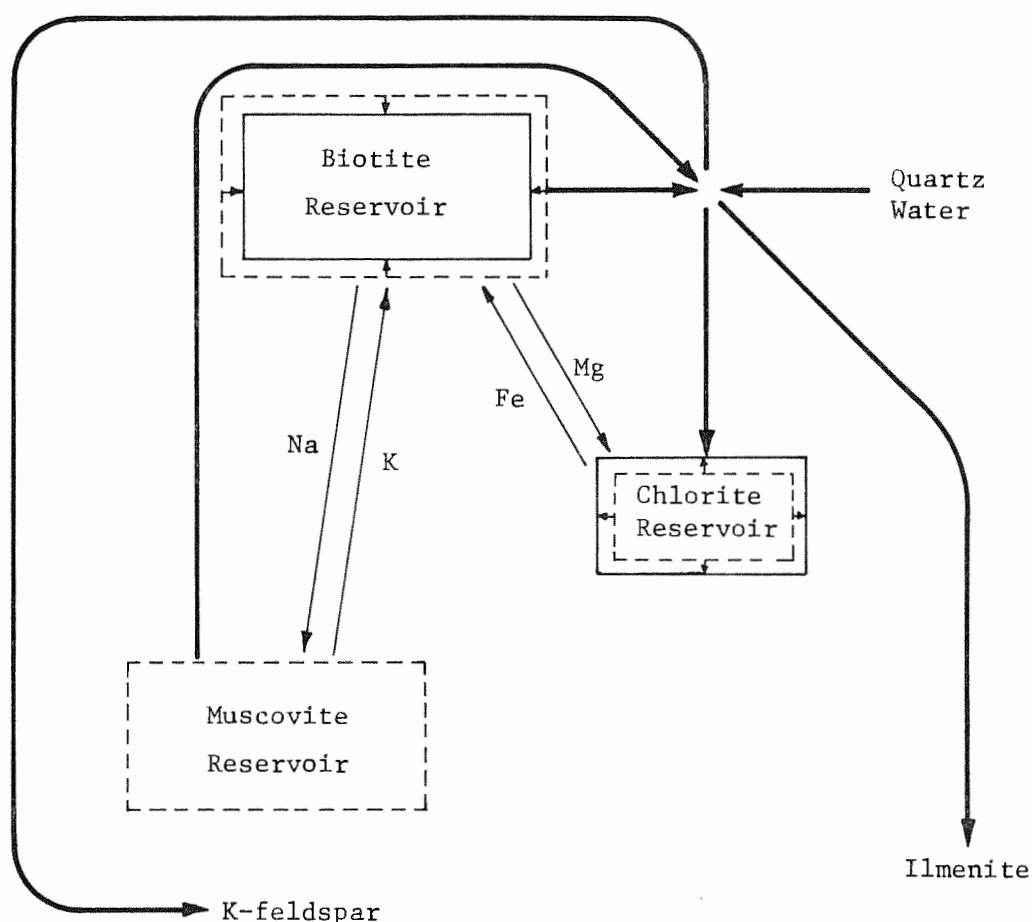


Figure 38. Schematic of the K-feldspar-in reaction: (5) Biotite + muscovite + quartz + water = chlorite + K-feldspar + ilmenite. Also shown are the continuous coupled cation exchange reactions necessary for the production of nearly end-member K-feldspar while changing sheet silicate compositions and maintaining rational tie lines. Although muscovite is consumed in this reaction, other reactions probably produced muscovite concurrently so the direction of change in the size of the muscovite reservoir is not certain.

2) The garnet is strongly zoned, with calcium-rich cores and calcium-poor rims. 3) In some severely retrograded rocks, the garnet cores are altered only after the final disappearance of biotite (based on relationships seen in thin section). This means that at least three reactions must govern garnet breakdown, depending on

bulk composition: Early reaction of garnet rims with biotite present, reaction of garnet cores with biotite present, and the terminal reaction of garnet cores with biotite absent. In addition, calcium from the grossular component must have had a place to go. Petrographic and chemical evidence indicates that the sink for calcium during garnet breakdown was probably sphene, similar to evidence found by Itaya and Banno (1980).

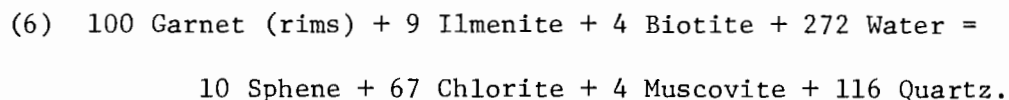
For simplicity, two different garnet compositions will be used to construct approximate chemical reactions, all of which will be normalized to 100 garnet formula units for comparison purposes. The two compositions will be representative of average core and rim analyses taken from the well analyzed garnet in sample U01A (Table 6 and Figure 10a), shown in Table 18.

Table 18. Ideal garnet core and rim compositions. Average core and rim analyses from the analyzed garnet in sample U01A. The average values are used to construct approximate chemical reactions involving garnet. Fe, Mn, and Mg are taken as being equivalent.

Element	Rim	Core
Si	3.000	3.000
Al	2.000	2.000
Fe	2.496	2.275
Mn	0.071	0.229
Mg	0.329	0.250
Ca	0.104	0.246
Total	8.000	8,000

Garnet rim, biotite present reaction. The first reaction involves the retrograding of low calcium garnet rims in the presence of biotite. The rim is about 0.4 mm thick on the common 2 mm diameter garnets, comprising about 85% of the garnet volume. Using the above

garnet rim composition and analyses of other coexisting minerals, the reaction may be written as follows:



This reaction can be depicted best in F-M edge projection (Figure 39),

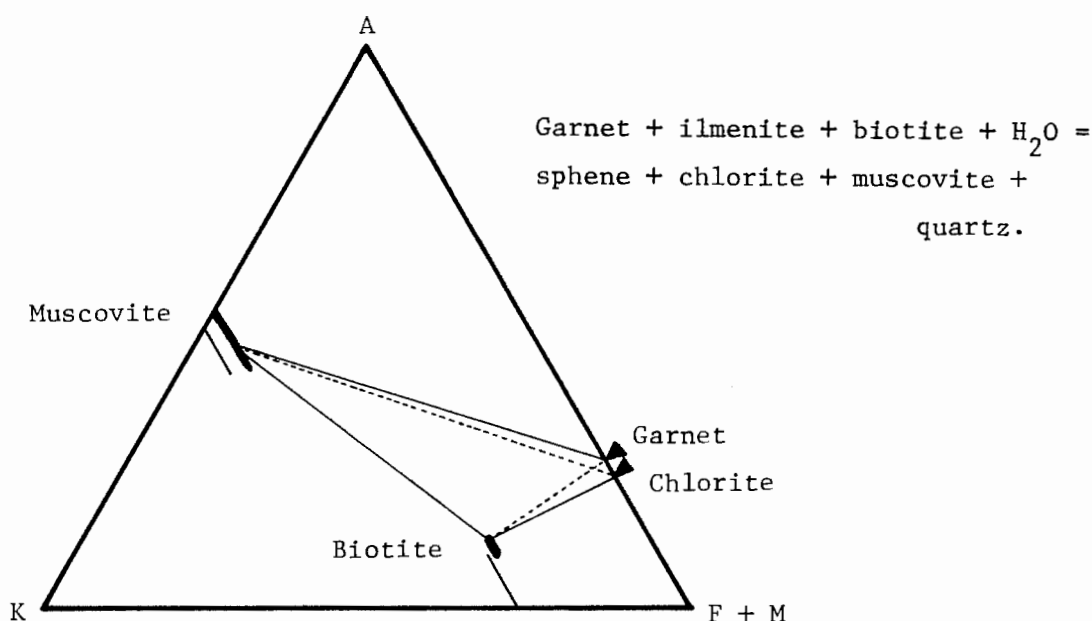
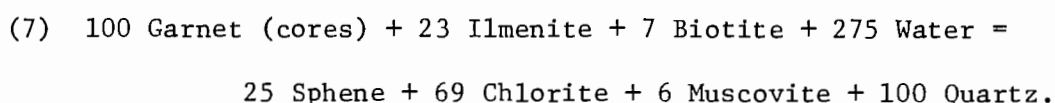


Figure 39. Garnet-out, biotite present phase relation changes shown in F-M edge projection. The general reaction may correspond closely to the reverse of the prograde garnet-in reaction in many metamorphic areas.

where the reaction is shown to take place by breaking garnet-biotite tie lines in favor of chlorite-muscovite tie lines. This reaction accounts for the presence of minor quantities of muscovite in pseudomorphs after garnet, and the association of sphene with relict ilmenite.

Garnet core, biotite present reaction. In many rocks the high calcium garnet cores are exposed with biotite still present. The higher proportion of calcium in garnet cores results in a large increase in the quantity of sphene produced and ilmenite consumed in the reaction. The reaction involving garnet cores and biotite can be written as follows:



It is commonly observed in thin section that pseudomorph cores after garnet contain a higher proportion of muscovite to chlorite than rims. The two preceding reactions suggest that the increase may be due in part to a greater availability of aluminum for muscovite production in the garnet core, as well as reduced diffusion rates caused by the thick chlorite mantle.

Garnet core, biotite absent reaction. The third reaction is that which consumes relict garnet cores in severely retrograded rocks in the absence of biotite. This reaction is proposed to explain the replacement of garnets, particularly just outside of the retrograde garnet-out isograd (Figure 9), in which no relict biotite is present.

The general reaction,  $\text{garnet} + \text{H}_2\text{O} = \text{chlorite} + \text{quartz}$  can proceed almost exactly as a stoichiometric equation because of the very similar  $\text{Al}_2/\text{Al}_2+\text{M}^{+2}$  ratios in those two minerals. In the absence of biotite there is a slight excess of aluminum left over from the simplified reaction, using the average chlorite composition in Table 10 as in other reactions proposed above. In the two



previous reactions, alkalis from biotite allowed the production of secondary muscovite as the aluminum sink, not possible under biotite-absent conditions. The aluminum excess is caused by the fact that the effective garnet core  $Al_2/Al_2+M^{+2}$  ratio (Table 18) is 0.266, higher than the stoichiometric 0.250, because calcium from the grossular component is subtracted from  $M^{+2}$  as sphene. This is done because calcium going into sphene requires little aluminum compared to the other divalent cations going into chlorite.

Although no samples were analyzed that actually had relict garnet in the absence of biotite, trends in chlorite chemistry in the various analyzed assemblages indicate that the garnet +  $H_2O$  = chlorite + quartz reaction may have taken place with a slightly more aluminous chlorite than the previous reactions use. Table 19 is a listing of assemblages in order of decreasing aluminum as seen in muscovite projection, and Figure 40 is a pictorial explanation of how the different assemblages constrain chlorite composition.

Table 19. Listing of various chlorite-muscovite assemblages in order of decreasing  $Al_2/Al_2+Fe+Mn+Mg$  ratios of chlorite. The effective  $Al_2/Al_2+M^{+2}$  ratio in garnet cores is 0.266, with calcium subtracted as a sphene component.

<u>Sample</u>	<u>Assemblage</u>	<u>Chlorite <math>Al_2/Al_2+M^{+2}</math></u>
NS71	Chloritoid-garnet	0.257
Not analyzed	Garnet	Estimated 0.248
U01A, NS118, NS18, NS87, NS85	Garnet-biotite	0.244
Not analyzed	Biotite	-
Not analyzed	Biotite-K-feldspar	-
NS90	K-feldspar	0.240

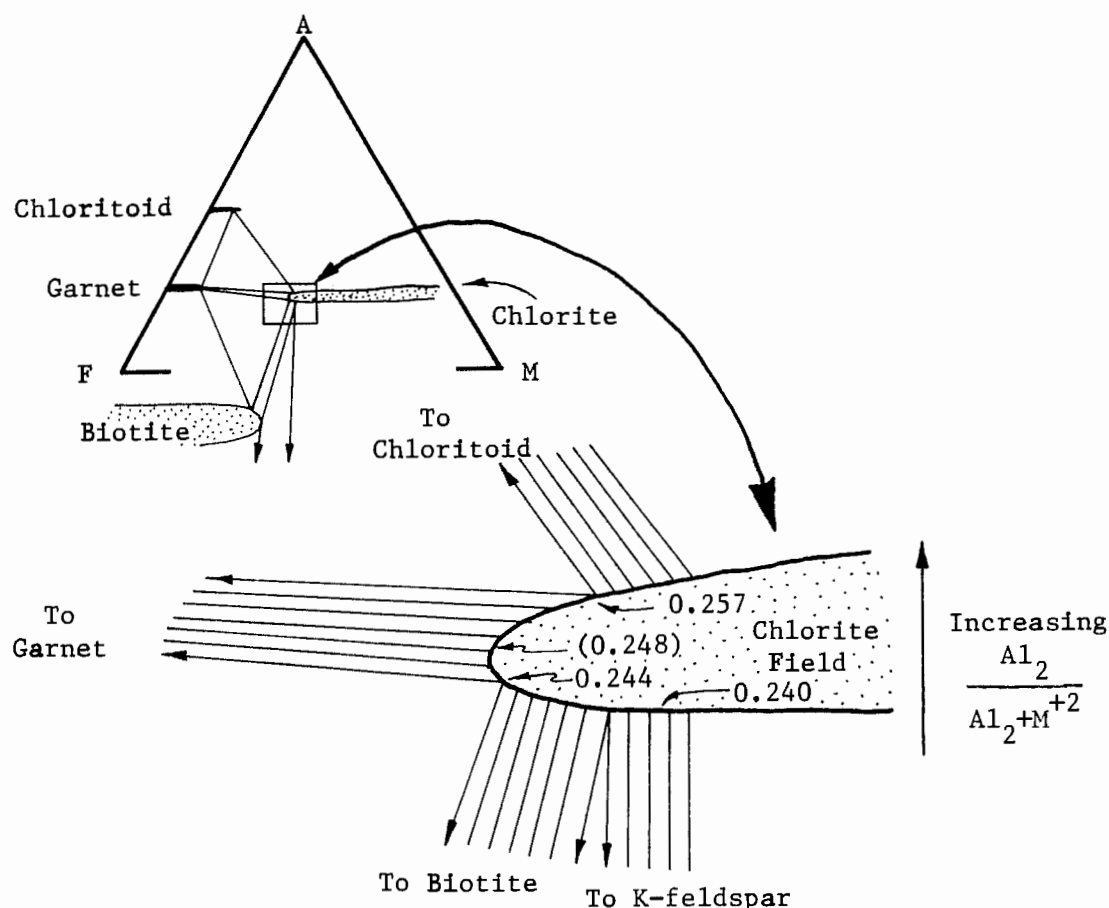
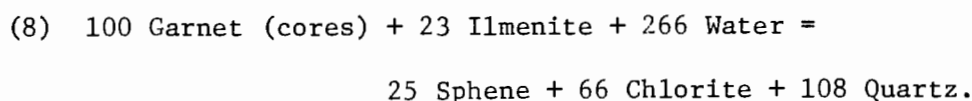


Figure 40. Expanded view of stability fields around chlorite that are pertinent to chlorite  $Al_2/Al_2+Fe+Mn+Mg$  ratios in the discussion of the garnet-out, biotite absent reaction (8). Biotite-absent assemblages allow more aluminous chlorite.  $Fe/Fe+Mg$  ratios at the corners of the three phase fields and the shape of the chlorite field are purely schematic.

Best-fit calculations indicate that the garnet = chlorite reaction can proceed with chlorite  $Al_2/Al_2+M^{+2}$  ratios of about 0.248, about 30% of the way from the average chlorite composition used in preceeding reactions and chlorite in sample NS71. The reaction may therefore be written as follows:



All of the reactions involved in the breakdown of garnet require extensive exchanges of aluminum, alkalis, and  $M^{+2}$  cations between the sheet silicates. Figure 4la schematically shows the first two, essentially similar biotite-present reactions (6 and 7), and Figure 4lb shows the biotite-absent reaction (8). Thick arrows show the pathways of major reaction components, and thin, labeled arrows show the important coupled cation exchange reactions that occur between the sheet silicates to maintain rational tie lines with changing composition. Note that muscovite is produced in the biotite-present reaction (Figure 4la) and is conserved in the biotite-absent reaction (Figure 4lb). It is assumed that muscovite may still become more phengitic during the garnet consuming reactions, although it is not explicit in the data.

#### Biotite-Out Reactions

The sillimanite-out and staurolite-out reactions, the K-feldspar-in reaction, and the two biotite-present garnet-out reactions all consume biotite, but are not necessarily terminal to biotite. In some rocks originally garnet-poor or biotite-rich, biotite was the last prograde ferromagnesian silicate to vanish, based on various types of textural evidence.

Two reactions may be construed to consume biotite in the absence of sillimanite, staurolite, and garnet. The first is the K-feldspar producing reaction (5), described above, that could consume all biotite in rocks with bulk compositions above the K-feldspar-chlorite

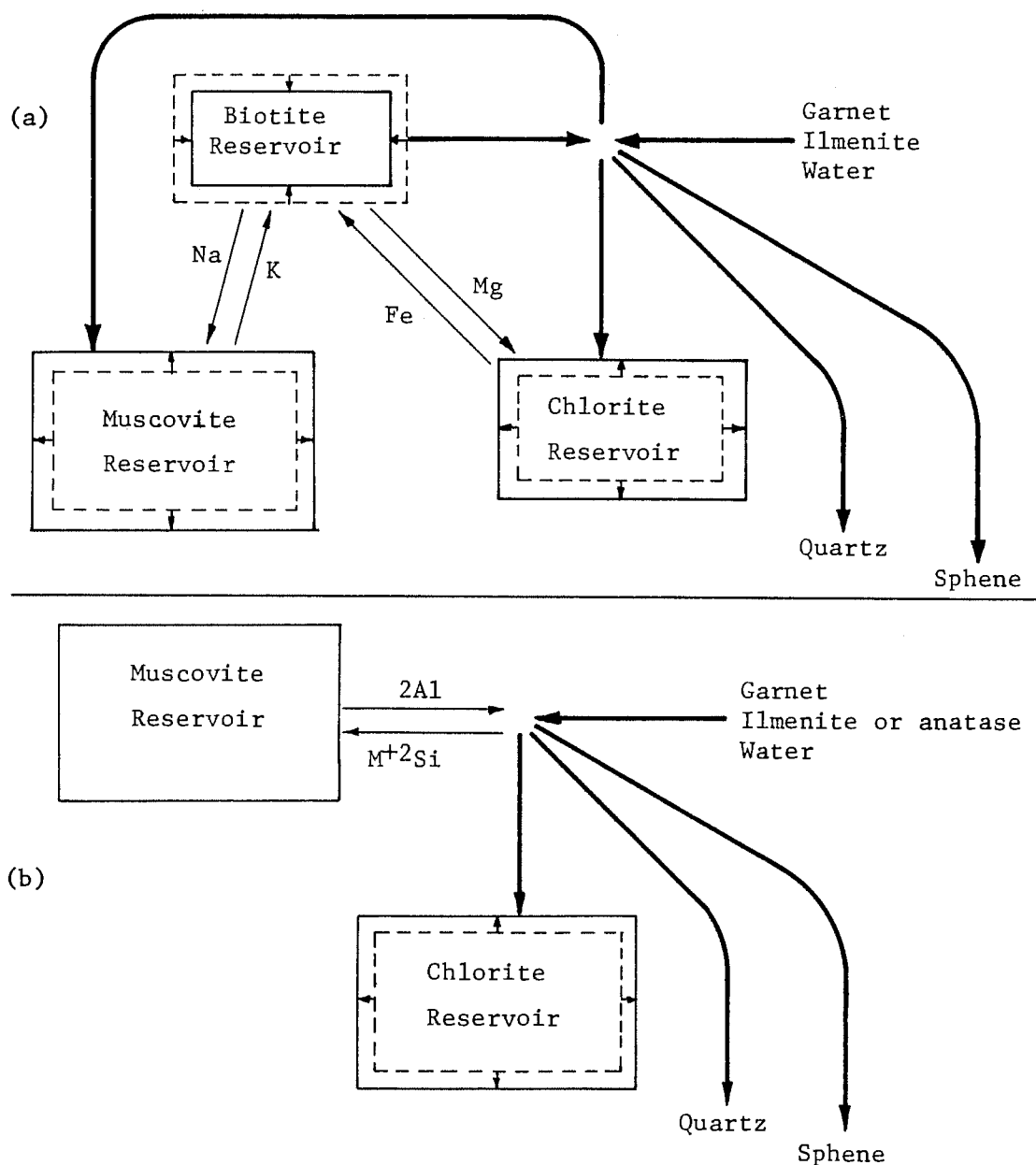
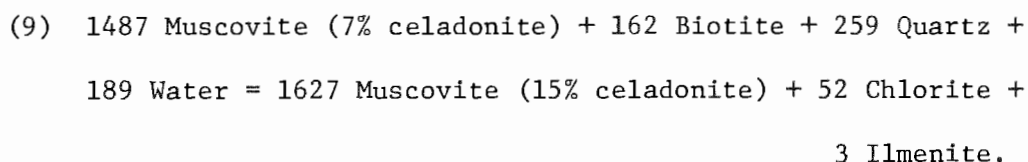


Figure 41. Schematic diagrams for the three garnet-out reactions. a) The biotite-present reactions (6 and 7), generally written as: Garnet + biotite + ilmenite + water = muscovite + chlorite + sphene + quartz. b) The biotite-absent reaction (8) involving a changing muscovite composition: Garnet + ilmenite + water = chlorite + sphene + quartz. Also shown are the coupled cation exchange reactions required to maintain rational tie lines with changing sheet silicate composition.

tie lines in Figure 36b.

A second reaction may be written that produces phengitic muscovite at the expense of biotite. Evidence supporting this reaction may be found in the fact that muscovite rims in the retrograded rocks tend to be more phengitic (up to 15% celadonite) than muscovite in the least retrograded rocks or in the cores of retrograded muscovite (about 7%). The reaction is balanced by assuming a change in muscovite composition from 7 to 15% celadonite component. These two compositions were idealized by taking the average muscovite analysis (Table 9) and substituting  $M^{+2}Si$  for  $VI Al^{IV} Al$  to reach the 7 and 15% celadonite component limits. The biotite is the average listed at the end of Table 8, although the slight aluminum depletion trend evident in Figure 27 suggests that the proper biotite composition would tend to become less aluminous with the more phengitic muscovite. The reaction may be written as follows:



A similar reaction has been proposed to make biotite during prograde metamorphism in some low grade rocks (Ramsay, 1973). However, such reactions have been called into question (Mather, 1970), and a celadonite component of only 15% does not seem high enough for the reaction in any case (Ernst, 1963; Fawcett, 1963; McNamara, 1965; Velde, 1965; Seifert, 1970).

One consequence of the above biotite-consuming reaction (9) is that it must take place in the absence of chlorite-K-feldspar tie lines. Because the chlorite-biotite-K-feldspar-muscovite four phase field sweeps toward higher iron compositions with retrograding, it is possible that the biotite-consuming, phengitic muscovite-producing reaction occurs at iron compositions higher than those analyzed in this study. Therefore, analytical evidence for reaction (9) must await further work.

#### Chloritoid-In Reactions

Introduction. As stated in previous sections, chloritoid has been identified from only one outcrop in the study area. The lack of appropriate bulk compositions at various locations within the retrograded zone makes it difficult to precisely define the mechanism of chloritoid formation at outcrop NS71. Given the data, it is quite impossible to describe the mechanism of the first stable occurrence of chloritoid in the AKFM system. Instead, the following will be a discussion of how chloritoid may have appeared in the rocks at outcrop NS71.

A few observations render clues as to the reactions leading to chloritoid genesis: Nowhere in outcrop NS71 can be found the characteristic muscovite-chlorite pseudomorphs after staurolite. In thin section the small patches of randomly oriented sheet silicate intergrowths that are characteristic of retrograded staurolite and sillimanite are also missing. Biotite is present in

parts of outcrop NS71, but neither biotite nor sheet silicate intergrowths after biotite occur in thin section with chloritoid. Therefore, sillimanite, staurolite, and biotite probably had nothing to do with chloritoid formation.

The observations mentioned above allow certain constraints to be placed on the bulk compositions of chloritoid-bearing rocks in AKFM space. Apparently the only abundant silicate minerals within the AKFM volume in the prograde assemblage of NS71 were garnet and muscovite (Table 1). The bulk composition of the rocks must therefore be within or very close to the tie line set connecting the fields of garnet and muscovite.

There are three ways to allow chloritoid to become a stable mineral at outcrop NS71, given the constraints described above:

- 1) Garnet-chlorite continuous reaction.
- 2) Phengitic muscovite continuous reaction.
- 3) Manganese stabilization of chloritoid.

Garnet-chlorite continuous reaction. The garnet-chlorite continuous reaction is depicted in Figure 42. Chlorite presumably formed through a biotite-absent reaction similar to reaction (9) in the section on garnet breakdown. In Figure 42b it can be seen that the hypothetical bulk composition was very close to that of garnet, as seen in muscovite projection (it is assumed that chloritoid was already a stable phase in more aluminous regions of the AKFM volume).

With retrograding, chlorite became more iron-rich due to the breakdown of iron-rich garnet and ilmenite, as the more Mg-poor garnet cores were exposed. This allowed the chloritoid-chlorite-

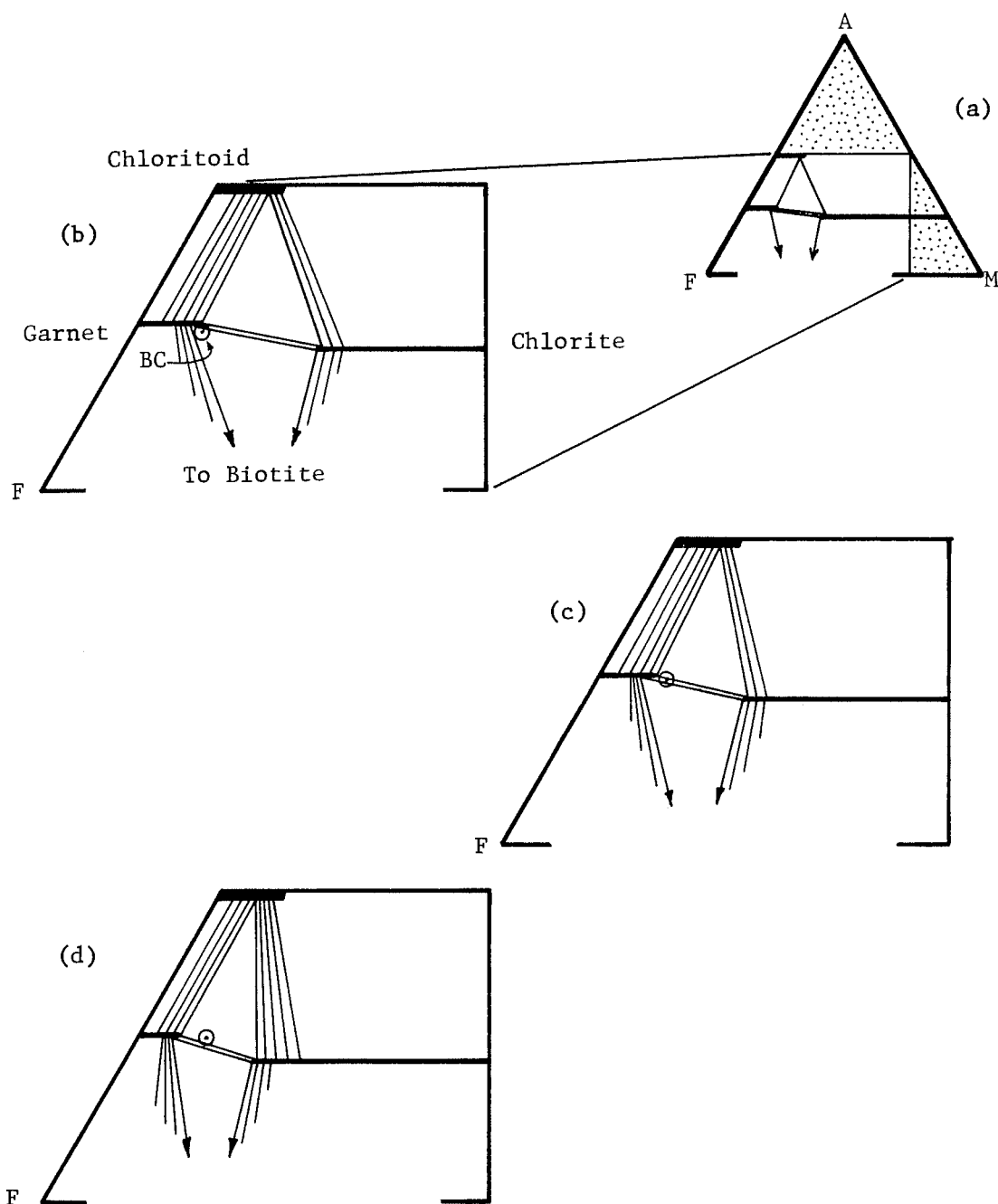
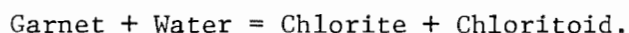


Figure 42. Chloritoid formation by the continuous reaction of garnet and chlorite, in muscovite projection (a). Bulk composition (BC) is originally very close to the garnet field (b). With rock hydration, chlorite becomes more iron-rich due to ilmenite and garnet breakdown, allowing garnet-chlorite tie lines to move toward higher iron compositions, eventually exposing BC to the chloritoid stability field (c). With further iron enrichment of chlorite, BC becomes embedded within the chloritoid-chlorite-garnet assemblage (d).



garnet field to swing toward higher iron compositions. Because of the slope of garnet-chlorite tie lines, the stability field of chloritoid would eventually intersect the bulk composition (Figure 42c). With further iron enrichment of chlorite and perhaps chloritoid, the bulk composition would become more deeply embedded in the chloritoid stability region, producing progressively larger quantities of chloritoid (Figure 42d). The reaction may be represented approximately as follows:



This reaction alone may produce chloritoid up to about 3.5 mole% of the quantity of chlorite, based on  $\text{Al}_2/\text{Al}_2 + \text{Fe} + \text{Mn} + \text{Mg}$  ratios of 0.257, 0.266, and 0.500 for chlorite, garnet, and chloritoid, respectively.

Phengitic muscovite continuous reaction. The second chloritoid forming mechanism is similar to the first, in that it involves the moving of a chloritoid-bearing stability field to intersect the bulk composition. Instead of changing the chlorite and effective garnet compositions, it is the muscovite composition that will change.

The retrograde muscovite at location NS71 is not so celadonite-rich as the other samples analyzed, probably due to composition constraints imposed on muscovite by chloritoid. There is, however, a distinct trend toward more phengitic muscovite, ranging from about 10.5% for old foliation muscovite to about 12.1% for recrystallized retrograde muscovite plates. Composition changes of prograde muscovite cores (Figure 16) and the difficulty in analyzing actual rim compositions suggests that the retrograde change in celadonite

component was greater than 2%.

Figure 43 shows the position of a hypothetical bulk composition located very close to the chlorite-muscovite-garnet tie plane set, as seen in F-M edge projection. Assuming that garnet and chlorite compositions do not change significantly in this projection, any increase in the celadonite component of muscovite will allow the chloritoid-muscovite-garnet-chlorite four phase volume to swing down toward the bulk composition. The bulk composition may be intersected (c), and included in the chloritoid-bearing assemblage (d). This mechanism may produce any ratio of chloritoid to chlorite, depending on the precise bulk composition chosen.

Manganese stabilization of chloritoid. The third mechanism by which chloritoid may be allowed to exist at outcrop NS71 is by stabilization with manganese. First it will again be assumed that the rock composition was close to the stability field of chloritoid, lying within or very close to the tie plane set connecting muscovite, chlorite, and garnet.

Figure 44a is a projection from muscovite and  $\text{Al}_2\text{O}_3$  onto an Fe-Mn-Mg plane. The small section shown in white is expanded (Figures 44b to 44e) to show detailed relations between garnet, chlorite, and chloritoid, and the hypothetical bulk composition. In most rocks Mn released during garnet breakdown went mainly into abundant chlorite, but in sample NS71 the rock composition had enough iron and aluminum to allow chloritoid to be stabilized by only minor Mn enrichment, thus making chloritoid the primary Mn sink. The

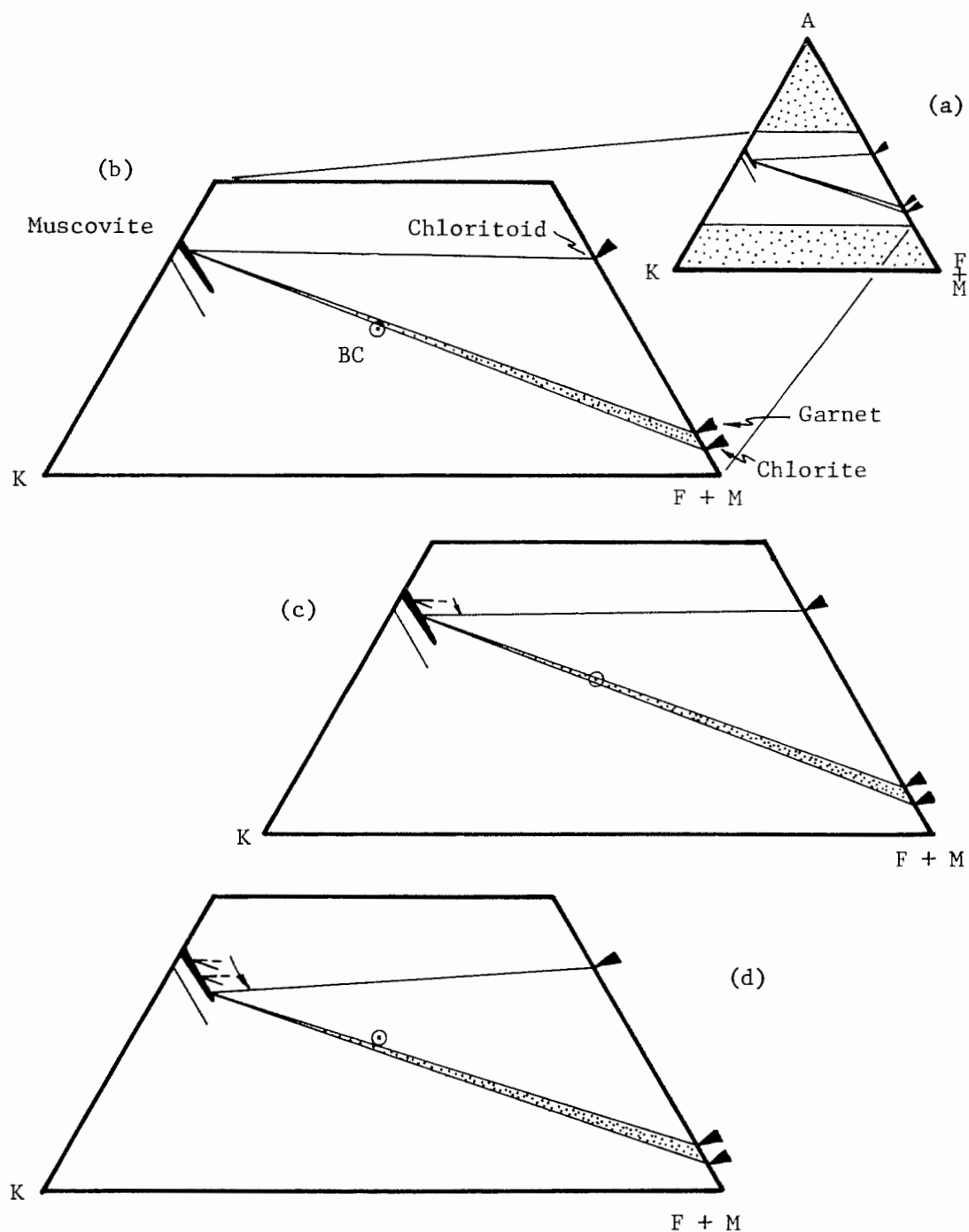


Figure 43. Chloritoid production by phengite enrichment of muscovite. a) F-M edge projection showing the area discussed in the text. The rock composition (BC) was originally below the muscovite-garnet-chlorite tie planes (b), with phengite-poor muscovite. With retro-grading, muscovite became richer in phengite, swinging the muscovite-garnet-chlorite tie planes toward lower aluminum compositions. BC is first intersected (c) and finally becomes embedded in the four phase chloritoid stability volume (d).

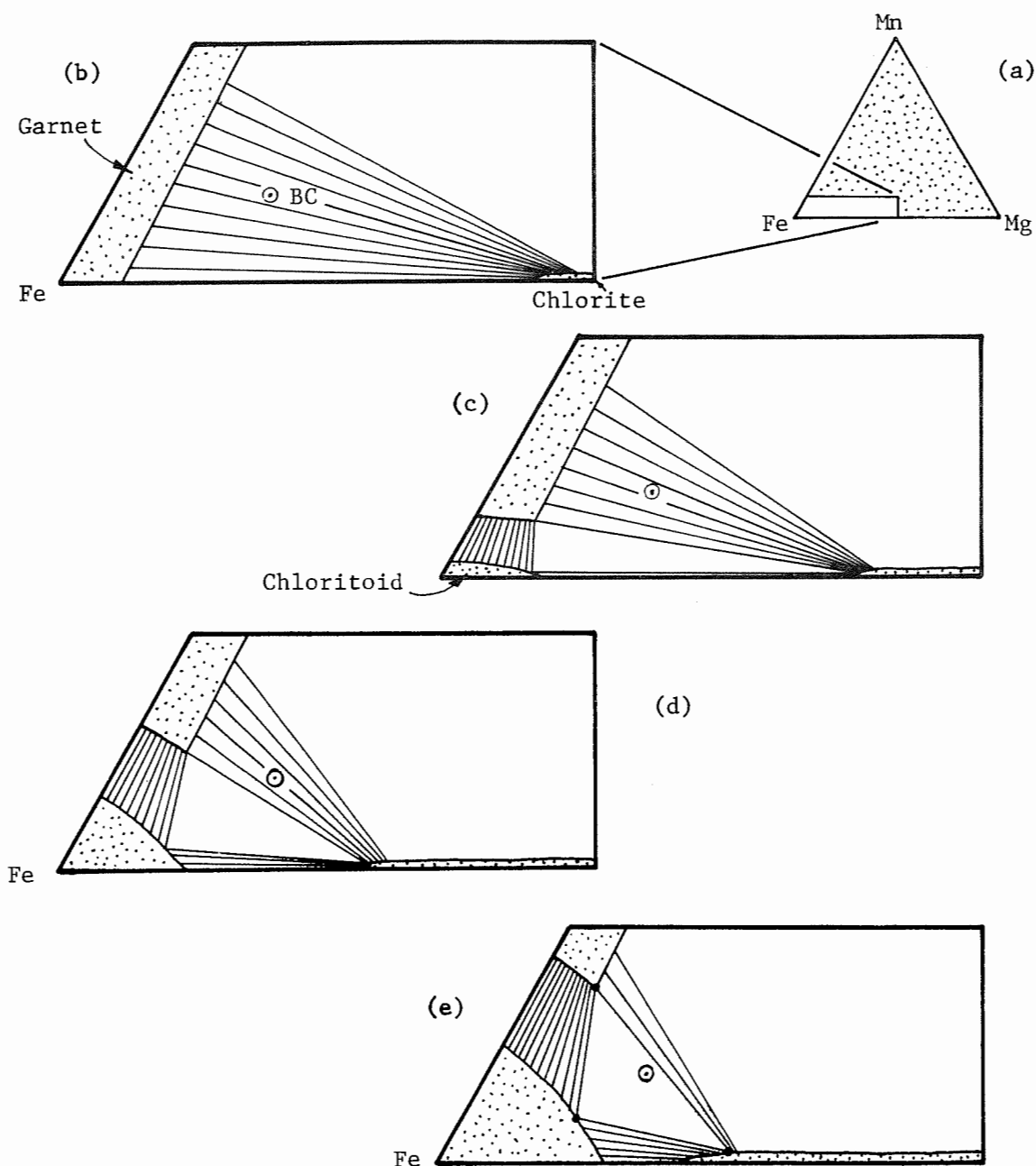


Figure 44. Chloritoid stabilization with manganese. (a) Projection from muscovite and  $\text{Al}_2\text{O}_3$  onto the Fe-Mn-Mg plane. Diagrams are distorted with the Fe-Mg side extending 50 mole%  $\text{MgO}$  and the Fe-Mn side extending to 10 mole%  $\text{MnO}$ . Rock composition is at BC, originally with no chloritoid stability field (b). With retrograding chloritoid becomes a stable phase (c). As manganese-rich garnet interiors are exposed, chlorite becomes more Fe-rich and the chloritoid stability field expands, absorbing most of the Mn released from garnet. The three phase field swings toward higher Mn compositions, intersecting BC (d), and finally embedding it (e) (actual compositions indicated by dots).

ratios of Fe/Fe+Mg and Fe/Fe+Mn for coexisting garnet, chloritoid, and chlorite in sample NS71 are shown in Table 20. As can be seen,

Table 20. Average Fe/Fe+Mg and Fe/Fe+Mn ratios for coexisting garnet, chloritoid, and chlorite in sample NS71.

	Fe/Fe+Mg	Fe/Fe+Mn
Garnet	0.945	0.926
Chloritoid	0.897	0.984
Chlorite	0.700	0.997

the preference for Mg follows the order chlorite>chloritoid>garnet. For Mn the order is reversed, following the order garnet>chloritoid>chlorite. The cation preferences are so because the eight coordinated site in garnet is largest and can most easily accommodate  $Mn^{+2}$  cations. The chloritoid octahedral sites are smaller, and the chlorite octahedral sites smaller still, and can most easily hold the small  $Mg^{+2}$  cation as well as aluminum.

Figure 44b shows the stability relations early in the retrograde sequence with no chloritoid stability field, and garnet containing most of the manganese. With retrograding, chlorite becomes more iron rich as higher Mn, higher Fe garnet interiors are exposed, and a small stability field of chloritoid appears in the iron corner (Figure 44c). The appearance of chloritoid produces the three phase field garnet-chlorite-chloritoid. With further destruction of garnet the chloritoid field enlarges (Figure 44d) until the three phase field intersects and overlaps the bulk composition (Figure 44e), where the corners of the three phase field are actual mineral compositions from sample NS71.

In outcrop NS71, it is probable that all three mechanisms discussed above aided in the appearance of chloritoid. All are plausible based on the limited evidence available. Because of the limited distribution of chloritoid-bearing assemblages the precise reactions creating chloritoid must remain obscure.

#### Ilmenite-Out, Anatase-In Reaction

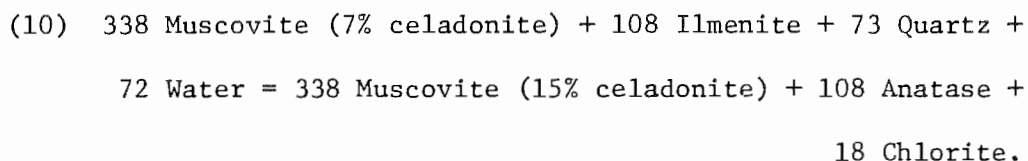
Ilmenite is the only oxide mineral in the prograde assemblages. In most rocks ilmenite is produced by biotite-consuming reactions during the breakdown of sillimanite, staurolite, and garnet. The formation of ilmenite from biotite-consuming reactions and the assumption that all anatase is pseudomorphic after ilmenite is based on textural evidence and has been discussed at length in previous sections.

In most rocks anatase becomes abundant within the staurolite-out isograd (Figure 7). Anatase is also common in retrograded rocks never having contained sillimanite, staurolite, garnet, or in the case of outcrop NS71, biotite. This evidence indicates that there must have been an anatase-producing reaction independent of those minerals, severely restricting the number of plausible reactions.

An obvious sink for iron from ilmenite is chlorite, which however, requires aluminum. Aluminum may come from muscovite, but there are constraints on how the aluminum may be extracted. Muscovite may not have been broken down directly because that would have required K-feldspar or some other alkali sink. K-feldspar is

found associated only with biotite and there is no textural evidence for muscovite breakdown. The only alternative is to make existing muscovite more phengitic, thus releasing aluminum for chlorite production.

In the reaction proposed below, the initial prograde muscovite composition contains 7% celadonite component and the retrograded composition has 15% celadonite, calculated by the tschermaks substitution method identical to that used for the biotite-out, phengite-producing reaction described above. The reaction appears as follows:



Because this reaction releases only Fe and minor Mn, it must produce an iron enrichment trend in coexisting sheet silicates. Rational tie lines were maintained by coupled cation exchange reactions, largely between chlorite and muscovite in severely retrograded rocks poor in biotite (Figure 45). This reaction may also explain the puzzling occurrence of muscovite that is zoned with respect to phengite, whereas other sheet silicates are not zoned. Reaction (10) may have continued during the waning stages of the retrograde episode when temperatures were presumably low. Low temperatures should have limited solid state diffusion in muscovite, allowing it to be zoned with phengite-poor cores and phengite-rich rims, whereas diffusion in chlorite may have been faster.

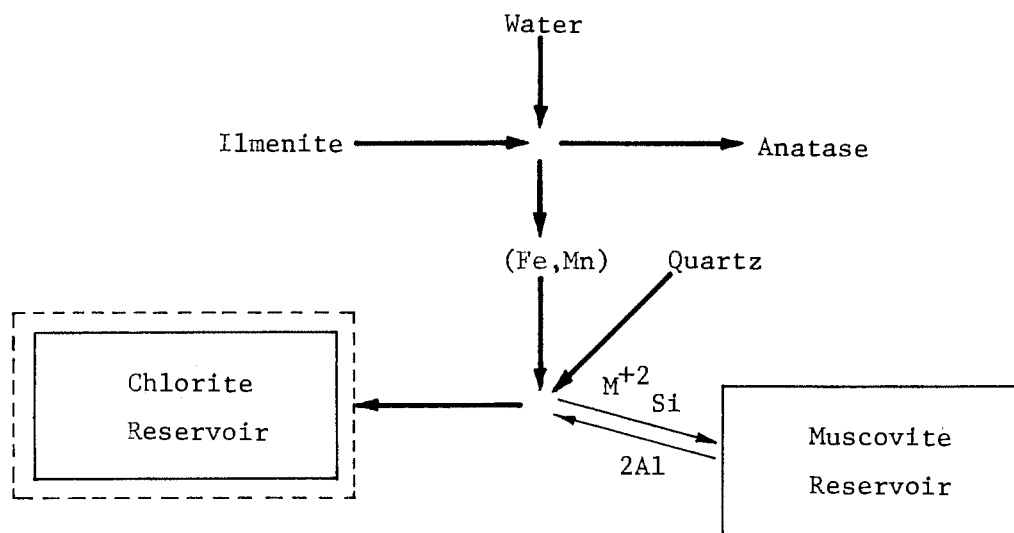


Figure 45. Schematic of the ilmenite-out, anatase-in reaction (10). Note that only iron and minor quantities of manganese are released from ilmenite, which then undergoes (Fe,Mn) for Mg and tschermak exchange with muscovite (and biotite if present), and goes into solid solution with chlorite.

#### Sulfide-Silicate Reactions

The presence of minor quantities of pyrite in the study area has raised questions as to retrograde silicate-sulfide phase relations. Prograde assemblages in schists in the Orange area typically contain pyrrhotite as the only sulfide mineral (Robinson, 1963; Tracy et al., 1976; Tracy, 1978), pyrite being restricted to extremely Mg-rich silicate compositions (Robinson, 1977) and to lower metamorphic grades, as has been found in other terranes (Kwak, 1968; Hutcheon, 1979). This is probably the result of prograde devolatilization reactions that produce  $\text{FeS}$ , Fe-poor silicates,  $\text{CO}_2$ ,  $\pm\text{H}_2\text{O}$ , at the expense of  $\text{FeS}_2$ , Fe-rich silicates, and graphite (Condie, 1967; Guidotti, 1970; Thompson, 1972; Robinson, 1977).



It seems that pyrite is the most abundant sulfide in low grade metamorphic rocks (McNamara, 1965) and in sedimentary rocks (Mason, 1966; Krauskopf, 1967; Blatt et al., 1972; Holland, 1978). Indeed native sulfur and sulfur plus pyrite rather than pyrrhotite, are relatively common in diagenetic environments (Mason, 1966; Krauskopf, 1967; Blatt et al., 1972).

With the above information a hypothetical set of retrograde sulfide-silicate phase relations has been constructed (Figure 46). The highly simplified ternary S-MgO-FeO system is a projection from quartz, muscovite, graphite,  $\text{TiO}_2$ ,  $\text{CO}_2$ , and  $\text{H}_2\text{O}$ . The silicates are biotite and chlorite, which is a reasonable approximation of many rocks in the retrograded area.

Figure 46a shows prograde phase relations, without chlorite and with pyrite restricted to very Mg-rich bulk compositions, and native sulfur restricted to Mg-end member biotite. With decreasing temperature and increasing activity of fluids, the pyrite-pyrrhotite-biotite three phase field moved toward the right, low temperatures favoring low entropy solid phases in place of high entropy gas plus solids. The first appearance of chlorite (Figure 46b) results in a discontinuous hydration reaction necessary to keep native sulfur at Mg-end member compositions. Further retrograding allows both three phase fields to move toward the right (Figure 46c) until at intermediate compositions a second discontinuous hydration reaction allows pyrrhotite to coexist with chlorite (Figure 46d). The three phase fields continue toward the right (Figure 46e)

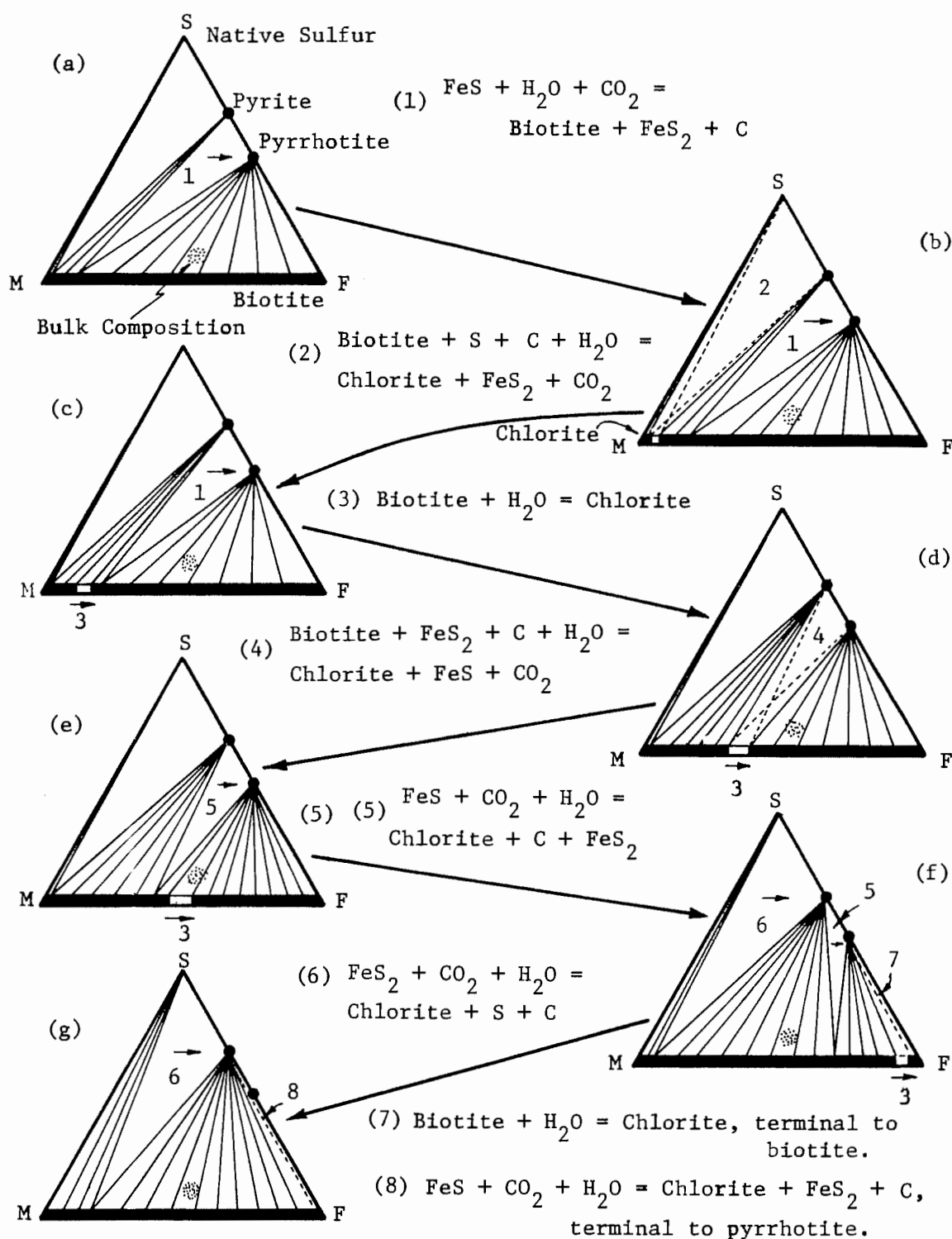


Figure 46. Sulfide-silicate phase relations, projected from quartz, muscovite, anatase,  $\text{CO}_2$ , and water. (a) Prograde relations; (b) to (d) transition relations; (e) and (f) proposed retrograde relations; (g) sediments and sedimentary rocks, showing the possibility of native sulfur at high Mg compositions, and a retrograde reaction terminal to pyrrhotite.

until the terminal reaction for biotite is reached (Figure 46f, also see Figure 30). Finally, Figure 46g shows a possible hydration reaction that is terminal to pyrrhotite. In Figures 46f and 46g, the field of native sulfur is shown to sweep toward Fe-rich compositions to demonstrate the possibility of native sulfur in diagenitic environments and extremely low grade magnesian rocks.

The above discussion is largely hypothetical, but serves to explain the sulfide assemblages found in schists at high metamorphic grades, retrograde pyrite rims on pyrrhotite (Guidotti, 1970), pyrite in the retrograded rocks of this study, and pyrite in very low grade metamorphic rocks and in sediments. The purpose of this discussion is to emphasize that sulfides should not be ignored in metamorphic rocks (usually described as "opaques" or "unidentified sulfides"), and to stimulate further investigation into sulfide-silicate phase relations.

#### Summary of Retrograde Reactions

The closest approximation of the phase relations that can be made based on the data collected in this study are shown in eight muscovite projections in Figure 47. The dearth of bulk compositions high in aluminum and very high in iron make speculation in those regions impossible, and have either been ignored or have been taken from Albee (1968 and 1972), Thompson (1976b and 1977), and Labotka (1980). The questionable area at high iron, low aluminum compositions in Figure 47h refers particularly to stilpnomelane

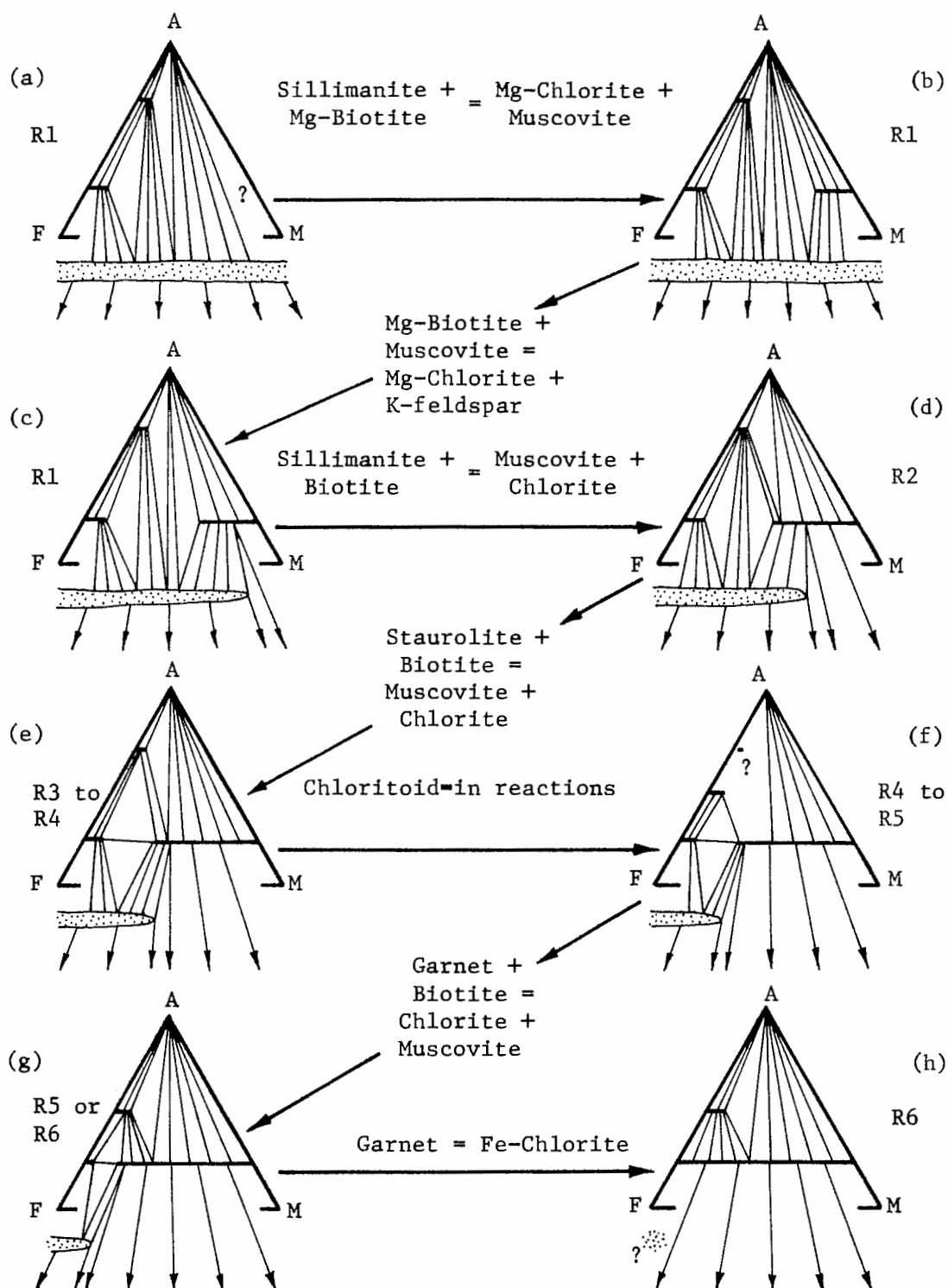


Figure 47. Summary of retrograde silicate phase relations in muscovite projection with simplified retrograde reactions, and related retrograde metamorphic zones. (a) Probable prograde phase relations, (h) proposed retrograde phase relations in zone R6.

(Zen, 1960; Atherton, 1968; Mather, 1970). For clarity the complex balanced reactions have been simplified to include only those phases which lie on the projected AFM face, plus muscovite.

Unfortunately, phase diagrams are of only limited value in portraying the complex reactions and largely metastable assemblages that appear in the retrograded rocks. Figure 48 probably better represents assemblages in the common rocks of the Littleton Formation in the New Salem area. The chart is a mode variation diagram (or "fish diagram") representing the abundance of various minerals with respect to degree of retrograding. The transition from the prograde assemblage to the limiting retrograde assemblage (quartz-muscovite-chlorite-plagioclase-K-feldspar-anatase-sphene) is based on the areal distribution of assemblages from the exterior of the retrograded zone, through the retrograde sillimanite, staurolite, and garnet isograds, to the most retrograded rocks of the interior. Chloritoid is not represented because it is only present in one outcrop with an unusual bulk composition. The limiting retrograde assemblage as shown at the base of Figure 48 is not seen, due to the fact that in no rock has all ilmenite vanished. In some of the most severely altered rocks, however, relict ilmenite is less than 5% of the anatase modal abundance.

#### Mobility of Chemical Components

The apparent relative mobility of the various chemical components is shown in Table 21. The order of listing from the most mobile to

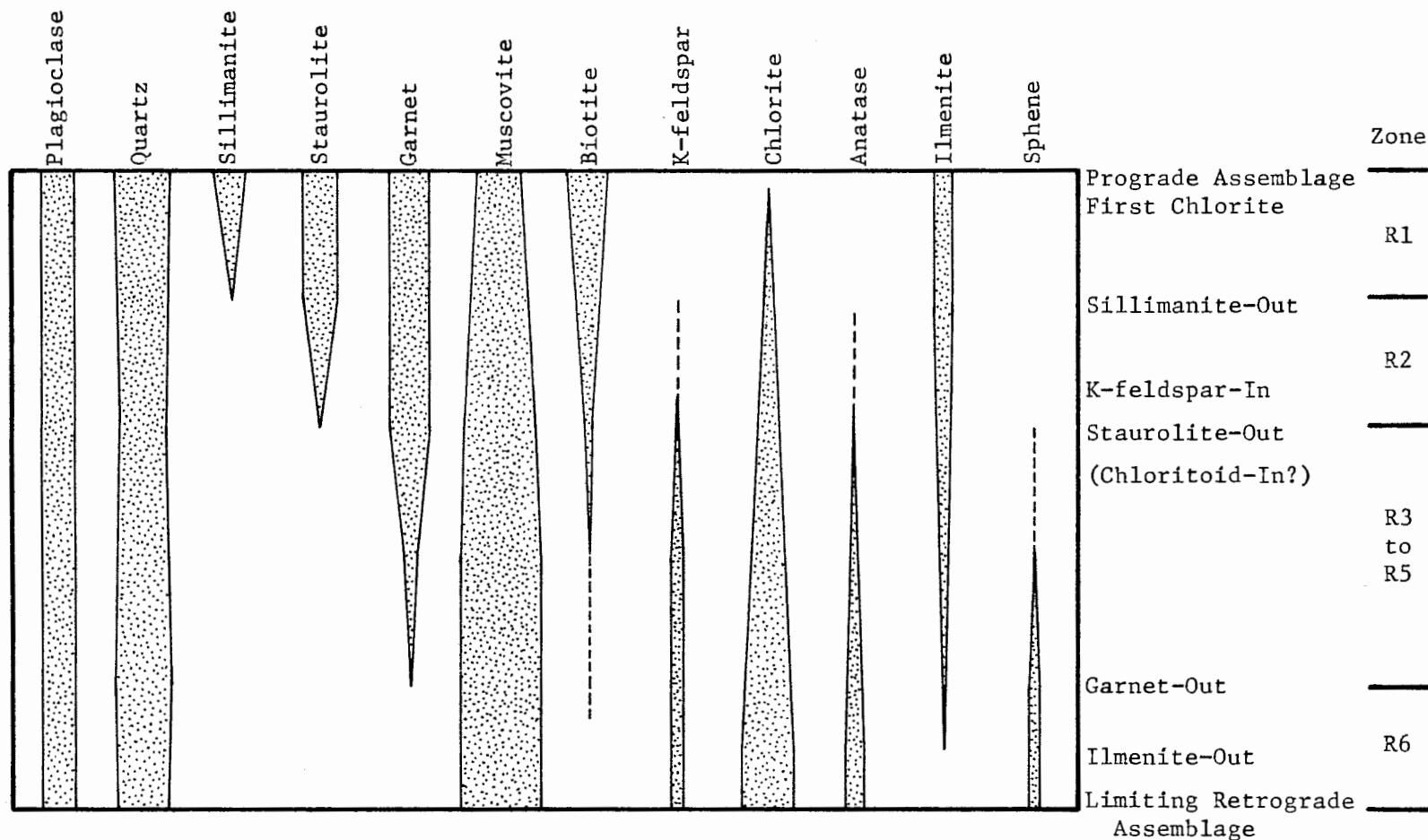


Figure 48. Diagram of mineral abundances versus degree of retrograding. At the top is represented the most complex limiting prograde assemblage found in the Littleton Formation in the study area. The limiting retrograde assemblage at the base of the chart is not quite attained due to traces of relict ilmenite in the most severely retrograded rocks. Major reactions are listed in their proper order to the right of the chart.

Table 21. Listing of the major chemical components in order of relative mobility during retrograde metamorphism. The order of listing is based largely on phase relationships seen in thin section, complemented with some field and analytical data.

Chemical Component	Relative Mobility
H <sub>2</sub> O	Extreme mobility
K Na Ca	High mobility
Mn Fe Mg	Moderate mobility
Al	Low mobility
Ti	Very low mobility

the least mobile was essentially based on observations in thin section, and complemented by interpretation of electron microprobe and field data. Those components that obviously moved large distances from their source mineral to a new retrograde-age mineral were judged more mobile than components that apparently moved little. By "large distances" is meant on the scale of a thin section as opposed to distances less than the size of a single grain. There is no call for any component to have moved more than a few centimeters in bulk, except for water which must have been mobile over distances on the order of kilometers.

For example, during the alteration of sillimanite the fibrolite bundles are replaced by muscovite, taking in water and alkalis and very minor Fe and Mg from elsewhere to combine with the relatively

immobile aluminum. Calcium is also very mobile, at least relative to titanium, because sphene that is produced from retrograding garnet is associated with ilmenite and anatase and not with the source garnet. Manganese, iron, and magnesium (listed in order of surface charge density) are extensively reequilibrated between coexisting phases, but they tend to become fixed in ferromagnesian silicates close to their source mineral. An obvious example of this is the chlorite pseudomorphs after garnet, which are probably due more to the relative immobility of aluminum compared to Mg, Mn, and Fe, as indicated by the fact that altering ilmenite never has a distinct chlorite halo. Aluminum must be less mobile than iron, manganese, and magnesium because of the chlorite mantles commonly associated with the aluminum-bearing silicates; garnet, biotite, and staurolite. Aluminum must be somewhat mobile to explain reactions involving phengitic muscovite and aluminous sphene. Titanium is the least mobile of the major chemical components. Ilmenite and rutile produced during biotite breakdown are always within or adjacent to the relict biotite. Anatase is present as pseudomorphs after ilmenite and apparently does not grow elsewhere.

## CONDITIONS OF METAMORPHISM

### Introduction

In principal, experimentally determined univariant reaction lines, thermodynamic calculations, and chemical compositions of minerals in known assemblages may be used to estimate metamorphic



conditions of pressure, temperature,  $f_{O_2}$ ,  $f_{H_2O}$ ,  $f_{CO_2}$ , and other metamorphic parameters (Mason, 1966; Ferry, 1980). This may be done by comparison of assemblages with experimentally determined metamorphic reaction lines, or by the degree of partitioning of certain diadocic chemical constituents between two coexisting phases. The requirements are a suitable limiting assemblage and calibration with respect to pressure, temperature, and other parameters, and equilibrium coexistence of all associated phases at the time of quenching. Unfortunately, attainment of equilibrium in the laboratory and in the field can rarely be assured and variables outside the scope of the calibration may have profound effects.

Mineral compositions of sample U01A, the least retrograded sample analyzed in this study, will be used for many temperature estimates. Compositions of minerals from other localities in the Orange area will be used to provide independent estimates of P and T. Various other samples, particularly average and extreme mineral compositions in samples NS87, NS85, NS90, and NS71 will be used to estimate retrograde metamorphic conditions.

#### Published Data on Univariant Reactions

Introduction. In this section, those reactions calibrated with respect to pressure and temperature will be used to set limits on conditions of prograde and retrograde metamorphism. Many reactions proposed for some schist terrains do not appear to apply in the New Salem area. (Turnock, 1960; Eugster and Wones, 1962; Fawcett, 1963;

Fawcett and Yoder, 1966; Chinner, 1967; Richardson, 1967b and 1968; Hsu, 1968; Ganguly, 1969 and 1972; Ferry, 1979) Those that are used have been carefully selected (Figure 49 and Table 22).

The precision with which dehydration reaction lines are located does not warrant the identification of invariant points and metastable extensions. This is particularly the case in graphitic rocks of the Littleton Formation where  $P_{H_2O}$  must be less than  $P_{fluid}$ , which in turn may be less than  $P_{total}$ , to variable degrees (French, 1965 and 1966; Ferry, 1976; Ohmoto and Kerrick, 1977).  $P_{H_2O}$  less than  $P_{total}$  results in a lowering of dehydration reaction temperatures, although components such as zinc in staurolite and titanium in biotite and muscovite would tend to stabilize low temperature assemblages against dehydration to some degree.

Explanation of reactions. Most reactions are self explanatory, but some require additional discussion. Figure 49 shows three different sets of data for the kyanite-sillimanite-andalusite invariant point and univariant lines, after Newton (1966), Richardson et al. (1968 and 1969), and Holdaway (1971). These sets of aluminosilicate data are widely quoted in the literature, although the two points at lower pressure and temperature are, perhaps, somewhat favored over the other point (Guidotti, 1974; Cheney and Guidotti, 1979).

Reaction 2 (Biotite + muscovite +  $H_2O$  = chlorite + K-feldspar) is critical for producing the retrograde limiting assemblage. Two polyvariant lines have been drawn between data points 2a through 2m, hopefully delimiting the approximate temperature limits for natural

Table 22. Explanation for reactions in Figure 49.

- 1 Analcime+quartz=albite+H<sub>2</sub>O. Campbell and Fyfe, 1965 (experiment).
  - 2 Chlorite+K-feldspar=biotite+muscovite+H<sub>2</sub>O.
    - 2a Glacial clays, McNamara, 1966.
    - 2b Low grade metamorphics, Coombs, et al., 1970
    - 2c Metasomatized tuffs, Dickinson, 1962.
    - 2d Zeolite facies sediments, Coombs, 1954.
    - 2e Low grade sediments, Harrison and Campbell, 1963.
    - 2f Hydrothermal field, Coombs, 1954.
    - 2g Zeolite facies sandstones, Boles and Coombs, 1977.
    - 2h Low grade phyllites, McNamara, 1965.
    - 2i Hydrothermal experiments on granites, Chayes, 1955.
    - 2j Mg-K-Al hydrothermal experiments, Fawcett, 1963.
    - 2k Hydrothermally altered granitic rocks, Ferry, 1979.
    - 2m Sanidine+clinochlore=chlorite+muscovite<sub>ss</sub>, indicating reaction 2 is metastable, Fawcett, 1963.
  - 3 Garnet+chlorite=biotite+staurolite+H<sub>2</sub>O
    - 3a Guidotti, 1974 (theory).
    - 3b Thompson, 1976c; Thompson et al., 1977 (theory).
  - 4 Chlorite+muscovite=staurolite+biotite+quartz+H<sub>2</sub>O, Mg-Fe system, Hoschek, 1967 and 1969 (experiment).
  - 5 Mg-chlorite+muscovite=kyanite+phlogopite+quartz+H<sub>2</sub>O, Bird and Fawcett, 1973 (experiment).
  - 6 Muscovite+staurolite+chlorite=biotite+Al-silicate+H<sub>2</sub>O, Thompson, 1976c; Thompson et al., 1977 (theory).
  - 7 Mg-chlorite+muscovite+quartz=cordierite+phlogopite+H<sub>2</sub>O, Seifert, 1970; Bird and Fawcett, 1973 (experiment); Thompson, 1976c (theory).
  - 8 Muscovite+albite=K-feldspar+Al-silicate+H<sub>2</sub>O, Chatterjee and Froese, 1975 (experiment); Thompson, 1974 (theory).
  - 9 Staurolite+muscovite+quartz=Al-silicate+biotite+H<sub>2</sub>O, Hoschek, 1968 and 1969 (experiment).
  - 10 Muscovite+quartz=K-feldspar+Al-silicate+H<sub>2</sub>O
    - 10a Chatterjee and Johannes, 1974; Chatterjee and Froese, 1975 (experiment).
    - 10b Evans, 1965 (experiment).
    - 10c Velde, 1965 (experiment).
    - 10d Day, 1973 (experiment).
- Andalusite-sillimanite-kyanite experimental equilibria.
- N Newton, 1966.
- RGB Richardson, et al., 1968 and 1969.
- H Holdaway, 1971.

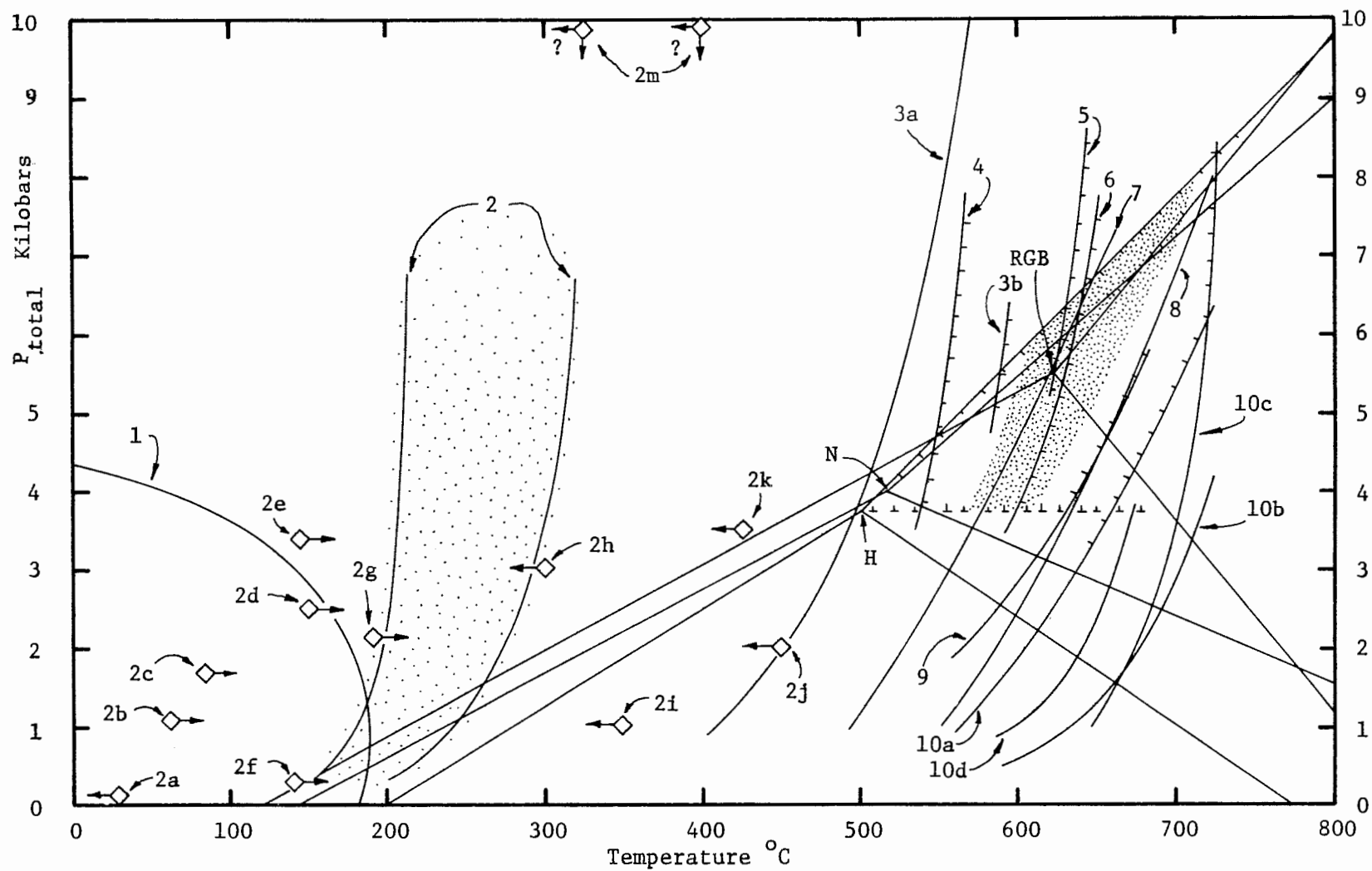


Figure 49. Reaction lines pertinent to rocks in the study area, explained on facing page and in the text. Stippled areas are limiting fields for prograde and retrograde metamorphism.

assemblages containing chlorite and K-feldspar (with Fe/Fe+Mg ratios between about 0.3 and 0.7). Data points come from a wide variety of geologic settings, and the locations of the points in P-T space is only approximate in most cases.

Increasing celadonite component in muscovite at elevated pressures (Ernst, 1963; Velde, 1965; Guidotti, 1973) probably limits the high pressure stability of K-feldspar-chlorite assemblages (Fawcett, 1963; Mather, 1970; Seifert, 1970; Mielke and Schreyer, 1972). The reaction indicated by the arrows in item 2m, K-feldspar + Mg-chlorite = Al-poor Mg-chlorite + phengitic muscovite + H<sub>2</sub>O (Fawcett, 1963), probably indicates that chlorite-K-feldspar assemblages are metastable at 10 kbar. Low  $P_{H_2O}$  also limits the stability field of hydrous chlorite-K-feldspar assemblages (particularly calcite-bearing assemblages; McNamara, 1965 and 1966; Coombs et al., 1970).

Probable field of prograde metamorphism. The reaction lines in Figure 49 allow loose preliminary constraints to be placed on prograde metamorphic conditions in the study area, shown as the stippled region located at high temperatures. As mentioned above, fluids in equilibrium with graphite at conditions similar to those in the stippled field cannot have  $P_{H_2O}$  equal to  $P_{total}$ , and are limited to a maximum of  $0.9P_{fluid}$  (French, 1966; Ohmoto and Kerrick, 1977). This results in a minimum displacement of the devolatilization equilibria by about -20°C (Kerrick, 1972), as has been indicated in Figure 49. The stippled field is delineated as follows:

- 1) The study area lies on the sillimanite side of the prograde

polymorph isograd (Figure 5), and the Littleton Formation contains traces of prograde sillimanite. Assuming the data of Holdaway (1971) to be a reasonable lower temperature limit for the kyanite = sillimanite reaction, then that reaction line may be considered an upper pressure, lower temperature limit for prograde metamorphism.

2) Because andalusite or its pseudomorphs are not found in the Orange-New Salem-Wendell area (Thompson, 1968), regional pressures during prograde metamorphism must have been higher than the andalusite stability field. Again, the Holdaway (1971) Al-silicate data is used to represent a conservative low pressure limit of 3.8 kbar.

3) Prograde metamorphic temperatures must have been higher than reaction lines 4 (chlorite-out reaction in muscovite schists) and 3b (staurolite-in isograd reaction), as seen by the absence of chlorite and presence of staurolite in fresh rocks. Similarly, minor amounts of sillimanite in prograde assemblages requires temperatures slightly above reaction 6 (sillimanite-in isograd reaction).

4) Temperatures must have been lower than reaction 9 (staurolite-out reaction in schists) and 10 (muscovite-out reaction in quartz-bearing rocks) which involves partial melting (Kerrick, 1972; Chatterjee and Froese, 1975; Tracy, 1978). Reaction 9, or one similar to it (Guidotti, 1970) appears to occur in the Partridge Formation at slightly higher grade, about 1 to 2 km east of the study area.

Probable field of retrograde metamorphism. Conditions of retrograde metamorphism are not closely constrained by published reaction lines. The stippled field located at low temperatures in Figure 49 represents the interpolated range of chlorite-K-feldspar assemblages in natural systems. This field is located at temperatures well below all inferred prograde and retrograde reactions cited in Table 22. The presence of albite and lack of analcime in the retrograded rocks indicates that retrograde conditions remained outside reaction 1, although reduced  $P_{H_2O}$  could shrink the analcime stability field.

#### Coexisting Mineral P-T Estimates

Garnet-biotite thermometers. The partitioning of iron and magnesium between coexisting garnet and biotite has received much attention for use as a geothermometer. Early workers attempted to correlate measured distribution coefficients with metamorphic grade and assemblage (Frost, 1962; Albee, 1965a; Saxena, 1968; Hall, 1970; Lyons and Morse, 1970; Guidotti, 1974). Garnet-biotite Fe/Mg distribution coefficients have been calibrated by various means (Hietanen, 1969; Saxena, 1969; Thompson, 1976c; Ferry and Spear, 1977 and 1978; Goldman and Albee, 1977), and have been used extensively to estimate temperatures in various metamorphic terrains (Tracy et al., 1976; Tracy, 1978; Ghent et al., 1979; Ferry, 1980).

The major substitution in biotite and garnet in most rocks is  $Fe = Mg$ , but additional components may substitute, possibly changing  $K_D^{garnet/biotite}_{Fe/Mg}$ . Garnets may contain substantial quantities of Mn

and Ca, and biotite may contain variable amounts of Ti,  $^{IV}Al$ ,  $^{VI}Al$ , and vacancies. Extra components have either been ignored (Ferry and Spear, 1978), corrected for empirically in the calibration method (Thompson, 1976c), or have been explicitly included in the correction procedure (Goldman and Albee, 1977).

Estimates of prograde temperatures for selected rocks in the study area, and elsewhere in metamorphic zones I and II (Tracy et al., 1976; Robinson, unpublished data), based on biotite-garnet geothermometers are listed in Table 23. Figure 50 illustrates the average values and ranges in temperature estimates based on this method. Sample U01A, representing the least retrograded rocks in the study area, records temperatures substantially lower than for those elsewhere in metamorphic zones I and II, possibly due to limited high temperature retrograde reequilibration between garnet and biotite (see, for example; Grant and Weiblen, 1971; Tracy et al., 1976), not evident in the analyses (Tables 6 and 8, and Figure 11). In contrast to sample U01A, sample NS87 has concentrically altered garnets with iron-rich rims coexisting with iron-rich biotite.

Sample NS85 is included to show the extreme situation of iron-rich biotite occurring with relict garnet of nearly prograde rim composition, resulting in anomalously high temperature estimates. This is dramatic evidence for severe disequilibrium between garnet and biotite. Garnet cannot reequilibrate readily with biotite or other minerals at low temperatures, and thus is incapable of taking into account retrograde changes in biotite composition.



Table 23. Estimated temperatures for various samples based on three garnet-biotite geothermometers. For the average temperatures in metamorphic zones I and II, the highest values for each thermometer were averaged, using all values for the first average, and with extreme values eliminated for the second average. These estimates agree with Robinson (1979). See Tracy et al. (1976) for sample locations.

	Zone I			Study area			Zone II	
	50	U94	4F5	U01A	NS87	NS85	36	86
Thompson, 1976								
Core	600°C	525	560	460			590	625
Interior		590	595	505				
Rim	530	490	515	510	540	620	555	505
Goldman and Albee, 1977								
Core	590	485	530	445			465	
Interior		545	540	450				
Rim	510	450	470	445	475	530	510	
Ferry and Spear, 1978								
Core	625	520	570	440			610	655
Interior		610	615	495				
Rim	530	475	510	500	540	645	560	500

Average for zone I: 9 values = 590°C, 7 values = 590°C.

Average for zone II: 5 values = 600°C, 3 values = 610°C.

Muscovite-paragonite solvus. The white mica solvus is limited at elevated temperatures by the terminal reaction for paragonite:  

$$\text{K-paragonite} + \text{quartz} = \text{Al-silicate} + \text{Na-muscovite} + \text{K-albite} + \text{H}_2\text{O}$$
(Thompson, 1974; Chatterjee and Froese, 1975). In principal, the highest Na content in muscovite should occur with the preceeding reaction assemblage. Because paragonite and sillimanite do not occur in the analyzed rocks, the paragonite-muscovite solvus curves can only suggest minimum temperatures.

Minimum temperature estimates have been made with muscovite analyses from the study area, using the solvus curves of Eugster et

al. (1972) and Thompson (1974) at 2 kbar. The solvus curve was corrected for higher pressure (4, 6, and 8 kbar) by raising the curves by interpolation between 0°K and the critical line of the white mica solvus (Eugster et al., 1972). Minimum temperature estimates are summarized in Table 24, and extreme estimates are shown in Figure 50.

Temperature estimates for sample U01A at all pressures are higher than are reasonable, being more consistent with magmatic

Table 24. Minimum temperature estimates for various samples based on a calculated pressure corrected white mica solvus. Estimates for sample U01A extend into the range of migmatite and felsic magmas, and the other estimates are generally too high for probable retro-grade conditions. Also given is a calculated univariant line for the reaction: K-paragonite = quartz = K-albite + Na-muscovite + Al-silicate + H<sub>2</sub>O.

Sample	Paragonite content	<u>2</u>	<u>4</u>	<u>6</u>	<u>8</u>
U01A	33.4% average	695°C	747	793	835
NS85	16.7% average	485	526	561	595
	9.5% minimum	375	410	440	469
NS90	19.2% average	525	568	605	640
NS71	22.1% average	565	610	650	686
Univariant reaction line	18.6%	515			
	19.2%		570		
	19.6%			615	
	20.0%				645

conditions. Similar anomalously high estimates may be made using muscovite data from elsewhere in the Orange area (Hall, 1970).

Estimated temperatures for samples NS90 and NS71 are not consistent with experimentally determined staurolite breakdown curves (reactions 3b and 4, Figure 49). Estimated temperatures for sample NS85,

particularly the lowest paragonite composition (paragonite 9.5%), may be compatible with low grade assemblages.

White mica-alkali feldspar solvi. In many published phase diagrams, muscovite is shown to have higher K/K+Na ratios than coexisting K-feldspar (Thompson, 1974; Tracy, 1978). In this study it has been found that muscovite K/K+Na ratios are much lower than coexisting K-feldspar. Thompson (1974) depicts the mica solvus curve crossing the feldspar solvus curve at about 410°C, at 2 kbar. Although equilibrium of the alkali-bearing minerals is doubtful, the fact that K-feldspar is more potassic than coexisting muscovite suggests that retrograding occurred below 410°C.

Muscovite celadonite component. It has been demonstrated that the celadonite component of muscovite tends to be high in low grade rocks and to decrease with increasing temperature (Ernst, 1963; Seifert, 1970), decreasing pressure (McNamara, 1965; Velde, 1965; Guidotti, 1973; Sassi and Scolari, 1974; Guidotti and Sassi, 1976; Thompson et al., 1977), or increasing metamorphic grade (Wenk, 1970; Labotka, 1980; This work). However, it has also been shown in lower sillimanite zone and higher grade rocks that Si-3 and Fe+Mg in muscovite tends to increase with increasing grade (Guidotti, 1973 and 1978; Tracy, 1975; Cheney and Guidotti, 1979). The amount of celadonite solid solution is also dependent on assemblage, being highest in biotite-muscovite-K-feldspar assemblages (Guidotti, 1973; Guidotti et al, 1975a; Guidotti and Sassi, 1976; Labotka, 1980).

Unfortunately, the physical-chemical systematics of muscovite composition are complex and the only attempt at calibrating muscovite celadonite component with pressure and temperature was by Velde (1965) for the general reaction: Phengitic muscovite = biotite + muscovite + K-feldspar + quartz. The present author has used Velde's data to construct a P-T- $X_{\text{celadonite}}$  (celadonite composition =  $\text{KAlFe}_{0.5}\text{Mg}_{0.5}\text{Si}_4\text{O}_{10}(\text{OH})_2$ ) grid for estimating temperatures in analyzed samples (Table 25).

Table 25. Temperature estimates for various samples at 2, 4, 6, and 8 kbar, based on the phengitic muscovite breakdown data of Velde (1965). Estimates for sample U01A intersect the range of probable prograde metamorphic conditions (Figure 50), but the other estimates are too high for probable retrograde conditions.

Sample	Celadonite content	Temperature, °C			
		2 kbar	4 kbar	6 kbar	8 kbar
U01A	6.7% average	600°C	630	650	670
NS87	9.1% average	570	600	630	650
NS85	15.0% maximum	500	540	570	600

Temperature estimates for sample U01A fall into the high temperature stippled field in Figure 50, supporting both the Velde (1965) calibration and the estimated field of prograde conditions (by bootstrap reasoning). The trend toward lower estimated temperatures in the more severely retrograded samples is well developed, although estimates for the most phengitic mica in sample NS85 are higher than are reasonable for chlorite-K-feldspar assemblages. Biotite in sample NS85 is present only in trace amounts and may be metastable, therefore not constraining muscovite composition.

Alkali feldspar solvus. At high temperature there is a complete solid solution series between K-feldspar and albite, interrupted at lower temperatures by a solvus. The solvus is raised by increased pressure, or by adding a calcium component in Na-Ca-K Space. The use of feldspar solvus curves or published determinative equations for estimating temperature are, however, of limited usefulness in medium and low grade metamorphic rocks (Ferry, 1980). The published determinative curves and equations for estimating temperature using two coexisting feldspars (Morse, 1970; Eugster, 1972; Thompson, 1974; Stormer, 1975; Whitney and Stormer, 1977; Ferry, 1978) are not considered accurate at low temperature, or at low values of Na/(Na+Ca+K) in either or both feldspars.

Using averaged feldspar analyses from the study area, temperature estimates were made at 2, 4, 6, and 8 kbar (Table 26), based on two

Table 26. Temperature estimates for retrograded rocks based on coexisting alkali feldspar geothermometers. Averaged K-feldspar and plagioclase analyses (Tables 12 and 13) were used in the calculations. The first column is for sanidine-plagioclase, and the second column for microcline-plagioclase solid solutions. The equation of Ferry (1978) is also for microcline-plagioclase pairs, but contained no pressure term.

<u>Pressure, kbar</u>	<u>Stormer, 1975</u>	<u>Whitney and Stormer, 1977</u>	<u>Ferry, 1978</u>
2	159°C	211	
4	171	224	218
6	184	237	(3.5 kbar)
8	196	251	

recently published determinative equations for sanidine-albite (Stormer, 1975) and microcline-albite (Whitney and Stormer,

1977) solid solutions. One point at 3.5 kbar after Ferry (1978) was also calculated for microcline-albite solid solutions.

The difference between the estimates is about 50°C, and is not significant when considering the probable extent of disequilibrium. The two "coexisting" feldspars in the study area have very small degrees of mutual solid solution, formed under radically different metamorphic conditions, and sanidine in the study area is metastable with respect to microcline. However, temperatures predicted by the two-feldspar geothermometers is consistent with other evidence for low temperature formation of K-feldspar and chlorite-K-feldspar assemblages.

Cordierite equilibria. Although the study area contains no cordierite, it does occur elsewhere in central Massachusetts and may be used to set limits on regional metamorphic conditions. Tracy et al. (1976), using cordierite-garnet and garnet-biotite equilibria, estimated temperatures in metamorphic zones I and II, and zone VI to have been about 595 and 675°C, respectively, or about 80°C apart. More recent estimates (Robinson, 1979) give temperatures of 610 and 690°C for zones II and VI, respectively, also 80°C apart. Tracy et al. (1976) also estimate minimum pressures of 5.5 to 6.5 kbar for most metamorphic zones (based on garnet-cordierite equilibria), and maximum pressures of generally 6 to 8.5 kbar (based on garnet composition coexisting with biotite, sillimanite, muscovite, cordierite, and quartz).

Using the chemical data of Tracy et al. (1976), and the cordierite-garnet partitioning data of Holdaway and Lee (1977, their Figure

6), indicate 670°C and 7.1 kbar (maximum pressure) for metamorphic zone VI, assuming maximum  $P_{H_2O} = P_{total}$  (after Ohmoto and Kerrick, 1977). Subtracting 80°C from 670°C yields 590°C as an estimate for metamorphic zones I and II. Similar comparisons of data to Newton (1979, his Figures 4 and 5) suggest maximum pressures of 6.8 kbar in metamorphic zone VI.

Data from Robinson (1977) for sulfide-rich sillimanite-biotite-cordierite-K-feldspar-graphite rocks, compared to the  $P-X_{Fe/Mg}$  reaction loop for biotite + sillimanite = cordierite + K-feldspar (at 675°C, Holdaway and Lee, 1977 their Figure 3) indicate  $P_{H_2O}$  in the range of 4 to 5 kbar. This is substantially less than other  $P_{total}$  estimates for the area, and supports calculations suggesting  $P_{H_2O}$  less than  $P_{total}$  in graphite-bearing rocks (French, 1965 and 1966; Condie, 1967; Thompson, 1972; Asokan and Chinner, 1973; Ferry, 1976; Ohmoto and Kerrick, 1977).

Garnet-plagioclase calcium partitioning. The reaction, grossular + Al-silicate + quartz = anorthite, is in part pressure dependent, and has been used to estimate pressure in metamorphic terrains (Tracy et al., 1976; Ghent et al., 1979; Ferry, 1980). Results obtained by Tracy et al. (1976) were erratic and generally lower than estimates by other methods.

Best-fit matrix calculations for the garnet-plagioclase data of Tracy et al. (1976) suggest a pressure estimate of about 6 kbar for sample U01A, assuming about 600°C. Using the data of Ghent et al. (1979) gives a pressure estimate of 5.9 kbar for sample U01A at an

assumed temperature of 600°C, and samples 50Y and Q76X (from Tracy et al., 1976, metamorphic zones I and II, respectively) yield pressures of 5.9 and 6.1 kbar. Although the garnet-plagioclase geothermometers require the presence of aluminosilicate, the pressure estimate for sample U01A is nevertheless similar to other estimates.

Biotite-muscovite titanium partitioning. Kwak (1968) found the quantities of titanium in coexisting biotite and muscovite to increase linearly with metamorphic grade, and  $K_D^{\text{biotite/muscovite}}_{\text{Ti}}$  to decrease in rutile-bearing rocks. Kwak estimated temperatures of 475°C for lowest grade and 575°C for the highest grade rocks, over which the distribution coefficient decreased from about 3.37 to 2.26. Kwak assumed no pressure effect, and Ti was taken as the cation fraction: Ti/Total cations. The resulting determinative equation is:

$$\log T^{\circ}\text{C} = -0.477 \log \frac{\text{biotite/muscovite}}{\text{Ti}} + 2.93.$$

Ignoring the effects of ilmenite and anatase in place of rutile as the titanium saturating phase, the equation gives temperatures of 420°C and 375°C for samples U01A and NS87, respectively, representing the extremes for samples analyzed in this study.

Increasing titanium in the micas with increasing metamorphic grade is well documented (Wenk, 1970; Guidotti et al, 1977; Guidotti, 1970 and 1978; Tracy, 1978; Cheney and Guidotti, 1979). However, changing  $K_D^{\text{biotite/muscovite}}_{\text{Ti}}$  with metamorphic grade is



equivocal because it is also critically dependent on the biotite Fe/Fe+Mg ratio (Guidotti, 1975 and 1977; Robinson, unpublished data), on pressure (Jean-Louis, 1975), and on the titanium saturating phase (Guidotti et al, 1977). Therefore,  $K_D^{\text{biotite/muscovite}}_{\text{Ti}}$  cannot be used reliably as a temperature indicator with the present state of calibration.

### Independent Constraints for Metamorphic Conditions

Prograde metamorphism. Nappe reconstruction over the Orange area yields a minimum projected overburden thickness of 7.8 km (Thompson et al., 1968) or 8.8 km (Robinson, 1979), corresponding to 2.2 and 2.5 kbar, respectively. A previous estimate of 30 km (8.4 kbar) by Robinson (1966) is no longer favored (Robinson, personal communication, 1980).

Tracy et al. (1976) and Robinson (1979) have published metamorphic isograd maps of central Massachusetts, with estimated temperatures for the different metamorphic zones. Assuming the relative estimated temperatures for metamorphic zones I through VI to be correct, a lateral paleo-geothermal gradient of 4°C/km may be interpolated to occur in the Prescott syncline, with low temperatures in the Pelham dome region increasing toward the southeast. Using the kyanite = sillimanite reaction line of Holdaway (1972) as a minimum temperature limit for the Al-silicate polymorph isograd (Figure 5 and 49), and a lateral geothermal gradient of 4°C/km, prograde temperatures in the study area could have been no higher

than a generous 25°C above Al-silicate polymorph isograd temperatures (Figure 50, item 10).

Retrograde metamorphism. A minimum continental shield geothermal gradient of 10°C/km may be assumed as an absolute lower temperature limit during retrograde metamorphism (Turner, 1968), although this gradient may be too high (Verne, 1864).

The ductile style of deformation and pervasive manner of retrograde metamorphism in the study area indicates that retrograde metamorphism occurred while the rocks were hotter and more deeply buried than during formation of the Connecticut Valley Mesozoic basins and associated faults. Structural reconstruction of the Connecticut Valley indicates about 5.0 km (Robinson, 1979) to 5.5 km (Robinson, 1966 and 1967b) of vertical displacement and subsequent erosion along the eastern border fault in the northern end of the basin. This corresponds to a minimum pressure during retrograde metamorphism of 1.4 to 1.5 kbar.

Because pressures during prograde metamorphism have been estimated to have been around 6 kbar (see preceeding section) an upper pressure limit for retrograde metamorphism may be had by assuming isobaric cooling from prograde temperatures. In effect this assumption requires cooling of the Bronson Hill orogenic terrain by about 340°C (Figure 50) without significant uplift and erosion; a very unlikely prospect.

Table 27. Summary explanations for various pressure and temperature estimates in Figure 50. The stippled areas in Figure 50 are from Figure 49, heavier stippling indicating more closely constrained conditions for prograde and retrograde metamorphism.

- 1 Feldspar geothermometer estimates, pressure corrected.
  - 1a Stormer, 1975; sanidine-plagioclase system.
  - 1b Whitney and Stormer, 1975; Ferry, 1978; microcline-plagioclase system.
- 2 Reaction line: Chlorite+K-feldspar=biotite+muscovite+H<sub>2</sub>O, interpolated curves for Fe/Fe+Mg=0.3 to 0.7 rocks (see Figure 49).
  - 2a Estimated lower limit in natural assemblages.
  - 2b Estimated upper limit in natural assemblages.
- 3 Structural reconstruction across Connecticut Valley eastern border fault, Robinson, 1966, 1967b, 1979.
- 4 Isobaric cooling from prograde pressures.
- 5 Na/K in K-feldspar less than Na/K in muscovite, Thompson, 1974.
- 6 Ti biotite/Ti muscovite geothermometer, Kwak, 1968.
- 7 Minimum temperature curves from pressure corrected white mica solvus, Eugster et al., 1972; Thompson, 1974.
  - 7a Sample NS85, minimum paragonite = 9.5%.
  - 7b Sample U01A, average paragonite = 33.4%.
- 8 Phengitic muscovite=biotite+muscovite+quartz, interpolated curves after Velde, 1965.
  - 8a Sample NS85, maximum celadonite component = 15.0%.
  - 8b Sample U01A, average celadonite component = 6.7%.
- 9 Nappe reconstruction over the New Salem area, Thompson et al., 1968; Robinson, 1979.
- 10 Limit of temperatures above Al-silicate isograd, interpolated after Tracy et al., 1976; Robinson, 1979.
- 11 Garnet-cordierite geobarometers, range of estimated values, after Tracy et al., 1976; Holdaway and Lee, 1977; Newton, 1979.
- 12 Garnet-plagioclase geobarometers, range of estimated values, after Tracy et al., 1976; Ghent et al., 1979.
- 13 Garnet-biotite geothermometers, average for zone I, Tracy et al., 1976; Thompson, 1976c; Goldman and Albee, 1977; Ferry and Speer, 1978.
- 14 Same as item 13, above, for zone II.
- 15 Garnet-biotite and garnet-cordierite geothermometers, after Table 21; Thompson, 1976c; Tracy et al., 1976.
- 16 P-T estimate for metamorphic zone II, Robinson, 1979.
- H Al-silicate data, lowest temperature lines, Holdaway, 1971.

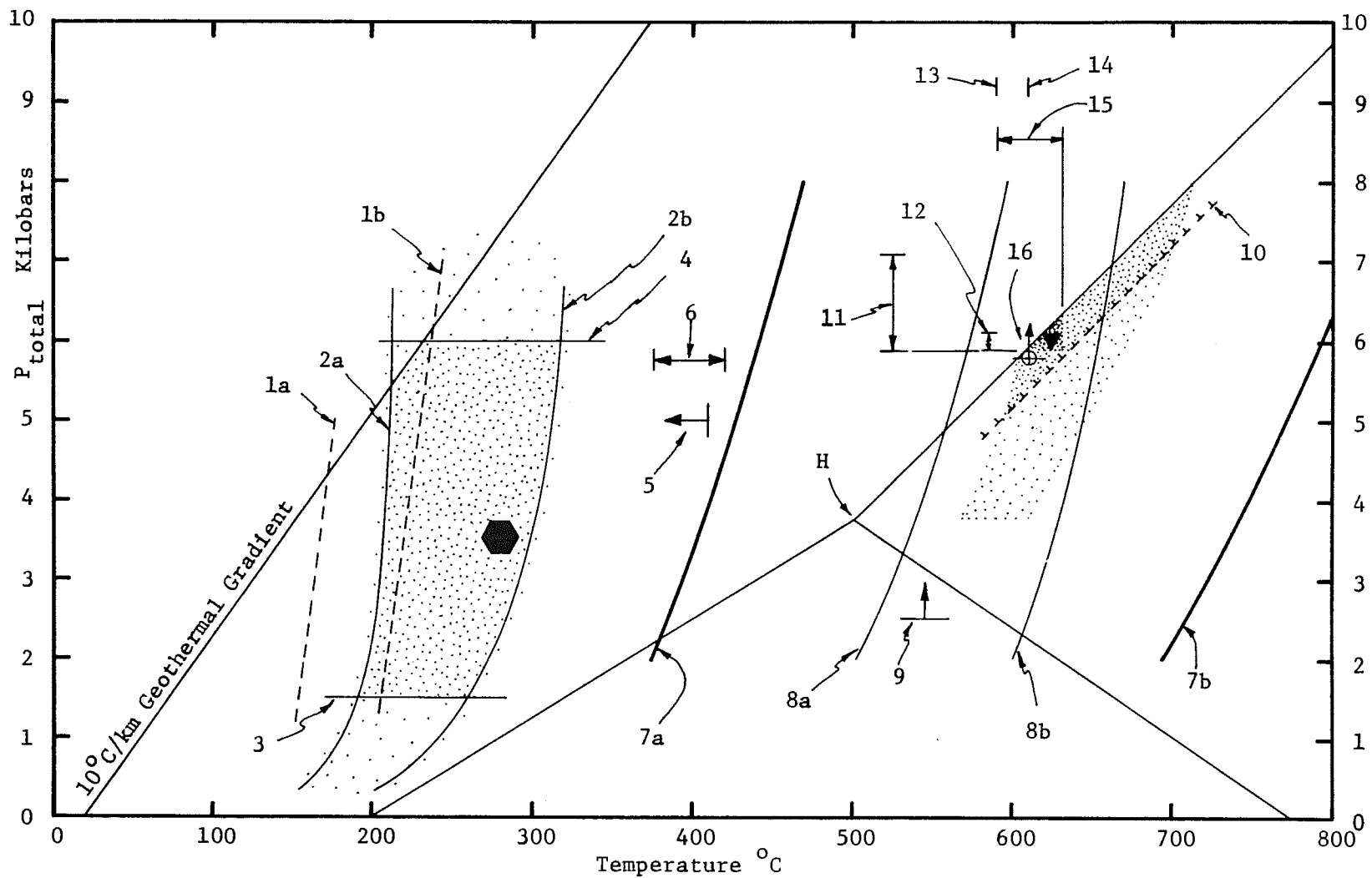


Figure 50. Estimates of temperatures and pressures for prograde and retrograde rocks, see Table 27 for summary explanations. Heavier stippling indicates more closely constrained conditions. Estimates are 620°C at 6.0 kbar for prograde rocks, and 280°C at 3.5 kbar for retrograde rocks.

### Discussion of Prograde P and T

Figure 50 (with Table 27) is a summary of the various pressure and temperature estimates for prograde and retrograde metamorphism. The dashed, hatched line (item 10) is the high temperature limit for prograde metamorphism imposed on the larger field from Figure 49 by the lateral  $4^{\circ}\text{C}/\text{km}$  geothermal gradient. The resulting field of probable prograde conditions based on published reaction lines and the lateral temperature gradient is therefore limited to a narrow strip,  $25^{\circ}\text{C}$  wide, extending from  $600^{\circ}\text{C}$  at 5 kbar to  $700^{\circ}\text{C}$  at 8 kbar.

Item 16 in Figure 50 is the range of temperature estimates based on garnet-biotite geothermometers for metamorphic zones I and II, and garnet-cordierite equilibria for metamorphic zone VI (minus  $80^{\circ}\text{C}$ ). The maximum estimate is  $630^{\circ}\text{C}$  (Table 23), and was chosen as a maximum limiting temperature. Items 12 and 13 are pressure estimates based on garnet-cordierite (Zone VI) and garnet-plagioclase (zones I and II) equilibria, respectively. The minimum of these estimates (5.9 kbar) is assumed to be the minimum limiting pressure for prograde conditions.

The field of probable conditions of prograde metamorphism in the study area is therefore limited by a maximum temperature of  $630^{\circ}\text{C}$ , minimum pressure of 5.9 kbar, and the sillimanite = kyanite reaction line of Holdaway (1971). The black triangle in Figure 50 has been arbitrarily drawn in the middle of the limiting field, and is located at  $620^{\circ}\text{C}$  and 6.0 kbar. This estimate indicates a paleo-geothermal gradient of  $28^{\circ}\text{C}/\text{km}$  during prograde metamorphism.

For comparison, Figure 50, item 16 is the estimated temperature and minimum pressure for metamorphic zone II in the Orange area (Robinson, 1979), representing the most comprehensive compilation of P-T estimates for west-central Massachusetts to date. The point is located at 610°C and 5.8 kbar (minimum), or 10°C and 0.2 kbar lower than that estimated in this work. In spite of the uncertainties involved, prograde conditions probably did not differ from 620°C and 6.0 kbar by more than  $\pm 30^\circ\text{C}$  and  $\pm 0.3$  kbar.

#### Discussion of Retrograde P and T

The conditions of formation of the retrograde limiting assemblage, chlorite-K-feldspar-albite-muscovite-quartz-anatase-sphene-graphite, is located within the low temperature, heavily stippled field in Figure 50. This field is more closely constrained than the one presented in Figure 49 by the following means: 1) Reaction curves 2a and 2b (Figure 49; curve 2, Figure 50) are taken as reasonable limits for naturally occurring chlorite-K-feldspar assemblages. 2) The minimum geothermal gradient of  $10^\circ\text{C}/\text{km}$  may be considered a reasonable maximum pressure, minimum temperature limit. 3) The suggested maximum pressure limit assuming isobaric cooling from prograde temperatures is assumed to be reasonable. 4) A minimum pressure set by assuming retrograde metamorphism preceded Mesozoic faulting.

The field of likely conditions for retrograde metamorphism is not so closely constrained as the field for prograde metamorphism.

However, the relatively coarse grain size of retrograde sheet silicates suggests that temperatures were within the upper range of those in the field of probable retrograde conditions. While pressures probably did not approach 6 kbar, they were probably substantially higher than the minimum of 1.5 kbar. A best guess of retrograde conditions is shown as a black hexagon in Figure 50, located at 280°C and 3.5 kbar. This pressure is at about the upper limit of chlorite-K-feldspar assemblages estimated for natural rocks and experimental data, and suggests a paleo-geothermal gradient of 20°C/km. The author doubts that retrograde metamorphism occurred under conditions differing from those stated by more than +50°C, -80°C, or  $\pm 1$  kbar.

#### METAMORPHIC FLUID COMPOSITION

Limits on oxygen fugacity during prograde and retrograde metamorphism are shown in Figure 51. The two vertical lines denote estimated prograde and retrograde temperatures, 620°C and 280°C, respectively. Lines on the right half of Figure 51 have been corrected for pressures of 6.0 kbar, and those on the left for 3.5 kbar. Solid lines are the solid-solid oxygen buffers: Hematite-magnetite (HM), fayalite-magnetite-quartz (FMQ), magnetite-iron (MI), magnetite-wüstite (MW) (Hutcheon, 1979), nickel-nickel oxide (NNO) (Huebner and Sato, 1970; pressure correction after Eugster and Wones, 1962), and iron wüstite (IW, schematic). Solid-solid oxygen buffers are for comparison purposes only.

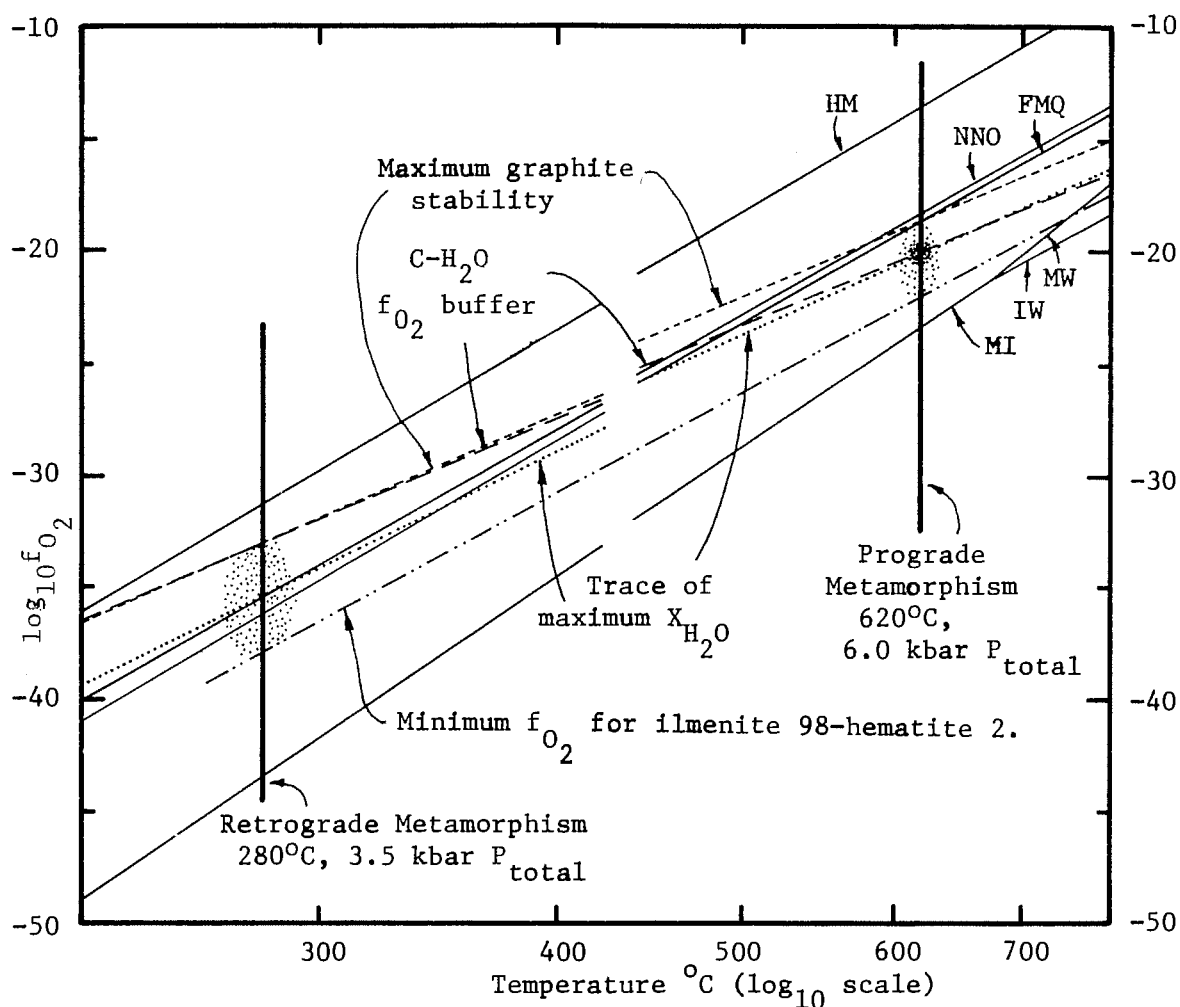


Figure 51. Plot of oxygen fugacity versus temperature. Retrograde and prograde P and T are shown as vertical lines, with all associated oxygen fugacity curves corrected for pressure. Lightly stippled areas are loosely constrained values of oxygen fugacity, and the heavily stippled area is more closely constrained by rock paragenesis arguments.

The short dash curve in Figure 51 denotes the maximum stability limit for graphite in the C-CO<sub>2</sub> system (Ohmoto and Kerrick, 1977), and is the upper  $f_{O_2}$  limit in graphite-bearing rocks of the study area. The dotted line is the trace of maximum  $X_{H_2O}$  in C-H-O fluids (Ohmoto and Kerrick, 1977), and is included for comparison. The long dash line represents the oxygen fugacity of the fluid in



equilibrium with graphite along the C-H<sub>2</sub>O join in the C-H-O ternary system. The line is essentially an extrapolated isobaric intersection of the C-H<sub>2</sub>O divariant surface in P-T-f<sub>O<sub>2</sub></sub> space, at appropriate pressures (French and Eugster, 1965).

The dash-dot-dot line is the oxygen fugacity for ilmenite with 2% hematite solid solution (see table 14) assumed to coexist with titanomagnetite (Rumble, 1971 and 1976; Asokan and Chinner, 1973; Spencer and Lindsley, 1978; line extrapolated to 280°C after Spencer and Lindsley, 1980), and is a lower f<sub>O<sub>2</sub></sub> limit for rocks containing this ilmenite (Lindsley, 1973 and 1976). A maximum limit of f<sub>O<sub>2</sub></sub> may be set by coexisting ilmenite (hematite 2%) and rutile. However, extrapolations from high temperature data (Tompkins et al., 1980) proved unsatisfactory at low temperatures, where the curve projected above the H-M buffer. Assuming that the ilmenite-rutile data is correct at high temperature, and that the lines are parallel to the ilmenite-magnetite data of Spencer and Lindsley (1980), it is reasonable to suggest that maximum f<sub>O<sub>2</sub></sub> was 10<sup>1.5</sup> to 10<sup>2</sup> higher than the ilmenite (hematite 2%)-magnetite curve in Figure 51.

The range in f<sub>O<sub>2</sub></sub> values between the graphite-out curve and the magnetite-ilmenite (hematite 2%) curve is about 10<sup>-18.6</sup> to 10<sup>-22.0</sup> bar for prograde P and T, and 10<sup>-33.0</sup> and 10<sup>-37.9</sup> bar for retrograde P and T, comparing favorably with estimates based on Ohmoto and Kerrick (1977), French (1966), and Condie (1967).

Prograde metamorphic dehydration reactions probably kept fluid X<sub>H<sub>2</sub>O</sub> rather high (Greenwood, 1975), near the trace of maximum X<sub>H<sub>2</sub>O</sub>

compositions. The maximum  $X_{\text{H}_2\text{O}}$  line intersects the C-H<sub>2</sub>O buffer curve near 620°C at an  $f_{\text{O}_2}$  of about  $10^{-20.0}$  bar, well below the FMQ buffer curve. On this basis, simultaneous equations were solved for conditions of  $P_{\text{total}} = 6000$  bars, 620°C, and  $f_{\text{O}_2} = 10^{-20.0}$  bar, after Ohmoto and Kerrick (1977). The estimated proportions of gas species are:  $X_{\text{H}_2\text{O}} = 0.35$ ,  $X_{\text{CO}_2} = 0.32$ ,  $X_{\text{CH}_4} = 0.25$ ,  $X_{\text{H}_2} = 0.08$ , and  $X_{\text{CO}} = 0.003$ , which may be recalculated as a mixture of the three components H<sub>2</sub>O, CO<sub>2</sub>, and CH<sub>4</sub> in the proportions 0.38 to 0.35 to 0.27.

Reduced temperatures would tend to increase the relative oxydation state of graphite-bearing metamorphic rocks (French, 1966), so  $f_{\text{O}_2}$  in retrograded rocks probably followed a trend, with cooling, more oxidizing than the solid-solid oxygen buffers. Unfortunately, disequilibrium conditions and broad constraints on oxygen fugacity make estimating retrograde fluid composition difficult. The complete lack of any carbonate suggests that  $f_{\text{O}_2}$  was not in the more oxidizing (CO<sub>2</sub>-rich) part of the low temperature stippled field in Figure 51. The ilmenite-rutile and ilmenite-magnetite data discussed above suggest reducing CH<sub>4</sub>-rich fluids, although the ubiquitous pyrophanite component in ilmenite suggests more oxidizing H<sub>2</sub>O-rich fluids are possible for 2% hematite solid solutions, near the FMQ buffer curve.

Because retrograde pyrite is present in the absence of pyrrhotite, a sulfur fugacity could not be calculated (Toulmin and Barton, 1964; Condie, 1967; Craig and Scott, 1974). However, calculations indicate a minimum  $f_{\text{S}_2}$  of between  $10^{-14}$  and  $10^{-18}$  bar.

## TIMING OF RETROGRADE METAMORPHISM

Because folds that developed during retrograde metamorphism deform dome phase and earlier phase structural features, retrograding occurred after the main phases of Acadian deformation. The brittle nature of Mesozoic deformation, as stated previously, indicates that retrograding occurred prior to the Triassic.

The interval between prograde metamorphism at 6.0 kbar (about 21.4 km) and Mesozoic faulting at 1.5 kbar (about 5.5 km) suggest an average erosion rate of 8.6 cm/1000 years. Assuming this linear erosion rate as a model, retrograde metamorphism at  $3.5 \pm 1$  kbar (about  $12.5 \pm 3.6$  km) suggests a time for retrograding between Middle Pennsylvanian and Upper Permian.

Erosion rates were, however, probably much faster during and soon after the Acadian orogeny, and during formation of the Connecticut Valley Mesozoic basin (Hubert et al., 1978). The constraints are poor, but various erosion curves generally suggest a time of retrograding between Lower Mississippian and Lower Permian. Overlap into the Permian, plus the estimated retrograde temperature of about 280°C supports the notion that Permian resetting of mica K/Ar ages (Zartman, 1970) and some Rb/Sr ages (Brookins, 1967) in central New England may have been caused by uplift and resultant cooling of the region to below mineral blocking temperatures (blocking temperatures of 100–200°C for micas, Zartman et al., 1970). This does not, however, preclude a discrete heating event in the Permian.

Therefore, retrograde metamorphism probably occurred between Lower Mississippian and Lower Permian time, during cooling and unroofing of the Acadian orogenic terrain.

#### WATER FOR RETROGRADE HYDRATION REACTIONS

##### Quantity

Simplified volume calculations were performed to estimate the amount of water necessary to produce the degree and extent of retrograding observed in the study area. The starting mineralogy was similar to sample U01A (Table 3), and four reactions were modeled in the sequence: Staurolite-out (4), garnet-out (rim, biotite present (6)), biotite-out (72% K-feldspar reaction (5) + 28% celadonite reaction (9), to conserve muscovite), ilmenite-out (10). Molar volumes were taken from Hall (1970), Weast (1976), and Robie et al. (1978). The molar volume of chlorite was taken as 208 cm<sup>3</sup>/mole, based on the unit cell parameters given by Deer et al. (1976), and a formula unit of (Fe,Mg,Al)<sub>6</sub>(Si,Al)<sub>4</sub>O<sub>10</sub>(OH)<sub>8</sub>. The results are shown in Table 28.

The calculated ilmenite-out assemblage is similar to the assemblage in sample NS90. Extending the calculations to all rocks in the area is somewhat unrealistic because many did not begin with assemblages similar to U01A. However, it was used as a first approximation to calculate bulk water and volume changes throughout the retrograde area (Table 29).

The results are striking. The entire area of retrograded rocks

Table 28. Model of retrograde metamorphism for a rock similar to sample U01A. Each column contains the volume fraction of each mineral, based on the original rock equal to 1.00, percent volume change of the rock, and percent volume of water added to the rock to drive each reaction to completion.

Completed reaction:	Original rock	Staurolite-out	Garnet-out	Biotite-out	Ilmenite-out
Quartz + albite	0.60	0.597	0.604	0.597	0.592
Staurolite	0.02	0			
Garnet	0.03	0.030	0		
Biotite	0.09	0.042	0.039	0	
Muscovite	0.25	0.289	0.292	0.292	0.292
Anatase + sphene			0.002	0.002	0.011
Ilmenite	0.01	0.011	0.009	0.010	0
K-feldspar				0.024	0.024
<u>Chlorite</u>	<u>      </u>	<u>0.040</u>	<u>0.077</u>	<u>0.103</u>	<u>0.113</u>
<u>Total</u>	<u>1.00</u>	<u>1.009</u>	<u>1.023</u>	<u>1.028</u>	<u>1.032</u>
$\Delta$ Volume (solids)	0	+0.9%	+2.3%	+2.8%	+3.2%
$\Delta$ H <sub>2</sub> O volume (STP)	0	+1.1%	+2.4%	+3.1%	+3.4%

Table 29. Volume changes induced by retrograde hydration reactions, based on the model presented in Table 28, and the mapped isograds in Figures 7 and 9. Due to the small quantities of sillimanite in the study area, it is ignored. Calculation parameters based on Table 28 and observed assemblages are: Within garnet isograd (zone R6, 1/2 biotite-out +1/2 ilmenite-out reactions; within the thin-rimmed garnet line (zones R4 and R5), 1/2 staurolite-out and 1/2 garnet-out reactions; within staurolite isograd (zone 3), staurolite-out reaction; outside staurolite isograd (zones R1 and R2) assumed parameters.

Metamorphic zone	Surface area km <sup>2</sup>	Percent volume change	Volume change km <sup>3</sup>	Water volume km <sup>3</sup> , STP
R6	0.7	+3.0%	+0.021	+0.023
R4 and R5	4.5	+1.6%	+0.072	+0.079
R3	7.8	+0.9%	+0.070	+0.086
<u>R1 and R2</u>	<u>13</u>	<u>+0.5%</u>	<u>+0.065</u>	<u>+0.072</u>
Total/km depth	(26 km <sup>2</sup> )	(+0.9%)	+0.23 km <sup>3</sup>	+0.26 km <sup>3</sup>

(about 26 km<sup>2</sup>) swelled by about 0.23 km<sup>3</sup> ( $2.3 \times 10^8$  m<sup>3</sup>) for every kilometer in depth (or into the air) the retrograded zone extends.

Similarly, the amount of water necessary to drive retrograde hydration reactions was about 0.26 km<sup>3</sup> ( $2.6 \times 10^8$  m<sup>3</sup>) for every kilometer of depth, equivalent to 25 minutes discharge of the Amazon River (after Holland, 1978), or about nine days discharge of the Connecticut River at Turners Falls, Massachusetts (after Baker and Callahan, 1976).

#### Water Source and Consequences of Expansion

The Prescott Intrusive Complex was emplaced during the gneiss dome formation phase of Acadian deformation, and displays little

evidence of retrograding. Also, the most severely retrograded rocks occur about 3.5 km north of the pluton, so the Prescott complex was probably not the water source. If retrograding occurred during the waning stages of Acadian metamorphism, it is possible that water could have been derived from continued prograde metamorphism at depth, water being channeled into the Prescott syncline between flanking gneiss domes. Alternatively, water could have been derived from deeply penetrating meteoric waters.

Permiability of water may have been higher parallel to the foliation in the Littleton Formation relative to flanking rocks. Water may therefore have migrated more easily into the Littleton Formation to create the observed pattern of retrograde isograds.

Water may have been concentrated in the study area as a result of a pressure shadow effect around the north end of the buttressing Prescott Complex, as proposed by H. W. Jaffe (personal communication to Robinson, 1966; and to this author, 1979), fluids tending to migrate into the low pressure zone. The ductile style of deformation in the retrograde area indicates that the increased volume of rocks was accommodated by folding, possibly represented by the crenulations and other folds of possible retrograde age (deformation phases 4, 5, and possibly 6). Whether the expansion was accommodated by lateral bulging, upward extrusion, or filling of an incipient void in a pressure shadow, is not known as of this writing. A detailed structural analysis of the retrograded region will be required for an answer.

## SUMMARY AND CONCLUSIONS

1) The most severely retrograded rocks occupy a small area in the Littleton Formation, straddling the axial surface of the Prescott syncline. Within the area of retrograded rocks (about 26 km<sup>2</sup>), concentric retrograde isograds for sillimanite-out, staurolite-out, and garnet-out reactions have been mapped. The area has been subdivided, based on these isograds and on the degree of garnet replacement by chlorite, into six retrograde metamorphic zones, designated R1 to R6 with increasing degree of retrograding.

2) The prograde limiting assemblage, quartz-plagioclase-muscovite-biotite-garnet-staurolite-ilmenite-graphite±sillimanite, was changed by a set of retrograde hydration reactions toward the limiting assemblage, quartz-plagioclase-muscovite-chlorite-anatase-sphene-graphite-K-feldspar. Another prograde assemblage, quartz-muscovite-garnet-graphite-ilmenite, was partially retrograded toward a limiting assemblage, quartz-muscovite-chlorite-chloritoid-sphene-anatase-graphite.

3) Garnets are primarily almandine in composition, but are strongly zoned with Mn-Ca-rich cores and Fe-Mg-rich rims. Zoning is relict from prograde metamorphism, with little or no retrograde change in garnet rim compositions. Calculations indicate <0.1% andradite component.

4) Garnet stoichiometry calculations indicate that the FeO weight percent value in the P130 (Nuevo) garnet standard is 21.51%, instead of the published value of 21.75%.



5) A preliminary staurolite structural formula is proposed:  $(\text{Fe}, \text{Al}, \text{Ti}, \text{Zn})_2 (\text{Al}, \text{Mg})_8 (\text{Al}, \text{Fe})_{0.7}$ , vacancy 1.3  $(\text{Fe}, \text{Mn})_{0.12}$ , vacancy 1.88  $(\text{Si}, \text{Al})_4 \text{O}_{22+x} (\text{OH})_{2-x}$ . The formula contains full tetrahedral sites, two largely empty and variable octahedral sites, and variable amounts of water. Staurolite analyzed in this study contained about 1.36  $\text{OH}^-$  per formula unit, based on 24 oxygens.

6) Anatase is an unstable mineral under all geological conditions. It is abundant in retrograded rocks as pseudomorphs after ilmenite because it was easier to nucleate than was rutile (for uncertain reasons), and because anatase is not very unstable with respect to rutile.

7) Retrograde hydration reactions were not the same as the reverse of prograde dehydration reactions that they superficially resemble. Retrograde reactions occurred under largely disequilibrium conditions, but did maintain rational tie lines between biotite-muscovite (K/K+Na), chlorite-biotite (Fe/Fe+Mg), and ilmenite-sheet silicate (Mn) pairs.

8) Chlorite-K-feldspar tie lines are probably stable under very low grade metamorphic conditions, and may be suitable for defining a prograde isograd in some terrains. The tie lines are unstable with respect to phengitic muscovite at some pressure at or above 4 kbar, and at low  $P_{\text{H}_2\text{O}}$ .

9) Retrograde sphene is produced with the grossular component released during garnet breakdown. Sphene exhibits the substitution of  $\text{AlOH}^{+2}$  for  $\text{TiO}_2^{+2}$ , up to 15%.

10) Prograde metamorphism is estimated to have occurred at  $620^{\circ}\text{C} \pm 30^{\circ}$  and  $6.0 \pm 0.3$  kbar, with a fluid dominated by  $\text{H}_2\text{O}$  and an  $f_{\text{O}_2}$  below the FMQ buffer curve. The conditions of retrograde metamorphism are poorly constrained to around  $280^{\circ}\text{C} +50^{\circ}$  to  $-80^{\circ}$  and  $3.5 \pm 1$  kbar, with  $f_{\text{O}_2}$  near the FMQ buffer curve and a fluid dominated by  $\text{H}_2\text{O}$  or  $\text{CH}_4$ .

11) Retrograde metamorphism occurred over an area of about  $26 \text{ km}^2$ , and required about  $0.26 \text{ km}^3$  of water and about  $0.23 \text{ km}^3$  of expansion for each kilometer in depth the retrograded zone extends. The volume change was apparently accommodated by folding. Four fold sets in the retrograded area post-date Acadian gneiss dome formation, some of which are probably related to the expansion.

12) The time of retrograde metamorphism has been loosely constrained by comparing pressure estimates for retrograde metamorphism to interpolated erosion rate curves for central Massachusetts. These indicate that retrograding occurred between Lower Mississippian and Lower Permian time. Average erosion rates were about 8.6 cm/1000 years between the Acadian Orogeny in the Middle Devonian and formation of the Connecticut Valley basin in the Triassic and Jurassic. Average erosion rates since the Mesozoic have been about 2.8 cm/1000 years.

# REFERENCES CITED

- Abbott, R.N., Jr. (1979) Polymetamorphism in the Silurian-Devonian Goshen Formation of western Massachusetts. *Geological Society of America Bulletin*, v. 90, p. 861-876.
- Albee, A.L. (1965a) Distribution of Fe, Mg, and Mn between garnet and biotite in natural mineral assemblages. *Journal of Geology*, v. 73, p. 155-164.
- \_\_\_\_\_, (1965b) A petrogenitic grid for the Fe-Mg silicates of pelitic schists. *American Journal of Science*, v. 263, p. 512-536.
- \_\_\_\_\_, (1965c) Phase equilibria in three assemblages of kyanite-zone pelitic schists, Lincoln Mountain Quadrangle, central Vermont. *Journal of Petrology*, v. 6, p. 246-301.
- \_\_\_\_\_, (1968) Metamorphic zones in northern Vermont, p. 329-241. In, Zen, White, Hadley, and Thompson, Editors, Studies in Appalachian Geology: Northern and Maritime. John Wiley and Sons, New York, 475 p.
- \_\_\_\_\_, (1972) Metamorphism of pelitic schists: Reaction relations of chloritoid and staurolite. *Geological Society of America Bulletin*, v. 84, p. 3249-3268.
- \_\_\_\_\_, and Chodos, A.A. (1965) Microporobe analysis of interlayered muscovite and paragonite, Lincoln Mountain Quadrangle, Vermont. *Geological Society of America Abstracts*, Special Paper 87, p. 2.
- \_\_\_\_\_, and Ray, Lily (1970) Correction factors for electron probe microanalysis of silicates, oxides, carbonates, phosphates, and sulfates. *Analytical Chemistry*, v. 42, p. 1408-1414.
- Anderson, D.E. and Glenn, R.B. (1973) Zoning in garnets-diffusion models. *Contributions to Mineralogy and Petrology*, v. 40, p. 87-104.
- Ashenden, D.D. (1973) Stratigraphy and structure of the northern portion of the Pelham dome, north-central Massachusetts. (M.S. thesis) Contribution no. 16, Geology Department, University of Massachusetts, Amherst, 133 p.
- Ashwal, L.D., Leo, G.W., Robinson, Peter, Zartman, R.E., and Hall, D.J. (1979) The Belchertown quartz monzodiorite pluton, west-central Massachusetts: A syntectonic Acadian intrusion. *American Journal of Science*, v. 246, p. 75-76.

- Asokan, S. and Chinner, G.A. (1973) Local modification of gas composition by graphite-iron oxide buffering. *Nature (Physical Science)*, v. 246, p. 75-76.
- Atherton, M. P. (1968) The variation in garnet, biotite, and chlorite composition in medium grade pelitic rocks from the Dalradian, Scotland, with particular reference to the zonation in garnet. *Contributions to Mineralogy and Petrology*, v. 18, p. 347-371.
- Baker, J.A. and Callahan, J.T. (1976) Water resources data for Massachusetts and Rhode Island, water year 1975. U.S. Geological Survey, Water Data Report MA-RI-75-1, 288 p.
- Beard, W.C. and Foster, W.R. (1976) High-temperature formation of anatase. *Journal of the American Ceramics Society*, v. 50, p. 493.
- Bence, A.E. and Albee, A.L. (1968) Empirical correction factors for the electron microanalysis of silicates and oxides. *Journal of Geology*, v. 76, p. 382-403.
- Billings, M.P. (1937) Regional metamorphism of the Littleton-Moosilauke area, New Hampshire. *Geological Society of America Bulletin*, v. 48, p. 463-566.
- \_\_\_\_\_, (1956) The Geology of New Hampshire, Part II-Bedrock Geology. New Hampshire State Planning and Development Commission, 203 p.
- Bird, G.W. and Fawcett, J.J. (1973) Stability relations of Mg chlorite-muscovite and quartz between 5 and 10 Kb water pressure. *Journal of Petrology*, v. 14, p. 415-423.
- Blatt, Harvey, Middleton, G.V., and Murray, Raymond (1972) Origin of Sedimentary Rocks. Prentice-Hall Incorporated, Englewood Cliffs, New Jersey, 634 p.
- Boles, J.R. and Coombs, D.S. (1977) Zeolite facies alteration of sanstones in the southland syncline, New Zealand. *American Journal of Science*, v. 277, p. 982-1012.
- Boucot, A.J. and Arndt, Robert (1960) Fossils of the Littleton Formation (Lower Devonian) of New Hampshire. U.S. Geological Survey Professional Paper 334-B, p. 37-60.
- \_\_\_\_\_, MacDonald, G.J.F., Milton, Charles, and Thompson, J.B., Jr. (1958) Metamorphosed middle Paleozoic fossils from central Massachusetts, eastern Vermont, and western New Hampshire. *Geological Society of America Bulletin*, v. 69, p. 855-870.

- \_\_\_\_\_, and Thompson, J.B. Jr. (1963) Metamorphosed Silurian brachiopods from New Hampshire. Geological Society of America Bulletin, v. 74, p. 1313-1334.
- Brindly, G.W. and Harrison, F.W. (1952) The structure of Chloritoid. Acta Crystallographica, v. 5, p. 688-692.
- Brookins, D.G. (1965) Rb-Sr study of the Ammonoosuc Volcanics-Monson gneiss problem, New England. Geological Society of America Abstracts, Kansas City Meeting, November 4-6, 1965, p. 19.
- \_\_\_\_\_, (1967) Rb-Sr age evidence for Permian metamorphism of the Monson gneiss, west central Massachusetts. Geochimica et Cosmochimica Acta, v. 31, p. 281-283.
- \_\_\_\_\_, (1968) Rb-Sr age of the Ammonoosuc Volcanics, New England. American Journal of Science, v. 266, p. 605-608.
- Campbell, A.S. and Fyfe, W.S. (1965) Analceme-albite equilibria. American Journal of Science, v. 263, p. 807-816.
- Chapman, C.A. (1942) Intrusive domes of the Claremont-Newport area, New Hampshire. Geological Society of America Bulletin, v. 53, p. 889-916.
- Chatterjee, N.D. and Froese, Edgar (1975) A thermodynamic study of the pseudobinary join muscovite-paragonite in the system  $\text{KAlSi}_3\text{O}_8\text{-NaAlSi}_3\text{O}_8\text{-Al}_2\text{O}_3\text{-SiO}_2\text{-H}_2\text{O}$ . American Mineralogist, v. 60, p. 985-993.
- \_\_\_\_\_, and Johannes, Wilhelm (1974) Thermal stability and standard thermodynamic properties of synthetic  $2\text{M}_1\text{-muscovite}$ ,  $\text{KAl}_2(\text{AlSi}_3\text{O}_{10})(\text{OH})_2$ . Contributions to Mineralogy and Petrology, v. 48, p. 89-114.
- Chayes, Felix (1955) Potash feldspar as a by-product of the biotite-chlorite transformation. Journal of Geology, v. 63, p. 75-82.
- Cheney, J.T. and Guidotti, C.V. (1979) Muscovite-plagioclase equilibria in sillimanite + quartz bearing metapelites, Puzzle Mountain area, northwest Maine. American Journal of Science, v. 279, p. 411-434.
- Chinner, G.A. (1967) Chloritoid, and the isochemical character of Barrow's zones. Journal of Petrology, v. 8, p. 268-282.

- Condie, K.C. (1967) Oxygen, carbon dioxide, and sulfur fugacities during diagenesis and low-grade metamorphism of late Precambrian subgraywackes from northern Utah. *American Mineralogist*, v. 52, p. 1153-1160.
- Coombs, D.S. (1954) The nature and alteration of some Triassic sediments from Southland, New Zealand. *Transactions of the Royal Society of New Zealand, Quarterly*, v. 82, pt. 1, p. 65-109.
- \_\_\_\_\_, Horodyski, R.J. and Naylor, R.S. (1970) Occurrence of prehnite-pumpellyite facies metamorphism in northern Maine. *American Journal of Science*, v. 268, p. 142-156.
- \_\_\_\_\_, Nakamura, Yasuo, and Vuagnat, M. (1976) Pumpellyite-actinolite facies schists of the Taveyanne Formation near Loèche, Valais, Switzerland. *Journal of Petrology*, v. 17, p. 440-471.
- Craig, J.R. and Scott, S.D. (1974) Sulfide phase equilibria. In, Ribbe, Editor, Sulfide Mineralogy, Mineralogical Society of America Short Course Notes, v. 1, p. CS-1 to CS-110.
- Cromer, D.T., and Herrington, K. (1955) The structures of anatase and rutile. *Journal of the American Chemical Society*, v. 77, p. 4708-4709.
- Dachille, Frank, Simons, P.Y., and Roy, Rustum (1968) Pressure-temperature studies of anatase, brookite, rutile, and  $\text{TiO}_2$ -II. *American Mineralogist*, v. 53, p. 1929-1939.
- \_\_\_\_\_, Simons, P.Y., and Roy, Rustum (1969) Pressure-temperature studies of anatase, brookite, rutile, and  $\text{TiO}_2$ -II: A reply. *American Mineralogist*, v. 54, p. 1481-1482.
- Day, H.W. (1973) The high temperature stability of muscovite plus quartz. *American Mineralogist*, v. 58, p. 255-262.
- Deer, W.A., Howie, R.A., and Zussman, Jack (1976) An Introduction to the Rock Forming Minerals. Longman Group Limited, London, 528 p.
- Dickinson, W.R. (1962) Metasomatic quartz keratophyre in central Oregon. *American Journal of Science*, v. 260, p. 249-266.
- Emerson, B.K. (1898) Geology of Old Hampshire county, Massachusetts, comprising Franklin, Hampshire, and Hampden Counties. U.S. Geological Survey Monograph, no. 29, 790 p.
- \_\_\_\_\_, (1917) Geology of Massachusetts and New Hampshire. U.S. Geological Survey Bulletin, no. 597, 289 p.

- Ernst, W.G. (1963) Significance of phengitic micas from low-grade schists. *American Mineralogist*, v. 48, p. 1357-1373.
- Eskola, P.E. (1948) The problem of mantled gneiss domes. *Geological Society of London Quarterly Journal*, v. 104, pt. 4, p. 461-476.
- Eugster, H.P., Albee, A.L., Bence, A.E., Thompson, J.B., Jr., and Waldbaum, D.R. (1972) The two-phase region and excess mixing properties of paragonite-muscovite crystalline solutions. *Journal of Petrology*, v. 13, p. 147-179.
- \_\_\_\_\_, and Wones, D.R. (1962) Stability relations of the ferruginous biotite, annite. *Journal of Petrology*, v. 3, p. 82-125.
- Evans, B.W. (1965) Application of a reaction-rate method to the breakdown equilibria of muscovite and muscovite plus quartz. *American Journal of Science*, v. 263, p. 647-667.
- \_\_\_\_\_, and Guidotti, C.V. (1966) The sillimanite-potash feldspar isograd in western Maine, U.S.A. *Contributions to Mineralogy and Petrology*, v. 12, p. 25-62.
- Van Eysinga, F.W.B. (1978) *Geologic Time Table*, 3rd Edition. Elsevier Scientific Publishing Company, Amsterdam, 1 sheet.
- Faul, Henry, Stern, T.W., Thomas, H.H., and Elmore, P.L.D. (1963) Ages of Intrusion and metamorphism in the northern Appalachians. *American Journal of Science*, v. 261, p. 1-19.
- Fawcett, J.J. (1963) The muscovite-chlorite-quartz assemblage. *Carnegie Institute of Washington Yearbook*, 1962 to 1963, no. 63, p. 137-141.
- \_\_\_\_\_, and Yoder, H.S. Jr. (1966) Phase relationships of chlorites in the system  $MgO-Al_2O_3-SiO_2-H_2O$ . *American Mineralogist*, v. 51, p. 353-380.
- Ferry, J.M. (1976)  $P, T, f_{CO_2}$ , and  $f_{H_2O}$  during metamorphism of calcareous sediments on the Waterville-Vassalboro area, south central Maine. *Contributions to Mineralogy and Petrology*, v. 57, p. 119-143.
- \_\_\_\_\_, (1978) Fluid interaction between granite and sediment during metamorphism, south-central Maine. *American Journal of Science*, v. 278, p. 1025-1056.

- \_\_\_\_\_, (1979) Reaction mechanisms, physical conditions, and mass transfer during hydrothermal alteration of mica and feldspar in granitic rocks from south-central Maine, U.S.A. *Contributions to Mineralogy and Petrology*, v. 68, p. 125-139.
- \_\_\_\_\_, (1980) A comparative study of geothermometers and geobarometers in pelitic schists from south-central Maine. *American Mineralogist*, v. 65, p. 720-732.
- \_\_\_\_\_, and Spear, F.S. (1977) Experimental calibration of the partitioning of Fe and Mg between biotite and garnet. *Geological Society of America Abstracts with Programs*, v. 9, p. 974.
- \_\_\_\_\_, and Spear, F.S. (1978) Experimental calibration of the partitioning of Fe and Mg between biotite and garnet. *Contributions to Mineralogy and Petrology*, v. 66, p. 113-117.
- French, B.M. (1966) Some geological implications of equilibrium between graphite and C-H-O gas phase at high temperatures and pressures. *Reviews of Geophysics*, v. 4, p. 223-253.
- \_\_\_\_\_, and Eugster, H.P. (1965) Experimental control of oxygen fugacities by graphite-gas equilibria. *Journal of Geophysical Research*, v. 70, p. 1529-1539.
- Frost, M.J. (1962) Metamorphic grade and iron-magnesium distribution between co-existing garnet-biotite and garnet-hornblende. *Geological Magazine*, v. 99, p. 427-438.
- Ganguly, Jibamitra (1969) Chloritoid stability and related parageneses: Theory, experiments, and applications. *American Journal of Science*, v. 267, p. 910-944.
- \_\_\_\_\_, (1972) Staurolite stability and related parageneses: Theory, experiments, and applications. *Journal of Petrology*, v. 13, p. 335-365.
- Ghent, E.D., Robbins, D.B., and Stout, M.Z. (1979) Geothermometry, geobarometry, and fluid compositions of metamorphosed calc-silicates and pelites, Mica Creek, British Columbia. *American Mineralogist*, v. 64, p. 874-885.
- Goldman, D.S. and Albee, A.L. (1977) Correlation of Fe/Mg partitioning between garnet and biotite with  $^{18}\text{O}/^{16}\text{O}$  partitioning between quartz and magnetite. *American Journal of Science*, v. 277, p. 750-767.



- Grant, J.A. and Weiblen, P.W. (1971) Retrograde zoning in garnet near the second sillimanite isograd. *American Journal of Science*, v. 270, p. 281-296.
- Gray, D.R. (1979) Microstructure of crenulation cleavages: An indicator of cleavage origin. *American Journal of Science*, v. 279, p. 97-128.
- Greenwood, H.J. (1975) Buffering of pore fluids by metamorphic reactions. *American Journal of science*, v. 275, p. 573-593.
- Griffen, D.T. and Ribbe, P.H. (1973) The crystal chemistry of staurolite. *American Journal of Science*, v. 273-A, p. 479-495.
- Guidotti, C.V. (1970) The mineralogy and petrology of the transition from the lower to upper sillimanite zone in the Oquossoc area, Maine. *Journal of Petrology*, v. 11, p. 277-336.
- \_\_\_\_\_, (1973) Compositional variation of muscovite as a function of metamorphic grade and assemblage in metapelites from N.W. Maine. *Contributions to Mineralogy and Petrology*, v. 42, p. 33-42.
- \_\_\_\_\_, (1974) Transition from staurolite to sillimanite zone, Rangely Quadrangle, Maine. *Geological Society of America Bulletin*, v. 85, p. 475-490.
- \_\_\_\_\_, (1978) Compositional variation of muscovite in medium- to high-grade metapelites of northwestern Maine. *American Mineralogist*, v. 63, p. 878-884.
- \_\_\_\_\_, Cheney, J.T., and Conatore, P.D. (1975a) Coexisting cordierite + biotite + chlorite from the Rumford Quadrangle, Maine. *Geology*, v. 3, p. 147-148.
- \_\_\_\_\_, Cheney, J.T., and Conatore, P.D. (1975b) Interrelationship between Mg/Fe ratio and octahedral Al content in biotite. *American Mineralogist*, v. 60, p. 849-853.
- \_\_\_\_\_, Cheney, J.T. and Guggenheim, Stephen (1977) Distribution of titanium between coexisting muscovite and biotite in pelitic schists from northwestern Maine. *American Mineralogist*, v. 62, p. 438-448.
- \_\_\_\_\_, and Sassi, F.P. (1976) Muscovite as a petrogenitic indicator mineral in pelitic schists. *Neues Jahrbuch für Mineralogie, Abhandlungen*, v. 127, no. 2, p. 97-142.

- Hadley, J.B. (1942) Stratigraphy, structure, and petrology of the Mt. Cube area, New Hampshire. Geological Society of America Bulletin, v. 53, p. 113-176.
- Halferdahl, L.B. (1961) Chloritoid: Its composition, X-Ray and optical properties, stability, and occurrence. Journal of Petrology v. 2, p. 49-135.
- Hall, D.J. (1970) Compositional variations in biotites and garnets from kyanite and sillimanite zone mica schists, Orange area, Massachusetts and New Hampshire. (M.S. thesis) Contribution no. 4, Department of Geology, University of Massachusetts, Amherst, 110 p.
- Harrison, F.W. and Brindley, G.W. (1957) The crystal structure of chloritoid. Acta Crystallographica, v. 10, p. 77-84.
- Harrison, J.E. and Campbell, A.B. (1963) Correlations and problems in Belt Series stratigraphy, northern Idaho and western Montana. Geological Society of America Bulletin, v. 74, p. 1413-1428.
- Harwood, D.S. and Berry, W.B.N. (1967) Fossiliferous lower Paleozoic rocks in the Cupsuptic Quadrangle, west-central Maine. U.S. Geological Survey Professional Paper 575-D, p. D16-D23.
- Hey, M.H. (1954) A new review of the chlorites. Mineralogical Magazine, v. 30, p. 277-292.
- Hietanen, Anna (1969) Distribution of Fe and Mg between garnet, staurolite, and biotite in aluminum-rich schist in various metamorphic zones north of the Idaho batholith. American Journal of Science, v. 267, p. 422-456.
- Hitchcock, C.H. (1877) Geology of the Connecticut Valley District, p. 271-465. In, Hitchcock, Huntington, Upham, and Hawes, Editors, The Geology of New Hampshire, Part II. Edward Jenks, State Printer, 685 p.
- \_\_\_\_\_, (1883) The early history of the North American continent. Science, v. 2, p. 293-297.
- \_\_\_\_\_, (1890) Significance of oval granitoid areas in the lower Laurentian. Geological Society of America Bulletin, v. 1, p. 557-558.
- Hitchcock, Edward (1841) Final Report on the Geology of Massachusetts, v. 2. 831 p.

- Holdaway, M.J. (1979) Stability of andalusite and the aluminum silicate phase diagram. *American Journal of Science*, v. 271, p. 97-131.
- \_\_\_\_\_, (1980) Chemical formulae and activity models for biotite, muscovite, and chlorite applicable to pelitic metamorphic rocks. *American Mineralogist*, v. 65, p. 711-719.
- \_\_\_\_\_, and Lee, S.M. (1977) Fe-Mg cordierite stability in high-grade pelitic rocks based on experimental, theoretical, and natural observations. *Contributions to Mineralogy and Petrology*, v. 63, p. 175-198.
- Holland, H.D. (1978) The Chemistry of the Atmosphere and Oceans. John Wiley and Sons, New York, 351 p.
- Hollister, L.S. (1966) Garnet zoning: An interpretation based on the Rayleigh fractionation model. *Science*, v. 154, p. 1647-1651.
- Hoschek, Gert (1967) Zur unteren stabilitätsgrenze von staurolith. *Naturwissenschaften*, v. 54, p. 200.
- \_\_\_\_\_, (1968) Zur oberen stabilitätsgrenze von staurolith. *Naturwissenschaften*, v. 55, p. 226-227.
- \_\_\_\_\_, (1969) The stability of staurolite and chloritoid and their significance in metamorphism of pelitic rocks. *Contributions to Mineralogy and Petrology*, v. 22, p. 208-232.
- Hsu, L.C. (1968) Selected phase relationships in the system Al-Mn-Fe-Si-O-H: A model for garnet equilibria. *Journal of Petrology*, v. 9, p. 40-83.
- Hubert, J.F., Reed, A.A., Dowdall, W.L., and Gilchrist, J.M. (1978) Guide to the Mesozoic redbeds of central Connecticut. State Geological and Natural History Survey of Connecticut, Guidebook no. 4, 129 p.
- Huebner, J.S. and Sato, Motoaki (1970) The oxygen fugacity-temperature relationships of manganese oxide and nickel oxide buffers. *American Mineralogist*, v. 55, p. 934-952.
- Huntington, J.C. (1975) Mineralogy and petrology of metamorphosed iron-rich beds in the Lower Devonian Littleton Formation, Orange area, Massachusetts. (M.S. thesis) Contribution no. 19, Geology Department, University of Massachusetts, Amherst, 106 p.

- Huntington, J.H. (1877) The gneissic area from Landaff to the southern boundary of the State, p. 466-517. In, Hitchcock, Huntington, Upham and Hawes, Editors, The Geology of New Hampshire, Part II, Chapter 5. Edward Jenks, State Printer, 685 p.
- Hutcheon, Ian (1979) Sulfide-oxide-silicate equilibria; Snow Lake, Manitoba. *American Journal of Science*, v. 279, p. 643-665.
- Itaya, Tetsumaru and Banno, Shohei (1980) Paragenesis of titanium-bearing accessories in pelitic schists of the Sanbagawa metamorphic belt, central Shikoku, Japan. *Contributions to Mineralogy and Petrology*, v. 73, p. 267-276.
- Jamieson, J.C. and Olinger, Bart (1969) Pressure-temperature studies of anatase, brookite, rutile, and  $\text{TiO}_2$ -II: A discussion. *American Mineralogist*, v. 54, p. 1477-1481.
- Jean-Louis, Robert (1975) An experimental study of phlogopite solid solutions in the system  $\text{K}_2\text{O}-\text{MgO}-\text{Al}_2\text{O}_3-\text{SiO}_2-\text{H}_2\text{O}$ , solubility of titanium in phlogopite solid solutions. *Geological Society of America*, abstracts with programs, v. 7, no. 6, p. 844-845.
- Juurinen, Aarno (1956) Composition and properties of staurolite. *Suomalaisen Tiededatemian Toimituksia, Annales, Academiae Scientiarum Fennicae*, series A-III, geologica-geographica, v. 48, p. 1-55.
- Kerrick, D.M. (1972) Experimental determination of muscovite + quartz stability with  $\text{PH}_2\text{O} < \text{P}_{\text{total}}$ . *American Journal of Science*, v. 272, p. 946-958.
- King, P.B. (1969) Tectonic Map of North America. Compiled by King, U.S. Geological Survey, scale 1:5,000,000, two sheets.
- Kramm, Ulrich (1973) Chloritoid stability in manganese rich low-grade metamorphic rocks, Venn-Stavelot Massif, Ardennes. *Contributions to Mineralogy and Petrology*, v. 41, p. 179-196.
- Krauskopf, K.B. (1967) Introduction to Geochemistry. McGraw-Hill Book Company, New York, 721 p.
- Kwak, T.A.P. (1968) Ti in biotite and muscovite as an indication of metamorphic grade in almandine amphibolite facies rocks from Sudbury, Ontario. *Geochimica et Cosmochimica Acta*, v. 32, p. 1222-1229.

- Labotka, T.C. (1980) Petrology of a medium-pressure regional metamorphic terrane, Funeral Mountains, California. *American Mineralogist*, v. 65, p. 670-689.
- Lindh, Anders (1972) A hydrothermal investigation of the system  $\text{FeO}$ ,  $\text{Fe}_2\text{O}_3$ ,  $\text{TiO}_2$ . *Lithos*, v. 5, p. 325-343.
- Lindsley, D.H. (1973) Delimitation of the hematite-ilmenite miscibility-gap. *Geological Society of America Bulletin*, v. 84, p. 657-662.
- \_\_\_\_\_, (1976) The crystal chemistry and structure of oxide minerals as exemplified by the Fe-Ti oxides, p. 1-88. In, Rumble, Editor, Oxide Minerals, Mineralogical Society of America Short Course Notes, v. 3, Southern Printing Company, Blacksburg, Virginia, 579 p.
- Lundgren, Lawrence Jr. (1962) Deep River area, Connecticut: Stratigraphy and structure. *American Journal of Science*, v. 260, p. 1-23.
- Lyons, J.B. and Morse, S.A. (1970) Mg/Fe partitioning in garnet and biotite from some granitic, pelitic, and calcic rocks. *American Mineralogist*, v. 55, p. 231-245.
- Makower, Jordan (1964) Geology of the Prescott intrusive complex, Quabbin Reservoir Quadrangle, Massachusetts. M.S. thesis, University of Massachusetts, Amherst, 91 p.
- Mason, Brian (1966) Principals of Geochemistry, 3rd edition. John Wiley and Sons, New York, 329 p.
- Mather, J.D. (1970) The biotite isograd and the lower greenschist facies in the Dalradian rocks of Scotland. *Journal of Petrology*, v. 11, p. 253-275.
- McNamara, M.J. (1965) The lower greenschist facies in the Scottish Highlands. *Geologiska Foreningens i Stockholm Forhandlingar*, v. 87, p. 347-389.
- \_\_\_\_\_, (1966) Chlorite-biotite equilibrium reactions in a carbonate-free system. *Journal of Petrology*, v. 7, p. 404-413.
- Mielke, H. and Schreyer, Werner (1972) Magnetite-rutile assemblages in metapelites of Fichtelgebirge, Germany. *Earth and Planetary Science Letters*, v. 16, p. 423-428.
- Mitchell, R.S. (1964) Pseudomorphs of anatase after sphene from Roanoke County, Virginia. *American Mineralogist*, v. 49, p. 1136-1139.

- Moore, G.E. (1949) Structure and metamorphism of the Keene-Brattleboro area, New Hampshire-Vermont. Geological Society of America Bulletin, v. 60, p. 1613-1670.
- Morse, S.A. (1970) Alkali feldspars with water at 5 kb pressure. Journal of Petrology, v. 11, p. 221-251.
- Müller, Georg and Schneider, Alfred (1979) Chemistry and genesis of garnets in metamorphic rocks. Contributions to mineralogy and Petrology, v. 31, p. 178-200.
- Náray-Szabó, I. and Sasvári, K. (1958) On the structure of staurolite,  $\text{HFe}_2\text{Al}_9\text{Si}_4\text{O}_{24}$ . Acta Crystallographica, v. 11, p. 862-865.
- Naylor, R.S. (1968) Origin and regional relationships of the core-rocks of the Oliverian domes, p. 231-240. In, Zen, White, Hadley, and Thompson, Editors, Studies of Appalachian Geology: Northern and Maritime. John Wiley and Sons, New York, 475 p.
- \_\_\_\_\_, (1969) Age and origin of the Oliverian domes, west-central New Hampshire. Geological Society of America Bulletin, v. 80, p. 405-428.
- \_\_\_\_\_, (1971a) Acadian orogeny: An abrupt and brief event. Science, v. 172, p. 558-560.
- \_\_\_\_\_, (1971b) Geology of Mascoma mantled gneiss dome near Hanover, New Hampshire, p. 28-37. In, Lyons and Stewart, Editors, New England Intercollegiate Geological Conference Guidebook, 63rd annual meeting, 125 p.
- \_\_\_\_\_, Boone, G.M., Boudette, E.L., Ashenden, D.D., and Robinson, Peter (1973) Pre-Ordovician rocks in the Bronson Hill and Boundary Mountain anticlinoria, New England, U.S.A. Transactions of the American Geophysical Union, v. 54, p. 495.
- \_\_\_\_\_, and Boucot, A.J. (1965) Origin and distribution of rocks of Ludlow age (Late Silurian) in the northern Appalachians. American Journal of Science, v. 263, p. 153-169.
- Newton, R.C. (1966) Kyanite-andalusite equilibrium from 700°C to 800°C. Science, v. 153, p. 170-173.
- \_\_\_\_\_, and Wood, B.J. (1979) Thermodynamics of water in cordierite and some petrologic consequences of cordierite as a hydrous phase. Contributions to Mineralogy and Petrology, v. 68, p. 391-405.

- Ohmoto, Hiroshi and Kerrick, D.M. (1977) Devolatilization equilibria in graphitic systems. *American Journal of Science*, v. 277, p. 1013-1044.
- Osborn, E.F. (1953) Subsolidus reactions in oxide systems in the presence of water at high pressures. *Journal of the American Ceramics Society*, v. 36, p. 147-151.
- Page, L.R. (1968) Devonian plutonic rocks in New England, p. 371-383. In, Zen, White, Hadley, Thompson, Editors, Studies of Appalachian Geology: Northern and Maritime, John Wiley and Sons, New York, 475 p.
- Ramsay, C.R. (1973) The origin of biotite in Archaean metasediments near Yellowknife, N.W.T., Canada. *Contributions to Mineralogy and Petrology*, v. 42, p. 43-54.
- Rao, C.N.R. (1961) Kinetics and thermodynamics of the crystal structure transformation of spectroscopically pure anatase to rutile. *Canadian Journal of Chemistry*, v. 36, p. 498-500.
- Ribbe, P.H. (1980a) Chloritoid, p. 155-169. In, Ribbe, Editor, Orthosilicates, Mineralogical Society of America Reviews of Mineralogy, v. 5, 381 p.
- \_\_\_\_\_, (1980b) Titanite, p. 137-154. In, Ribbe, Editor, Orthosilicates, Mineralogical Society of America Reviews of Mineralogy, v. 5, 381 p.
- Richardson, S.W. (1967a) The composition of synthetic Fe-staurolite. *Carnegie Institute of Washington Yearbook*, 1966-1967, v. 66, p. 397-398.
- \_\_\_\_\_, (1967b) The stability of Fe staurolite + quartz. *Carnegie Institute of Washington Yearbook*, 1966-1967, v. 66, p. 398-402.
- \_\_\_\_\_, (1968) Staurolite stability in a part of the system Fe-Al-Si-O-H. *Journal of Petrology*, v. 9, p. 467-488.
- \_\_\_\_\_, Bell, P.M., and Gilbert, M.C. (1968) Kyanite-sillimanite equilibrium between 700°C and 1500°C. *American Journal of Science*, v. 266, p. 513-541.
- \_\_\_\_\_, Gilbert, M.C., and Bell, P.M. (1969) Experimental determination of Kyanite-andalusite and andalusite-sillimanite equilibria; the aluminum silicate triple point. *American Journal of Science*, v. 267, p. 259-272.

- Robie, R.A., Hemingway, B.S., and Fisher, J.R. (1978) Thermodynamic properties of minerals and related substances at 298.15°K and 1 bar (10<sup>5</sup>pascals) pressure and higher temperatures. U.S. Geological Survey Bulletin, no. 1452, 456 p.
- Robinson, Peter (1963) Gneiss Domes of the Orange Area, Massachusetts and New Hampshire. Ph.D. Thesis, Harvard University, Cambridge, 253 p.
- \_\_\_\_\_, (1966) Aluminosilicate polymorphs and Paleozoic erosion rates in central Massachusetts. Transactions of the American Geophysical Union, v. 47, p. 424.
- \_\_\_\_\_, (1967a) Gneiss domes and recumbent folds of the Orange area, west central Massachusetts, p. 12-47. In, Robinson and Drake, Editors, New England Intercollegiate Geological Conference Guidebook, 59th annual meeting, 194 p.
- \_\_\_\_\_, (1967b) Introduction to the Geology of the Connecticut Valley of Massachusetts, p. 1-6. In, Robinson and Drake, Editors, New England Intercollegiate Geological Conference Guidebook, 59th annual meeting, 194 p.
- \_\_\_\_\_, (1967c) Progress of bedrock geologic mapping in west central Massachusetts, p. 29-44. In, Farquhar, Editor, Economic Geology in Massachusetts: Proceedings of a conference in January 1966. Published by the Graduate School, University of Massachusetts, 569 p.
- \_\_\_\_\_, (1977) Sulfide-silicate-oxide equilibria in sillimanite-K-feldspar grade pelitic schists, central Massachusetts. Transactions of the American Geophysical Union, v. 58, p. 524.
- \_\_\_\_\_, (1979) Bronson Hill anticlinorium and Merrimack synclinorium in central Massachusetts, p. 126-174. In, The Caledonides in the U.S.A., Contributions to the International Geological Correlation Program, Project 27. Western Observatory Publishers, 250 p.
- \_\_\_\_\_, Thompson, J.B. Jr., and Rosenfeld, J.L. (1979) Nappes, gneiss domes, and regional metamorphism in western New Hampshire and central Massachusetts, p.93-116. In, The Caledonides in the U.S.A., Contributions to the International Geological Correlation Program, Project 27. Western Observatory Publishers, 250 p.



- \_\_\_\_\_, Tracy, R.J., and Ashwal, L.D. (1975) Relict sillimanite-orthoclase assemblage in kyanite-muscovite schist, Pelham dome, west-central Massachusetts. *Transactions of the American Geophysical Union*, v. 56, p. 466.
- Rosenfield, J.L. (1956) Paragonite in the schist of Glebe Mountain, southern Vermont. *American Mineralogist*, v. 41, p. 144-147.
- \_\_\_\_\_, Thompson, J.B., and Zen, E-an (1958) Data on coexistent muscovite and paragonite. *Geological Society of America Bulletin*, v. 69, p. 1637.
- Rumble, Douglas III (1971) Fe-Ti oxide minerals and the behavior of oxygen during regional metamorphism. *Carnegie Institute of Washington Yearbook*, 1970-1971, v. 70, p. 157-160.
- \_\_\_\_\_, (1976) Oxide minerals in metamorphic rocks, p. R-1 to R-20. In, Rumble, Editor, Oxide Minerals, Mineralogical Society of America Short Course Notes, v. 3, 499 p.
- \_\_\_\_\_, (1978) Geochemistry of the Clough Formation, Black Mountain, Western New Hampshire, U.S.A. *Journal of Petrology*, v. 19, p. 317-340.
- Sassi, F.P. and Scolari, A. (1974) The  $b_0$  value of the potassic white micas as a barometric indicator in low-grade metamorphism of pelitic schists. *Contributions to Mineralogy and Petrology*, v. 45, p. 143-152.
- Saxena, S.K. (1968) Distribution of elements between coexisting minerals and the nature of solid solution in garnet. *American Mineralogist*, v. 53, p. 994-1014.
- \_\_\_\_\_, (1969) Silicate solid solutions and geothermometry. *Contributions to Mineralogy and Petrology*, v. 22, p. 259-267.
- Schuling, R.D. and Vink, B.W. (1967) Stability relations of some titanium-minerals (sphen, perovskite, rutile, anatase). *Geochimica et Cosmochimica Acta*, v. 31, p. 2399-2411.
- Seifert, Friedrich (1970) Low-temperature compatibility relations of cordierite in haplopelites of the system  $K_2O-MgO-Al_2O_3-SiO_2-H_2O$ . *Journal of Petrology*, v. 11, p. 73-99.
- Shannon, R.D. and Pask, J.A. (1965) Kinetics of the anatase-rutile transformation. *Journal of the American Ceramic Society*, v. 48, p. 391-398.

- Smith, J.V. (1968) The crystal structure of staurolite. *American Mineralogist*, v. 53. p. 1139-1155.
- \_\_\_\_\_, (1975) Phase equilibria of plagioclase, p. Sm-1 to Sm-17. In, Ribbe, Editor, Feldspar Mineralogy, Mineralogical Society of America Short Course Notes, v. 2, Southern Printing Company, Blacksburg, Virginia, 362 p.
- Spencer, K.J. and Lindsley, D.H. (1978) New experimental results on the magnetite-ulvöspinel, hematite-ilmenite solution model using the Co-CoO buffer. *Geological Society of America Abstracts with Programs*, v. 10, p. 496.
- \_\_\_\_\_, and Lindsley, D.H. (in press) A solution model for coexisting iron-titanium oxides. 24 p.
- Springer, Gunter (1976) Correction procedures in electron-probe analysis, p. 45-62. In, Smith, Editor, Mineralogical Association of Canada, Short Course in Microbeam Techniques, v. 1. Co-Op Press, Edmonton, 186 p.
- Steiger, R.H. and Jager, Ernst (1977) Subcommittee on Geochronology: Convention on the use of decay constants in geo- and cosmo-chronology. *Earth and Planetary Science Letters*, v. 36, p. 359-362.
- Stone, B.D. (1976) Stratigraphy and field analysis of glacial deposits near Worcester, Massachusetts, p. 975-182. In, Cameron, Editor, New England Intercollegiate Geological Conference Guidebook, 68th annual meeting, 513 p.
- Stormer, J.C. Jr. (1975) A practical two-feldspar geothermometer. *American Mineralogist*, v. 60, p. 667-674.
- Tompkins, L.A., McMahon, Brendan, and Haggerty, S.E. (1980) Experimental studies in the system  $\text{FeO-TiO}_2\text{-Fe}_2\text{O}_3$  with a bearing on the Fe-Ti oxide geobarometer-geothermometer. Unpublished manuscript, Department of Geology, University of Massachusetts, Amherst.
- Thompson, A.B. (1974) Calculation of muscovite-paragonite-alkali feldspar phase relations. *Contributions to Mineralogy and Petrology*, v. 44, p. 173-194.
- \_\_\_\_\_, (1976a) Continuous reaction histories deduced from compositional zonation and mineral inclusions in garnet from Gassetts, Vermont. *Transactions of the American Geophysical Union*, v. 57, p. 339.

- \_\_\_\_\_, (1976b) Mineral reactions in pelitic rocks: I. Prediction of P-T-X(Fe-Mg) phase relations. *American Journal of Science*, v. 276, p. 401-424.
- \_\_\_\_\_, (1976c) Mineral reactions in Pelitic rocks: II. Calculation of some P-T-X(Fe-Mg) phase relations. *American Journal of Science*, v. 276, p. 425-454.
- \_\_\_\_\_, Lyttle, P.T., and Thompson, J.B. Jr. (1977) Mineral reactions and A-Na-K and A-F-M facies types in the Gassetts schist, Vermont. *American Journal of Science*, v. 277, p. 1124-1151.
- Thompson, J.B. Jr. (1957) The graphical analysis of mineral assemblages in pelitic schists. *American Mineralogist*, v. 42, p. 842-858.
- \_\_\_\_\_, (1972) Oxidies and sulfides in regional metamorphism of pelitic schists. 24th International Geological Congress, Section 10, p. 27-78.
- \_\_\_\_\_, Robinson, Peter, Clifford, T.N., and Trask, N.J. (1968) Nappes and gneiss domes in west-central New England, p. 203-213. In: Zen, White, Hadley, and Thompson, Editors, Studies of Appalachian Geology: Northern and Maritime. John Wiley and Sons, New York, 475 p.
- \_\_\_\_\_, and Thompson, A.B. (1976) A model system for mineral facies in pelitic schists. *Contributions to Mineralogy and Petrology*, v. 58, p. 243-277.
- Toulmin, Priestley III, and Barton, P.B. Jr. (1964) A thermodynamic study of pyrite and pyrrhotite. *Geochimica et Cosmochimica Acta*, v. 28, p. 641-671.
- Tracy, R.J. (1975) High Grade Metamorphic Reactions and Partial Melting in Pelitic Schists, Quabbin Reservoir Area, Massachusetts, Ph.D. Thesis, University of Massachusetts, Amherst, 128 p.
- \_\_\_\_\_, (1978) High grade metamorphic reactions and partial melting in pelitic schist, west-central Massachusetts. *American Journal of Science*, v. 278, p. 150-178.
- \_\_\_\_\_, Robinson, Peter, and Thompson, A.B. (1976) Garnet composition and zoning in the determination of temperature and pressure of metamorphism, central Massachusetts. *American Mineralogist*, v. 61, p. 762-775.

- Tucker, R.D. (1977) Bedrock geology of the Barre area, central Massachusetts. (M.S. thesis) Contribution no. 30, Department of Geology, University of Massachusetts, Amherst, 132 p.
- Turner, F.J. (1968) Metamorphic Petrology, Mineralogical and Field Aspects. Press, Editor, McGraw-Hill Book Company, New York, 403 p.
- Turnock, A.C. (1960) The stability of iron chlorites. Carnegie Institute of Washington Yearbook 1959-1960, v. 59, p. 98-103.
- Van der Voort, J.L. (1978) Inclusion patterns in garnets from the Puzzle Mountain area, Maine: Their relationship to crystal growth and structure. Honors Thesis, Smith College, 100 p.
- Velde, Bruce (1965) Phengite micas: Synthesis, stability, and natural occurrence. American Journal of Science, v. 263, p. 886-913.
- Verne, Jules (1864) A Journey to the Center of the Earth. Great Illustrated Classics, Dodd and Mead and Company, New York, 1959 ed., 242 p.
- Weast, R.C. (1976) Handbook of Chemistry and Physics. Weast, Editor, CRC Press, Cleveland, Ohio, 2390 p.
- Wenk, Eduard (1970) Distribution of Al between coexisting micas in metamorphic rocks from the central Alps. Contributions to Mineralogy and Petrology, v. 26, p. 50-61.
- Whitney, J.A. and Stormer, J.C. Jr. (1977) The distribution of  $\text{NaAlSi}_3\text{O}_8$  between coexisting microcline and plagioclase and its effect on geothermometric calculations. American Mineralogist, v. 62, p. 687-691.
- Wolff, R.A. (1978) Ultramafic lenses in the Middle Ordovician Partridge Formation, Bronson Hill anticlinorium, central Massachusetts. (M.S. thesis) Contribution no. 34, Department of Geology, University of Massachusetts, Amherst, 162 p.
- Yakowitz, H., Myklebust, R.L., and Heinrich, K.F.J. (1973) FRAME: An on-line correction procedure for quantitative electron probe microanalysis. U.S. National Bureau of Standards, Technical Note no. 796, 47 p.
- Zartman, R.E., Hurley, P.M., Krueger, H.W., and Giletti, B.J., (1970) A Permian disturbance of K-Ar radiometric ages in New England: Its occurrence and cause. Geological Society of America Bulletin, v. 81, p. 3359-3374.

- Zen, E-An (1960) Metamorphism of lower Paleozoic rocks in the vicinity of the Taconic Range in west-central Vermont. American Mineralogist, v. 45, p. 129-175.
- \_\_\_\_\_, and Albee, A.L. (1964) Coexistent muscovite and paragonite in pelitic schists. American Mineralogist, v. 49, p. 904-925.



